Effective Date: June 3, 2011
Revision -

GSFC JPSS CMO
January 3, 2012
Released

Joint Polar Satellite System (JPSS) Ground Project
Code 474
474-00096

Joint Polar Satellite System (JPSS) NPP Operational Algorithm Proxy and Synthetic Test Data Description

For Public Release

The information provided herein does not contain technical data as defined in the International Traffic in Arms Regulations (ITAR) 22 CFC 120.10. This document has been approved For Public Release.

Goddard Space Flight Center
Greenbelt, Maryland

National Aeronautics and Space Administration

Check the JPSS MIS Server at https://jpssmis.gsfc.nasa.gov/frontmenu_dsp.cfm to verify that this is the correct version prior to use.

This page intentionally left blank.

Joint Polar Satellite System (JPSS) NPP Operational Algorithm Proxy and Synthetic Test Data Description

JPSS Electronic Signature Page

Prepared By:

Neal Baker
JPSS Data Products and Algorithms, Senior Engineering Advisor
(Electronic Approvals available online at (https://jpssmis.gsfc.nasa.gov/mainmenu_dsp.cfm)

Approved By:

Heather Kilcoyne
DPA Manager
(Electronic Approvals available online at (https://jpssmis.gsfc.nasa.gov/mainmenu_dsp.cfm)

Goddard Space Flight Center
Greenbelt, Maryland

Check the JPSS MIS Server at https://jpssmis.gsfc.nasa.gov/frontmenu_dsp.cfm to verify that this is the correct version prior to use.

This page intentionally left blank.

Check the JPSS MIS Server at https://jpssmis.gsfc.nasa.gov/frontmenu_dsp.cfm to verify that this is the correct version prior to use.

Preface

This document is under JPSS Ground AERB configuration control. Once this document is approved, JPSS approved changes are handled in accordance with Class I and Class II change control requirements as described in the JPSS Configuration Management Procedures, and changes to this document shall be made by complete revision.

Any questions should be addressed to:

JPSS Ground Project Configuration Management Office
NASA/GSFC
Code 474
Greenbelt, MD 20771

Check the JPSS MIS Server at https://jpssmis.gsfc.nasa.gov/frontmenu_dsp.cfm to verify that this is the correct version prior to use.

This page intentionally left blank.

Check the JPSS MIS Server at https://jpssmis.gsfc.nasa.gov/frontmenu_dsp.cfm to verify that this is the correct version prior to use.

Change History Log

Revision	Effective Date	Description of Changes (Reference the CCR & CCB/ERB Approve Date)
Original	06/03/2011	This version incorporates **474-CCR-11-0110** which converts D45702, NPP Operational Algorithm Proxy and Synthetic Test Data Description, Rev A dated 10/30/2008 to a JPSS document, Rev -. This was approved by the JPSS Ground Algorithm ERB on June 3, 2011.

Check the JPSS MIS Server at https://jpssmis.gsfc.nasa.gov/frontmenu_dsp.cfm to verify that this is the correct version prior to use.

This page intentionally left blank.

Check the JPSS MIS Server at https://jpssmis.gsfc.nasa.gov/frontmenu_dsp.cfm to verify that this is the correct version prior to use.

Northrop Grumman Space & Mission Systems Corp.
Space Technology
One Space Park
Redondo Beach, CA 90278

Engineering & Manufacturing Development (EMD) Phase
Acquisition & Operations Contract

CAGE NO. 11982

NPP Operational Algorithm
Proxy and Synthetic Test Data Description

Document Number: D45702

Document Date: 10/30/08 **Revision: A**

Point of Contact: Bruce Hauss,
Algorithms, Models and Simulation

ELECTRONIC APPROVAL SIGNATURES:

_____ _____
Merit Shoucri, Algorithms, Models and Simulation Lead

_____ _____

_____ _____

_____ _____

Prepared by
Northrop Grumman Space Technology
One Space Park
Redondo Beach, CA 90278

Prepared for
Department of the Air Force
NPOESS Integrated Program Office
C/O SMC/CIK
2420 Vela Way, Suite 1467-A8
Los Angeles AFB, CA 90245-4659

Under
Contract No. F04701-02-C-0502

COMMERCE DESTINATION CONTROL STATEMENT

The export of these commodities, technology or software are subject to the U.S. Export Laws and Regulations in accordance with the Export Administration Regulations. Diversion contrary to U.S. law is prohibited.

Use or disclosure of data contained on this page is subject to the export restriction(s) on the title page of this document.

D45702, A. PDMO Released: 2009-02-18 (VERIFY REVISION STATUS)
PDMO

Northrop Grumman Space & Mission Systems Corp.
Space Technology
One Space Park
Redondo Beach, CA 90278

NORTHROP GRUMMAN

Raytheon

Revision/Change Record

Document Number D45702

Revision	Document Date	Revision/Change Description	Pages Affected
---	20 Dec 07	Original PCIM release	All
A	30 Oct 08	Upgrading NPP VIIRS Proxy Data for Field Terminal Compression Studies	Sec 3.3

Use or disclosure of data contained on this page is subject to the export restriction(s) on the title page of this document.

D45702, A. PDMO Released: 2009-02-18 (VERIFY REVISION STATUS)
PDMO

Table Of Contents

1.0 INTRODUCTION 2
2.0 SYNTHETIC DATA FROM END-TO-END SIMULATION 4
2.1 Geophysical Data Generation 4
2.1.1 Assembling Atmospheric and Surface Properties from NWP Analyses 5
2.1.2 Validation Status of the NCEP AVN-FNL Tropospheric Data 5
2.1.3 Extending the Atmospheric Profiles to Top-of-Atmosphere 8
2.1.4 Generating the Physical and Optical Properties of High-Resolution 3D Clouds 10
2.1.5 Atmospheric and Cloud Properties for Structured Scenes 12
2.1.6 Aerosol Properties for Global Datasets 13
2.1.7 Terrain Properties 14
2.2 Generating Sampled Global Test Dataset 47
2.3 Radiative Transfer Models 53
2.3.1 RTMs Used for VIIRS Testing 53
2.3.2 RTM(s) for CrIS/ATMS Testing 54
2.3.3 RTM for CMIS Testing 54
2.4 Sensor Models 70
2.4.1 VIIRS Sensor Model 71
2.4.2 CrIS/ATMS Sensor Models 71
2.4.3 CMIS Sensor Model 72
3.0 PROXY DATA - UTILIZING DATA FROM DEPLOYED SENSORS 74
3.1 Proxy Data used for Extended Functionality and Performance Testing 74
3.2 Proxy Data used for End-to-End Testing of Operational Code by IDPS 76
3.3 Upgrading NPP VIIRS Proxy Data for Field Terminal Compression Studies 79
3.3.1 Mirroring Instead of Replicating Pixels beyond MODIS Edge-of-Swath 79
3.3.2 Fixing Pixel Striping in VIIRS Band M10 80
3.3.3 Improved Radiance Values for Replacing Saturated Pixels 81
3.3.4 Adjusting MODIS Radiance Values for Consistency with VIIRS RSRs 84
3.3.5 Pixels Assigned a Zero Radiance 85
4.0 SPECIAL GLOBAL TEST DATASETS FOR VERIFYING THE ACO/OCC ALGORITHMS 111
4.1 New Global Synthetic and *In Situ* Datasets 112

Use or disclosure of data contained on this page is subject to the export restriction(s) on the title page of this document.

D45702, A. PDMO Released: 2009-02-18 (VERIFY REVISION STATUS)
PDMO

4.1.1 Datasets for Assessing the Performance of the VIIRS OCC Algorithm.... 112
4.1.2 Dataset for Assessing the Performance of the VIIRS ACO Algorithm..... 119

Use or disclosure of data contained on this page is subject to the export restriction(s) on the title page of this document.

D45702, A. PDMO Released: 2009-02-18 (VERIFY REVISION STATUS)
PDMO

List of Figures

Figure 2-1. Process for Generating Global Synthetic Test Datasets 17

Figure 2-2. Illustration of several of the atmospheric profiles provided in the NCEP AVN-FNL tropospheric datasets 19

Figure 2-3. CEP atmospheric profiles have been assessed against other NWP models and observations. Analysis of Temperature Fields Versus RS90/Lidar at Barking Sands, Kauai (courtesy of John Wessel, Aerospace Corp) 20

Figure 2-4. CEP atmospheric profiles have been assessed against other NWP models and observations. Analysis of Moisture Fields Versus RS90/Lidar at Barking Sands, Kauai (courtesy of John Wessel, Aerospace Corp) 21

Figure 2-5. Comparison of NCEP SSWS with SSM/I SSWS for July 26th 2001 at 12Z . 22

Figure 2-6. Comparison of NCEP sea-surface temperature with the sea-surface temperature measured by TMI 23

Figure 2-7. NCEP distributions of the difference between the near-surface air temperature and the land and sea skin temperatures exhibit the natural correlations that should exist in realistic environmental data. 24

Figure 2-8. Comparison of NCEP AVN-FNL total cloud liquid water to a GMS infrared satellite image of South East Asia 25

Figure 2-9. Illustration of process for smoothly transitioning between NCEP and climatology temperature profiles 26

Figure 2-10. Extending other key atmospheric profiles (H_2O_v and O_3) to TOA..... 27

Figure 2-11. Sample profiles of temperature, moisture and ozone constructed from NCEP NWP reanalysis data and CIRA-86 and UARS reference atmospheres 28

Figure 2-12. CSSM process for generating water/ice content and precipitation data on a high-resolution gridded domain for each input NCEP AVN profile 29

Figure 2-13. Scatter plot of ln(CIWMMR/CLWMMR) and temperature for points in the ECMWF 60L-SD global dataset. The red curve represents a third-order polynomial best fit to the data 30

Figure 2-14. ISCCP radiometric cloud classification 31

Figure 2-15. High-resolution, 3D cloud structure and physical properties for Global Synthetic Test Datasets generated by the NGIT Cloud Scene Simulation Model 32

Figure 2-16. Cloud properties computed within each sensor FOV are tailored to the sensor-specific footprint sizes for VIIRS, CrIS, ATMS, and CMIS, as well as the required RTM inputs for each sensor 33

Figure 2-17. Utilizing CSSM clouds with 3x3 CrIS footprints for use by AER OSS RTM34

Use or disclosure of data contained on this page is subject to the export restriction(s) on the title page of this document.

D45702, A. PDMO Released: 2009-02-18 (VERIFY REVISION STATUS)
PDMO

Figure 2-18. One way of verifying Mie Scattering computations of cloud optical properties is by comparison with optical properties for cloud models used by LOWTRAN/MODTRAN 36

Figure 2-19. Final cloud type is assigned based on liquid/ice water content and cloud height 37

Figure 2-20. Comparisons of MM5 results with RaObs data have been made to check that MM5 provides “realistic” profiles 38

Figure 2-21. Altitude dependent aerosol concentration is scaled via the surface meteorological range to approximate the MODIS 8-day AOT values 39

Figure 2-22. Comparisons of the spectral albedo as a function of snow grain size, soot particle size, soot concentration, and solar angle were made to data in the ASTER Spectral Library and to the literature 40

Figure 2-23. Laboratory measurements of the spectral reflectance for vegetation components (e.g., leaves from a deciduous tree or needles from a coniferous tree) compared to in-field measurements of the entire tree 42

Figure 2-24. Expected correlation between SWIR and visible reflectance is contained in new PRA spectral albedo library 44

Figure 2-25. National Land Cover Database (NLCD) provides land cover type at 30 meter resolution over CONUS 45

Figure 2-26. Synthetic true color, high-resolution reflectance imagery generated from NLCD land cover types with directional-hemispherical reflectances generated from the ASTER Spectral Libraries 46

Figure 2-27. Spatial sampling approach produces comprehensive and representative test datasets 49

Figure 2-28. Illustration of new crosstrack pixel sampling approach 50

Figure 2-29. Sampling approach provides near uniform global coverage 51

Figure 2-30. The Global Synthetic Test Dataset covers a comprehensive set of atmosphere/surface conditions for assessing system performance..... 52

Figure 2-31. Verifying modifications to MODTRAN-4 for utilizing user-supplied terrain/ocean BRDF tables..... 59

Figure 2-32. Atmospheric Profiles (42) Supplied by ITWG for Intercomparison Study .. 60

Figure 2-33. Difference Between PW Derived from ITWG Profiles and that Specified by ITWG Value 61

Figure 2-34. Brightness Temperature Comparison for AMSU-A Channel 6 62

Figure 2-35. Brightness Temperature Differences for Channel 6 Using Different LBL Models as Reference 63

Figure 2-36. Brightness Temperature Comparison for AMSU-A Channel 10 64

Use or disclosure of data contained on this page is subject to the export restriction(s) on the title page of this document.

D45702, A. PDMO Released: 2009-02-18 (VERIFY REVISION STATUS)
PDMO

Figure 2-37. Brightness Temperature Differences for Channel 10 Using Different LBL Models as Reference 65

Figure 2-38. Brightness Temperature Comparison for AMSU-A Channel 14 66

Figure 2-39. Brightness Temperature Differences for Channel 14 Using Different LBL Models as Reference 67

Figure 2-40. Brightness Temperature Comparison for AMSU-B Channel 18 68

Figure 2-41. Brightness Temperature Differences for Channel 18 Using Different LBL Models as Reference 69

Figure 2-42. NGST Generic Vis/IR sensor model used for VIIRS 73

Figure 3-1. Geographical and seasonal coverage by proxy granules selected for extended performance testing 86

Figure 3-2. End-to-end process for generating proxy data used for assessing readiness of NPP ground processing 88

Figure 3-3. Spacecraft ephemeris for each of the 6 two-orbit NPP proxy datasets 89

Figure 3-4. Alignment of NPP and EOS-Aqua orbits for each two-orbit proxy dataset .. 90

Figure 3-5. Example of differences in auxiliary data between that computed for VIIRS scan and that from heritage MODIS sensor providing the corresponding radiance values 91

Figure 3-6. Relationship between the heritage AMSU-A / HSB bands and the bands used for ATMS 92

Figure 3-7. Simulated sensor brightness temperatures used to develop regression coefficients for AMSU/HSB-to-ATMS spectral mapping 93

Figure 3-8. Predicted accuracy of spectral mapping for ATMS moisture-sounding channels 19 and 21 94

Figure 3-9. Predicted accuracy of synthesizing ATMS window channel 4 (51.76GHz) using either linear interpolation or statistical regression with brightness temperatures from channels 3 and 5 95

Figure 3-10. Predicted accuracy of synthesizing ATMS window channel 4 (51.76GHz) using statistical regression with brightness temperatures from channels 1, 2, 3 and 5 96

Figure 3-11. Verifying that regression coefficients trained on synthetic data give similar results when applied to real sensor data 97

Figure 3-12. Results from pixel replication and mirroring approaches for populating radiance values of VIIRS pixels falling outside MODIS edge-of-swath 98

Figure 3-13. Simple pixel striping in MODIS band 6 becomes complex pixel striping for VIIRS band M10 99

Figure 3-14. Map-space imagery for VIIRS band M10 before and after processing to remove pixel striping and edge-of-swath pixel replication 100

Use or disclosure of data contained on this page is subject to the export restriction(s) on the title page of this document.

D45702, A. PDMO Released: 2009-02-18 (VERIFY REVISION STATUS)
PDMO

Figure 3-15. COART simulations of ocean scenes with clouds shows that the logarithm of the radiance varies approximately linearly with logarithm of the wavelength for wavelengths less than 0.55 microns 101

Figure 3-16. Results from using linear extrapolation approach to estimate the TOA reflectance for saturated pixels in bands M1 and M2 102

Figure 3-17. Comparison of error from linear extrapolation approach using reflectance from bands M3 and M4 to emulate band M1 to just using reflectance from Band M3 103

Figure 3-18. Comparison of error from linear interpolation approach using reflectance from bands M1 and M3 to emulate band M2 to just using reflectance from Band M3 104

Figure 3-19. Approach for interpolating reflectance to replace band M6 saturated pixels is based on whether TOA reflectance has a vegetation signature, as determined by the TOA NDVI 105

Figure 3-20. Results of employing interpolation approach based on TOA NDVI to estimate the TOA reflectance for saturated pixels in band M6..... 106

Figure 3-21. Relationship between the relative spectral responses for VIIRS bands M12 & M13 and those for MODIS bands 20 & 22 107

Figure 3-22. Illustration of problem with SDR calibration code brightness temperatures computed from MODIS radiances using VIIRS radiance-to-brightness temperature LUTs 108

Figure 3-23. Approach to adjusting and checking radiances for VIIRS thermal-emissive bands 109

Figure 3-24. Examples of granules with problems in the MODIS to VIIRS spatial resampling 110

Figure 4-1. Chlorophyll concentration and specific absorption spectra from Bricaud database 114

Figure 4-2. Addition of variability to other absorption and scattering IOPs 115

Figure 4-3. Accuracy of remote-sensing reflectance computed from water-leaving BRDF116

Figure 4-4. Real *in situ* data from NOMAD and IOCCG for testing the OCC algorithm118

Figure 4-5. Comparison of TOA Rayleigh radiance from ACO LUT to COART RTM for a flat ocean surface as a function of sensor zenith angle for solar zenith angle of 30^0 and relative azimuths of 0^0 (a) and 90^0 (b)..... 123

Figure 4-6. Comparison of TOA Rayleigh radiance from ACO LUT to COART RTM for a flat ocean surface as a function of sensor zenith angle for solar zenith angle of 30^0 and relative azimuths of 130^0 (a) and 180^0 (b)..... 124

Figure 4-7. Comparison of TOA Rayleigh radiance from ACO LUT to COART RTM for a flat ocean surface as a function of sensor zenith angle for solar zenith angle of 60^0 and relative azimuths of 0^0 (a) and 90^0 (b)..... 125

Use or disclosure of data contained on this page is subject to the export restriction(s) on the title page of this document.

D45702, A. PDMO Released: 2009-02-18 (VERIFY REVISION STATUS)
PDMO

Figure 4-8. Comparison of TOA Rayleigh radiance from ACO LUT to COART RTM for a wind-roughened ocean surface as a function of sensor zenith angle for solar zenith angle of 30^0 and relative azimuths of 0^0 (a) and 90^0 (b) 126

Figure 4-9. Example of Shettle and Fenn aerosol optical properties used in the Aerosol ACO LUTs and input into the COART RTM to verify the aerosol and aerosol-Rayleigh radiance produced by the LUTs. The Maritime Aerosol (70%RH) for an AOT at 865nm of 0.12 is shown here 127

Figure 4-10. Comparison of TOA aerosol and aerosol-Rayleigh radiance from ACO LUT to COART RTM for a flat ocean surface as a function of sensor zenith angle for solar zenith angle of 30^0 and relative azimuths of 0^0 (a) and 90^0 (b) 128

Figure 4-11. Comparison of TOA total path radiance (Rayleigh, aerosol and aerosol-Rayleigh) from ACO LUTs to COART RTM for a flat ocean surface as a function of sensor zenith angle for solar zenith angle of 30^0 and relative azimuths of 0^0 (a) and 90^0 (b) 129

Figure 4-12. Comparison of TOA total path radiance (Rayleigh, aerosol and aerosol-Rayleigh) from ACO LUTs to COART RTM for a flat ocean surface as a function of sensor zenith angle for solar zenith angle of 30^0 and relative azimuths of 130^0 (a) and 180^0 (b) 130

Figure 4-13. Anomalies produced by diffuse transmittance LUT for pure Rayleigh atmosphere 131

Figure 4-14. Accuracy of diffuse transmittance from ACO LUT at low end of open-ocean AOT range 132

Figure 4-15. Accuracy of diffuse transmittance from ACO LUT at high end of open-ocean AOT range 133

Figure 4-16. ACO model for two-way ozone transmittance has been verified against the COART RTM 134

Figure 4-17. Sampling of geophysical properties and sun-sensor geometry based on Global Synthetic Datasets 135

Figure 4-18. Nominal noise characteristics obtained from sun-sensor NEDN-Radiance LUTs 136

Figure 4-19. Distribution of sensor noise added to Global Synthetic Dataset TOA radiances 137

Use or disclosure of data contained on this page is subject to the export restriction(s) on the title page of this document.

D45702, A. PDMO Released: 2009-02-18 (VERIFY REVISION STATUS)
PDMO

List of Tables

Table 2-1.Comparison of Global Dataset Characteristics for NWP Models..... 18

Table 2-2. Water and ice cloud types contained in Global Synthetic Test Datasets..... 35

Table 2-3. Land Cover Materials in PRA Materials Database 41

Table 2-4. Re-generating spectral reflectance properties (0.4 to 2.5microns) for some PRA materials using Data from USGS SPLIB05a 43

Table 2-5. Summary of Gaps Between Spec Range and NCEP Global Data..... 48

Table 2-6. Radiative Transfer Models used for Generating Synthetic Test Datasets ... 58

Table 3-1. MODIS to VIIRS nearest-neighbor spectral mapping scheme 87

Use or disclosure of data contained on this page is subject to the export restriction(s) on the title page of this document.

D45702, A. PDMO Released: 2009-02-18 (VERIFY REVISION STATUS)
PDMO

PREFACE

This document describes tools, models and processes utilized to generate real (proxy) and simulated (synthetic) data used for testing the NPOESS/NPP algorithms. Many of these tools, models and processes were provided by NGST's Integrated Weather Products Testbed or IWPTB, aka the EVEREST modeling and simulations test bed. EVEREST and its tools, models and processes are Northrop Grumman Proprietary – Level 1, developed with NGST's internal funds. The resulting proxy and synthetic test data is provided to the government with unlimited rights.

Use or disclosure of data contained on this page is subject to the export restriction(s) on the title page of this document.

D45702, A. PDMO Released: 2009-02-18 (VERIFY REVISION STATUS)
PDMO

1.0 INTRODUCTION

A rigorous way to determine the impact of a given sensor/spacecraft/ground system design on the EDRs, SDRs, and IPs it produces is by a direct comparison of retrieved values using the proposed system with the corresponding ground-truth values from the observed environmental conditions within the sensor field of view. However, until the actual system is built and fielded, this can only be done by utilizing data from an existing, similar sensor/spacecraft system (i.e., proxy data) or through an end-to-end simulation of the proposed system (i.e., synthetic data). There are advantages and disadvantages associated with each method. Our approach involves a judicious application of each method as warranted.

Synthetic data is based on an end-to-end simulation of the system, employing a compilation of global and/or regional environmental scene datasets, validated radiative transfer models (RTMs), and rigorous models of the sensors and spacecraft platform. To predict the performance of a developmental sensor for which no heritage sensor exists, simulation is the primary recourse. In addition, global synthetic test datasets provide an approach for assessing EDR performance over a broad range of conditions, both typical and extreme. In fact, the greatest strength of global datasets is their ability to capture temporal variability and complete geographic coverage, encompassing a wide range of environmental conditions, with a relatively small number of sample points. Synthetic data also allows for exact knowledge of the physical scene, sensor, and spacecraft conditions used in generating the simulated sensor measurements, thereby providing the “truth” needed for assessing EDR performance. Finally, it permits the analyst to isolate and assess the impact of different sources of error and/or effects, both scene and sensor/spacecraft, on retrieval accuracy.

Proxy data, on the other hand, uses SDRs from an NPOESS-similar heritage sensor to emulate those obtained from the development sensor. The generation of proxy data requires calibrated radiance data (SDRs) from a heritage sensor with similar characteristics to the development sensor, a model to map (spatially and/or spectrally) values of the radiance from the surrogate sensor to those of the development sensor, and a validated source of “truth” EDR data, including estimates of the measurement uncertainty. The use of proxy data provides increased confidence in the performance of the algorithms by checking that all real world phenomenology, as well as the vagaries found in actual sensor/spacecraft data, has been considered in assessing performance. Proxy data is also needed for supplying test data for scenes that are too difficult or costly to simulate. Finally, use of proxy data is the only effective means of producing the large volume of test data necessary for fully exercising the IDPS operational data processing system.

The approach of using real data from similar deployed sensors or using data from a simulation of the proposed sensor each has its adherents in the community who can no doubt add to the lists of advantages (and disadvantages) discussed above. We believe that both methods can and should be used to assess system performance and reduce

Use or disclosure of data contained on this page is subject to the export restriction(s) on the title page of this document.

D45702, A. PDMO Released: 2009-02-18 (VERIFY REVISION STATUS)
PDMO

risk. It is a thorough understanding of the errors, constraints, and advantages associated with each method that allows a judicious selection of application.

Use or disclosure of data contained on this page is subject to the export restriction(s) on the title page of this document.

D45702, A. PDMO Released: 2009-02-18 (VERIFY REVISION STATUS)
PDMO

2.0 SYNTHETIC DATA FROM END-TO-END SIMULATION

The end-to-end simulation process for generating the global synthetic test datasets is shown in Figure 2-1. It starts with the compilation of environmental scenes that provide a “complete” description of the geophysical parameters needed in modeling the measurements made by the sensors as they view the scene. For assessing EDR, SDR, and IP performance, the environmental scenes must be based on a well-chosen, screened set of atmospheric profiles and land/ocean backgrounds that reflect a wide distribution of global conditions and that cover the required EDR measurement range. These environmental scenes are used both to provide the “truth” values of the geophysical parameters and as input to the radiative transfer models (RTMs), which transform the physical scene properties viewed by the sensor into the spectral radiance at the sensor’s entrance aperture. There are several different RTMs used in the IWPTB, spanning the frequency regime from UV to microwave. The output from the RTMs is then input into models of the NPOESS sensors/spacecraft that add the optical, electrical and mechanical effects introduced by the sensor and spacecraft platform. The result is a set of synthetic sensor measurements (RDRs or SDRs). These synthetic RDR/SDRs, along with the associated auxiliary and ancillary data, are then used as input to the science grade retrieval algorithm code in the IWPTB, which transform the sensor measurements into the retrieved environmental data products (EDRs and IPs). The generated EDRs and IPs are compared against the geophysical parameter truth-values in order to establish EDR and IP quality metrics.

2.1 Geophysical Data Generation

The environmental datasets used in assessing EDR performance are of two types; global datasets, for assessing performance over a broad range of geophysical parameter values, both typical and extreme, and high-resolution, mesoscale-sized, or smaller, structured scenes, for looking at EDRs, SDRs, and IPs that involve dependencies between sensor pixels. The fundamental requirement for these datasets is that they provide a “complete” description of the environmental scene that includes all of the geophysical parameters needed in modeling measurements made by the sensors as they view the scene. The scenes must also provide the necessary horizontal, vertical and temporal coverage and resolution needed in simulating TOA radiances and assessing each EDR. The environmental datasets must be realistic. Geophysical parameter values for a given scene should be those that occur in nature and should exhibit the natural correlations that exist between the various geophysical parameters. The environmental datasets should also be representative of naturally occurring conditions. Both the range and frequency of occurrence of the geophysical parameter values should be representative of that observed in nature, and also as viewed by sensors on NPOESS. Finally, the environmental datasets must be comprehensive. A significant range of all naturally occurring scenes must be adequately sampled in the test data, and there must be a sufficient number of samples to assess EDR performance over all required stratifications.

Use or disclosure of data contained on this page is subject to the export restriction(s) on the title page of this document.

D45702, A. PDMO Released: 2009-02-18 (VERIFY REVISION STATUS)
PDMO

2.1.1 Assembling Atmospheric and Surface Properties from NWP Analyses

When deciding on the source of global environmental data for building our global test datasets, we selected global datasets produced from coarse numerical weather prediction (NWP) global data assimilation (GDAS) model analyses, such as that produced by the National Center for Environmental Prediction (NCEP). An advantage of this selection is that it provides a nearly complete set of globally distributed environmental parameters needed as input to the RTMs and to establish a comprehensive set of "truth data" for testing purposes. For example, it includes difficult to measure parameters such as snow cover, sea-ice, and soil moisture on a global scale. In addition, using NWP model analyses generated from validated first-principle physics models helps to ensure that the data will be geophysically consistent, capturing the common meteorological correlations in the atmosphere. The particular NWP analyses being used in generating our global test datasets are the NCEP AVN-FNL and NCEP Stratospheric GDAS analyses. The FNL or Final analysis is identical to the other AVN analyses except that it is run at a later time to accommodate late arriving observational data from the GDAS system. It is mainly used as the initializing analysis for the next set of AVN forecast model runs 12 hours later; however, our interest in it stems from the fact that it provides a somewhat more accurate set of geophysical parameter values since it uses actual observations at the model output time as part of the analysis. Table 2-1 summaries the NCEP AVN-FNL and Stratospheric data characteristics and how they compare to other model analyses available for use in generating environmental scene properties.

The NCEP AVN-FNL tropospheric datasets provide a fairly complete set of geophysical parameter values describing the state of the atmosphere and terrain/ocean background. This data have been assimilated from a number of sources (radiosondes, buoys, and satellite) and re-generated onto a uniform 1° equal-angle lat/lon grid covering the globe. Atmospheric profiles of temperature, geo-potential height, relative humidity, cloud liquid water, ozone, and vector-winds are specified at up to 26 pressure levels, from 1000 mbar to 10 mbar, as illustrated in Figure 2-2. With the inclusion of the NCEP stratospheric data, the geopotential height and temperature profiles are extended to the 0.4mb pressure level. In addition to atmospheric profiles, the NCEP tropospheric datasets provide a rather extensive set of near-surface, surface and subsurface geophysical properties, including surface elevation, air-temperature (2m height), pressure, vector-winds (10 m height), relative humidity (2m height), skin temperature, soil subsurface-profiles of moisture content and temperature (0-10 cm and 10-200 cm), snow cover, and land/sea and ice masks. This data is available four-times daily, at 00Z, 06Z, 12Z, and 18Z.

2.1.2 Validation Status of the NCEP AVN-FNL Tropospheric Data

The NCEP AVN-FNL tropospheric datasets are generated, provided, and maintained by the U.S. government. Since these datasets are provided to the public on a daily basis, the government performs an extensive and thorough validation of the models and data on a continuing basis. The IWPTB leverages the validation work already done by the government, as the scene simulation capability is built knowing that the tools and data we are using to establish physical "truth data" are largely validated. This section is

Use or disclosure of data contained on this page is subject to the export restriction(s) on the title page of this document.

D45702, A. PDMO Released: 2009-02-18 (VERIFY REVISION STATUS)
PDMO

intended to provide a brief survey of the extensive validation efforts at NCEP and by others in the community.

As part of its NWP charter, NCEP collects massive amounts of in-situ observations and satellite derived measurements that are assimilated into the NWP models to produce better forecasts and analyses. In addition to using these data as input to NWP models, NCEP also makes use of the data to track comparisons between NWP model results and actual weather observations. This allows NCEP to continuously monitor its NWP model performance and quantify model errors, biases, and differences between model output and observations. NCEP generally tracks four types of comparisons: 1) comparisons of model forecasts to observations, 2) comparisons of model analyses to observations, 3) comparisons of model forecasts to its analyses, and 4) comparisons of model output to NCEP's competitors such as NOGAPS, the European Center for Medium-Range Weather Forecast (ECMWF) model, and UKMET. As an example, routine comparisons are made between surface observations and AVN and ETA surface and near surface parameters 2 meter air temperature and moisture, and 10 meter winds). This applies to both the AVN and ETA forecasts and analyses. AVN and ETA model forecasts and analyses are also verified against the Aircraft Communications And Reporting System (ACARS) and radiosonde data, which include temperature, vector-winds, geopotential height, and moisture at several levels in the atmosphere, as well as surface pressure. Many of these comparisons are stratified by regions around the world, and are updated and tracked on a daily, weekly, and monthly basis. By comparing the model forecasts to actual observations one can track model skill scores and determine the accuracy of forecasts for parameters such as temperature, humidity, and precipitation. The comparisons of model analyses to observations allow one to determine how close an analysis comes to representing the actual conditions observed. Since the analyses are used as the initial conditions for the next forecast model run, one prefers the analyses to be as representative of the actual weather as possible. To get good analyses the NWP models assimilate the massive quantities of satellite and in-situ data collected every day, and use the data to influence the model so that it does not stray too far from the actual conditions, thus producing an accurate definition of the atmospheric state for initialization. Therefore comparisons of analyses to observations must be considered carefully since some comparisons will represent more independent validation than others depending on what data types and sources are used in the assimilation process.

Comparisons have also been made by others in the community, who have in turn provided them to NGST. One such example is the comparisons of temperature and moisture profiles from NCEP AVN with both in situ LIDAR measurements and ECMWF model analyses. Figures 2-3 and 2-4 are examples of the type of information that were collected by Aerospace in its Cal/Val effort of SSMIS. Figure 2-3 shows the excellent agreement between the NCEP AVN temperature profile both with the ECMWF analyses and the in situ LIDAR measurements, with the AVN temperatures agreeing slightly better with the in situ measurements than ECMWF. Figure 2-4 shows similar comparisons for the moisture profiles, but with ECMWF analyses outperforming AVN at the higher altitude (i.e., lower pressures).

Use or disclosure of data contained on this page is subject to the export restriction(s) on the title page of this document.

D45702, A. PDMO Released: 2009-02-18 (VERIFY REVISION STATUS)
PDMO

In addition to validation using in-situ observations, comparisons between model analyses such as the AVN-FNL and satellite derived measurements such as SSM/I sea surface wind speed (SSWS) and total precipitable water are useful. Figure 2-5 summarizes an example of one such comparison between ANV-FNL and SSM/I SSWS performed by NGST. It should be noted that SSM/I SSWS is assimilated into the AVN model when producing the FNL analysis, so the comparison of the two datasets is not an independent comparison, and good agreement should be expected. Even though this is not an independent validation, the information can still provide a sanity check to see how realistic the model analyses are as compared to the actual weather measured by the satellites. The uncertainty in the difference between the NCEP and SSM/I wind speed is 1.999 m/s, which is within the total uncertainty threshold of the SSM/I sensor measurement of SSWS. This provides a good sanity check to be sure that the model analyses we are using are credible and realistic.

The SST in the AVN-FNL analysis is referred to as the daily Optimum Interpolated (OI) SST, has a coarse 1^0 horizontal resolution, is a relatively smooth SST, and is available once per day with the 12Z analysis. The OI SST is a bulk SST that is derived from a combination of sources including: bias corrected AVHRR SST retrievals, ship and buoy reports. However, in our modeling, we use the SST field from the AVN-FNL analysis as the skin SST, directly observed by the thermal IR and microwave sensors on NPP and NPOESS. Figure 2-6 shows the comparison between the SST from AVN-FNL for March 2, 2002 and June 15, 2002 and measurements made by the TMI on TRIMM. As mentioned earlier, by using a consistent set of atmospheric and surface environmental parameters developed from first-principle physics models, one should expect that the natural correlations that exist between geophysical parameters are maintained. Figure 2-7 shows that the NCEP distributions of the difference between the near-surface air temperature and the corresponding land or sea skin temperatures exhibit these correlations.

While many quantitative comparisons can be made, qualitative comparisons also yield useful information. Figure 2-8 shows a comparison of NCEP total cloud liquid water to a Southeast Asia infrared satellite image from the Japanese Geostationary Meteorological Satellite (GMS). The comparison is a favorable one as the cloud systems in the satellite image generally coincide with the total cloud liquid water seen in the NCEP analyses. This same type of comparison can be found at the data assimilation group web site at NCEP, where they routinely overlay total cloud liquid water from the NCEP AVN-FNL GDAS analysis onto GMS satellite images to get a better verification of the model products. This is an example of a more independent validation since the GMS data are not used in the GDAS system to produce total cloud liquid water.

NCEP also verifies each model against its own analysis and tracks comparisons by computing RMS errors and anomaly correlation statistics for each model and compares them to competitor models such as ECMWF, Navy NOGAPS, and UKMET NWP model output. NCEP also takes great care to examine and document model biases, which sometimes arise when new physics parameterizations are introduced. NCEP spends considerable effort documenting the biases in hopes that identification of the biases will help forecasters interpret the output correctly and provide them with guidance on how to adjust the model output.

Use or disclosure of data contained on this page is subject to the export restriction(s) on the title page of this document.

D45702, A. PDMO Released: 2009-02-18 (VERIFY REVISION STATUS)
PDMO

It should also be noted that the Navy (FNMOC) and Air Force (AFWA) monitor NWP model output for their specific models. Validation of NWP models and products are extensively documented and can be found at the following websites:

- http://sgi62.wwb.noaa.gov:8080/STATS/STATS.html - This website summarizes AVN, Medium Range Forecast (MRF), and ETA model performance statistics where each model is verified against its analysis, and against other competitive models.
- http://205.156.54.206/er/bgm/models.htm - This website is a general reference on operational NWP models and includes background information, model performance characteristics such as errors and biases, and model verification statistics.
- http://www.emc.ncep.noaa.gov/modelperf/index.html - This website documents AVN, MRF, and ETA model performance statistics that includes validation of forecasts and analyses against in-situ data.
- http://sgi62.wwb.noaa.gov:8080/RTPUB/ - This website summarizes data assimilation techniques and validation of AVN, MRF, and ETA model analyses against satellite and in-situ data.
- http://www.fnmoc.navy.mil/PUBLIC/MODEL_REPORTS/MONTHLY_MODEL_SUMMARY/AUG1999/DOCUMENT/toc.html - This website documents NOGAPS and COAMPS model verification and performance statistics.

2.1.3 Extending the Atmospheric Profiles to Top-of-Atmosphere

The atmospheric profiles provided by the NCEP AVN-FNL tropospheric analyses only extend at most to 10 mbar. Radiatively-active gases, such as water vapor, are particularly important atmospheric constituents in radiative transfer processes that extend upwards to the top-of-atmosphere (TOA) at 100 km or approximately $3x10^{-4}$ mbar. To characterize the upper atmosphere (i.e., stratosphere, mesosphere, and thermosphere) for pressures between 10 mbar and TOA, we use a combination of NWP and climatologic datasets.

We start with the global stratospheric analysis produced daily by NCEP at 12Z. These analyses are available for download in GRIB format at the DSS web site (http://dss.ucar.edu/datasets/ds067.3/). The stratospheric analysis provides geopotential height and temperature on a fixed-pressure grid extending throughout the upper atmosphere (8 pressure levels ranging from 70 mbar to 0.4 mbar), with the bottom 4 levels overlapping with the tropospheric dataset. The data are available on a 2.5^0 x 2.5^0 polar stereographic grid projection, with a grid size of 65x65 I/J grid points. Each file contains two grids – one each for the northern and southern hemisphere.

To extend the geopotential height and temperature profiles further to TOA, we use the COSPAR International Reference Atmosphere (CIRA-86). The CIRA-86 provides us with the atmospheric temperature and geopotential height on a fixed-pressure grid from 1013 mbar to $2.54x10^{-5}$ mbar, stretching from the troposphere through the mesosphere, and capturing the boundaries between layers of the atmosphere, such as the tropopause, stratopause, and mesopause, where critical temperature changes occur. These data have been compiled from various sources including ground based and satellite (NIMBUS 5, 6, and 7) measurements. The data include tables of the monthly

Use or disclosure of data contained on this page is subject to the export restriction(s) on the title page of this document.

D45702, A. PDMO Released: 2009-02-18 (VERIFY REVISION STATUS)
PDMO

mean zonal temperature and geopotential height for the latitude range of 80N to 80S in 5 degree latitudinal zones. The CIRA reference atmosphere data can be found at (http://nssdc.gsfc.nasa.gov/space/model/atmos/cospar1.html).

While the previously mentioned datasets define the temperature and geopotential height of the upper atmosphere as a function of pressure, none of them specify the trace gas profiles in the atmosphere. The profiling of trace gases becomes an especially acute problem in the upper atmosphere where few measurements have been taken. In 1991 the Upper Atmosphere Research Satellite, UARS, was launched with the mission of continuously observing the upper atmosphere. Observations cover the region from the upper troposphere (100 mbar) to the mesosphere, with a geographic coverage of 80N to 80S in 4 degree latitudinal zones. Trace gas data are provided as monthly zonal means from January to December. By analyzing the ten years of observations, various climatological reference atmospheres were generated for a number of trace gases including: water vapor, ozone, methane, and nitrogen oxides. We use the UARS Reference Atmosphere for the year between 4/92 and 3/93, extracting water vapor from 100 mbar to 0.003 mbar and ozone from 100 mbar to 0.1 mbar. The UARS reference atmospheres can be found at (http://code916.gsfc.nasa.gov/Public/Analysis/UARS/urap/home.html).

It should be noted that the high-altitude profiles described above may lack the spatial and temporal structure found in real-world situations. However, for the majority of NPP/NPOESS sensors, other than CMIS which retrieves atmospheric temperature and moisture above 60km, this should have a negligible impact. For the less important and/or less variable trace gases, we use the standard atmospheres provided in the RTM being used, such as MODTRAN with its 6 standard atmospheres, to provide their profiles to TOA.

The atmospheric profiles obtained from the various NWP and climatologic datasets do not necessarily merge smoothly as a function of pressure from one dataset to the next. This can be seen quite clearly in the plot of atmospheric temperature versus pressure profile in the left-hand side of Figure 2-9. In order to generate atmospheric profiles without the anomalous kinks shown in that figure, we have developed an approach that smoothly transitions from the profile in one dataset to that of the next higher altitude (lower pressure) dataset over a transition region which is selected based on the uncertainty of the profile information in each dataset. Briefly stated, the procedure takes the difference in the value of the atmospheric parameter, say temperature, from the two datasets at the transition pressure and uses this as an offset, gradually increasing the value of the offset, as a function of pressure over the transition region, from 0 to 100%. The result of applying this approach to the atmospheric temperature profile is shown in the right-hand side of Figure 2-9. Figure 2-10 provides similar examples for the joining of the water vapor and ozone profiles. These transitions are also performed in a physically consistent manner so that dependent variables like pressure, temperature and height remain in hydrostatic equilibrium, or that the water vapor mass mixing ratio never results in a relative humidity greater than 100%, the limiting mass-mixing ratio for which is shown as the red-curve in the left-hand side of Figure 2-10. Figure 2-11 illustrates the wide variety of atmospheric profiles for temperature, water vapor, and ozone generated for various geographic locations around the globe.

Use or disclosure of data contained on this page is subject to the export restriction(s) on the title page of this document.

D45702, A. PDMO Released: 2009-02-18 (VERIFY REVISION STATUS)
PDMO

2.1.4 Generating the Physical and Optical Properties of High-Resolution 3D Clouds

Although the cloud liquid water profile is provided in the NCEP tropospheric datasets, a means of generating individual cloud layers with their corresponding physical and optical properties is required. The cloud layers and physical properties are generated using Northrop Grumman's cloud scene simulation model (CSSM). This code makes use of individual NCEP profiles of cloud liquid water, relative humidity, temperature, and height, in a statistically based empirical model to define a high-resolution 3D cloud structure and their associated physical properties. Given the physical properties for each cloud, an output processor generates the appropriate cloud layer information needed by each sensor (CrIS/ATMS, VIIRS and CMIS) and their respective RTMs.

The atmospheric and terrestrial data in global datasets are very sparse, and therefore, do not lend themselves to a physics based cloud simulation, which is dependent on a well specified starting scenario. Instead we apply a stochastic solution using an empirical model, called the Cloud Scene Simulation Model (CSSM), developed for the US Air Force Phillips Laboratory and the Defense Modeling and Simulation Office (DMSO). CSSM has the ability to take a single vertical profile containing basic meteorological parameters commonly found in soundings or NWP-model output and construct a 3D high-resolution cloud liquid/ice water scene as a function of time. It is important to note that the point of CSSM is not to exactly replicate existing cloud conditions as observed on a particular day, but rather to generate realistic cloud scenes representative of the given weather state. Using the cloud water scene generated by CSSM, one can compute the various cloud physical properties using commonly accepted community empirical techniques.

As mentioned above, CSSM is an empirical model that generates high resolution, four dimensional (three spatial and time), multi-layer cloud fields consistent with larger scale cloud conditions; that is, it simulates realistic structure (typical resolutions of 10-500 meters) within a model domain defined by general meteorological characteristics. CSSM relies on efficient stochastic field generation techniques to simulate realistic cloud and precipitation structure. One output field is generated by the model for each specified output time and contains cloud water density values arranged on a regular volumetric grid, as shown in Figure 2-12. The model uses a fractal algorithm to specify the horizontal distribution of cloud elements across the user-specified model domain, where parameters within the fractal algorithm are tuned to fit observed cloud data. CSSM simulates a variety of cloud types including cirriform (high, thin cloud streaks), stratiform (low, homogeneous cloud layers), and cumuliform (puffy, vertically-developed convective clouds). The vertical growth of the clouds is modeled using convection physics (cumuliform types) and heuristics (stratiform and cirriform types).

The calculation starts by interpolating the AVN-FNL meteorological profile data to vertical levels, beginning with the first level above the surface elevation and extending upward in 300 m increments to 19,800 m. Next, the locations of potential cloud layers are identified by using input profiles of the cloud liquid water mixing ratio (CLWMR) and cloud ice water mixing ratio (CIWMR). Since the NCEP AVN profiles have the total amount of cloud water in liquid phase, an empirical relation between CLWMR and

Use or disclosure of data contained on this page is subject to the export restriction(s) on the title page of this document.

D45702, A. PDMO Released: 2009-02-18 (VERIFY REVISION STATUS)
PDMO

CIWMR as a function of temperature had to be developed. This was accomplished with the use of the ECMWF 60L-SD dataset, which contains cloud water in both liquid and ice phases. The resulting relation between the natural logarithm of the CIWMR-to-CLWMR ratio and the atmospheric temperature, T, is shown in Figure 2-13. The correlation coefficient for the fit is greater than 0.97. This relationship was used to convert the original CLWMR in the AVN profiles into separate liquid and ice water mixing ratios, applying it where $0°\boldsymbol{C} \geq \boldsymbol{T} \geq -24°\boldsymbol{C}$. For temperatures colder than $-24°C$ (warmer than $0°C$), all cloud water in the NCEP data is assumed to be in the ice (water) phase. This temperature range was determined by calculating the number of data points in 2ºC bins where both the CLWMR and CIWMR met the 10^{-6} kg/kg criteria in the ECMWF data.

Those levels for which the CLWMR or CIWMR exceed specified thresholds are identified as potential water or ice cloud layers, respectively. Using the AVN-FNL meteorological data (i.e., temperature, moisture, cloud liquid and/or ice water, pressure, and height), CSSM computes a cloud fraction for each potential cloud layer and then uses the ISCCP cloud classification scheme to identify each layer as one of nine internal cloud types, including precipitating clouds. Figure 2-14 provides an illustration of the ISCCP radiometric cloud classification methodology used by the code. CSSM then determines the appropriate cloud liquid/ice water content for the identified cloud type from the Feddes table and distributes this cloud water, based on the cloud fraction, within the volumetric grid using the aforementioned fractal algorithm.

The output of CSSM is a high-resolution 3D cloud water and precipitation scene over the volumetric domain. Figure 2-15 illustrates the high-resolution 3D cloud structure generated for a particular AVN-FNL profile. A postprocessor determines how this information is used to generate the cloud inputs for the various sensor (e.g., CrIS/ATMS, VIIRS and CMIS) RTMs, as each of these will have different requirements on spatial resolution (see Figure 2-16) and the fidelity needed for treating the radiometric effect of clouds.

When generating inputs for CrIS, for example, the postprocessor divides the horizontal extent of the volumetric domain into 3x3 sub-regions, coinciding with the 3x3 FOVs in the CrIS FOR. Although there may be multiple cloud layers at each grid point within a sub-region, the postprocessor keeps only the topmost cloud. This is because the AER OSS RTM treats clouds as opaque surfaces, so only non-overlapping clouds are seen by the sensor. The postprocessor then groups the grid points within each sub-region by cloud type/altitude to form cloud layers, providing the cloud top pressure and cloud fraction seen by the sensor. Finally, a maximum of two cloud layers per FOV are retained as input to the RTM. A depiction of the overall logic for constructing the clouds for CrIS is shown in Figure 2-17.

By contrast, the modeling for VIIRS requires that the clouds have both high spatial resolution and high fidelity in terms of their optical properties (i.e., optical thickness, single-scattering albedo and scattering phase function). Since the VIIRS spatial resolution for imagery-resolution pixels is comparable with the CSSM grid resolution, the postprocessor picks the 2x2 grid cells about the center of the grid as representative of the clouds within a moderate-resolution pixel for the particular AVN-FNL profile

Use or disclosure of data contained on this page is subject to the export restriction(s) on the title page of this document.

D45702, A. PDMO Released: 2009-02-18 (VERIFY REVISION STATUS)
PDMO

sampled. This provides the VIIRS cloud algorithms with sub-pixel clouds within each moderate-resolution pixel. For each grid cell, only the top 4 cloud layers generated by CSSM are retained, since it is assumed that the sensor cannot see below 4 cloud layers, even in the infrared.

Because of the requirements for the VIIRS cloud algorithms in terms of covering a wide range of water and ice cloud types and effective particle sizes, we have generated accurate optical properties for each of 19 ice and water cloud models. These models are listed in Table 2-2. Separate water and ice cloud spectral libraries of optical properties, including the full scattering phase function, have been generated for describing the 19 cloud types. Both libraries go from 0.4 to 14μm in steps of 5cm^{-1}. The optical properties for water clouds are based on Mie scattering computations of 13 water cloud models (10 from Silverman & Sprague (1970) and 3 from UCLA for precipitating cumulus clouds). As a check of the accuracy of the optical properties computed by our Mie Scattering code, we compared the optical properties for the 7 MODTRAN cloud types (5 water cloud types and 2 “spherical” ice cloud types) with those computed for the corresponding cloud models in Table 2-2. The optical properties (i.e., extinction coefficient, single-scattering albedo, and asymmetry parameter) were essentially identical, as illustrated in Figure 2-18. For ice clouds, the optical properties are based on geometric ray tracing and Finite Difference Time Domain computations of 6 ice cloud models, all with hexagonal column ice crystal habits but varying particle size distributions.

The CSSM postprocessor uses the logic shown in Figure 2-19 to map the clouds generated by CSSM in each grid cell into one of the 19 cloud types defined in Table 2-2. It first determines whether the cloud has been identified by CSSM as a precipitating cumulus cloud. If so, it is randomly assigned as one of the three UCLA liquid water cloud types. Otherwise, the postprocessor determines the phase of the cloud, based on the greater of the ice-water and liquid-water content. A liquid-water cloud is assigned to one of the 10 non-precipitating water cloud models in Table 2-2 based on height and liquid water content. The ice cloud type is always cirrostratus, but with 6 cloud sub-types having different crystal sizes, where a climatological size/temperature relationship is used with the cloud temperature from CSSM to assign the sub-type.

2.1.5 Atmospheric and Cloud Properties for Structured Scenes

To evaluate the performance of EDRs that require high spatial resolution imagery or to assess the effects of certain sensor/spacecraft design parameters (e.g., sensor PSF or band-to-band registration), which also require high-resolution physical scenes, we have also developed the capability of generating mesoscale-sized, or smaller, high-resolution structured scenes. The same general process shown earlier in Figure 2-1 for generating the global test datasets can also be used in building high-resolution structured scenes. The major difference in the process is the need to run a mesoscale NWP model, such as MM5 or WRF, to generate the atmospheric and surface properties, which for sparsely sampled global datasets would be acquired from NCEP. The tool that we have employed for this purpose is NCAR’s MM5 (5th Generation Mesoscale Model) code. MM5 provides all of the atmospheric and many of the surface parameters found in the NCEP AVN-FNL data; however, the horizontal spatial

Use or disclosure of data contained on this page is subject to the export restriction(s) on the title page of this document.

D45702, A. PDMO Released: 2009-02-18 (VERIFY REVISION STATUS)
PDMO

resolution can be much higher (up to 30 arc-seconds, or approximately 1km at the equator). Using NCEP AVN-FNL data to initialize MM5, we can generate meteorologically consistent, high-resolution scene patches anywhere over the globe. In addition to providing improved resolution, MM5 also allows us to generate high-resolution, high fidelity clouds. Starting with the atmospheric information from NCEP, MM5 computes the self-consistent, high-resolution cloud water profiles (either in liquid or ice phase) over the scene domain, which can be used to generate high-resolution clouds in the scene. Comparisons with RaObs data have been made to check that MM5 provides "realistic" atmospheric profiles. An illustration of one such comparison is shown in Figure 2-20. As can be seen, the agreement of the temperature profiles is excellent, so that one could certainly argue that the MM5 profiles are both realistic and representative of actual measured data. As evident by comparing the MM5 and radiosonde moisture profiles, the instantaneous measurements embodied by the sharp zigs and zags in the profile from the humidity instrument as it passes in and out of cloud layers are not observed in the smoother MM5 profile. This same smoothing effect will be observed in the moisture profiles contained in the AVN-FNL profiles, but to an even larger degree. To this extent, our modeled profiles may not capture all of the high-resolution vertical structure in the atmosphere.

2.1.6 Aerosol Properties for Global Datasets

The radiometric effect of aerosols is only included in our modeling of the VIIRS sensor. The current AER-OSS IR RTM used for CrIS does not address the scattering and absorption by aerosols; neither does any of the microwave RTMs. Since, as will be explained in the section on RTMs, our general global test datasets for VIIRS have been generated using MODTRAN-4, we have relied on the standard MODTRAN/LOWTRANN aerosol models in generating our global synthetic test datasets for VIIRS. These are based on the widely used models of Shettle and Fenn, first introduced in LOWTRAN back in the late 1970's. These aerosol models are composite or internally mixed aerosols constructed for rural, urban, and maritime regions, where the aerosol particle is modeled as a homogeneous mixture of water soluble, dust-like, soot, and sea salt component aerosols. We have used the rural aerosol over land and the maritime aerosol over ocean. The particle size distribution for each region is represented as either a lognormal or sum of two lognormal distributions. These aerosols are hygroscopic, so that their particle size and refractive index vary as a function of relative humidity, which is determined from the input atmospheric moisture profile. MODTRAN provides the resulting wavelength-dependent optical properties (i.e., normalized extinction coefficient, single-scattering albedo, asymmetry parameter, and scattering phase function) for these aerosols at relative humidities of 0, 70, 80 and 99%, interpolating between these for the actual relative humidity. The default altitude-dependent aerosol concentration can be scaled via the surface meteorological range to approximate any desired aerosol optical thickness (AOT) at 0.55 microns. To simulate realistic aerosol concentrations, we used the AOT at 0.55 microns extracted from the MODIS L3 8-Day Joint Aerosol/Water Vapor/Cloud Product (MOD08_E3), selecting those datasets that are the closest match in date to the NCEP datasets used in generating the other atmospheric properties of the global synthetic dataset. Figure 2-21

Use or disclosure of data contained on this page is subject to the export restriction(s) on the title page of this document.

D45702, A. PDMO Released: 2009-02-18 (VERIFY REVISION STATUS)
PDMO

shows an illustration of the agreement between the input AOT from MODIS and the resulting AOT actually used by MODTRAN in its computation of the TOA radiance.

2.1.7 Terrain Properties

The logic employed to assign the appropriate surface spectral reflectance, emissivity or BRDF for each point sampled from the global synthetic dataset is initially based on the NCEP surface type. NCEP identifies the background type of each grid cell as ocean, land, ice, or snow-covered. For an ocean background, NGST's proprietary ocean RTM, Hydrolight-BRDF, provides an ocean IOP and wind-dependent spectral BRDF to describe the scattering and emission from the ocean. For ice and snow-covered surfaces, the UCSB DISCORD and NGST ISBRDF RTMs provide either a spectral BRDF or spectral reflectance and emissivity. For land surfaces, the spectral reflectance and emissivity for each sample point is generated based on the surface type, obtained from high-resolution global land-cover databases, and spectral reflectance libraries. The spatial resolution of the land–cover databases goes from 1/20th of a degree to 3 arc-seconds. We will provide a brief description of each of the tools and/or databases used to produce either the spectral reflectance/emissivity or the spectral BRDF at the terrain/ocean boundary

HydroLight-BRDF is a special version of HydroLight that computes ocean BRDFs on a tabular format suitable for input to atmospheric RTMs (e.g., MODTRAN-4, SBDART and 6S(V)). HydroLight, which is the driver for HydroLight-BRDF, is a validated, "industry standard" code for ocean radiative transfer used by optical oceanographers for over a decade to accurately compute in-water radiance distributions. HydroLight-BRDF uses the core code of HydroLight to generate an ocean BRDF by cycling the sun through different locations in a black sky, generating the incident collimated irradiances necessary in defining the ocean BRDF. Given a set of ocean IOPs and the near-surface wind speed, HydroLight-BRDF outputs separate BRDFs for computing the water-leaving, surface reflected, and total upwelling radiances at the ocean surface.

Although values of the spectral reflectance for pure snow were available from several sources (e.g., the ASTER Spectral Library contains the spectral reflectance for fine, medium and coarse grain snow), we didn't feel that these were sufficient to adequately test the VIIRS Snow Cover algorithm. Therefore, to more thoroughly test the Snow Cover algorithm, a wider variety of physical properties for both pure snow and snow with soot impurities were included in the global synthetic test data. This included a range of 6 snow grain sizes, from 50 to 1000 μm, and 4 soot concentrations ranging from 0 to 100ppmw, for a soot particle radius of 0.1 μm. The UCSB DISCORD and MIEFAST codes, available in the UCSB IPW Toolkit, v1.1, were used in modeling the spectral BRDF and reflectance from snow. The MIEFAST code, a Mie scattering code, was used to generate the snow and soot optical properties. Then DISCORD, a multi-stream (i.e., DISORT) RTM, was used to compute the spectral BRDF at the air-snow boundary for the range of pure snow and snow with impurities conditions. A spectral diffuse albedo (i.e., bi-hemispherical reflectance) was computed from the spectral BRDF for each snow-soot type and added to our spectral albedo library. Predictions of directional-hemispherical spectral reflectance computed from the DISCORD generated spectral BRDFs for fine, medium and coarse snow have been compared with those in the

Use or disclosure of data contained on this page is subject to the export restriction(s) on the title page of this document.

D45702, A. PDMO Released: 2009-02-18 (VERIFY REVISION STATUS)
PDMO

ASTER Spectral Library, as one check of our approach to computing spectral reflectance for pure snow. A second set of comparisons of the spectral albedo as a function of snow grain size, soot particle size, soot concentration, and solar angle were made to the literature. An example of one such comparison (*Warren & Wiscombe, 1980, J. Atmos. Sci., 37, 2712-2733 and 2734-2745)* is shown in Figure 2-22.

Requirements for producing sea-ice and snow-covered sea-ice test data have initiated the development of a new coupled sea-ice/ atmosphere RTM. Working with Geminor (Knut Stamnes), we have developed the capability for generating spectral BRDFs at the surface of a coupled air-snow-ice-ocean system. Based on CASIO-DISORT, the ISBRDF RTM treats the change in complex refractive index at the air-ice interface and includes scattering and absorption due to brine and air pockets in sea-ice, as well as water and impurities in snow. This code has just recently been verified against the literature and will soon be producing test data for the broad-band albedo from bare and snow-covered sea-ice.

For land surfaces, spectral reflectance and emissivity properties are defined by utilizing high-resolution terrain-factors data consisting of digital elevation, land cover type and other terrain factors information, along with spectral reflectance/emissivity libraries. As mentioned at the start of this section, the spatial resolution of these databases ranges from 30 meters (1 arc-second) to 1/20th of a degree (~6 km). The majority of our global synthetic test data has been generated using the land cover and terrain factors databases from Photon Research Associates (PRA). The PRA Global 1KM Land Cover database provides information on the terrain material types contained within each grid cell of a 30 arc-second (~1km at the equator) equal-angle lat/lon grid. Using 3 material layers per grid cell, the database allows for including emissivity variations within each IGBP land cover type for the LST algorithm. The PRA land cover database contains a total of 28 different material categories, as listed in table 2-3, providing detailed global surface material specifications.

For wavelengths ranging from 0.2 to 15 micrometers, the PRA database also provides each terrain material's optical properties in the form of a spectral albedo and emissivity. The PRA Spectral Library, like the ASTER Spectral Libraries (i.e., comprised of individual libraries from JHU, JPL, and USGS), is based on reflectance measurements carried out in a laboratory setting. Furthermore, for vegetation land cover types, these measurements are actually made with only vegetation components (e.g., a single leaf for a deciduous tree or a pile of needles for a coniferous tree). Until recently, none of the available spectral libraries had reflectances which were actually measured in the field. The USGS recently released the SPLIB05a Digital Spectral Library (N. Clark, G. A. Swayze, R. Wise, K. E. Livo, T. M. Hoefen, R. F. Kokaly, and S. J. Sutley, 2003, USGS Digital Spectral Library splib05a, *U.S. Geological Survey, Open File Report 03-395*). This library provides AVIRIS radiative-transfer-ground-calibrated spectral reflectance data for a variety of vegetation types measured in the field. Rather than measuring the directional-hemispherical reflectance of the back of a single Aspen leaf in the lab, these measurements provide the reflectance for a stand of Aspen trees. For some vegetation types, SPLIB05a has data for certain vegetation types which were measured in the lab and in the field. One would expect some difference in the spectral reflectance measurements for individual components versus an entire vegetation

Use or disclosure of data contained on this page is subject to the export restriction(s) on the title page of this document.

D45702, A. PDMO Released: 2009-02-18 (VERIFY REVISION STATUS)
PDMO

canopy measured in the field. An illustration of this is seen in Figure 2-23, which shows the reflectance for a single aspen leaf compared with that for a stand of aspen trees. This is also seen when looking for the expected correlations between SWIR and visible band reflectances observed in remote sensing data (e.g., AVIRIS and MODIS), as reported by Kaufman, which are typically not well captured in either the PRA or ASTER Spectral Libraries. The vegetation materials from SPLIB05a do appear to contain the expected correlations in the spectral reflectance between wavelengths in the red (670nm), blue (450nm) and SWIR (2,150nm) bands described in the literature. As a result of this, the visible portion (0.4 to 2.5mm) of the PRA Spectral Library has been upgraded to include the new AVIRIS reflectance data for a variety of vegetation types. Table 2-4 provides the PRA vegetation types that were replaced and the material or materials from SPLIB05a that were used to replace them. The resulting change in the PRA Spectral Library's ability to now capture the expected correlations between SWIR and visible bands is clearly seen in Figure 2-24, which shows "before" and "after" plots of the predicted reflectance in the red and blue bands (based on the correlation with the SWIR band) and the measured reflectance for these visible bands.

To deal with the occasional need for very high spatial resolution synthetic imagery, we have utilized the National Land Cover Dataset (NLCD-92) . This dataset is a 21-category land cover classification database for the conterminous U.S. The land cover legend is shown in Figure 2-25, along with a high-resolution land cover map extracted for Southern Florida. Based primarily on unsupervised classification of 1992 Landsat TM imagery, along with other ancillary data, the NLCD dataset provides land cover type on an equal-angle, 1 arc-second (~30m) grid. Using directional-hemispherical reflectance data from the ASTER Spectral Libraries (with wavelengths between 0.4 and 14 microns), we have generated reflectance spectra for the 21 NLCD land cover classes. Figure 2-26 shows an RGB synthetic image generated from the surface reflectance in the VIIRS red, green and blue bands for a high-resolution terrain scene extracted from the land cover map in Figure 2-25.

Use or disclosure of data contained on this page is subject to the export restriction(s) on the title page of this document.

D45702, A. PDMO Released: 2009-02-18 (VERIFY REVISION STATUS)
PDMO

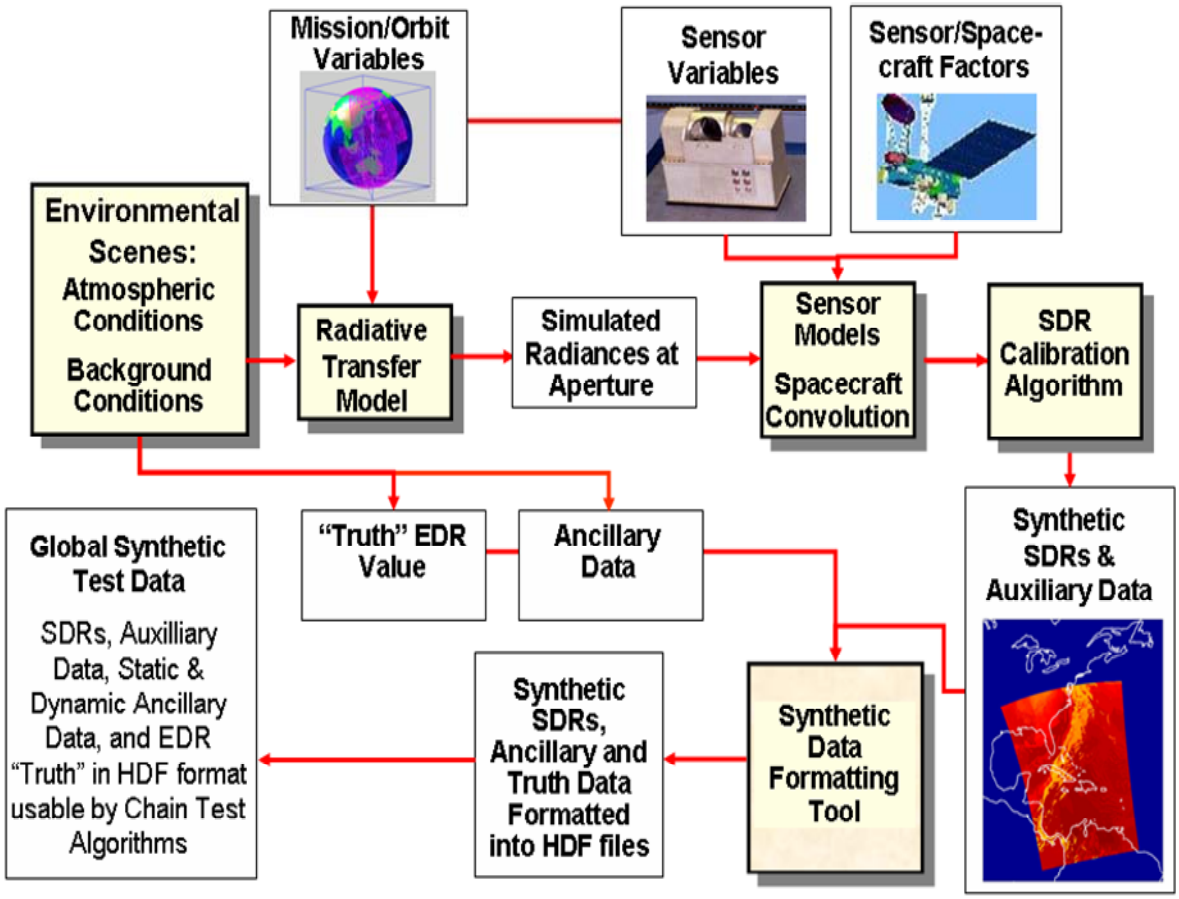

Figure 2-1. Process for Generating Global Synthetic Test Datasets

Use or disclosure of data contained on this page is subject to the export restriction(s) on the title page of this document.

D45702, A. PDMO Released: 2009-02-18 (VERIFY REVISION STATUS)
PDMO

Table 2-1.Comparison of Global Dataset Characteristics for NWP Models

Dataset Attribute	NOGAPS	NCEP AVN-FNL	NCEP ETA	NCEP Stratospheric
Horizontal Resolution	1x1 degree	1x1 Degree	40kmx40km	TBD
Grid Size	360x181 = 65,160 grid points	360x181 = 65,160 grid points	185x129 = 23,865 grid points	65x65 = 8.450 grid points
Grid Projection	Equidistant Lat/Lon	Equidistant Lat/Lon	Lambert-Conformal	Polar Stereographic
Grid Coverage	Global	Global	Regional – North America	Global
Analysis vs. Forecast	Forecast	Analysis based on data assimilation	Analysis based on data assimilation	Analysis based on data assimilation
Total Vertical levels	20 levels	26 Levels	27 Levels	8 levels
Cost	Free	TBD	Free	TBD
Source	Master Environmental Lab	NCAR DSS	NCAR DSS	NCAR DSS
Data Format	GRIB	GRIB	GRIB	GRIB
Decoder S/W	MEL Decoder	MEL Decoder/Bruce's SW	MEL Decoder/Bruce's SW	MEL Decoder/ Bruce's SW
Data Output Interval	6 hours (00,06,12,18Z)	6 hours (00,06,12,18Z)	3 Hours (00, 03, 06, 09, 12, 15, 18, 21Z)	24 hours (12Z)
Data Assimilation Cycle	6 Hour cycle (+08 is final analysis for cycle)	6 Hour Cycle	3 Hour cycle?	24 Hours
Analyses per Assimilation Cycle	3 (+01, +03, +08)	TBD	TBD	N/A
Forecast Length	TBD	84 hours at 06, 18Z; 126 hours at 00, 12Z	TBD	N/A – One analysis at 12Z only

Use or disclosure of data contained on this page is subject to the export restriction(s) on the title page of this document.

D45702, A. PDMO Released: 2009-02-18 (VERIFY REVISION STATUS)
PDMO

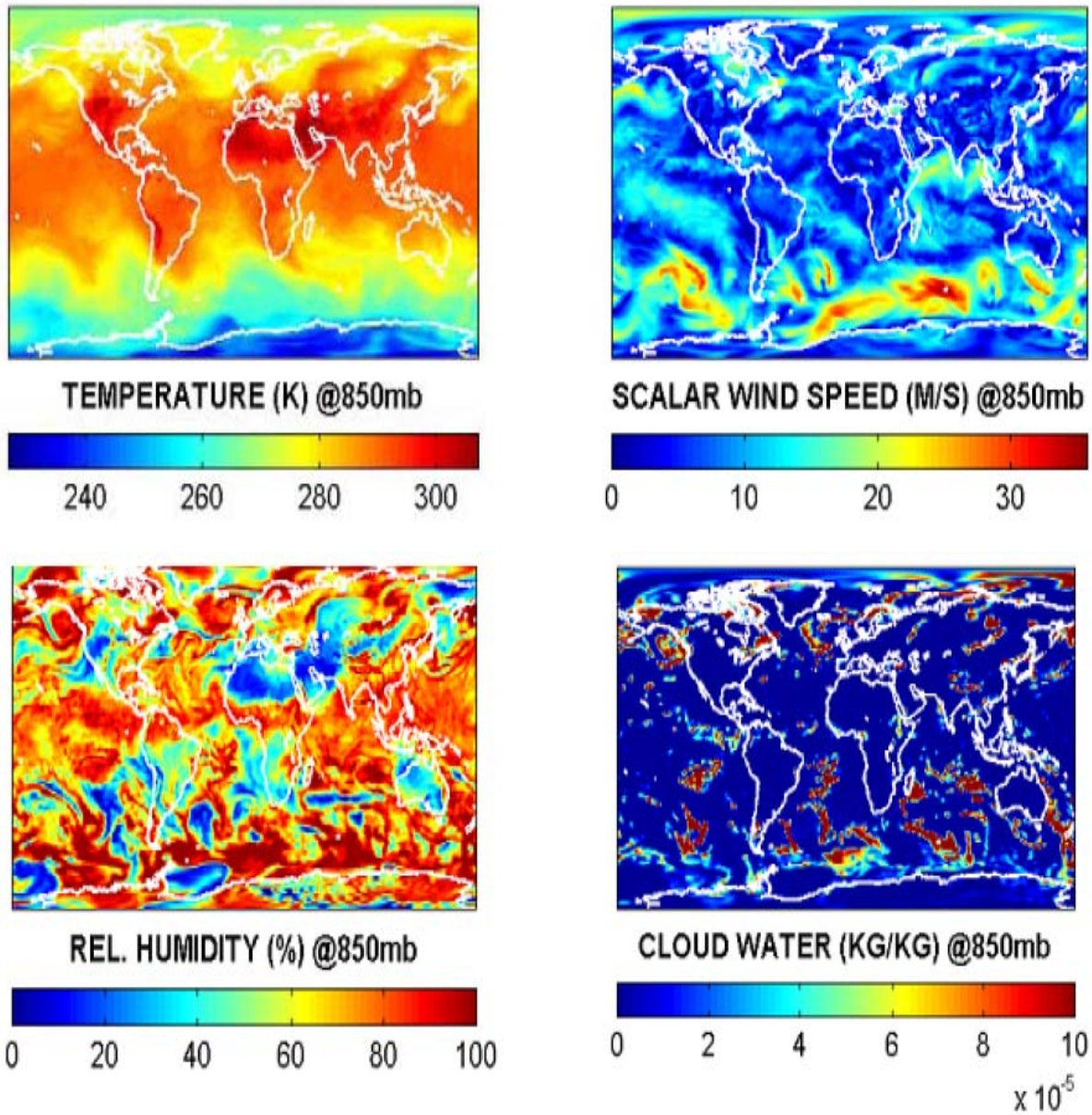

Figure 2-2. Illustration of several of the atmospheric profiles provided in the NCEP AVN-FNL tropospheric datasets

Use or disclosure of data contained on this page is subject to the export restriction(s) on the title page of this document.

D45702, A. PDMO Released: 2009-02-18 (VERIFY REVISION STATUS)
PDMO

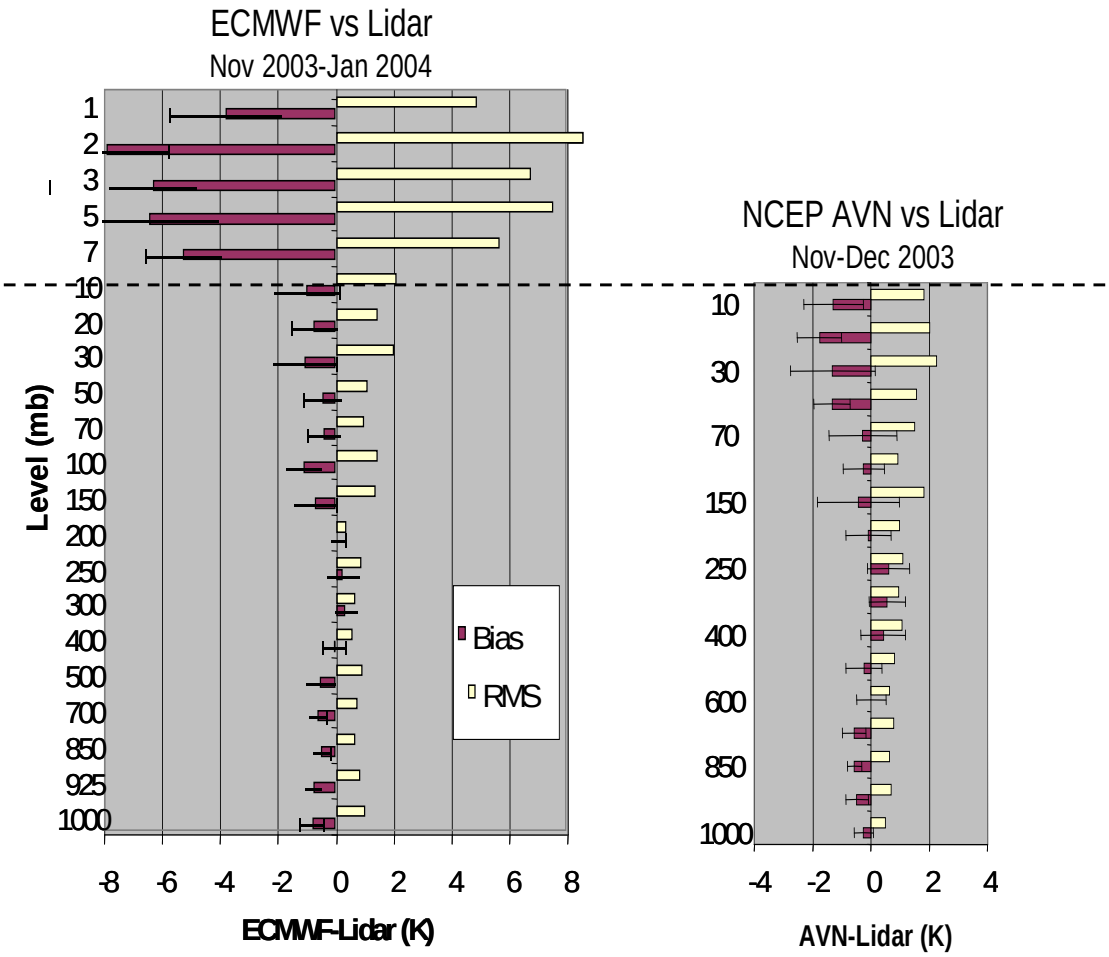

Figure 2-3. CEP atmospheric profiles have been assessed against other NWP models and observations. Analysis of Temperature Fields Versus RS90/Lidar at Barking Sands, Kauai (courtesy of John Wessel, Aerospace Corp)

Use or disclosure of data contained on this page is subject to the export restriction(s) on the title page of this document.

D45702, A. PDMO Released: 2009-02-18 (VERIFY REVISION STATUS)
PDMO

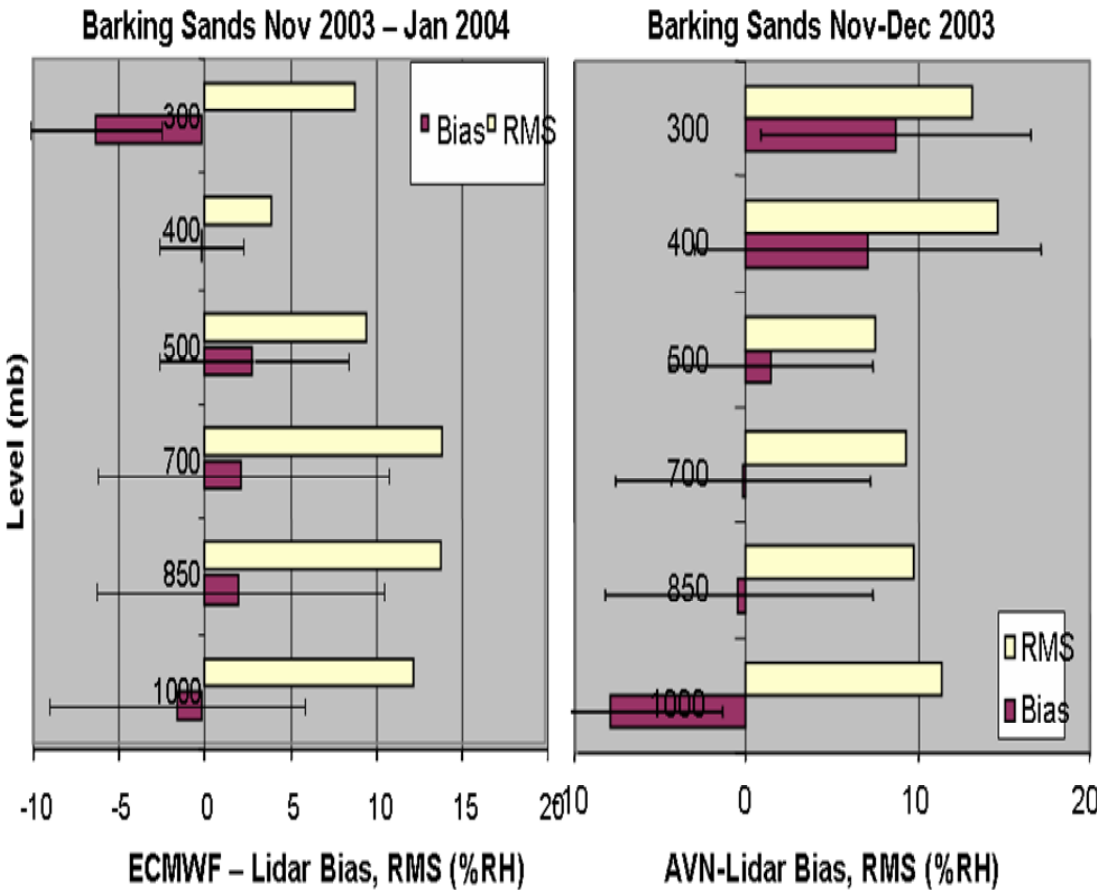

Figure 2-4. CEP atmospheric profiles have been assessed against other NWP models and observations. Analysis of Moisture Fields Versus RS90/Lidar at Barking Sands, Kauai (courtesy of John Wessel, Aerospace Corp)

Use or disclosure of data contained on this page is subject to the export restriction(s) on the title page of this document.

D45702, A. PDMO Released: 2009-02-18 (VERIFY REVISION STATUS)
PDMO

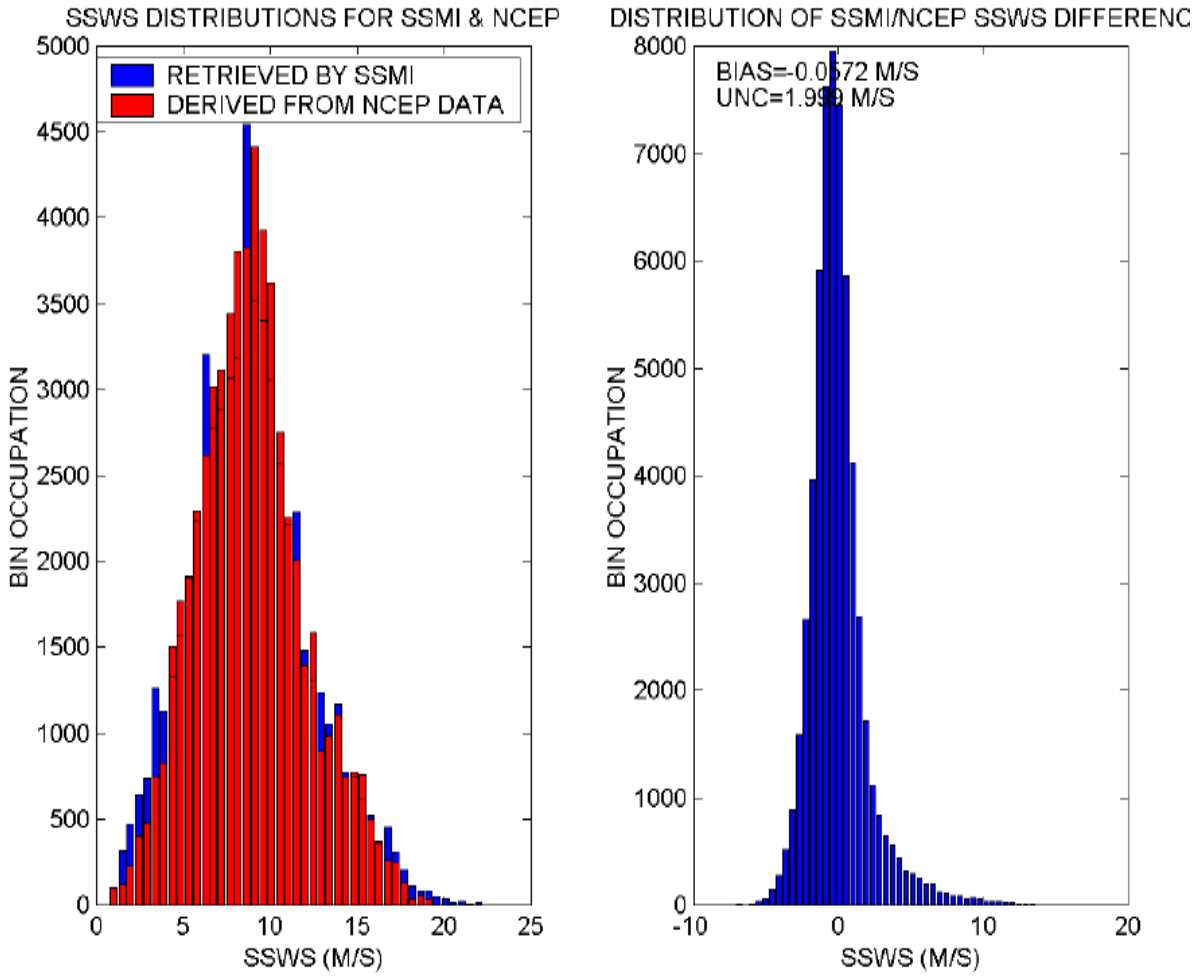

Figure 2-5. Comparison of NCEP SSWS with SSM/I SSWS for July 26th 2001 at 12Z

Use or disclosure of data contained on this page is subject to the export restriction(s) on the title page of this document.

D45702, A. PDMO Released: 2009-02-18 (VERIFY REVISION STATUS)
PDMO

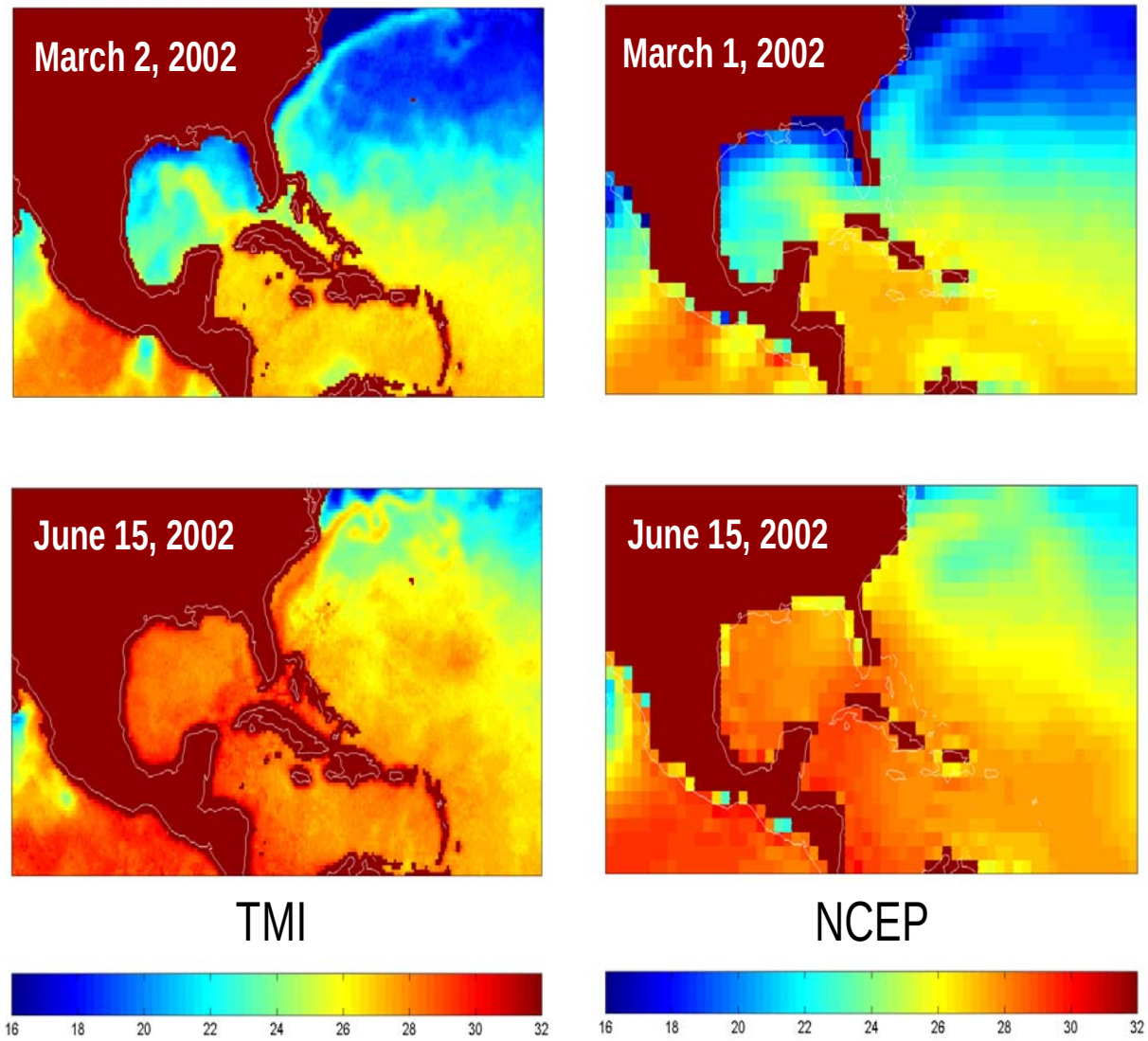

Figure 2-6. Comparison of NCEP sea-surface temperature with the sea-surface temperature measured by TMI

Use or disclosure of data contained on this page is subject to the export restriction(s) on the title page of this document.

D45702, A. PDMO Released: 2009-02-18 (VERIFY REVISION STATUS)
PDMO

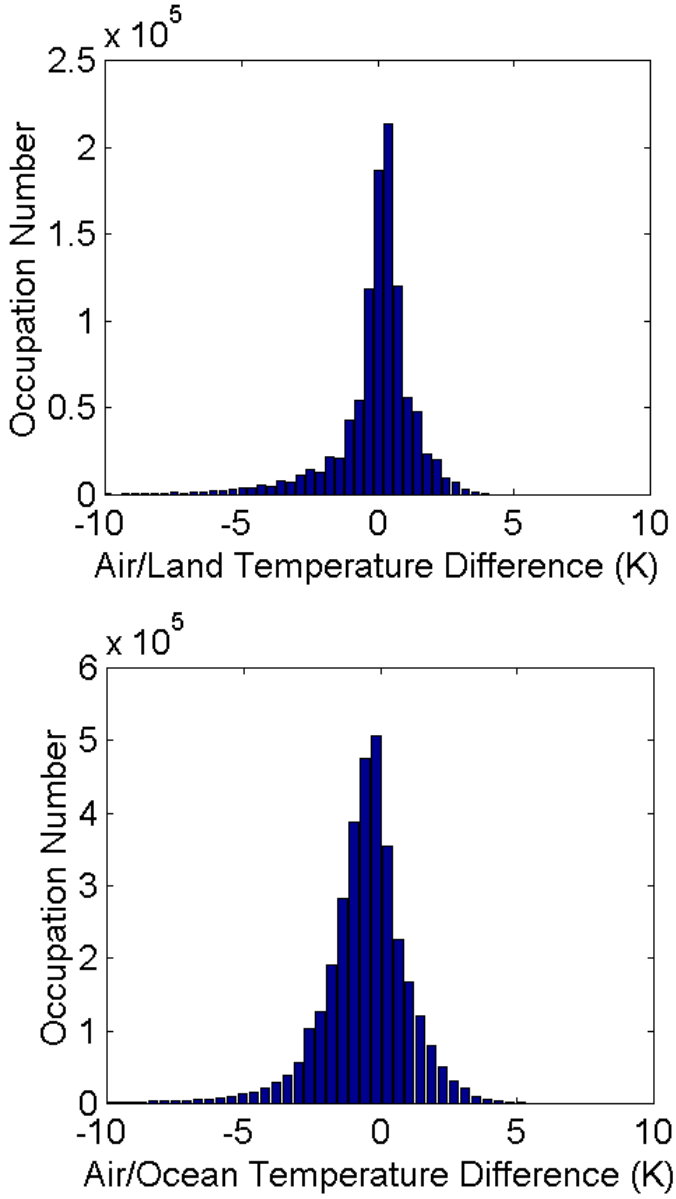

Figure 2-7. NCEP distributions of the difference between the near-surface air temperature and the land and sea skin temperatures exhibit the natural correlations that should exist in realistic environmental data.

Use or disclosure of data contained on this page is subject to the export restriction(s) on the title page of this document.

D45702, A. PDMO Released: 2009-02-18 (VERIFY REVISION STATUS)
PDMO

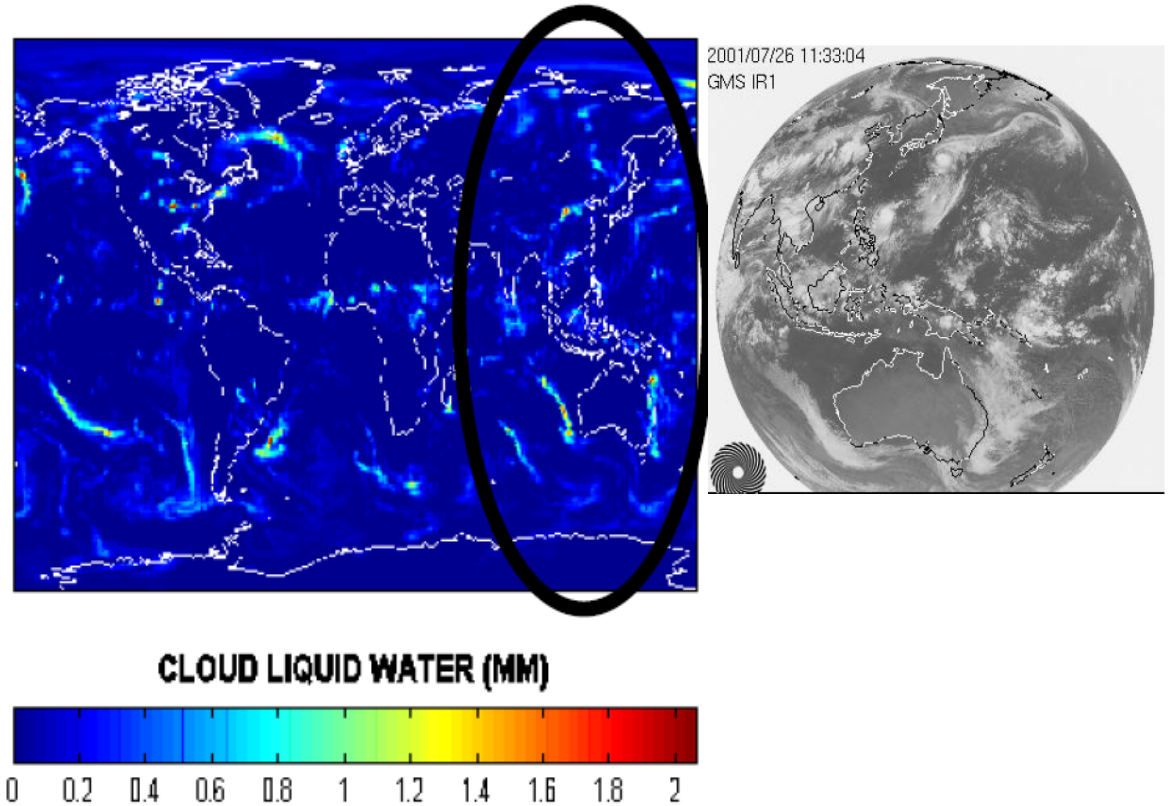

Figure 2-8. Comparison of NCEP AVN-FNL total cloud liquid water to a GMS infrared satellite image of South East Asia

Use or disclosure of data contained on this page is subject to the export restriction(s) on the title page of this document.

D45702, A. PDMO Released: 2009-02-18 (VERIFY REVISION STATUS)
PDMO

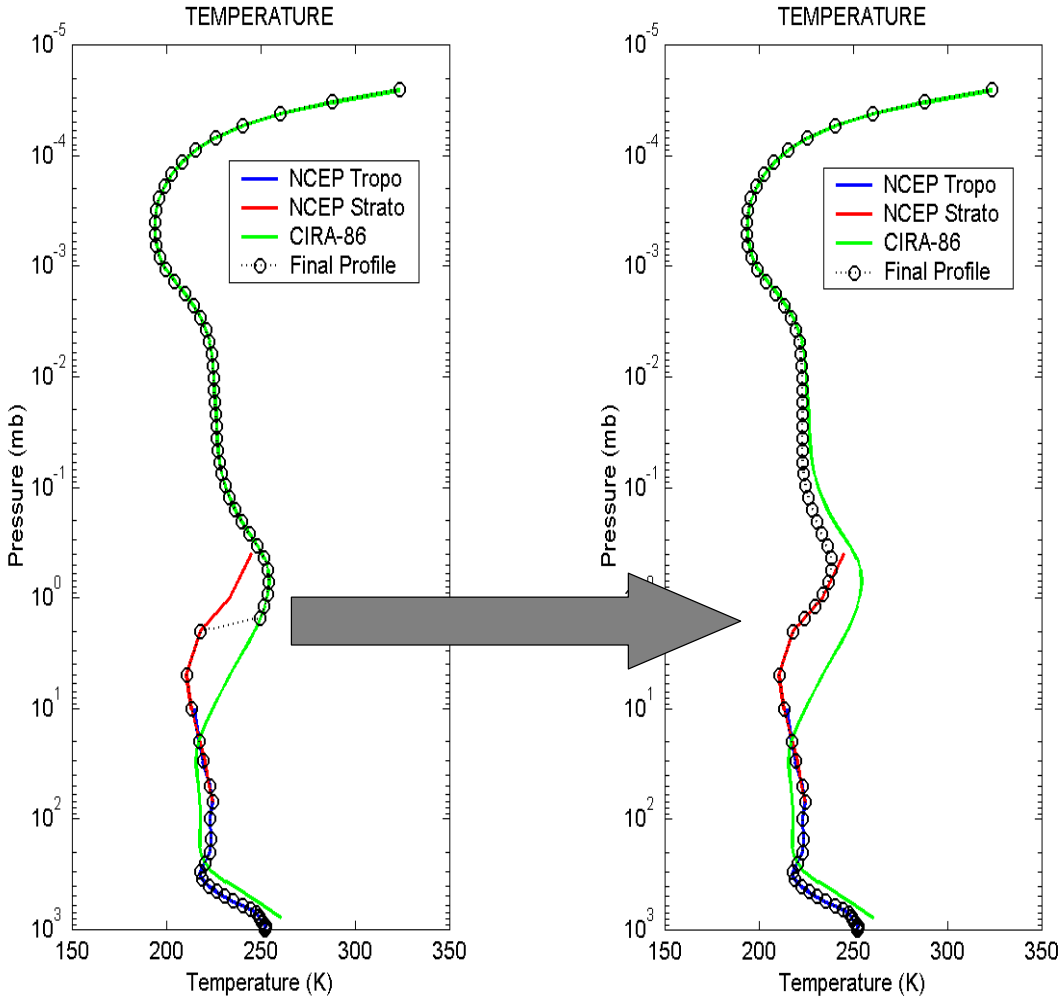

Figure 2-9. Illustration of process for smoothly transitioning between NCEP and climatology temperature profiles

Use or disclosure of data contained on this page is subject to the export restriction(s) on the title page of this document.

D45702, A. PDMO Released: 2009-02-18 (VERIFY REVISION STATUS)
PDMO

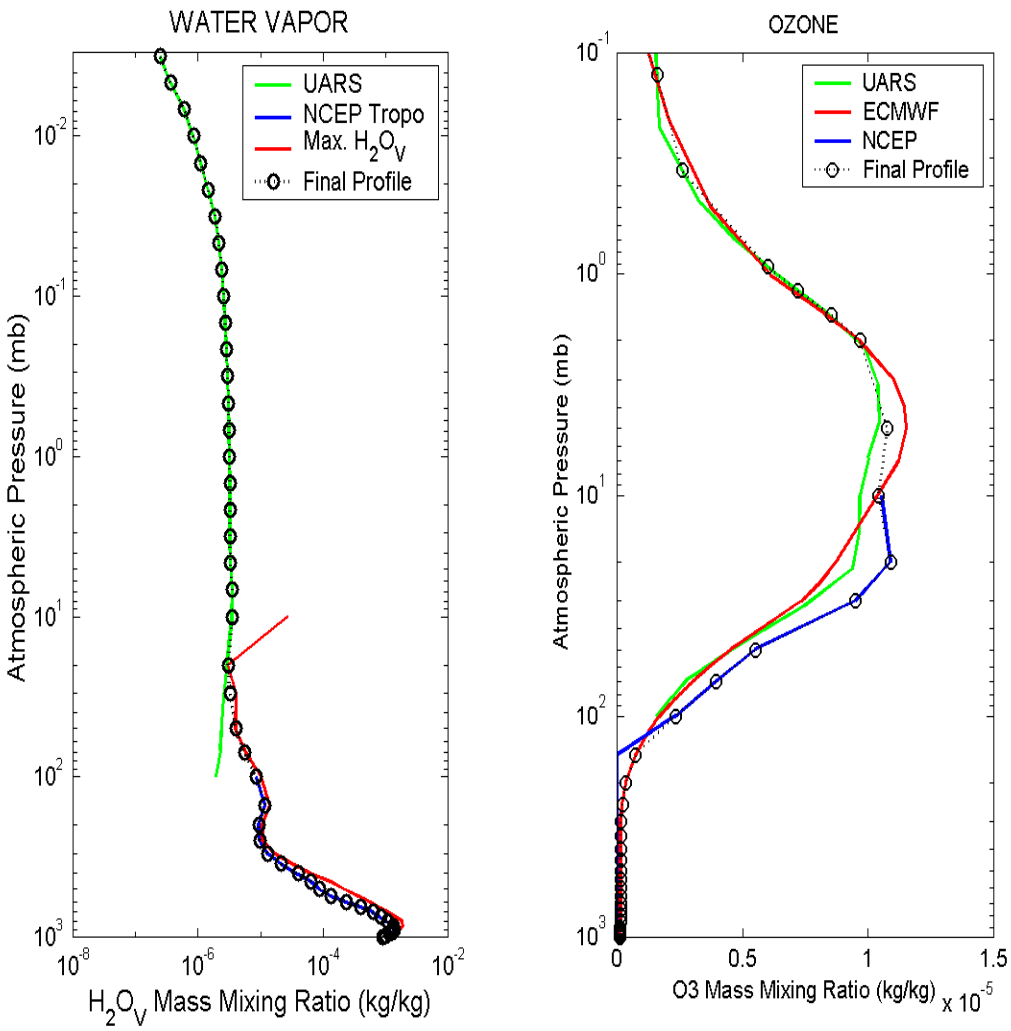

Figure 2-10. Extending other key atmospheric profiles (H_2O_v and O_3) to TOA

Use or disclosure of data contained on this page is subject to the export restriction(s) on the title page of this document.

D45702, A. PDMO Released: 2009-02-18 (VERIFY REVISION STATUS)
PDMO

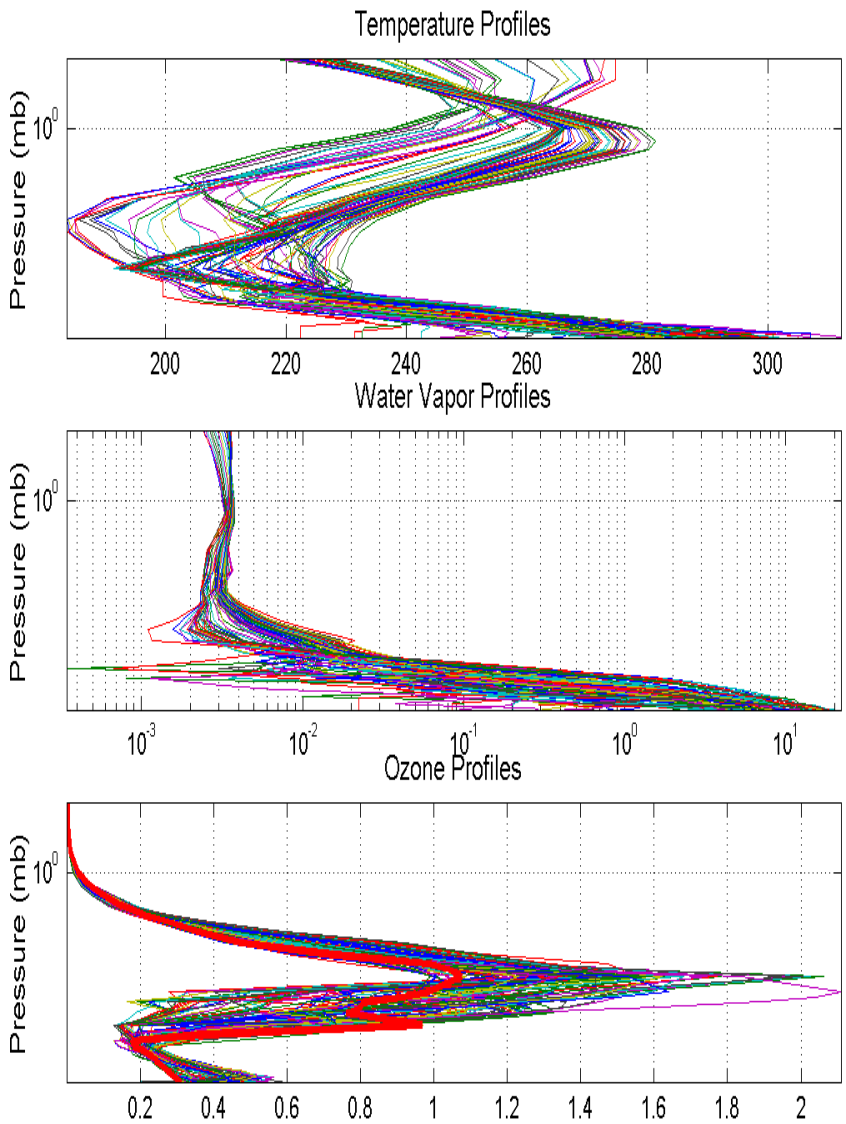

Figure 2-11. Sample profiles of temperature, moisture and ozone constructed from NCEP NWP reanalysis data and CIRA-86 and UARS reference atmospheres

Use or disclosure of data contained on this page is subject to the export restriction(s) on the title page of this document.

D45702, A. PDMO Released: 2009-02-18 (VERIFY REVISION STATUS)
PDMO

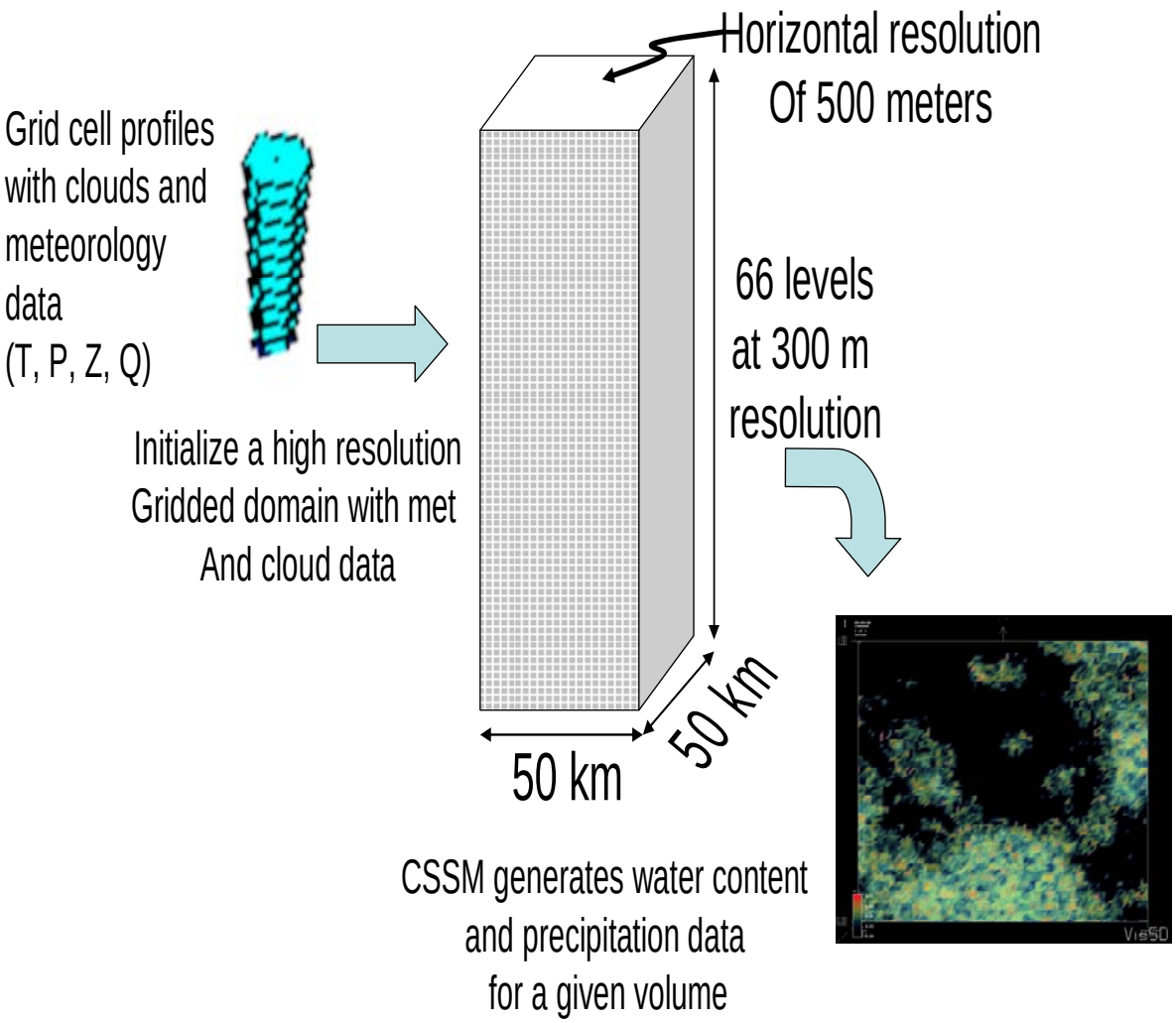

Figure 2-12. CSSM process for generating water/ice content and precipitation data on a high-resolution gridded domain for each input NCEP AVN profile

Use or disclosure of data contained on this page is subject to the export restriction(s) on the title page of this document.

D45702, A. PDMO Released: 2009-02-18 (VERIFY REVISION STATUS)
PDMO

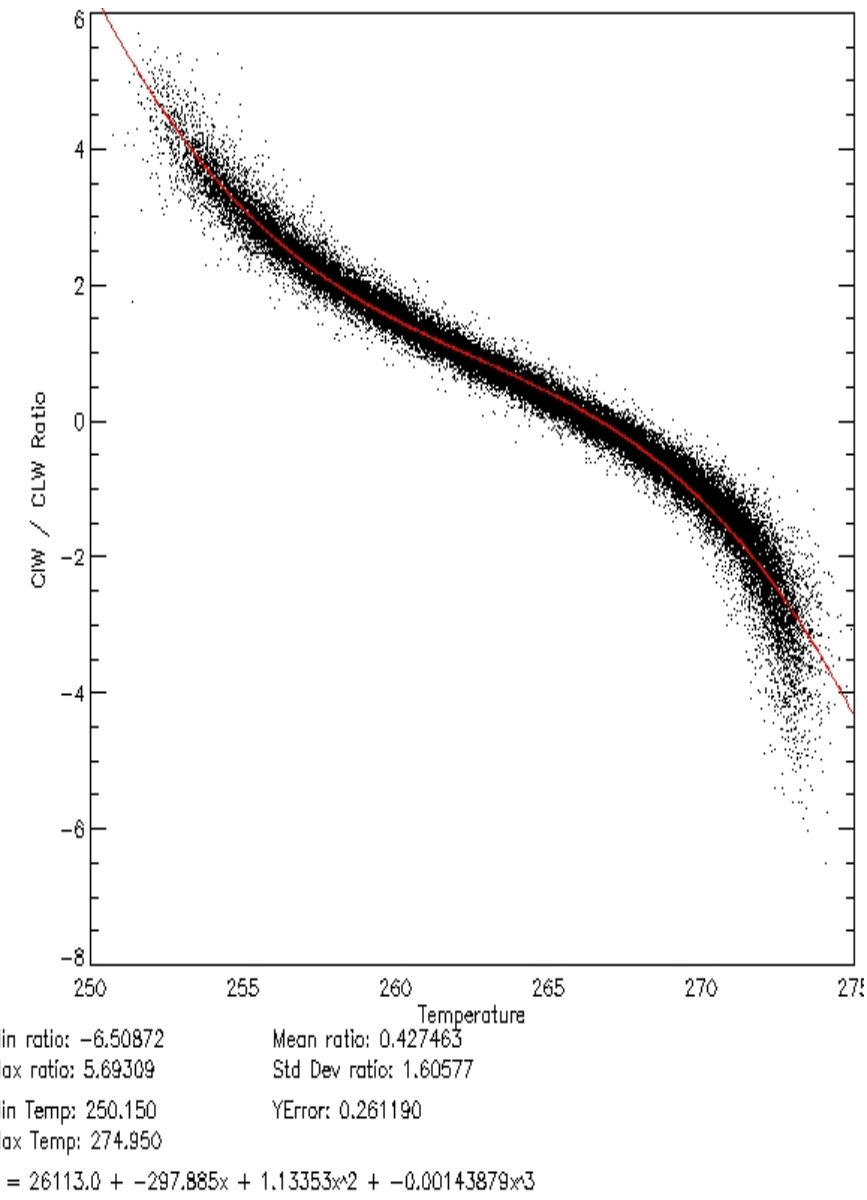

Figure 2-13. Scatter plot of ln(CIWMMR/CLWMMR) and temperature for points in the ECMWF 60L-SD global dataset. The red curve represents a third-order polynomial best fit to the data

Use or disclosure of data contained on this page is subject to the export restriction(s) on the title page of this document.

D45702, A. PDMO Released: 2009-02-18 (VERIFY REVISION STATUS)
PDMO

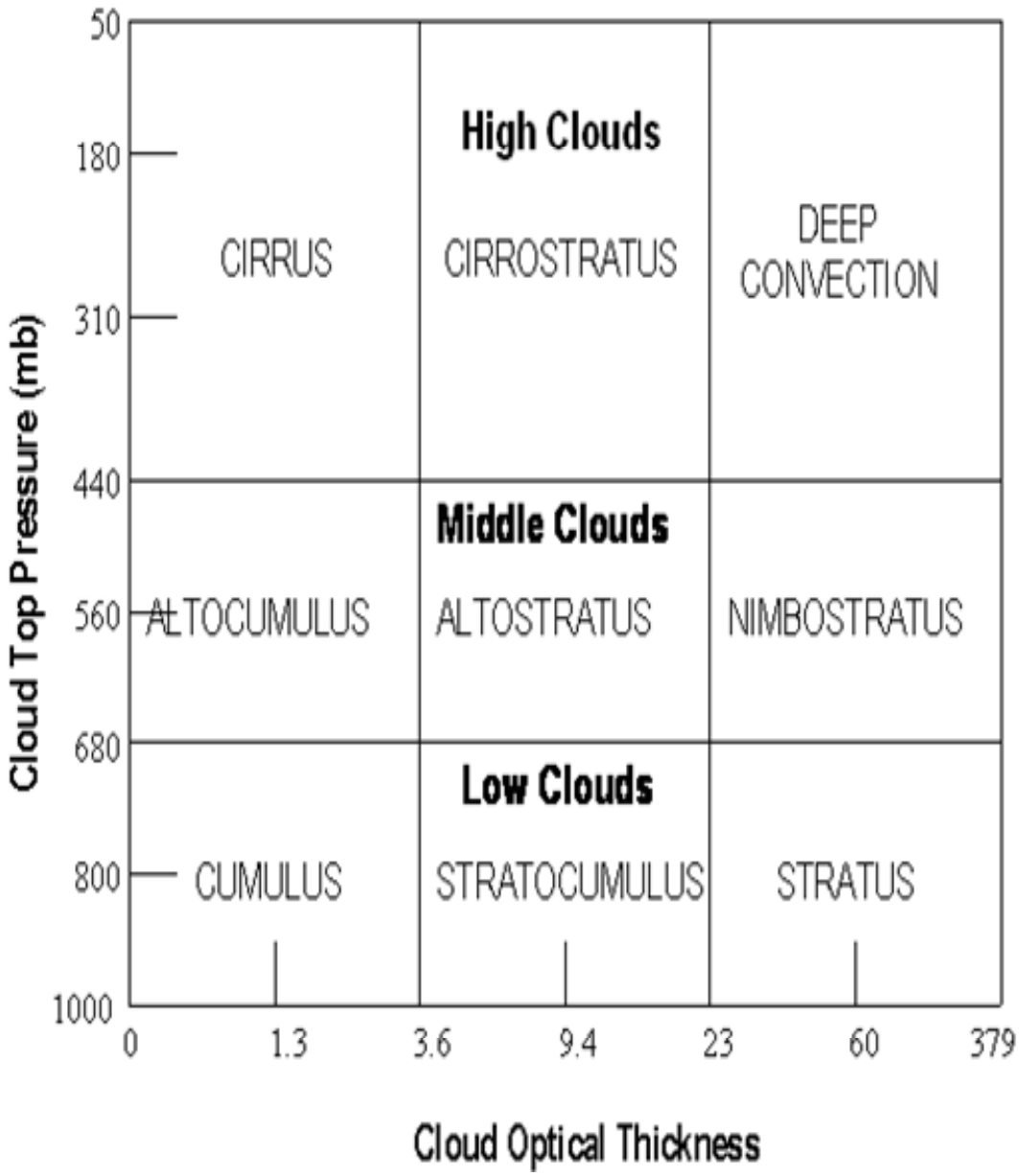

Figure 2-14. ISCCP radiometric cloud classification

Use or disclosure of data contained on this page is subject to the export restriction(s) on the title page of this document.

D45702, A. PDMO Released: 2009-02-18 (VERIFY REVISION STATUS)
PDMO

Oblique View

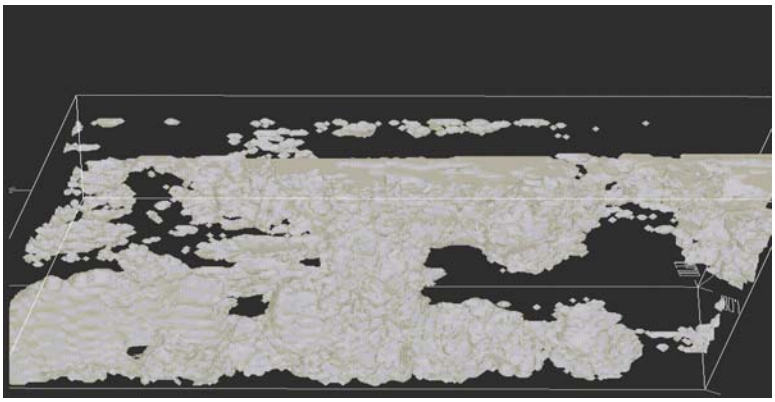

Top View

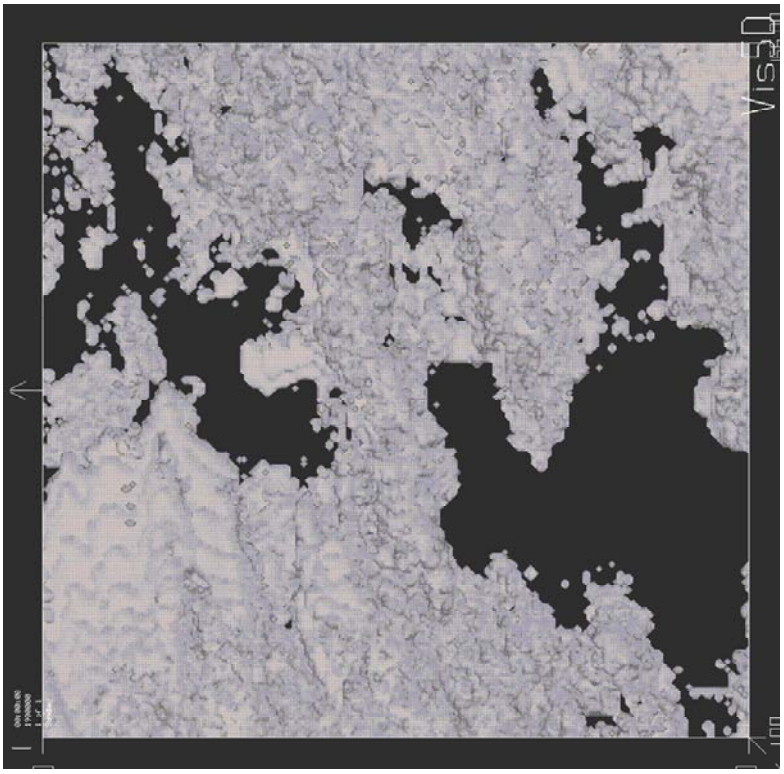

Figure 2-15. High-resolution, 3D cloud structure and physical properties for Global Synthetic Test Datasets generated by the NGIT Cloud Scene Simulation Model

Use or disclosure of data contained on this page is subject to the export restriction(s) on the title page of this document.

D45702, A. PDMO Released: 2009-02-18 (VERIFY REVISION STATUS)
PDMO

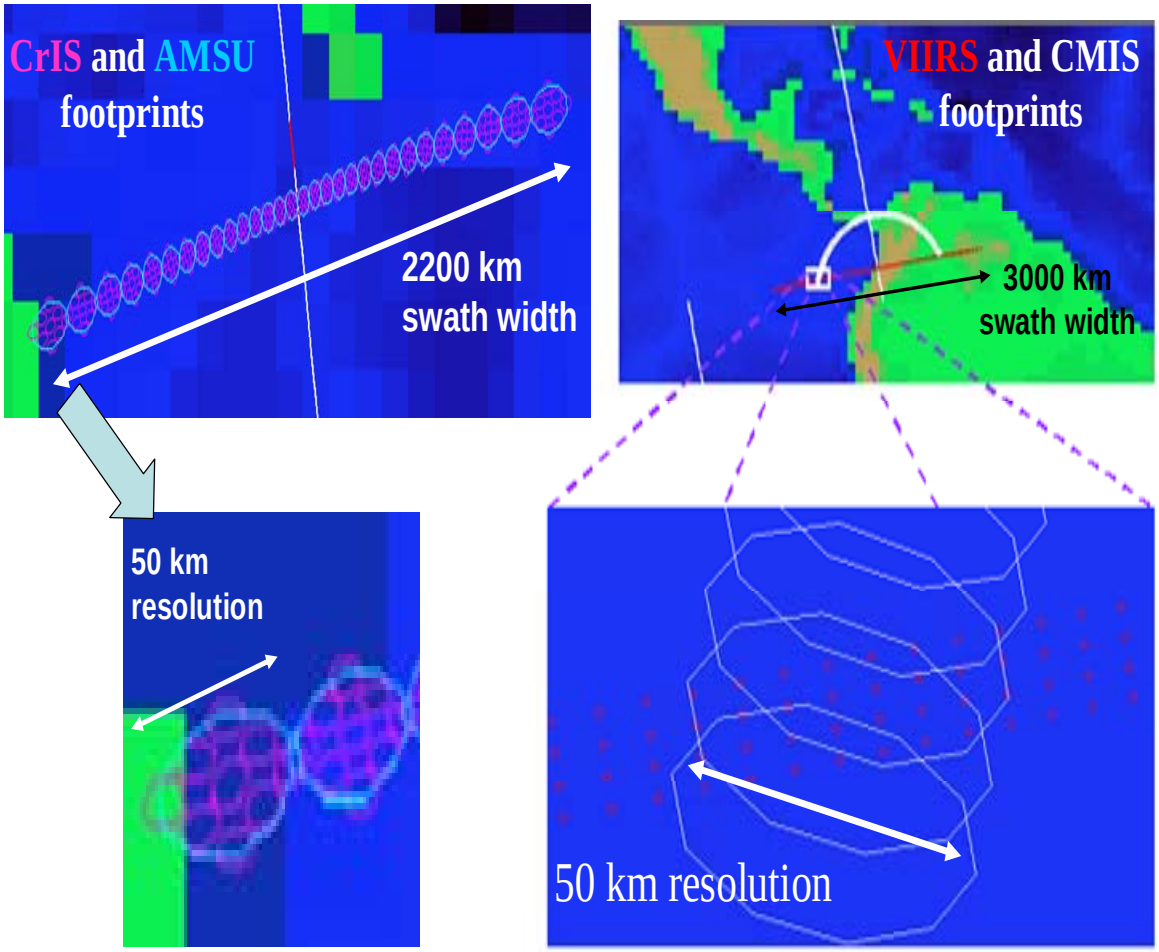

Figure 2-16. Cloud properties computed within each sensor FOV are tailored to the sensor-specific footprint sizes for VIIRS, CrIS, ATMS, and CMIS, as well as the required RTM inputs for each sensor

Use or disclosure of data contained on this page is subject to the export restriction(s) on the title page of this document.

D45702, A. PDMO Released: 2009-02-18 (VERIFY REVISION STATUS)
PDMO

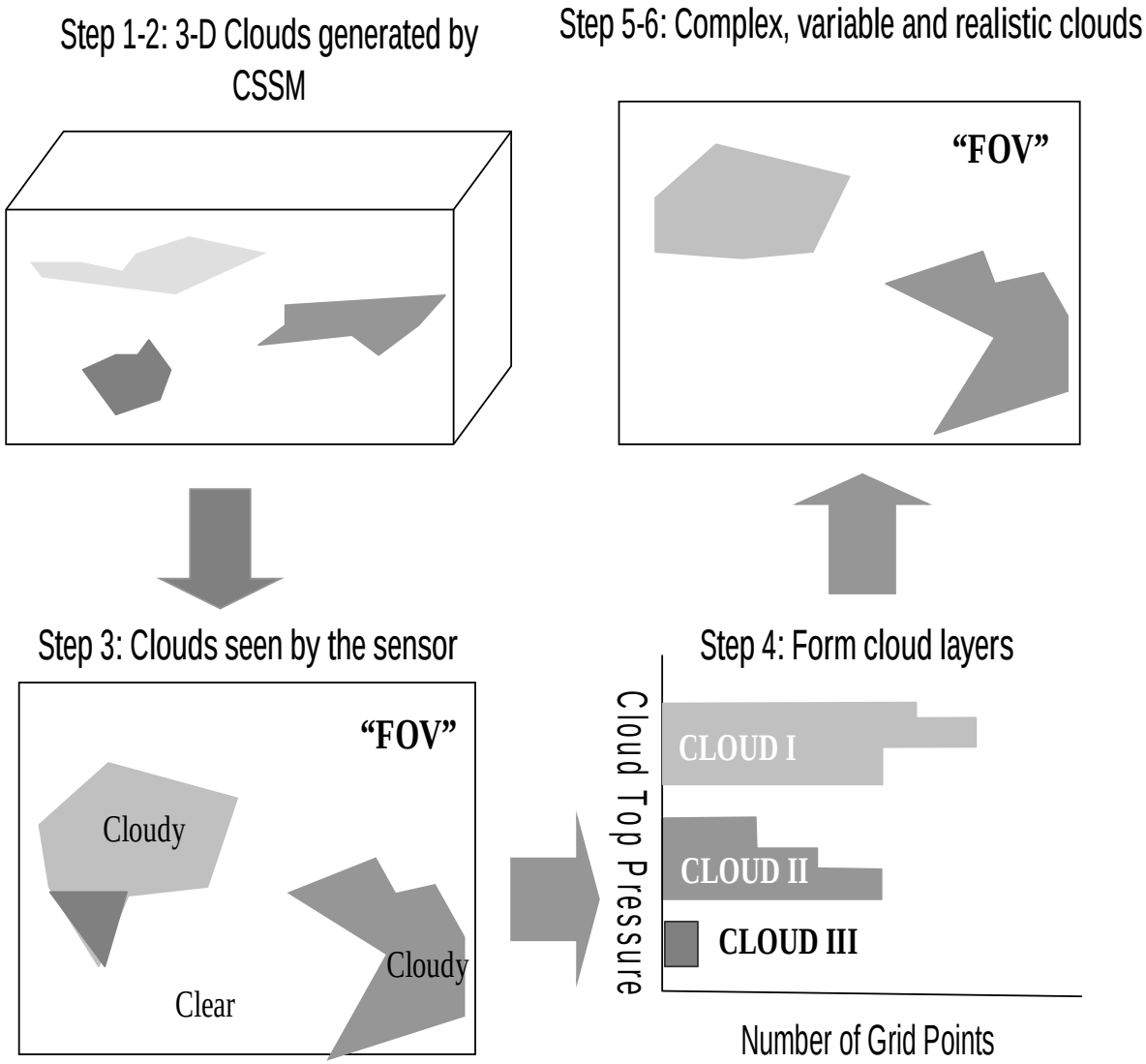

Figure 2-17. Utilizing CSSM clouds with 3x3 CrIS footprints for use by AER OSS RTM

Use or disclosure of data contained on this page is subject to the export restriction(s) on the title page of this document.

D45702, A. PDMO Released: 2009-02-18 (VERIFY REVISION STATUS)
PDMO

Table 2-2. Water and ice cloud types contained in Global Synthetic Test Datasets

Type	Phase	PSD	r_e(microns)
1	ice	UCLA – Cold Ci (D_e < 27)	23.9
2	ice	UCLA – T= -60°C (34 > D_e > 27)	30.4
3	ice	UCLA – Cs (58.5 > D_e > 34)	41.5
4	ice	UCLA – FIRE-I Nov 1 (84 > D_e > 58.5)	75.1
5	ice	UCLA – FIRE-I Nov 2 (108.5 > D_e > 84)	93
6	ice	UCLA – Ci Uncinus D_e > 108.5	123.6
7	water	UCLA – Precipitating Cumulus #1	16
8	water	UCLA – Precipitating Cumulus #2	24
9	water	UCLA – Precipitating Cumulus #3	30
10	water	SS Cumulus	12
11	water	SS Altostratus	7.21
12	water	SS Stratocumulus #1	10
13	water	SS Nimbostratus #1	12.01
14	water	SS Stratus #1	8.996
15	water	SS Stratus #2	8.333
16	water	SS Stratus-Stratocumulus	6.667
17	water	SS Stratocumulus #2	10
18	water	SS Nimbostratus #2	11.76
19	water	SS Cumulus-Cumulus Congestus	15.24

Use or disclosure of data contained on this page is subject to the export restriction(s) on the title page of this document.

D45702, A. PDMO Released: 2009-02-18 (VERIFY REVISION STATUS)
PDMO

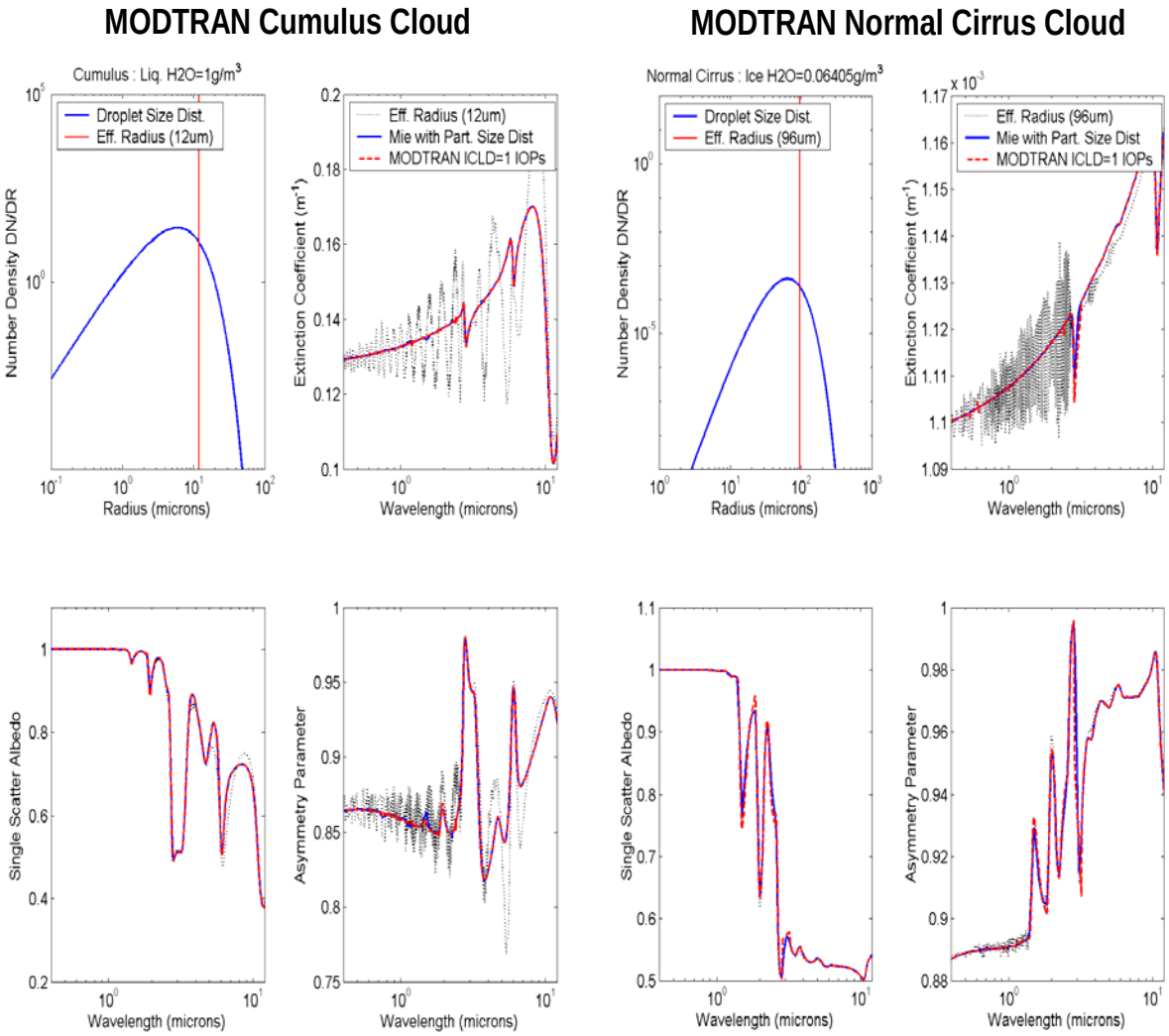

Figure 2-18. One way of verifying Mie Scattering computations of cloud optical properties is by comparison with optical properties for cloud models used by LOWTRAN/MODTRAN

Use or disclosure of data contained on this page is subject to the export restriction(s) on the title page of this document.

D45702, A. PDMO Released: 2009-02-18 (VERIFY REVISION STATUS)
PDMO

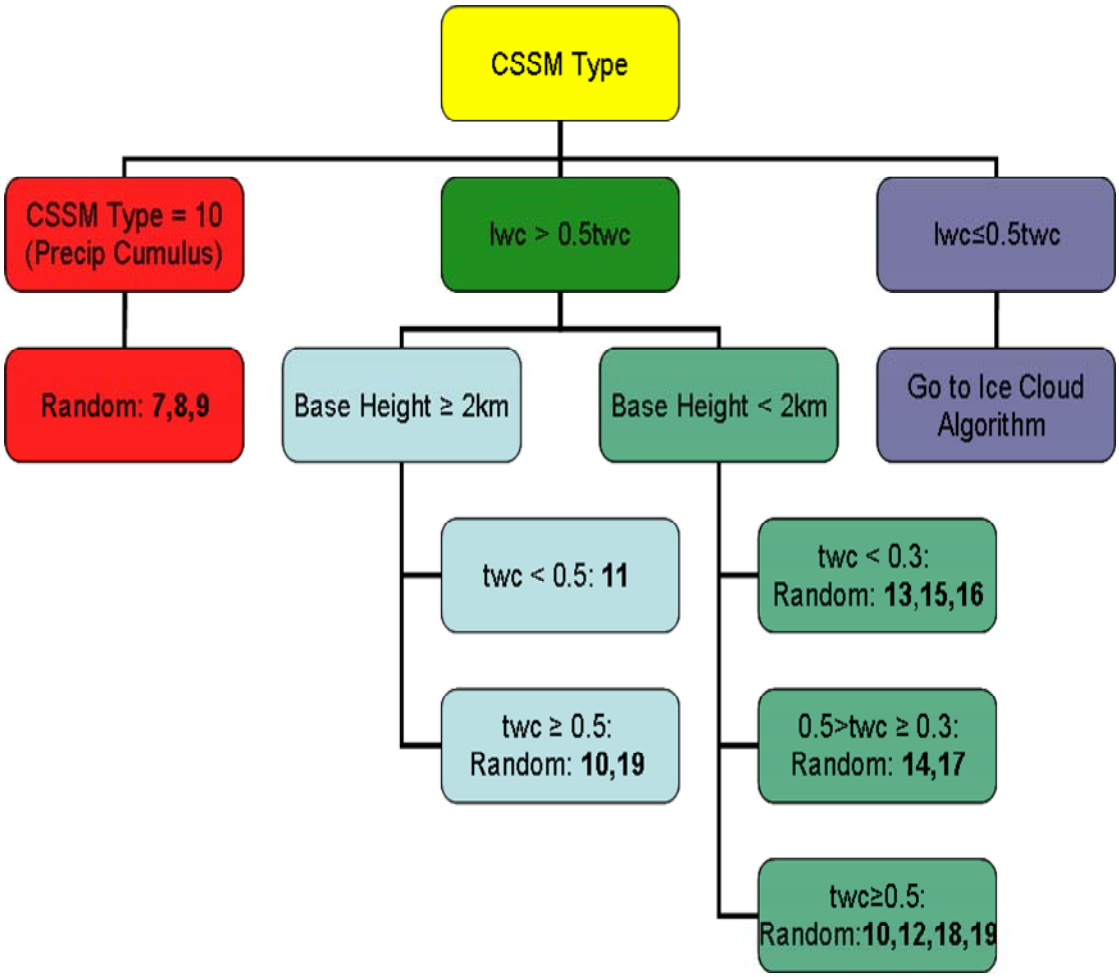

Figure 2-19. Final cloud type is assigned based on liquid/ice water content and cloud height

Use or disclosure of data contained on this page is subject to the export restriction(s) on the title page of this document.

D45702, A. PDMO Released: 2009-02-18 (VERIFY REVISION STATUS)
PDMO

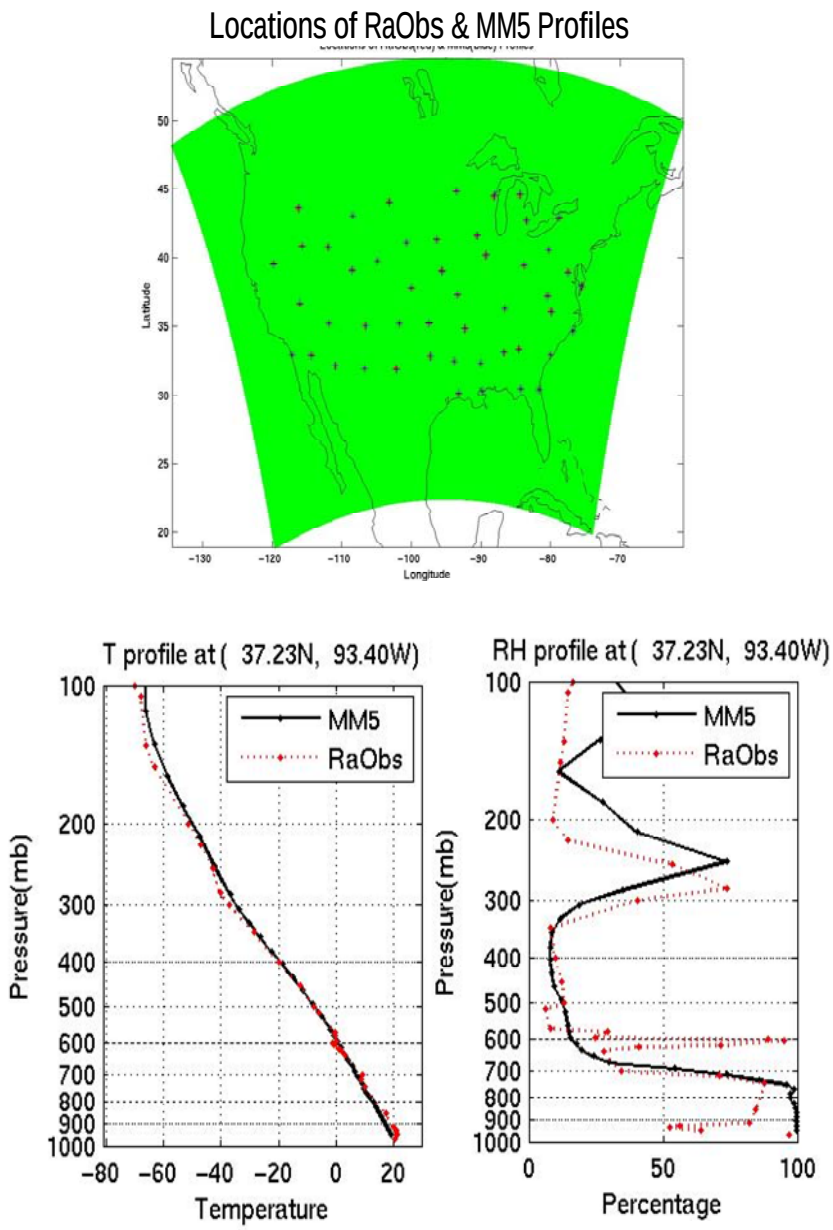

Figure 2-20. Comparisons of MM5 results with RaObs data have been made to check that MM5 provides "realistic" profiles

Use or disclosure of data contained on this page is subject to the export restriction(s) on the title page of this document.

D45702, A. PDMO Released: 2009-02-18 (VERIFY REVISION STATUS)
PDMO

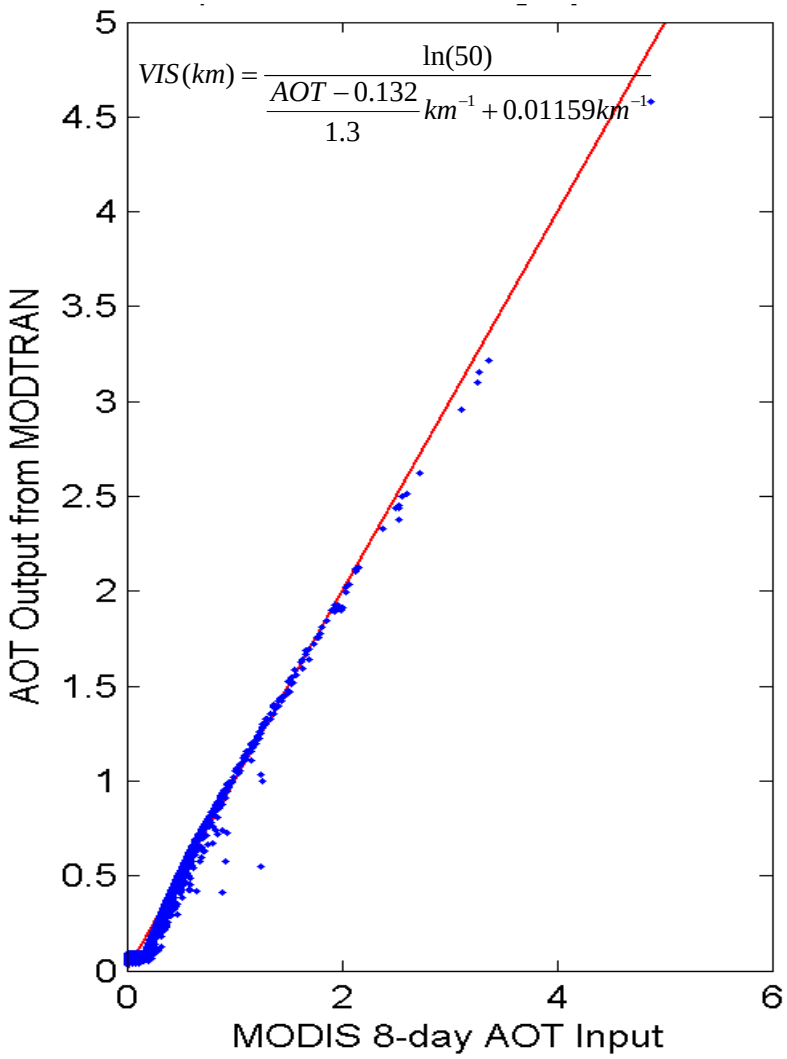

Figure 2-21. Altitude dependent aerosol concentration is scaled via the surface meteorological range to approximate the MODIS 8-day AOT values

Use or disclosure of data contained on this page is subject to the export restriction(s) on the title page of this document.

D45702, A. PDMO Released: 2009-02-18 (VERIFY REVISION STATUS)
PDMO

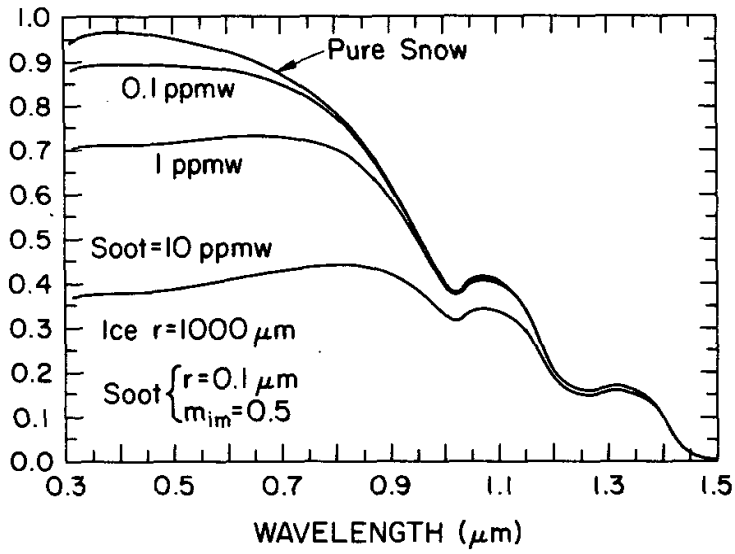

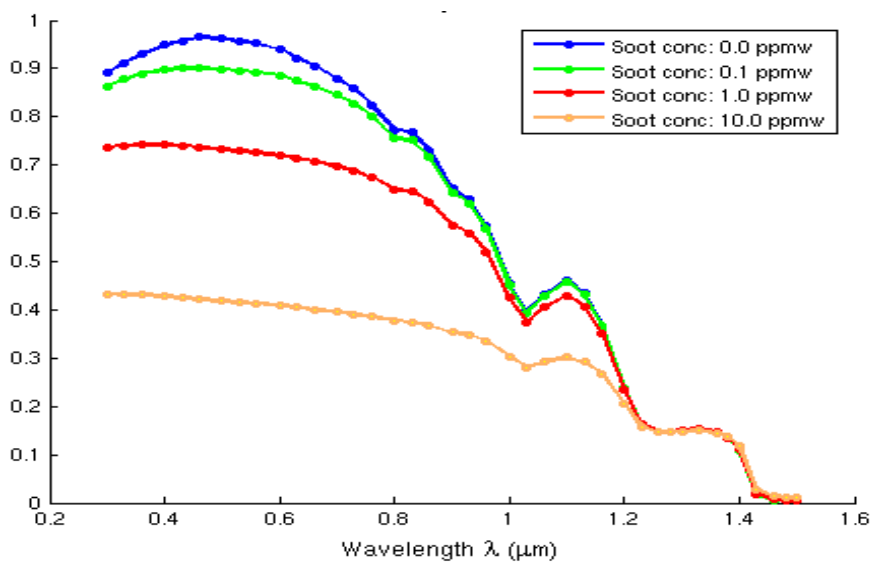

Figure 2-22. Comparisons of the spectral albedo as a function of snow grain size, soot particle size, soot concentration, and solar angle were made to data in the ASTER Spectral Library and to the literature

Use or disclosure of data contained on this page is subject to the export restriction(s) on the title page of this document.

D45702, A. PDMO Released: 2009-02-18 (VERIFY REVISION STATUS)
PDMO

Table 2-3. Land Cover Materials in PRA Materials Database

Material ID	Material	Material ID	Material
1	Urban Commercial	15	Rice Fields
2	Sparse Vegetation	16	Savanna
3	Conifers	17	Wetland
4	Deciduous Broadleaf	18	Scrub
5	Evergreen Broadleaf	19	Shrublands
6	Grasses Shrubs	20	Wooded Wetland
7	Sand	21	Grass Crops
8	Tundra	22	Irrigated Crops
9	Snow	23	Polar Barren
10	Water	24	Urban Residential
11	Mixed Forest	25	Soil
12	Crops Town	26	Sea Ice 3m Thick
13	Crops	27	Chlorophyll Water
14	Tropical Forest	28	Thin Ice

Use or disclosure of data contained on this page is subject to the export restriction(s) on the title page of this document.

D45702, A. PDMO Released: 2009-02-18 (VERIFY REVISION STATUS)
PDMO

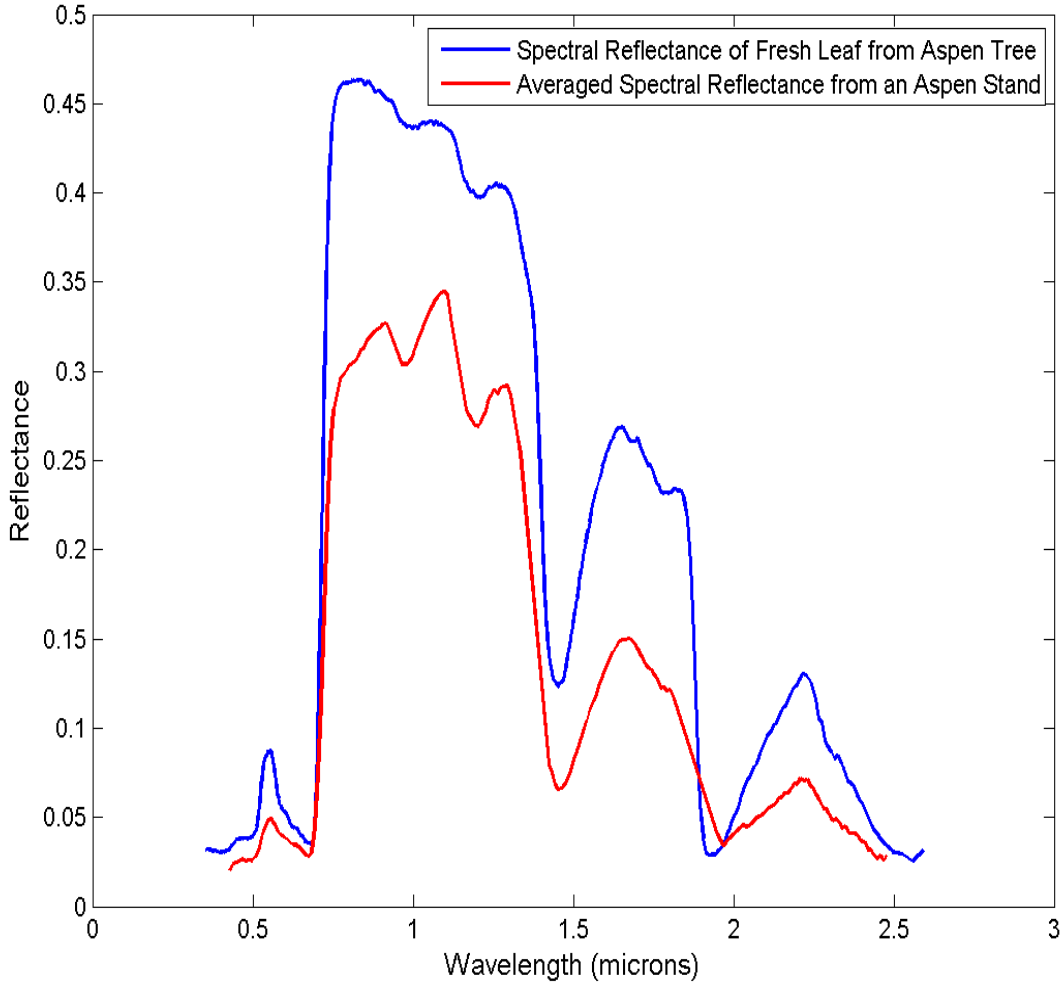

Figure 2-23. Laboratory measurements of the spectral reflectance for vegetation components (e.g., leaves from a deciduous tree or needles from a coniferous tree) compared to in-field measurements of the entire tree

Use or disclosure of data contained on this page is subject to the export restriction(s) on the title page of this document.

D45702, A. PDMO Released: 2009-02-18 (VERIFY REVISION STATUS)
PDMO

Table 2-4. Re-generating spectral reflectance properties (0.4 to 2.5microns) for some PRA materials using Data from USGS SPLIB05a

Material ID	Material	New Material from SPLIB05a
2	Sparse Vegetation	75% Sand (PRA) + 25% Grass – Fescue Wheat (36 – splib05a)
3	Conifers	Lodgepole Pine (75 – splib05a)
4	Deciduous Broadleaf	Aspen (8 – slib05a)
6	Grasses Shrubs	Grass – Fescue Wheat (36 – splib05a)
8	tundra	50% Soil (PRA) + 50% Grass – Fescue Wheat (36 – splib05a)
12	Crops Town	Grass – Fescue Wheat (38 – splib05a)
13	Crops	Grass – Fescue Wheat (39 – splib05a)
15	Rice Fields	Sedge (92 – splib05a)
16	Savanna	Grass – Fescue Wheat (36 – splib05a)
17	Wetland	Cattail Marsh (13 – splib05a)
19	Shrublands	Big Sagebrush (90 – splib05a)
20	Wooded Wetland	Wetlands (98 – splib05a)
22	Irrigated Crops	Smooth Brome (40 – splib05a)

Use or disclosure of data contained on this page is subject to the export restriction(s) on the title page of this document.

D45702, A. PDMO Released: 2009-02-18 (VERIFY REVISION STATUS)
PDMO

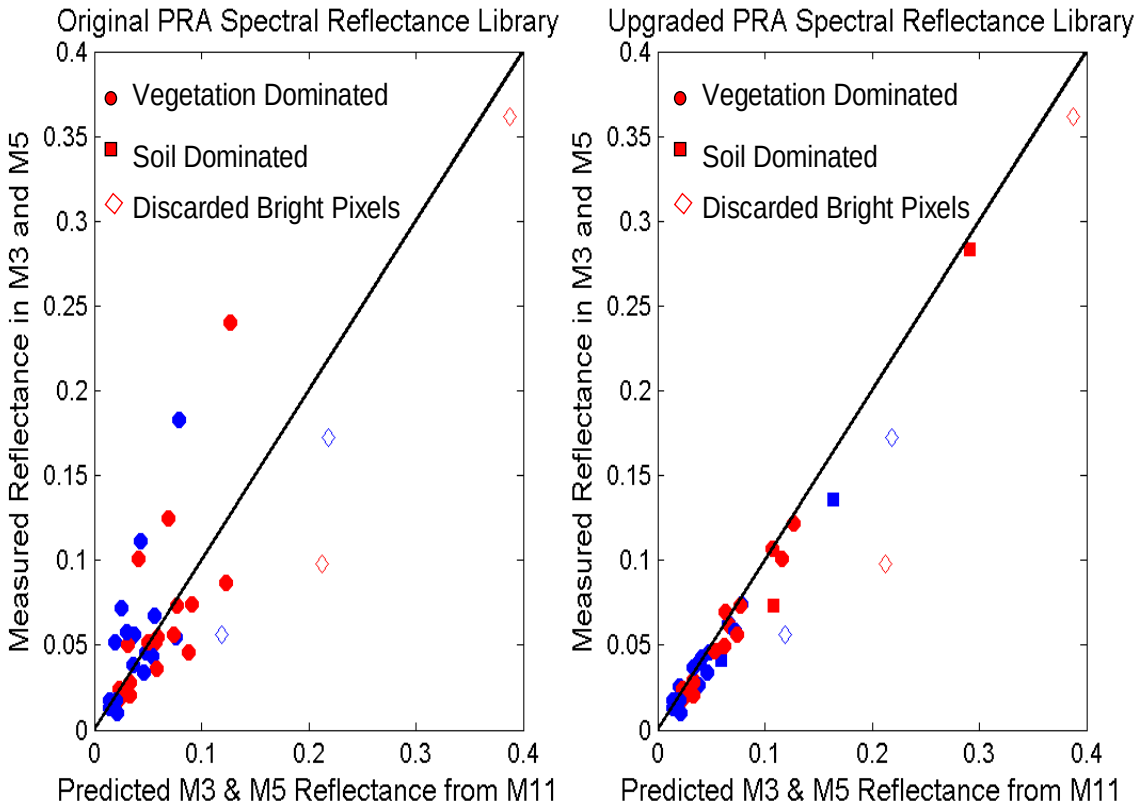

Figure 2-24. Expected correlation between SWIR and visible reflectance is contained in new PRA spectral albedo library

Use or disclosure of data contained on this page is subject to the export restriction(s) on the title page of this document.

D45702, A. PDMO Released: 2009-02-18 (VERIFY REVISION STATUS)
PDMO

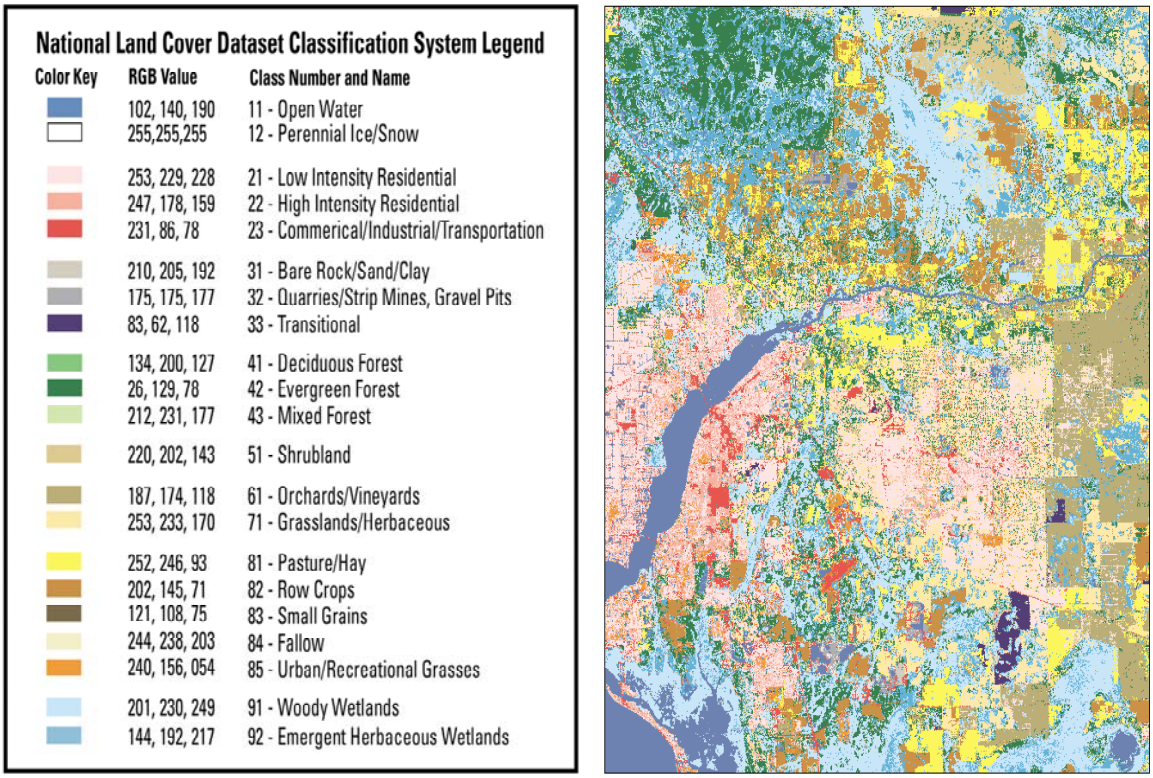

Figure 2-25. National Land Cover Database (NLCD) provides land cover type at 30 meter resolution over CONUS

Use or disclosure of data contained on this page is subject to the export restriction(s) on the title page of this document.

D45702, A. PDMO Released: 2009-02-18 (VERIFY REVISION STATUS)
PDMO

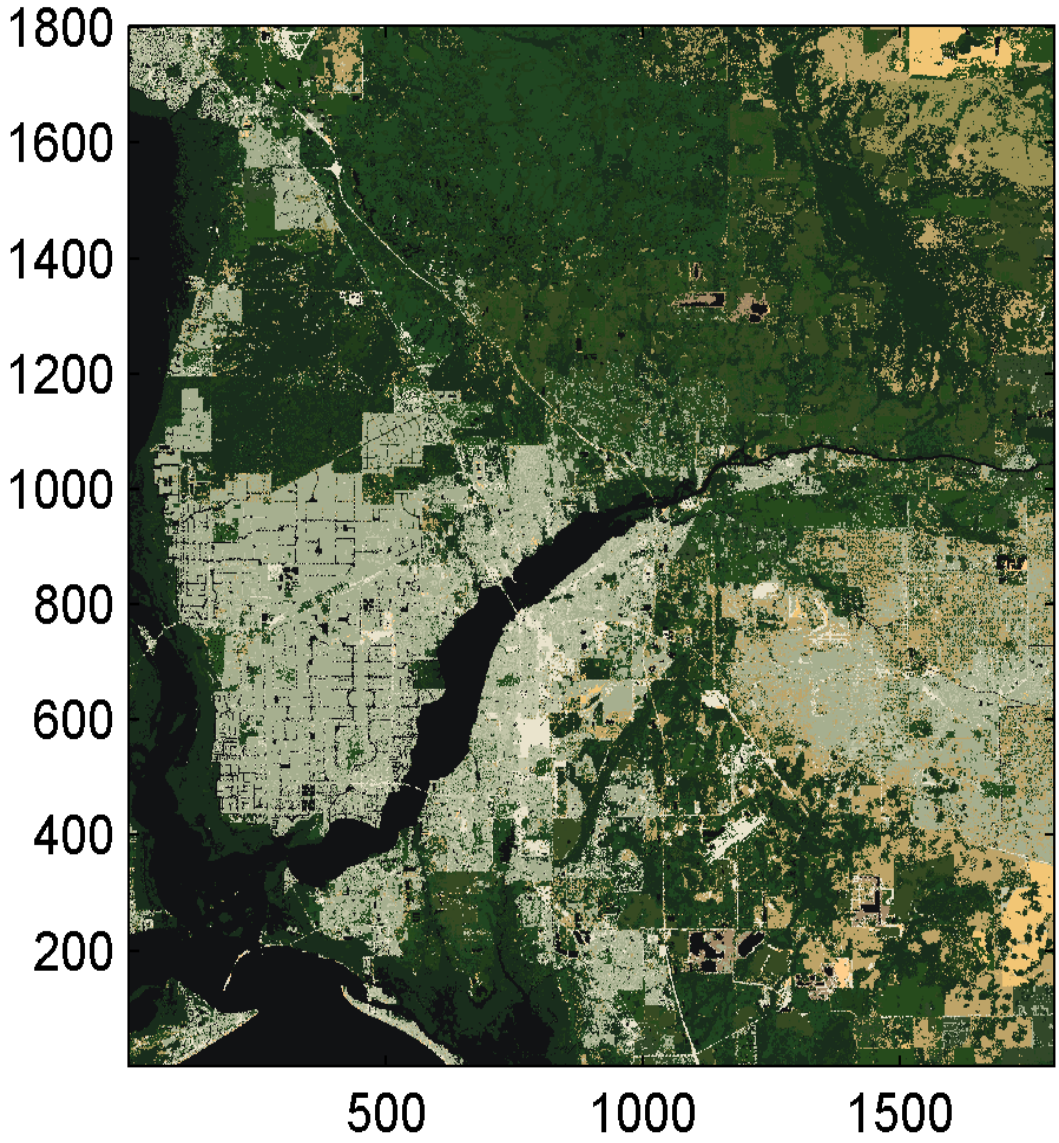

Figure 2-26. Synthetic true color, high-resolution reflectance imagery generated from NLCD land cover types with directional-hemispherical reflectances generated from the ASTER Spectral Libraries

Use or disclosure of data contained on this page is subject to the export restriction(s) on the title page of this document.

D45702, A. PDMO Released: 2009-02-18 (VERIFY REVISION STATUS)
PDMO

2.2 Generating Sampled Global Test Dataset

The global environmental data for the current EDR assessments is based on 12 days of NCEP analyses, consisting of 1 day/month between July 2001 and June 2002. This data set provides an ensemble of over 3 million possible surface/atmosphere situations that can be sampled to construct the global test datasets. Although the range of values for some EDRs is sufficient for covering the required measurement range specified in the NPOESS System Specification document, there are a number of EDRs for which coverage of the required range is either missed by a considerable margin or just barely met, but with insufficient samples for making a statistical assessment of performance at these extreme values. In the latter case, we will try and identify additional global data to fill the gaps at either end of the measurement range. However, it may be necessary to obtain a waiver for the required measurement range of those EDRs for which the observed range of values fall far short of those specified in the NPOESS System Specification document. A summary of the gaps between the required measurement range and that observed from the NCEP data is provided in Table 2-5.

To generate the set of sampled global positions, times and viewing angles (with respect to solar zenith and azimuth angles, as well as wind direction) for each sensor, we simulate the actual flight of the sensor as it scans over the earth for the 14 orbits of each day. The sampling approach is illustrated in Figure 2-27. For the VIIRS sensor, we take 7 positions along-scan (or cross-track) for every 30th along-track scan. Furthermore, these 7 cross-track sample positions change from orbit to orbit, as prescribed in the Engineering Memorandum NP-EMD.2006.510.0001, allowing multiple orbits of decimated data to be packed into one pseudo-orbit. Figure 2-28 provides an illustration of how the cross-track pixel sampling changes from orbit to orbit. This was done for several reasons. First, it provides improved sampling of the different cross-track aggregation zones, with their corresponding noise levels. Second, it allows better testing of scan-dependent sensor effects (e.g., response vs scan and emission vs scan). Finally, it results in more efficient processing by the SDR Calibration algorithm, which is designed to process fully populated granules. This sampling procedure produces 798 moderate-resolution pixel samples per orbit or 11,172 samples per day for each orbit plane. Figure 2-29 shows the global coverage achieved by this sampling scheme. The difference in uniformity of this coverage compared with that provided by the NOAA88B dataset supplied by the government is also seen in Figure 2-29. By sampling data from at least one day per month over a year, the final number of samples for each orbit plane is 134,064. Rather than generating pixel information for these moderate resolution pixels, we actually generate 4 (i.e., 2x2) “imagery-resolution” pixel samples for both Imagery and Moderate-Resolution bands, so as to allow generation of sub-pixel surface and cloud properties for testing algorithms like Cloud Mask, STIP and Snow Cover. Some properties (e.g., the NCEP atmospheric parameters) will be identical for each of the imagery resolution pixels within a moderate resolution sample, while properties such as clouds, snow cover, and surface temperature, can change from one imagery-resolution pixel to the next. The resulting global dataset provides the wide range of environmental conditions needed for a comprehensive evaluation of EDR performance under global, diurnal and seasonal conditions. Figure 2-30 shows the

Use or disclosure of data contained on this page is subject to the export restriction(s) on the title page of this document.

D45702, A. PDMO Released: 2009-02-18 (VERIFY REVISION STATUS)
PDMO

range of conditions embodied in the global environmental dataset compiled for assessing several of the environmental data products

Table 2-5. Summary of Gaps Between Spec Range and NCEP Global Data

Parameter	Spec Range	Test Data Range	Gap
AVTP* (K)	180 - 335	180 - 324	11k (max)
CTH (km)	0 - 20	0.15 - 17.4	2.6 km (max)
CTT* (K)	175 - 310	188 – 301.3	13K (min), 9K (max)
CTP (mb)	50 - 1050	89.2 – 1043.2	40mb (min), 7mb (max)
CBH (km)	0 - 20	0 - 16.5	3.5 km (max)
CCF	0 - 1.0	0.1 - 1.0	0.1 (min)
APS (α)	-1 - +3	-0.21 - +5	0.79 (min)
LST* (K)	213 - 343	227 - 329	14 (min), 14 (max)
IST* (K)	213 - 275	233 - 275	20 (min)
Soil Moisture* (cm/m)	0 - 100	3.1 - 46.8	3.1 (min), 53.2 (max)

Use or disclosure of data contained on this page is subject to the export restriction(s) on the title page of this document.

D45702, A. PDMO Released: 2009-02-18 (VERIFY REVISION STATUS)
PDMO

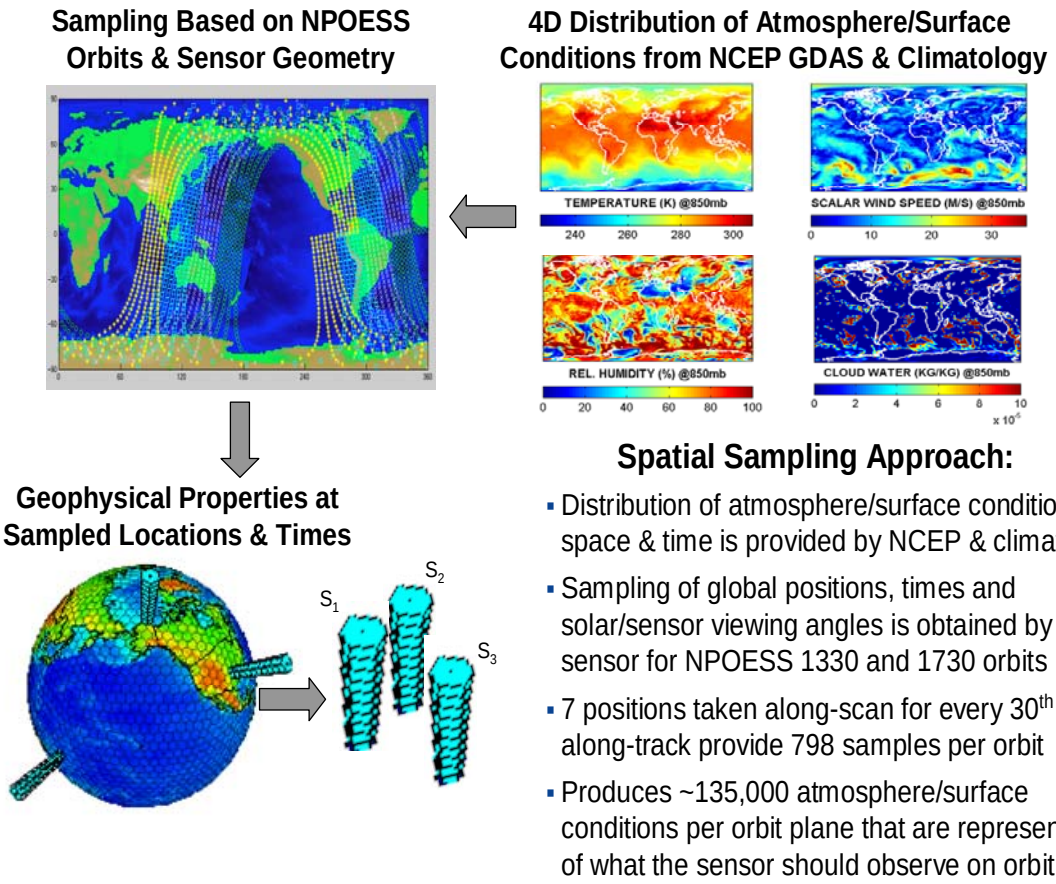

Figure 2-27. Spatial sampling approach produces comprehensive and representative test datasets

Use or disclosure of data contained on this page is subject to the export restriction(s) on the title page of this document.

D45702, A. PDMO Released: 2009-02-18 (VERIFY REVISION STATUS)
PDMO

Day of Month	Orbit	Scan # of 30	Moderate Resolution Cross track pixel #						
			1	2	3	4	5	6	7
1	1	1	40	495	950	1405	1860	2315	2770
1	2	12	105	560	1015	1470	1925	2380	2835
1	3	23	170	625	1080	1535	1990	2445	2900
1	4	4	235	690	1145	1600	2055	2510	2965
1	5	15	300	755	1210	1665	2120	2575	3030
1	6	26	365	820	1275	1730	2185	2640	3095
1	7	7	430	885	1340	1795	2250	2705	3160
1	8	18	40	495	950	1405	1860	2315	2770
1	9	29	105	560	1015	1470	1925	2380	2835

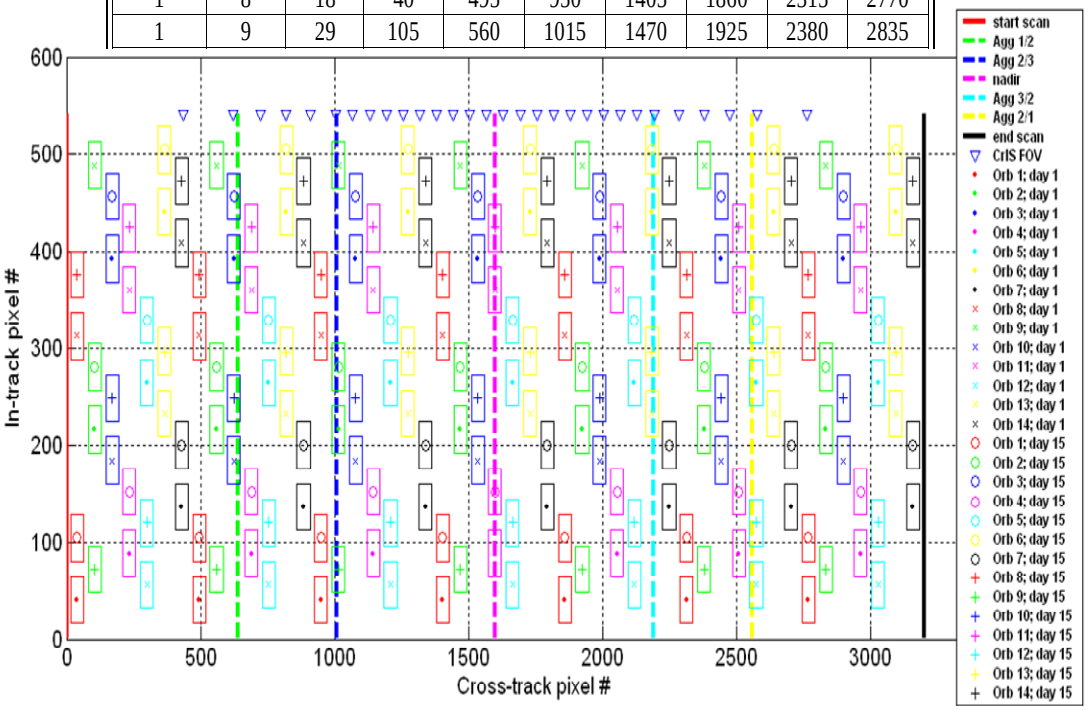

Figure 2-28. Illustration of new crosstrack pixel sampling approach

Use or disclosure of data contained on this page is subject to the export restriction(s) on the title page of this document.

D45702, A. PDMO Released: 2009-02-18 (VERIFY REVISION STATUS)
PDMO

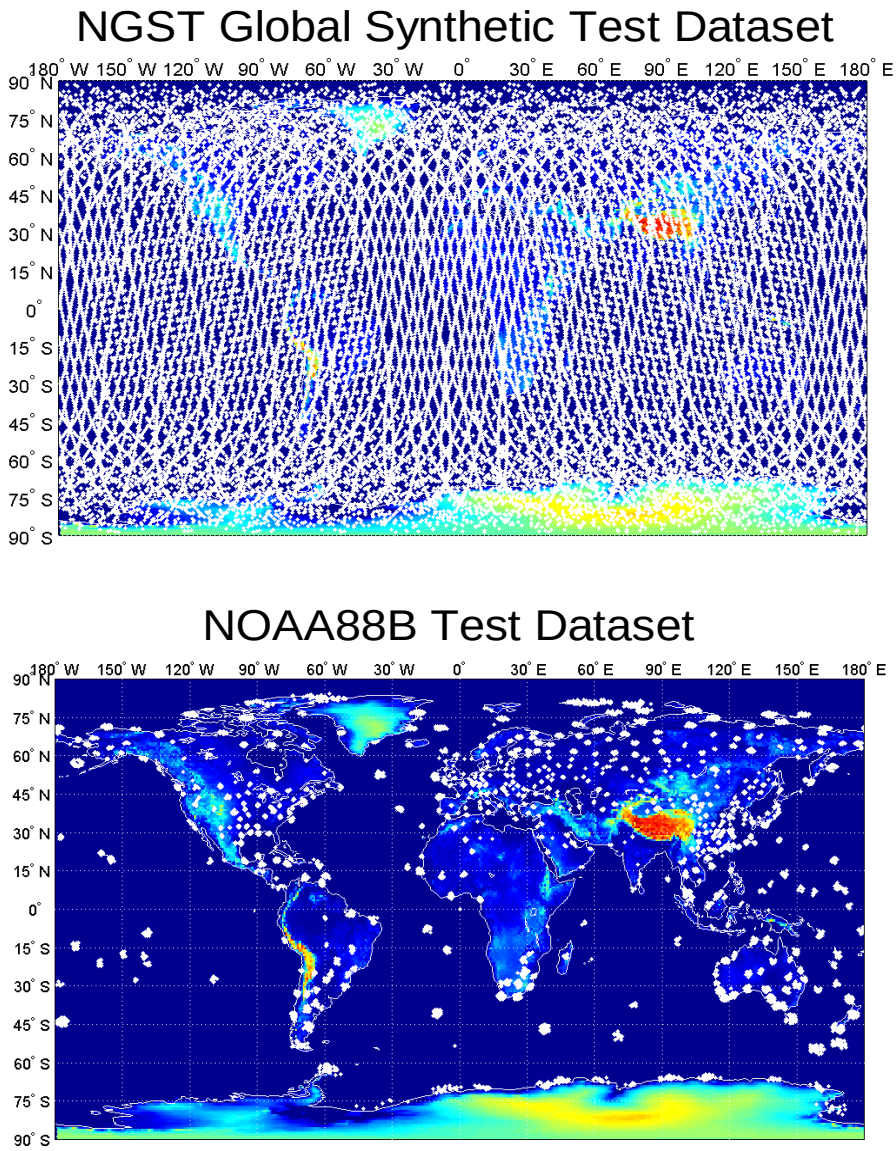

Figure 2-29. Sampling approach provides near uniform global coverage

Use or disclosure of data contained on this page is subject to the export restriction(s) on the title page of this document.

D45702, A. PDMO Released: 2009-02-18 (VERIFY REVISION STATUS)
PDMO

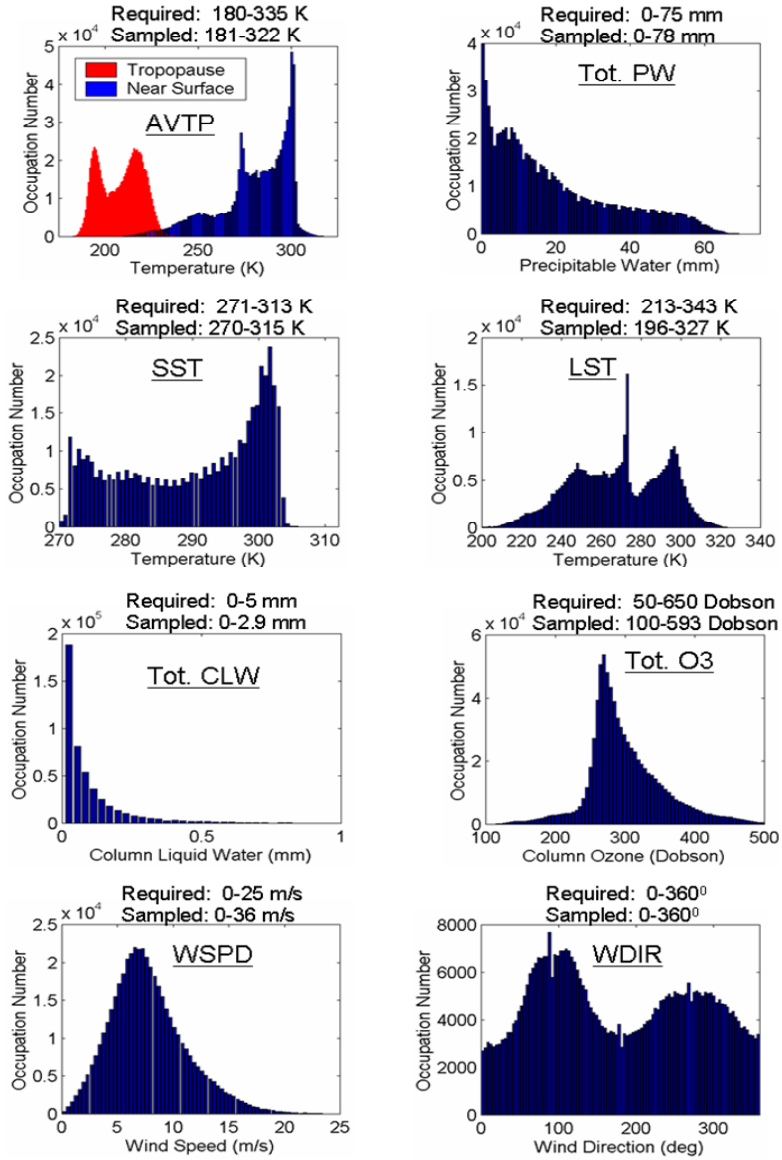

Figure 2-30. The Global Synthetic Test Dataset covers a comprehensive set of atmosphere/surface conditions for assessing system performance

Use or disclosure of data contained on this page is subject to the export restriction(s) on the title page of this document.

D45702, A. PDMO Released: 2009-02-18 (VERIFY REVISION STATUS)
PDMO

2.3 Radiative Transfer Models

A radiative transfer model (RTM) predicts the total radiances at the sensor entrance as a function of the atmospheric and terrain geophysical parameters for the environmental scene being viewed. Upon inputting the specific system parameters of a prototype sensor (e.g., instrument line shape (ILS) and earth incidence angle), the RTM computes the radiometric properties resulting from atmospheric absorption, emission, and scattering, as well as describing the mix of scattering and emission by the land/ocean background. There are a variety of general and special-purpose RTMs used in IWPTB/EVEREST, spanning the frequency regime from UV to microwave. These are listed in Table 2-6, along with the wavelength regimes where they have typically been used and a short description of their status and key features.

The radiative transfer model (RTM) predicts the radiances at the sensor entrance as a function of the atmospheric and terrain geophysical parameters for the environmental scene being viewed under the illumination of the relevant sources such as, for example, the Sun or the Moon. Upon inputting the specific system parameters of a prototype sensor (e.g., frequency, bandwidth, and earth incidence angle), the RTM computes the radiometric properties resulting from atmospheric absorption, emission, and scattering, as well as describing the mix of scattering and emission by the land/ocean background. Currently available RTMs include TOMRAD (UV/Visible), MODTRAN, 6S(V) (Second Simulation of the Satellite Signal in the Solar Spectrum), the UCLA Line-By-Line-Equivalent RTM, and AER's OSS RTM in the Visible/IR regime, and for the micro-/millimeter- wave bands NGST's ARMSS (Advanced Radiometric Microwave Sensor Simulation). A summary of current IWPTB RTMs is provided in Table 2-6. Brief descriptions of these RTMs follow.

2.3.1 RTMs Used for VIIRS Testing

MODTRAN (MODerate resolution atmospheric TRANsmittance and radiance code) is the U.S. Air Force and community standard moderate resolution radiative transport model for wavelengths extending from the thermal InfraRed (IR) into the ultraviolet (UV). This model, developed by the Air Force Research Laboratory and Spectral Sciences, Inc., provides a fast alternative to first principles line-by-line (LBL) radiative transport models, like FASCODE, without large sacrifices in accuracy and while providing additional capabilities. It has been widely used for a number of remote sensing applications, including the analysis of AVIRIS data. A regular workshop, the AFRL Transmission Meeting, as well as the effective responsiveness of AFRL personnel, insure that the quality of the code is up to community expectations. MODTRAN's major strength is in its ability to model molecular and aerosol/cloud emission and scattering, not to mention atmospheric attenuation, efficiently and accurately. IWPTB personnel is well versed in the use of this family of codes from LOWTRAN into the latest MODTRAN-4, Version-1 Release-2 which has incorporated several new scattering upgrades that produce more accurate radiances under cloudy and heavy aerosol loading conditions. It also includes modeling of the bi-directional reflectance distribution functions (BRDFs) of surfaces, which is extremely important for modeling the scattering and emission of visible and short wave IR from the ocean surface. We have relied on MODTRAN for our modeling of VIIRS and have implemented additional features in MODTRAN to facilitate

Use or disclosure of data contained on this page is subject to the export restriction(s) on the title page of this document.

D45702, A. PDMO Released: 2009-02-18 (VERIFY REVISION STATUS)
PDMO

this modeling. Firstly, we have developed an interface between the 3D geophysical scenes obtained from MM5, NCEP and NOAA88b and the atmospheric and land/ocean properties required as input to MODTRAN. This effort has also involved linking PRA's (Photon Research Associates) high-resolution global database of digital elevation and terrain factors data for describing the terrestrial background as a function of pixel geolocation. We have used this to extend MODTRAN's description of the spectral emissivity/scattering properties (i.e., spectral albedo) of the terrestrial background by including the spectral albedo for many additional terrain materials (28 in all) and improving the spectral resolution over the 0.2 to 15 micron range for which most of the material albedos in the PRA database are defined. We have improved our capability by integrating an existing wind-speed dependent ocean spectral BRDF model into MODTRAN, and implementing the UCLA RTM, which provides a more rigorous treatment of the scattering of radiation by ice clouds. Planned improvements to our vis/IR modeling capability include implementing an enhanced spectral resolution version of MODTRAN, MODTRAN-5, when it becomes available. Many comparisons between radiometric measurements and RTM predictions have been carried out by the community to justify their improvement. We have compared MODTRAN predictions for the Ground Demo 3 Scene with AVHRR data. Such comparisons to real measurements provide the basis for a selection of the best-of-breed RTM for each environmental condition.

2.3.2 RTM(s) for CrIS/ATMS Testing

A critical requirement for the CrIS RTM is to accurately model the CrIS instrument ILS or Spectral Response Function (SRF) because of the combination of CrIS' very high spectral resolution and the complexity of the atmospheric gaseous emission line structures. In addition, the RTM has to be computationally efficient because of the large amount of data to be simulated. Based upon these practical considerations, AER's Optimal Spectral Sampling (OSS) RTM was chosen, which is an accurate and efficient forward model developed for the CrIMSS retrieval algorithm. According to AER, this RTM has orders of magnitude improvement in computational efficiency compared with line-by-line (LBL) radiative transfer codes, and at the same time is able to meet stringent requirements on accuracy.

According to the CrIMSS ATBD, this fast RTM has been validated against AER's line-by-line model. It was concluded that the error in this RTM is less than 0.1K for all channels, and less than 0.05K for most of the channels. This is sufficiently accurate considering the magnitude of sensor noise and other sensor-related uncertainties and the uncertainties in the physics of the line-by-line database. For more details regarding the validation approach and results, please refer to the CrIMSS ATBD.

For simulating ATMS radiances, we used AER's MW RTM. This RTM was developed based on the same optimal spectral sampling technique used for CrIS.

2.3.3 RTM for CMIS Testing

In the millimeter-wave and microwave regimes, we are currently using NGST's Advanced Radiometric Microwave Scene Simulation (ARMSS) code as the RTM generating input to our CMIS sensor model. ARMSS is a rigorous, benchmarked,

Use or disclosure of data contained on this page is subject to the export restriction(s) on the title page of this document.

D45702, A. PDMO Released: 2009-02-18 (VERIFY REVISION STATUS)
PDMO

passive millimeter and microwave modeling and scene simulation code. Many of the physics models employed are “first principles” models, requiring only measurable physical conditions to accurately predict radiances at the sensor’s entrance aperture. The primary component of the code is the phenomenology routine, which includes the following key features:

- A comprehensive clear air atmospheric attenuation and emission model, including absorption and scattering models for clouds, fog, haze and rain – Liebe, 1987
- “First-principles” physics models for land/ocean scattering and emission, allowing for multiple dielectric layers, bi-static shadowing, and diffuse scattering by vegetation
- A Library of frequency dependent dielectric models covering a variety of land/ocean materials and material properties.
- A full 3D ray tracing solution of MW RTE (Radiative Transport Equation)
- Explicit integration of the apparent temperature over the sensor’s far-field antenna pattern and sensor channel bandwidth

A unique new feature in ARMSS is the development of a two-scale ocean scattering/emission model for computing the radiometric Stokes vector, which fully characterizes the polarization state of radiation scattered/emitted off the wind roughened ocean surface. This feature is critical for accurately assessing the capability of polarimetric radiometry, as implemented on CMIS, to measure ocean surface wind speed and direction to within EDR threshold requirements. The Ocean Polarimetric brightness Temperature In the MIcrowave SpEctral Range (OPTIMISER) model is ideally suited for scene generation and retrieval algorithm development related to the CMIS SST, wind speed and wind direction EDRs. The physical basis of the model is the same as that of the Yueh model. Two significant advantages of our version of this model are that it is fast, and the required spectral properties of the rough ocean surface have been reduced to 6 discrete parameters. This discrete representation permits the parameter values to be initially estimated from one of the available model ocean spectra (such as the Durden-Vesecky spectrum used by Yueh), and subsequently fine-tuned by a least-squares minimization of the variance between predictions and ground-truthed on-orbit data. The agreement of the model predictions with the JPL circle flight data is comparable to that of the Yueh model. The optimization technique has been tested on synthetic data and is robust. Since it is a physics-based model, simulations at other frequencies and wind speeds than those for which circle flight data are available are as reliable as is the ocean wave spectrum used to describe the surface roughness, provided that no new unmodeled phenomena appear under the extrapolated conditions. The rather wide spread between available ocean wave spectral models emphasizes the importance of the demonstrated ability to fine-tune the model parameters using on-orbit data.

As with the other RTMs described above, we have modified the ARMSS code to utilize the atmospheric profiles and surface conditions obtained from MM5, NCEP and NOAA88b, and have linked it to PRA’s terrain database to describe the background material type and properties as a function of pixel geolocation.

Use or disclosure of data contained on this page is subject to the export restriction(s) on the title page of this document.

D45702, A. PDMO Released: 2009-02-18 (VERIFY REVISION STATUS)
PDMO

The ARMSS code has been validated in a number of ways over the years since its development. Some of these include:

- Comparison of component models from the ARMSS with the published literature for other microwave models
- Comparison of simulated results from ARMSS with field measurements on previous NGST programs
- Sanity check with simulated SSM/I and AMSU data
- Comparison of ARMSS with other models

One particular validation study which highlighted ARMSS capability for generating the test data needed for the CMIS atmospheric sounding algorithms was based on the ITWG Microwave RTM Intercomparison Study. In this validation, we compared ARMSS with other radiative transfer models (RTM) commonly used in the community. More specifically, this comparison benchmarked the atmospheric absorption and emission component of the ARMSS RTM at those sensor frequencies important for the retrieval of the atmospheric vertical temperature profile (AVTP) and the atmospheric vertical moisture profile (AVMP).

In 1999 the working group on radiative transfer of the International TOVS Working Group (ITWG) proposed an intercomparison of RTMs for several HIRS vis/IR channels and AMSU microwave/millimeter-wave channels. The purpose of this intercomparison study was to assess the impact of RTM quality on temperature and humidity profile retrievals. This is especially relevant for the fast “broadband” RTMs that are the basis for many physically based retrieval algorithms as well as direct assimilation models used in NWP. Several of the AMSU-A channels, channels 6, 10 and 14, were selected because they were deemed to be most representative to study the impact of the quality of RTMs on temperature retrieval. Similarly, channel 18 from AMSU-B was chosen to assess the impact of RTM quality on humidity profile retrieval. Technical details on the channels, in terms of center frequency, number of bands, and bandwidths, is provided in the table below. It is assumed that each channel has a boxcar shape.

Channel Number	Channel Frequency (MHz)	Number of Bands	Measured 3-db Bandwidth (MHz)
6	54400	1	380.54
10	57290.344 ± 217	2	76.58
14	57290.344 ± 322.2 ± 4.5	4	2.94
18	183310 ± 1000	2	500.00

A group of 42 profiles representative of most meteorological situations, including extremes in temperature and integrated water vapor or precipitable water (PW), were processed to produce TOA brightness temperatures for this study. The profiles are defined on 43 pressure levels. These levels are those of the RTOV5 RTM, which is widely used in NWP. In addition to geometric height and temperature at each pressure level, concentrations are provided for 8 gases: H_2O_{vapor}, CO_2, O_3, N_2O, CH_4, CO, N_2,

Use or disclosure of data contained on this page is subject to the export restriction(s) on the title page of this document.

D45702, A. PDMO Released: 2009-02-18 (VERIFY REVISION STATUS)
PDMO

and O_2. These concentrations are specified as volume mixing ratios (v/v). The procedure for converting between volume mixing ratios and specific concentration (kg/kg) was also prescribed in the study. For the ARMSS MW RTM, an additional conversion for water vapor from specific humidity to relative humidity was also necessary, as this is what the code inputs. Also specified for each profile is the total columnar water vapor or precipitable water (PW), which allowed us to also assess the effect of interpolating atmospheric properties from the pressure levels on which they were supplied to those used by the ARMSS code. These profiles, including the derived quantity of PW are shown in Figure 2-32. Looking at the plot of PW, we note that there are three anomalous points, profiles 7, 9 and 30, where there is a noticeable difference between the PW derived from the temperature and humidity profiles and that supplied by ITWG with each set of profiles. Starting with the supplied humidity profiles (given as water vapor volume mixing ratios) and employing different approaches to arrive at and integrate the corresponding water vapor density profiles through the atmosphere, we arrived at nearly identical results, both of which are different than that reported by ITWG, for these three profiles. This is shown in Figure 2-33. Even though we do not know the cause of the discrepancy in PW for these three profiles, we still perform brightness temperature comparisons for these profiles.

In addition to specifying the atmospheric profiles to be used, the intercomparison study also legislates the corresponding surface properties for each profile and the sensor viewing geometry. The surface skin temperature and pressure are specified by their values at the bottom most (i.e., highest pressure) level. The surface emissivity is set at 0.6 for all of the AMSU channels. Finally, the brightness temperatures are computed for a nadir-view of the scene and with the downwelling atmospheric radiation (used in determining the scattered temperature at the surface) also generated along the nadir path.

Both line-by-line (LBL) and “broadband” fast RTMs are compared here. Of the LBL models that were submitted for the intercomparison study, we have selected three: AER-LBL, CIMMS-MWLBL, and MSC-MWLBL. Similarly, we have included four of the submitted broadband RTMs; they are: AER-OSS, MIT, RAYTHEON, and RTOV5. The brightness temperatures from these seven RTMs were compared against each other as well as against those from the NGST ARMSS RTM and the AER OSS RTM that came bundled with the CrIS-1.23 code and which has been used at NGST to produce the MW SDRs for the CrIMMS AVTP and AVMP retrieval algorithm. Each LBL RTM was taken individually as the reference by which all other models were compared. The results for these comparisons are shown in Figures 2-34 through 2-41. Regardless of the LBL RTM used as reference, the NGST ARMSS RTM was within 0.5K and in most cases less than 0.25K.

Use or disclosure of data contained on this page is subject to the export restriction(s) on the title page of this document.

D45702, A. PDMO Released: 2009-02-18 (VERIFY REVISION STATUS)
PDMO

Table 2-6. Radiative Transfer Models used for Generating Synthetic Test Datasets

Frequency Regime	RTM	Status of EVEREST RTMs
Vis/IR	MODTRAN4+ UCLA LBL-RTM 6S(V), SBDART Hydrolight-BRDF DISCORD ISBRDF	▪ Community standard atmospheric RTMs with known fidelity and limitations ▪ Modifications to MODTRAN, 6S(V) and SBDART allow input of ocean/terrain BRDF tables ▪ Hydrolight-BRDF ocean RTM and DISCORD & ISBRDF snow/ice RTMs generate BRDF tables read by MODTRAN & 6S(V) to provide coupled ocean-atmosphere and snow/ice-atmosphere radiative transfer modeling capabilities
IR/μ–wave Sounder	AER-OSS HS IR NGST- ARMSS	▪ High spectral resolution atmospheric RTM for modeling hyperspectral IR sounders ▪ AER-OSS IR and MW RTMs utilize optimal spectral sampling ▪ NGST's ARMSS model for microwave RTMs (see below)
UV	MODTRAN 4+ HERMAN	▪ Community standard, useful for ozone column and profile ▪ HERMAN used in Limb Profile retrieval software [Not a flat earth & horizontal inhomogeneity to be implemented into EVEREST scene generation]
Microwave/ Millimeter wave	NGST-ARMSS	▪ Components compared with published results for other MW models ▪ End-to-end RT compared with field experiments on previous NGST programs ▪ Sanity check with simulated SSM/I and AMSU data ▪ Ongoing validation effort using SSM/I, TMI, AMSR-E and WindSat data

Use or disclosure of data contained on this page is subject to the export restriction(s) on the title page of this document.

D45702, A. PDMO Released: 2009-02-18 (VERIFY REVISION STATUS)
PDMO

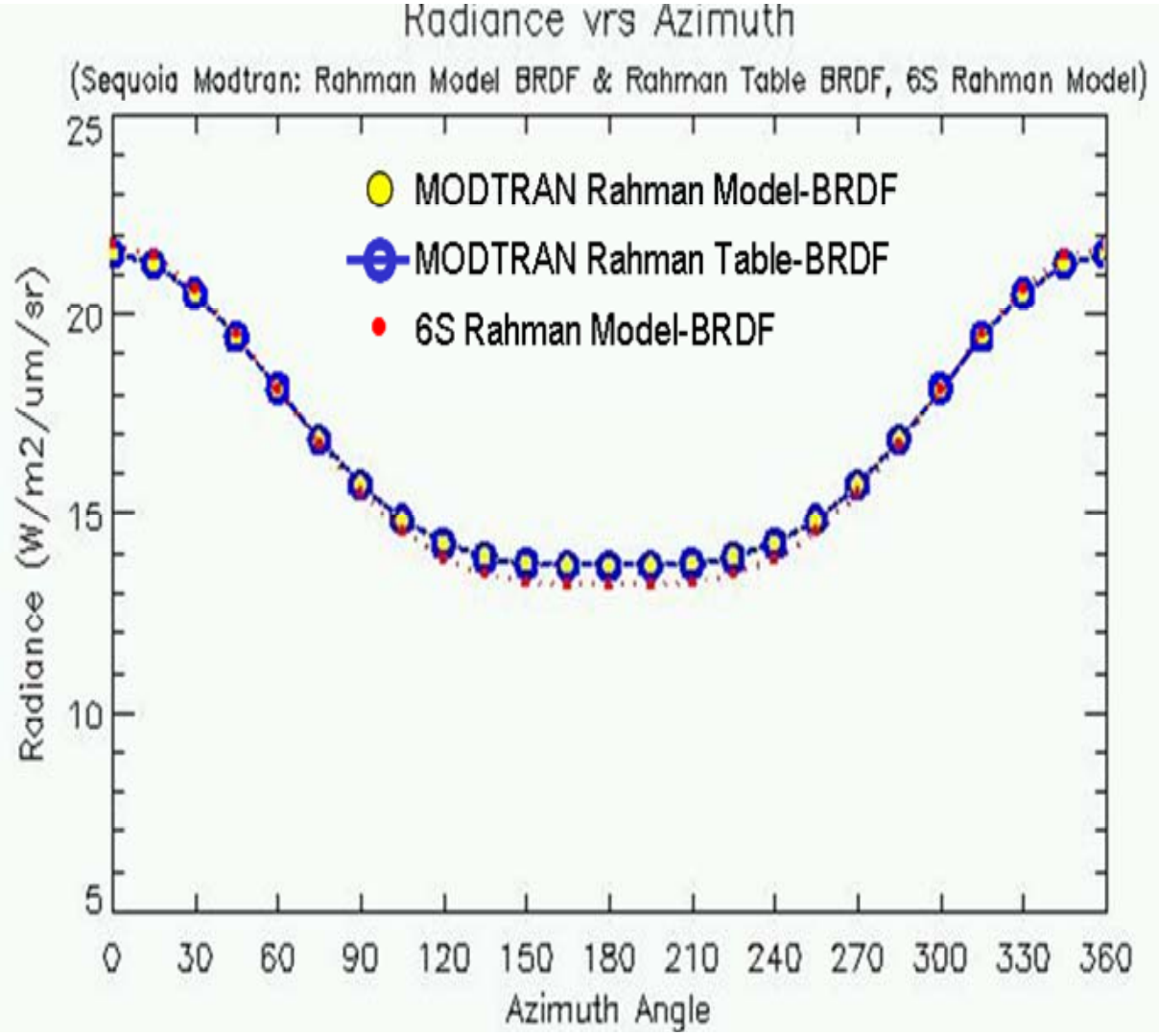

Figure 2-31. Verifying modifications to MODTRAN-4 for utilizing user-supplied terrain/ocean BRDF tables

Use or disclosure of data contained on this page is subject to the export restriction(s) on the title page of this document.

D45702, A. PDMO Released: 2009-02-18 (VERIFY REVISION STATUS)
PDMO

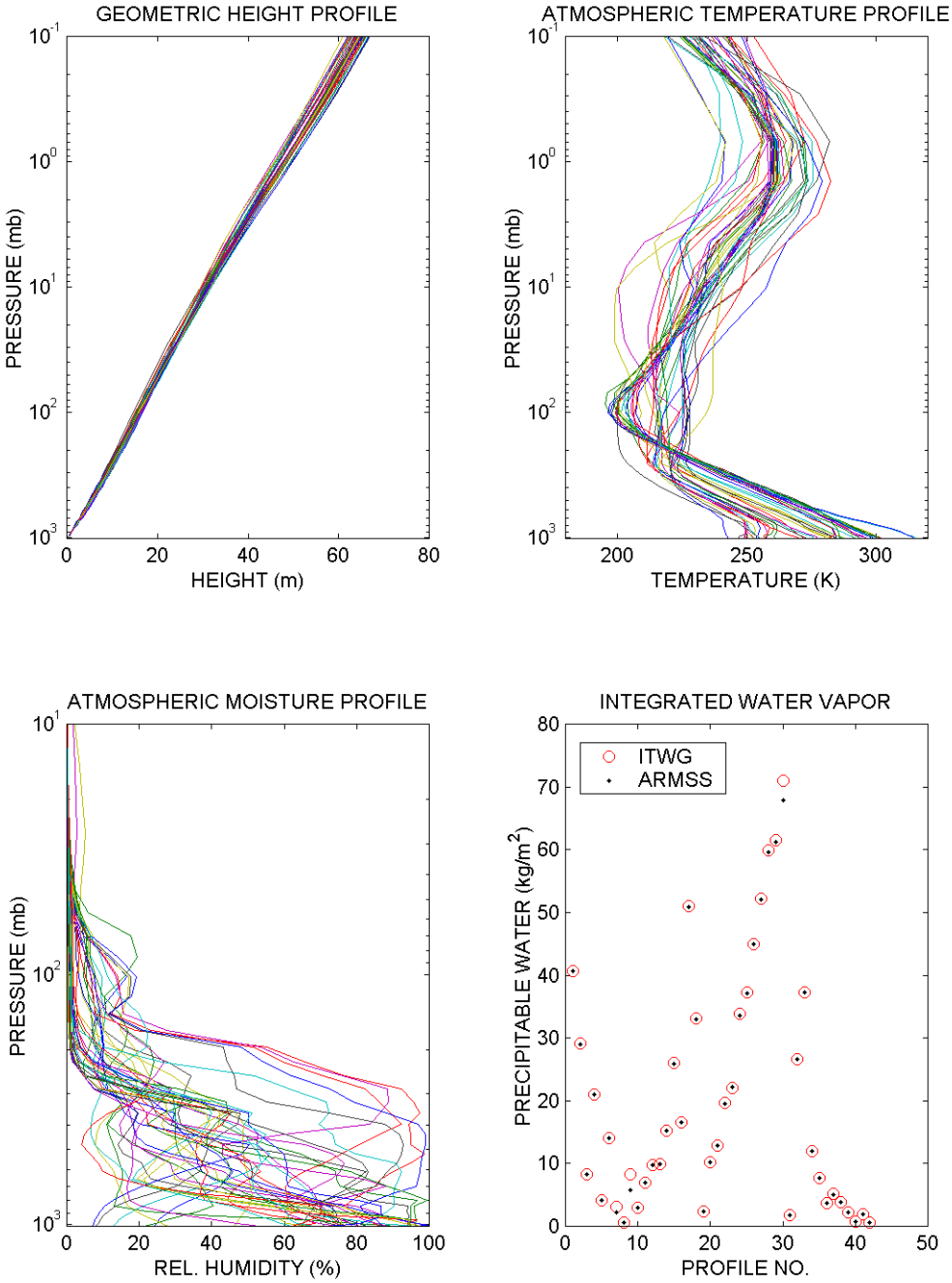

Figure 2-32. Atmospheric Profiles (42) Supplied by ITWG for Intercomparison Study

Use or disclosure of data contained on this page is subject to the export restriction(s) on the title page of this document.

D45702, A. PDMO Released: 2009-02-18 (VERIFY REVISION STATUS)
PDMO

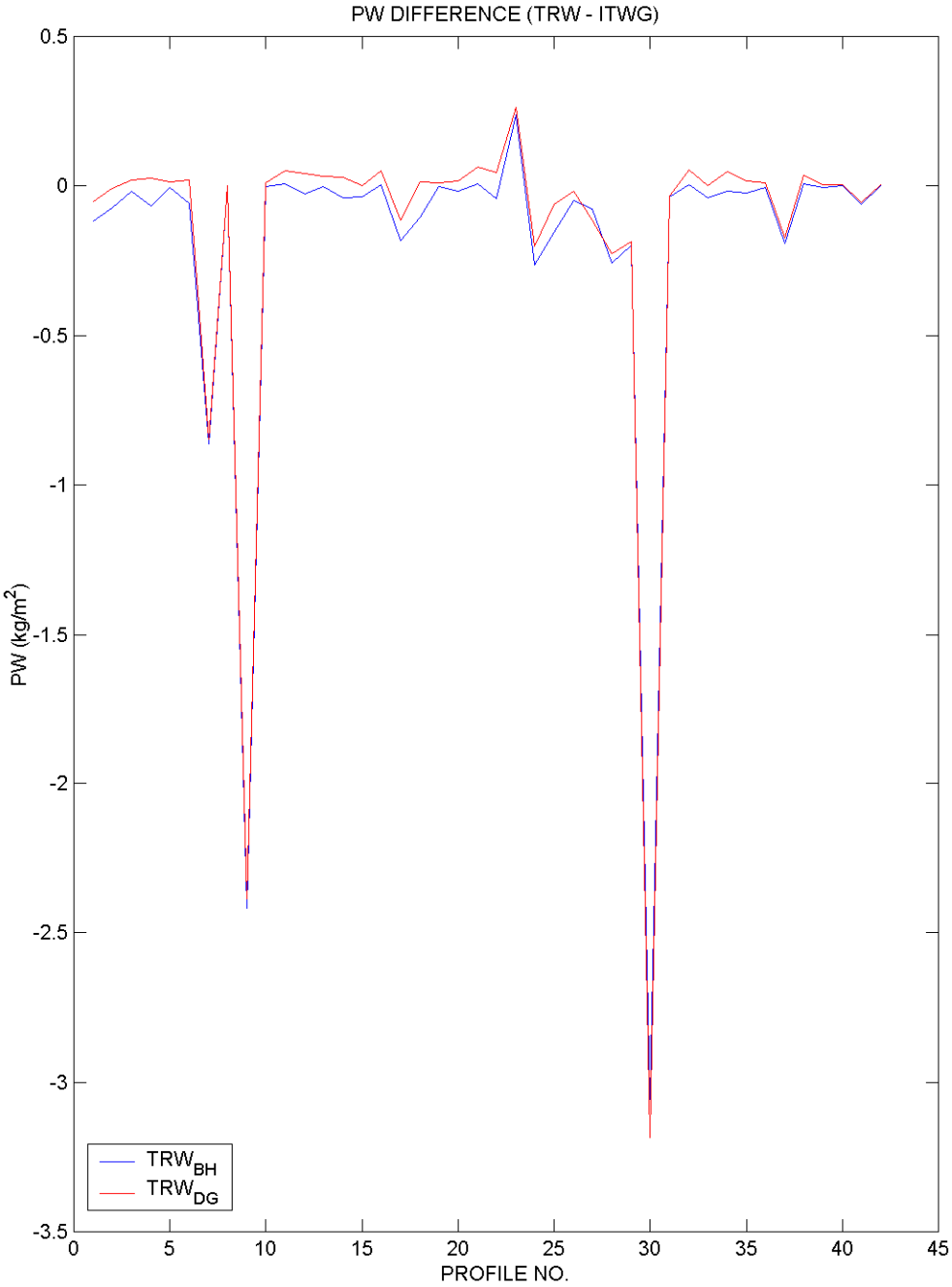

Figure 2-33. Difference Between PW Derived from ITWG Profiles and that Specified by ITWG Value

Use or disclosure of data contained on this page is subject to the export restriction(s) on the title page of this document.

D45702, A. PDMO Released: 2009-02-18 (VERIFY REVISION STATUS)
PDMO

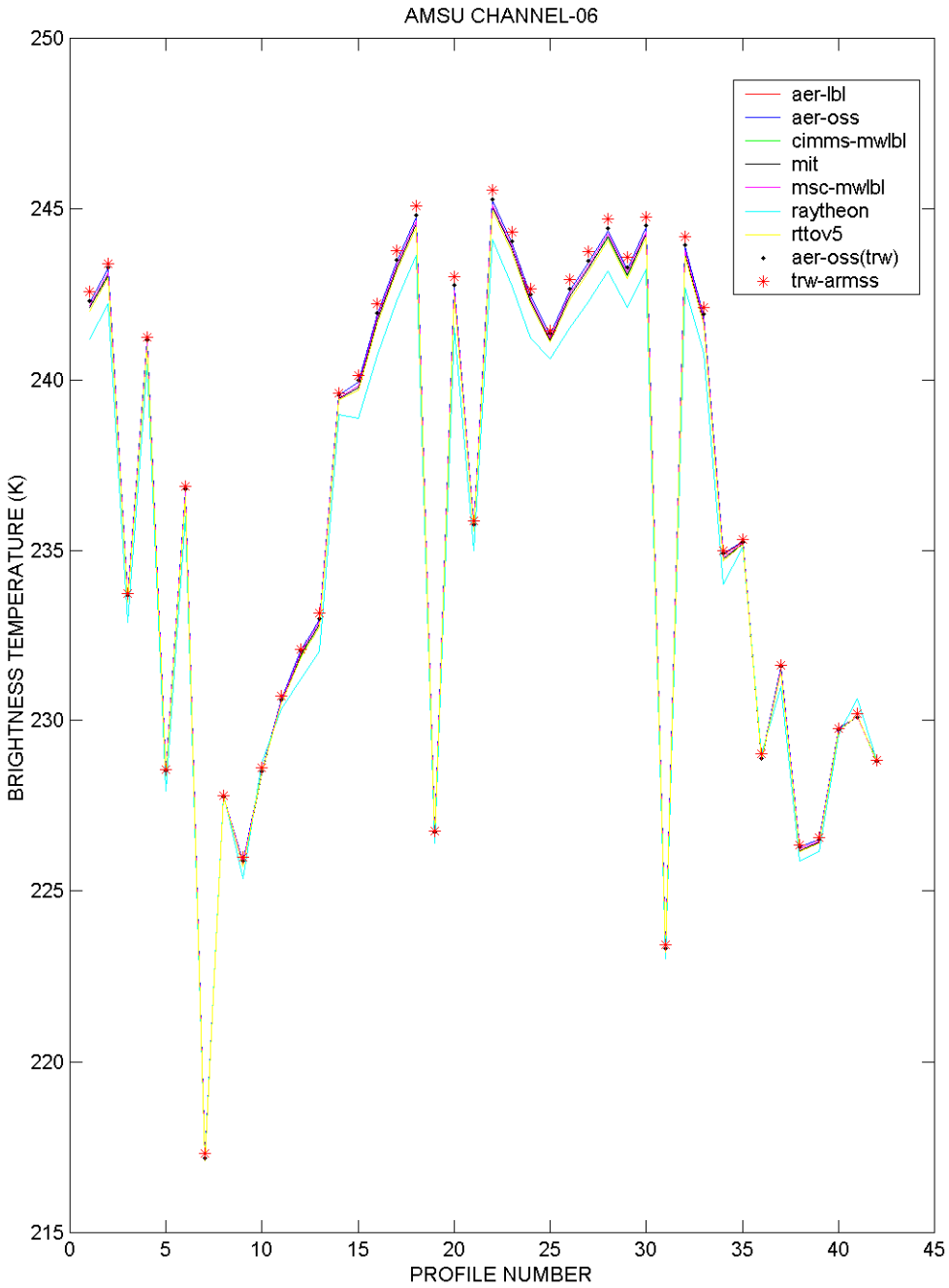

Figure 2-34. Brightness Temperature Comparison for AMSU-A Channel 6

Use or disclosure of data contained on this page is subject to the export restriction(s) on the title page of this document.

D45702, A. PDMO Released: 2009-02-18 (VERIFY REVISION STATUS)
PDMO

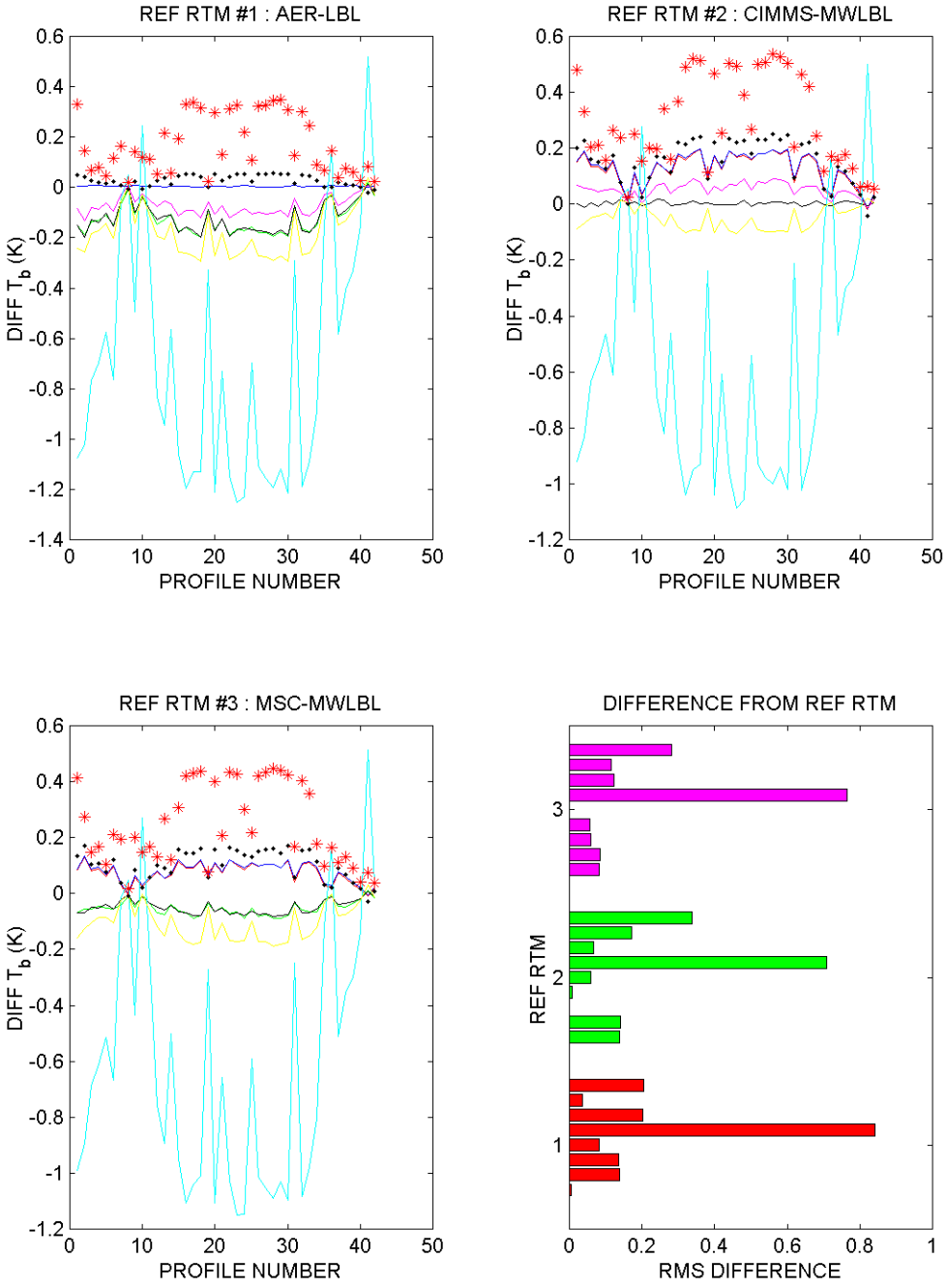

Figure 2-35. Brightness Temperature Differences for Channel 6 Using Different LBL Models as Reference

Use or disclosure of data contained on this page is subject to the export restriction(s) on the title page of this document.

D45702, A. PDMO Released: 2009-02-18 (VERIFY REVISION STATUS)
PDMO

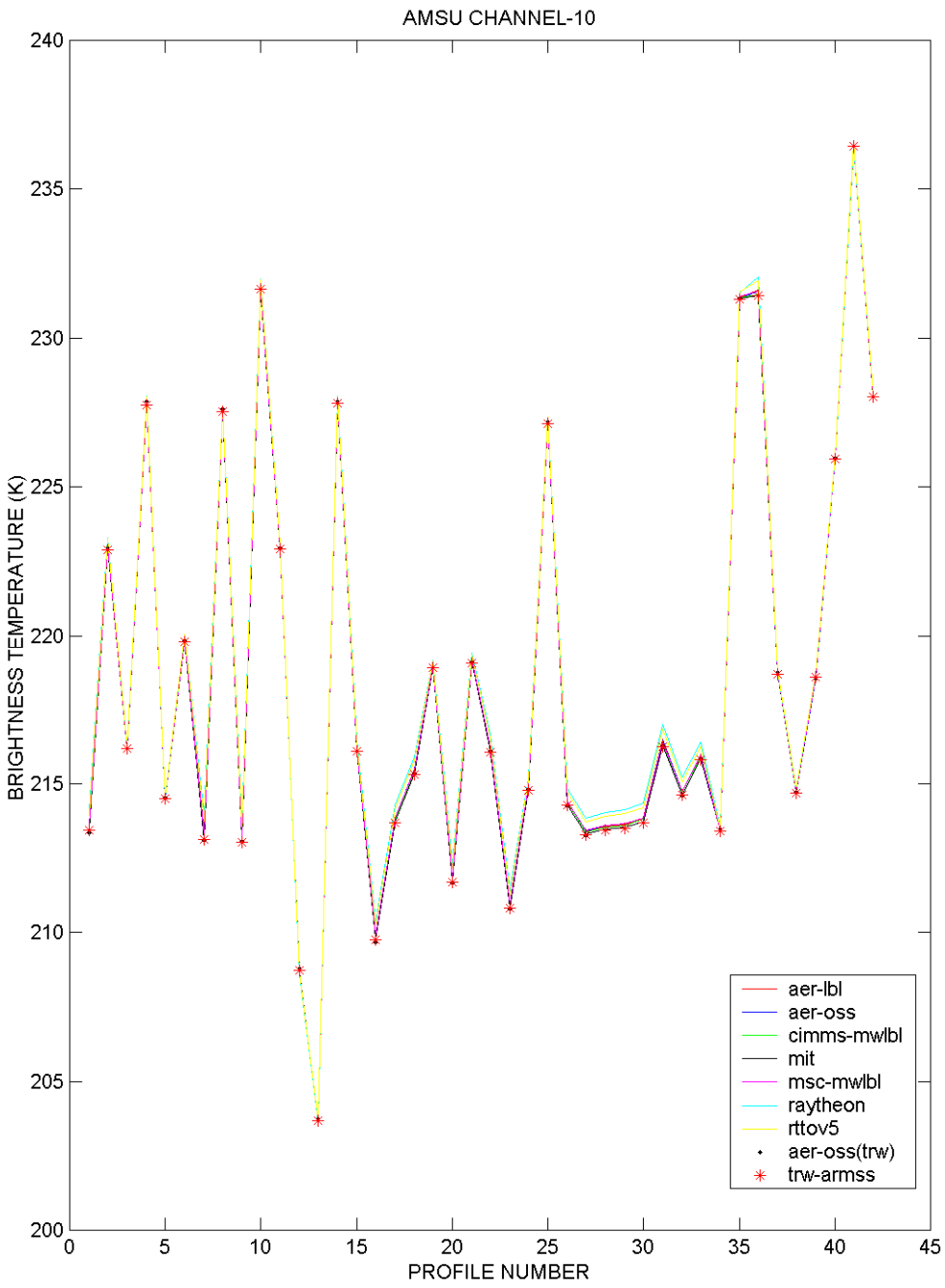

Figure 2-36. Brightness Temperature Comparison for AMSU-A Channel 10

Use or disclosure of data contained on this page is subject to the export restriction(s) on the title page of this document.

D45702, A. PDMO Released: 2009-02-18 (VERIFY REVISION STATUS)
PDMO

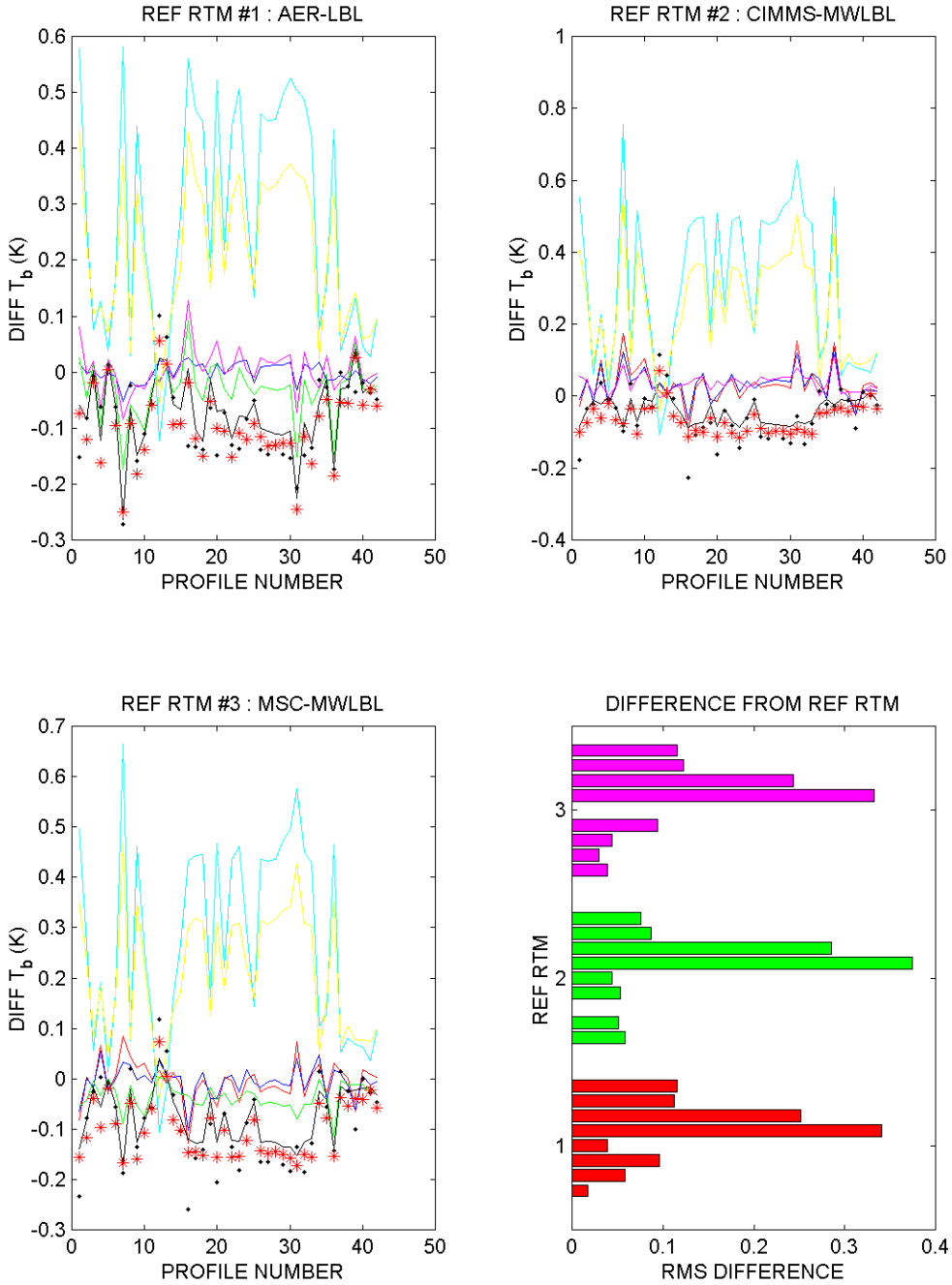

Figure 2-37. Brightness Temperature Differences for Channel 10 Using Different LBL Models as Reference

Use or disclosure of data contained on this page is subject to the export restriction(s) on the title page of this document.

D45702, A. PDMO Released: 2009-02-18 (VERIFY REVISION STATUS)
PDMO

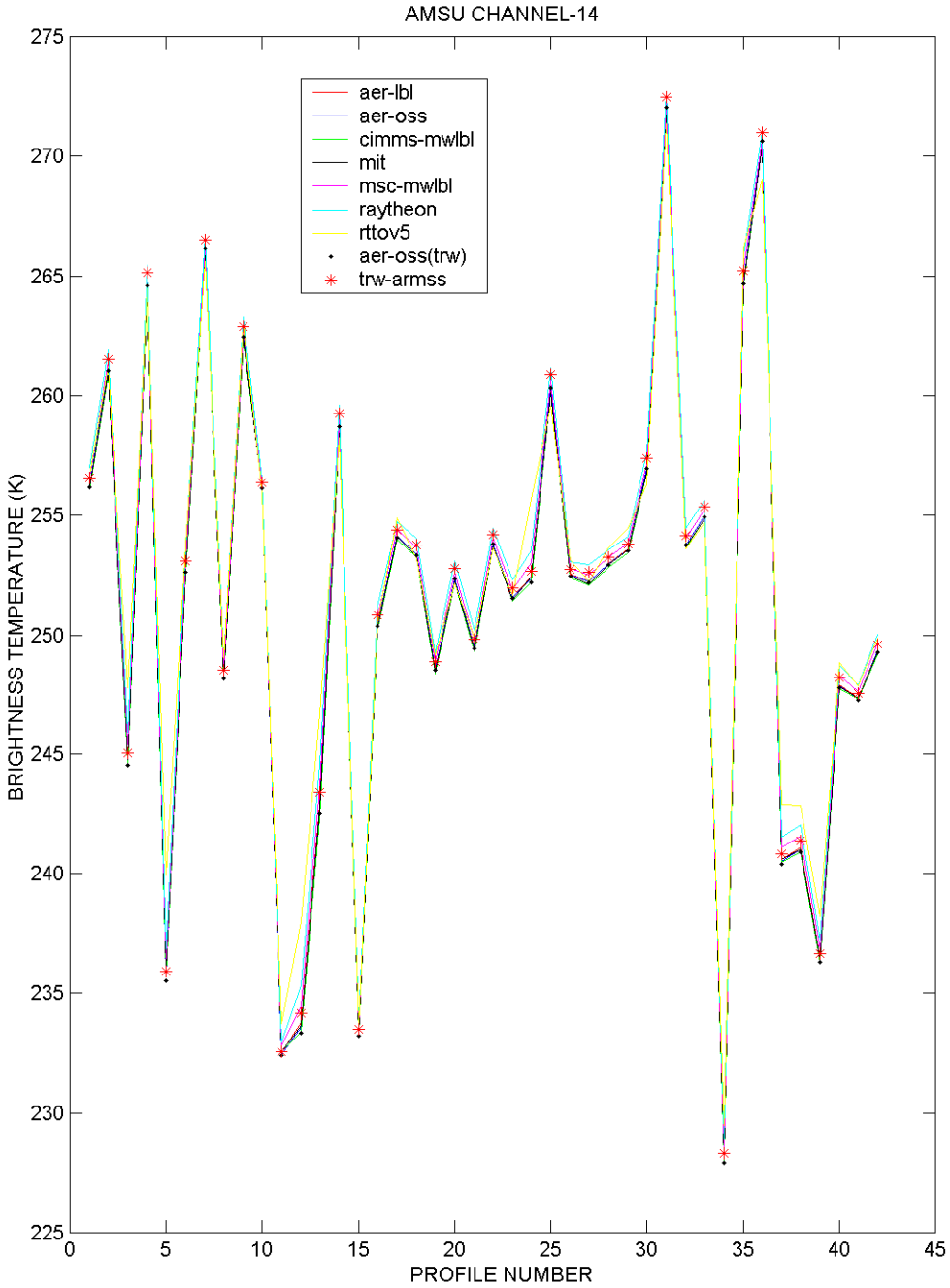

Figure 2-38. Brightness Temperature Comparison for AMSU-A Channel 14

Use or disclosure of data contained on this page is subject to the export restriction(s) on the title page of this document.

D45702, A. PDMO Released: 2009-02-18 (VERIFY REVISION STATUS)
PDMO

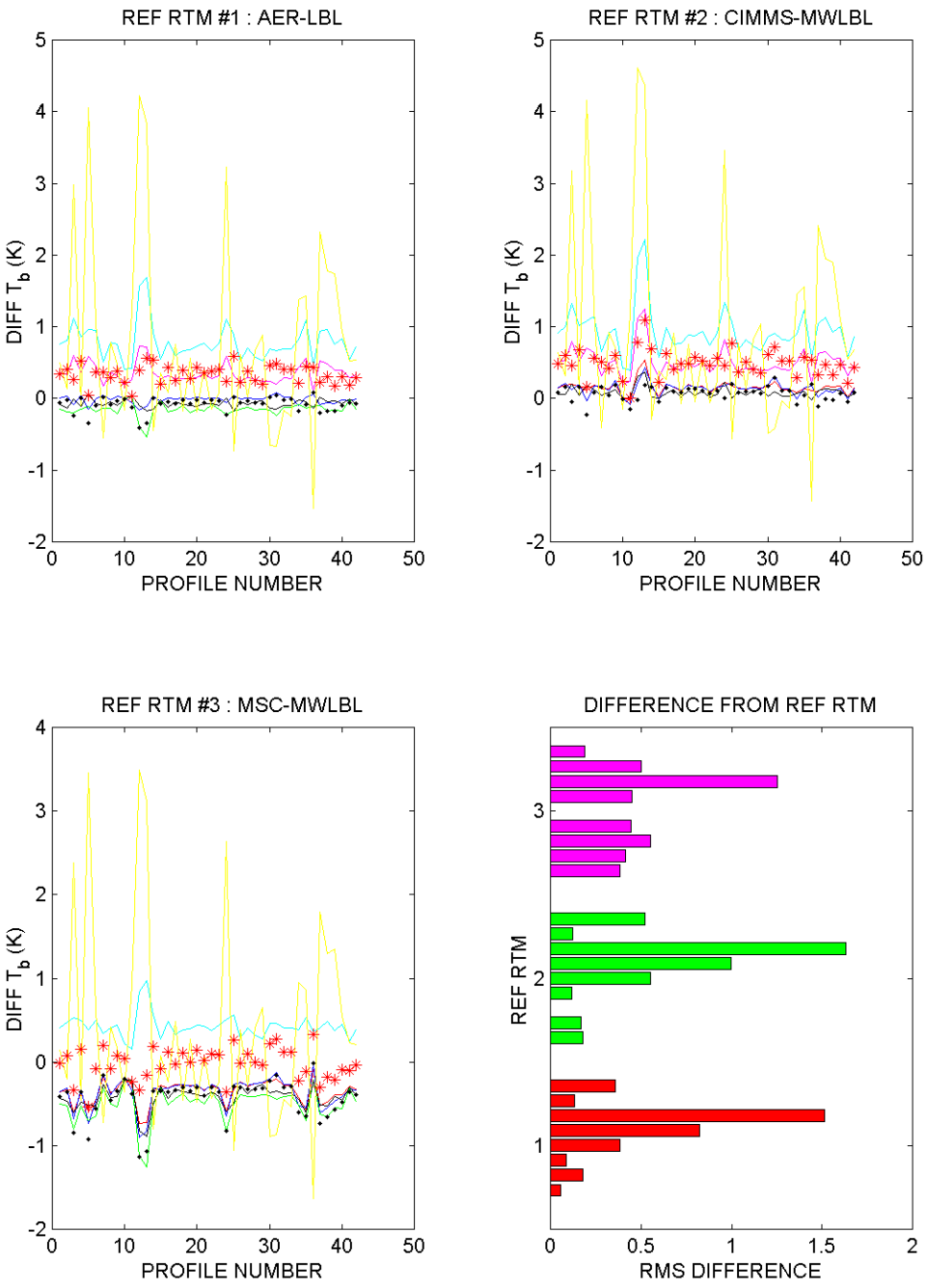

Figure 2-39. Brightness Temperature Differences for Channel 14 Using Different LBL Models as Reference

Use or disclosure of data contained on this page is subject to the export restriction(s) on the title page of this document.

D45702, A. PDMO Released: 2009-02-18 (VERIFY REVISION STATUS)
PDMO

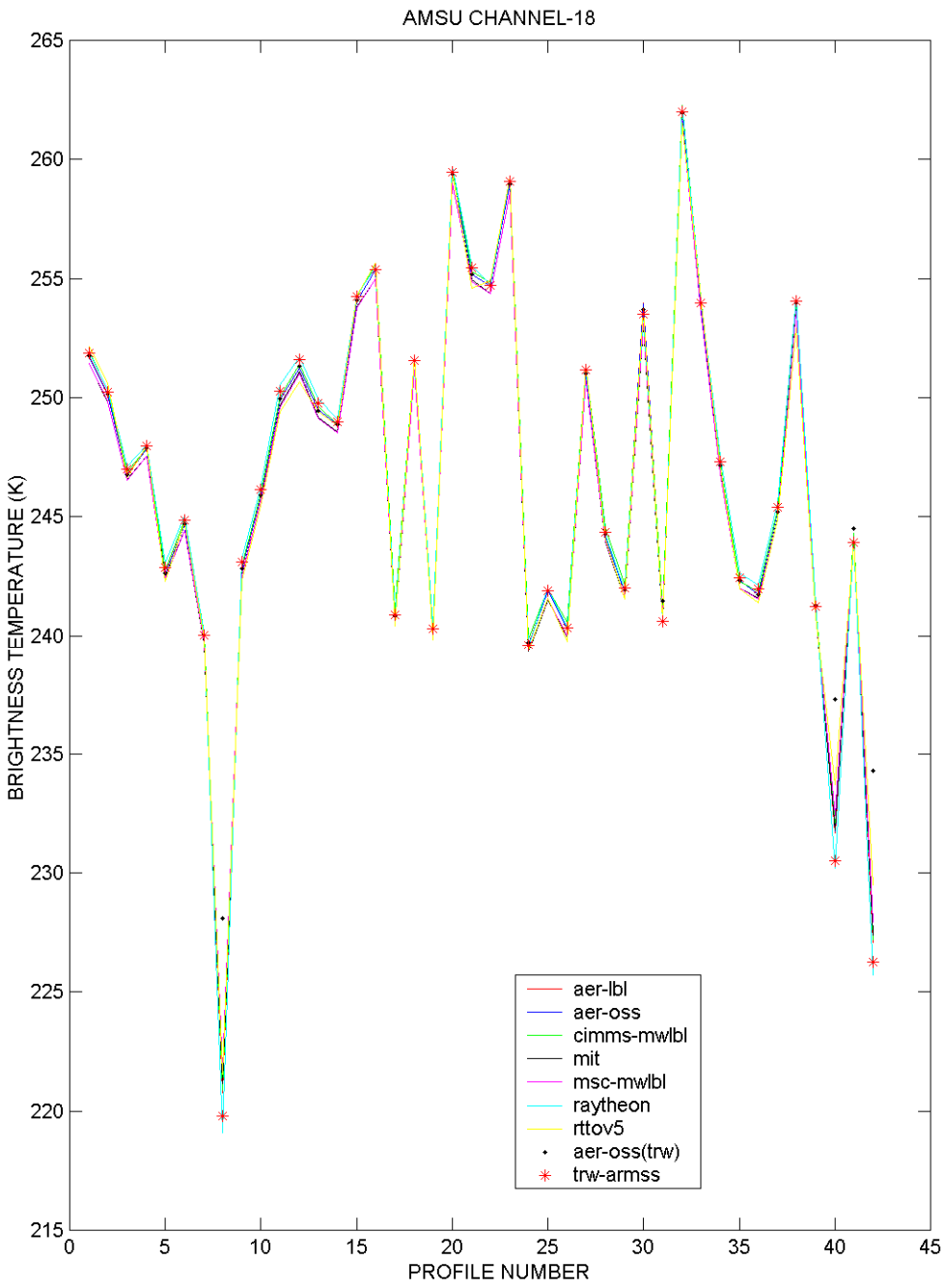

Figure 2-40. Brightness Temperature Comparison for AMSU-B Channel 18

Use or disclosure of data contained on this page is subject to the export restriction(s) on the title page of this document.

D45702, A. PDMO Released: 2009-02-18 (VERIFY REVISION STATUS)
PDMO

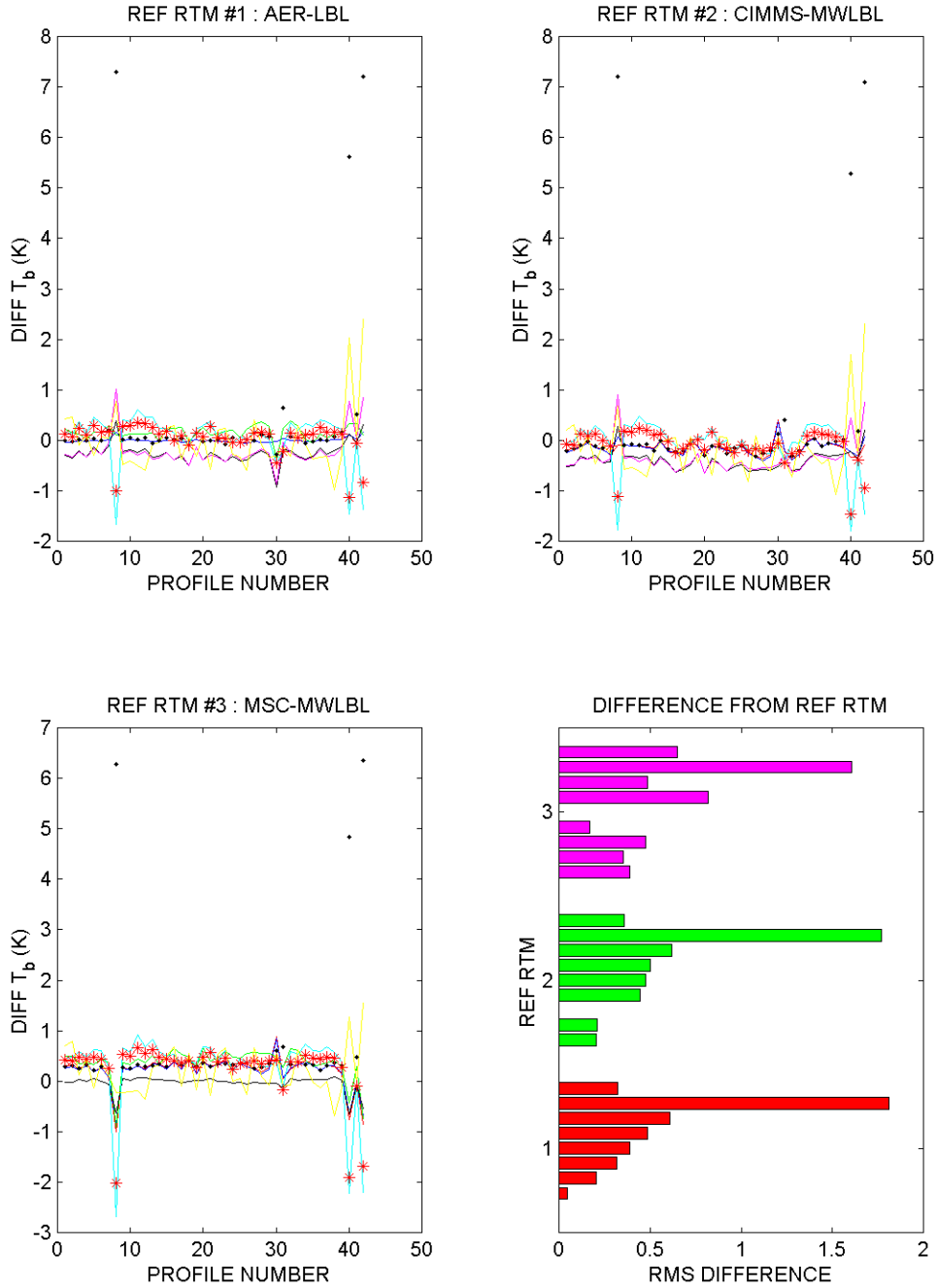

Figure 2-41. Brightness Temperature Differences for Channel 18 Using Different LBL Models as Reference

Use or disclosure of data contained on this page is subject to the export restriction(s) on the title page of this document.

D45702, A. PDMO Released: 2009-02-18 (VERIFY REVISION STATUS)
PDMO

2.4 Sensor Models

The sensor/spacecraft models provide the “transfer functions” which transform the incoming scene radiances at the sensor entrance aperture to the output sensor signal. To allow us to proceed with our IWPTB efforts, we have developed our own generic vis/IR and MW sensor models. These are parametric models, only requiring parameters/errors from the various NPOESS sensor designs to make them sensor specific. Also, as sensor hardware development proceeds and there is actual hardware test data, our sensor models, parameters and errors will be updated. The IWPTB models for Vis/IR and MW sensors are briefly discussed below.

Amplifier gains, component losses, stray light, calibration errors and uncertainties, and system noise all introduce measurement error to the “true” scene radiances observed by the sensor. Additional factors such as variation in the earth incidence angle due to spacecraft pointing error and jitter, and off-axis radiation incident on the sensor through its sidelobes also contribute to the uncertainty in the measured radiances. We have employed parametric models that capture the essence of the sensor/spacecraft system without modeling the detailed flow through every system component. These models either generate simulated raw sensor data (RDRs), where it is assumed that subsequent RDR-to-SDR processing will be performed to remove the known system errors, or SDRs, where the RDR-to-SDR processing has already been taken into account. In the latter case, only sensor and spacecraft errors that cannot be removed by the RDR-to-SDR processing are added to the “true” scene radiances viewed by the sensor. Examples of these types of errors are sensor noise, calibration uncertainties (e.g., uncertainties in the blackbody temperature and emissivity of the calibration sources), and pointing uncertainty due to spacecraft jitter and limitations in pointing knowledge. The resulting sensor/spacecraft errors consist of both random and systematic errors. The random errors (e.g., sensor noise and variations in earth incidence angle due to spacecraft jitter) are simulated by Monte Carlo techniques, using assumed probability distributions and specifying the requisite distribution parameters. Systematic errors include both constant bias errors, such as those due to sensor miscalibration, and time dependent errors, which change during the orbit trajectory or even during the sensor scan (e.g., errors in sensor self-emission versus scan angle). These have been modeled through a combination of fixed and time- or scan-angle dependent parameters. A list of the sensor and spacecraft effects currently modeled for generic vis/IR and MW sensors are presented below.

Use or disclosure of data contained on this page is subject to the export restriction(s) on the title page of this document.

D45702, A. PDMO Released: 2009-02-18 (VERIFY REVISION STATUS)
PDMO

2.4.1 VIIRS Sensor Model

The Vis/IR sensor model has been adapted for VIIRS and has been extensively validated against that of SBRS. It includes effects from:

- Spatial processing – scan definition, aggregation, and resampling from the radiance scene
- Sensor noise – Johnson noise, 1/f noise, quantum noise, electronic noise, dark current, dual gain, and readout noise
- Sensor bias – quantum efficiency drift, self-emission versus scan angle, response versus scan angle, blackbody temperature and emissivity knowledge, and solar diffuser reflectance knowledge
- Spatial resolution – sensor PSF, scan and jitter blur
- Spacecraft – static pointing error and pointing knowledge, dynamic (e.g., drift and jitter) pointing error and pointing knowledge

A functional flow for the Vis/IR sensor model used for VIIRS is shown in Figure 2-42.

2.4.2 CrIS/ATMS Sensor Models

We have directly used the CrIS sensor subcontractor's model output to simulate CrIS SDRs. The effects simulated and applied to our synthetic data include

- Spatial processing – actual sensor viewing geometry
- Sensor noise
- Sensor bias – including calibration uncertainty
- Spatial resolution – band-to-band co-registration error
- Spectral noise – spectral uncertainty.

This sensor model has been used to derive mission parameters and continues to be validated with EDU test data by the subcontractor. Using this sensor model, instead of the generic one developed in the IWPTB, allowed us to focus on the overall sensor effects on EDR algorithm performance.

The ATMS sensor model was coupled with the AER MW RTM and includes the following elements:

- Boxcar shaped band
- Nominal center frequency
- Nominal bandwidth
- Nominal polarization alignment
- Narrow antenna beam
- Temperature sensitivity NEDT

Use or disclosure of data contained on this page is subject to the export restriction(s) on the title page of this document.

D45702, A. PDMO Released: 2009-02-18 (VERIFY REVISION STATUS)
PDMO

2.4.3 CMIS Sensor Model

The IWPTB sensor model used for the MW sensor CMIS utilizes a noise model based on, and validated against, that of Boeing. The model includes effects from:

- Scan geometry – scan type (conical or thru nadir), scan definition (look-angle, alongtrack and along-scan GSD, spin period, active scan angle or swath width)
- Antenna pattern – channel frequency, aperture shape and size, aperture distribution, feed-horn spillover factor and uncertainty
- Sensor noise – radiometer type (total power, Dicke), front-end loss, receiver noise figure or noise temperature, gain variation, channel bandwidth, integration time (sample and hold times), video delta T, quantization delta T,
- Calibration bias and noise – cold sky calibration (radiometer noise when viewing cold sky, beam fraction and its uncertainty falling on cold sky, spillover falling onto Earth or spacecraft), warm load calibration (radiometer noise when viewing warm load, beam fraction and its uncertainty falling on warm load, spillover falling into cold sky, emissivity and its uncertainty of warm load, physical temperature and its uncertainty of warm load, leakage signal from local oscillator reflected off warm load), and non-linearity and its uncertainty of the radiometric transfer function (RTF)
- Spacecraft – static pointing error and pointing knowledge, dynamic (e.g., drift and jitter) pointing error and pointing knowledge

Use or disclosure of data contained on this page is subject to the export restriction(s) on the title page of this document.

D45702, A. PDMO Released: 2009-02-18 (VERIFY REVISION STATUS)
PDMO

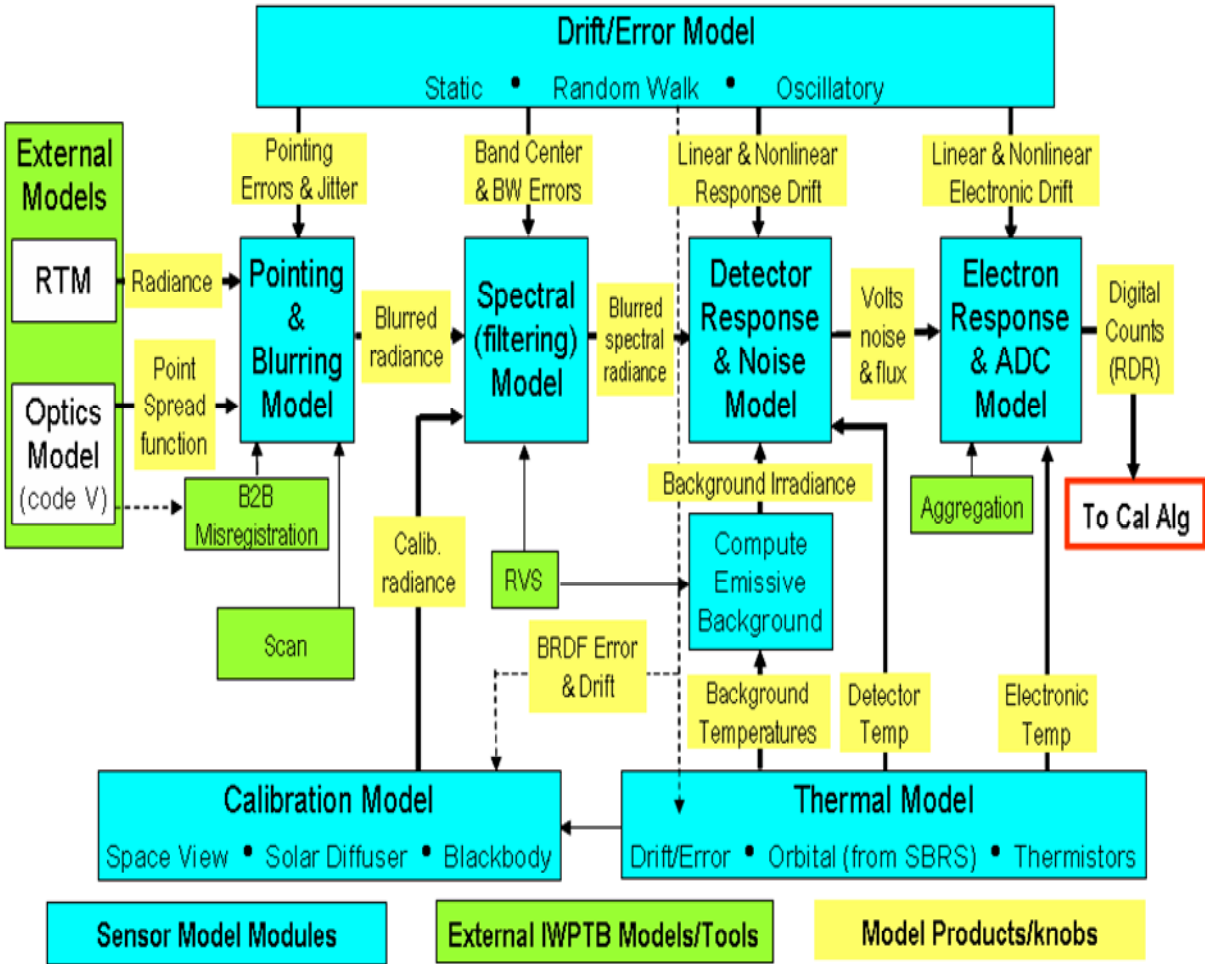

Figure 2-42. NGST Generic Vis/IR sensor model used for VIIRS

Use or disclosure of data contained on this page is subject to the export restriction(s) on the title page of this document.

D45702, A. PDMO Released: 2009-02-18 (VERIFY REVISION STATUS)
PDMO

3.0 PROXY DATA - UTILIZING DATA FROM DEPLOYED SENSORS

The generation of proxy data is based on the utilization of sensor output data from an existing deployed or heritage sensor/spacecraft system (e.g., MODIS on EOS Terra or Aqua platform), where the heritage sensor is similar to the planned NPOESS sensor. The steps taken in this method are as follows:

- Ascertain the similarities and differences between the proposed NPOESS sensor and the heritage sensor to determine whether the heritage sensor is a reasonable surrogate for the corresponding NPOESS sensor. Differences in design and sensor performance/degradation would propagate to an impact/error in the assessment of predicted NPOESS EDR performance.
- Collect SDR datasets from the heritage sensor and the corresponding EDR products, as well as any corresponding in-situ data that match the satellite overpass. This would include, for example, airborne measurements taken at the same time of cloud properties, or ship buoy measurements of sea surface temperature. If the data collections have all been associated with a cal/val campaign, they will have been corrected to some extent.
- Possibly adjust the deployed sensor output data to account for the differences in sensor attributes with the proposed NPOESS sensor, for example, bandwidths and centers (i.e., spectral resampling) and/or spatial resampling.

There are two types of proxy data being produced and used on the NPOESS program. The first type of proxy data is for extended functionality and performance testing of the individual Science algorithms and the Science algorithm chain. This data consists of individual granules of heritage data that are selected for their scene content. They are not spatially remapped and no sensor effects are added. The second type of proxy data is that used for end-to-end functionality testing of the Operational code by the IDPS. This type of proxy data involves one or more continuous orbits of proxy RDR sensor data which have been spatially remapped to the NPOESS sensor granules and formatted into Application Packets. Sensor effects are added to this data to allow for full testing of the SDR software. The requirements and generation process are distinctly different for these two types of proxy data.

3.1 Proxy Data used for Extended Functionality and Performance Testing

The use of proxy data for carrying out extended functionality and performance testing of the individual science algorithms and the algorithm chain has been almost exclusively for VIIRS. The main requirements in generating the proxy data are the proper selection of proxy granules, and not modifying the original SDR data, other than reformatting it so that it can be read by the Science algorithms.

For this type of proxy data, the granules selected were primarily chosen because they provide the variety of scene content useful for assessing the performance of the various retrieval algorithms. In particular, we were looking for scenes with latitudes ranging from tropical to subarctic, with a variety of cloud types and aerosols (e.g., blowing sand), and with a wide range of surface backgrounds, including ice, snow, desert, vegetated and bare land, and ocean. Other than scene content, we were looking for

Use or disclosure of data contained on this page is subject to the export restriction(s) on the title page of this document.

D45702, A. PDMO Released: 2009-02-18 (VERIFY REVISION STATUS)
PDMO

geographic and seasonal coverage. The only other consideration in selecting the scenes was to choose dates and times consistent with those of the NCEP data that have already been collected for building the global test datasets, described in Section 2.1; that is, the 1st and 15th of months between July 2001 and June 2002. In this way, the ancillary data needed by the retrieval algorithms, currently based on NCEP analyses, would be readily available. Figure 3-1 shows some of the 35 granules selected based on the above criteria. As can be seen, they provide both global and seasonal coverage.

The proxy data used to emulate the VIIRS SDRs are all derived from the MODIS Level 1B calibrated radiances and reflectances. These are collected from the MODIS MOD021KM and MOD02HKM L1B products. The MOD021KM product contains the 1km reflective solar band (RSB) data, bands 8-19 and 26, and the 1km thermal emissive band (TEB) data, bands 20-36, excluding band 26. The MODIS 250m and 500m RSB data, bands 1-2 and 3-7 respectively, aggregated to a 1km spatial resolution, are also contained in the MOD021KM product. The MOD02HKM product contains a subset of the RSB data, including only the first 7 bands, with bands 1-2 aggregated to 500m and bands 3-7 at their nominal 500m nadir resolution. The NGST SDRGEN tool uses these two datasets to generate all of the 750m and 375m proxy SDRs for VIIRS, except for the VIIRS day/night band (DNB). The tool maps a single MODIS band to each of the VIIRS bands, primarily based on the best spectral match between the bands. However, it also takes into consideration the several VIIRS dual gain bands (M4, M5 and M7) that correspond to two different single-gain MODIS bands. The band mapping currently employed by the SDRGEN tool is shown in Table 3-1. There is no spatial resampling of the MODIS pixel data to emulate the resolution of the VIIRS pixels, except that the MODIS bands with higher spatial resolution than their VIIRS counterparts are aggregated to provide the comparable resolution while a couple of the MODIS bands with lower resolution than that of the VIIRS imagery-resolution bands they're emulating are replicated to provide the correct number of along-track and along-scan imagery-resolution pixels compared with the corresponding moderate-resolution pixels.

To emulate the VIIRS DNB (500-900nm), we actually combine four of the MODIS RSB bands, bands 1 (620-670nm), 2 (841-876nm), 4 (545-565nm) and 17 (890-920nm). The weights used in combining these bands (0.3834, 0.3133, 0.2712, and 0.0321 respectively) are based on the transmittance of the DNB bandpass filter at the wavelength of each of the MODIS bands and the predicted SNR for each band, detecting a radiance signal that is 1% of the reflected radiance from a TOA albedo of 1 and solar zenith of 0. The spatial resampling of the VIIRS DNB data to produce the near-constant along-scan spatial samples of 740m is not done for the SDRs that are generated; rather, that processing is performed in the post-processing of the output of the NCC algorithm.

This SDR data, along with the corresponding granulated ancillary data, are converted into an HDF4 format that is readable by the VIIRS Science algorithms.

Use or disclosure of data contained on this page is subject to the export restriction(s) on the title page of this document.

D45702, A. PDMO Released: 2009-02-18 (VERIFY REVISION STATUS)
PDMO

3.2 Proxy Data used for End-to-End Testing of Operational Code by IDPS

The proxy data requirements for testing of the Operational code by IDPS are driven by the need to perform full functionality testing of the IDP segment, demonstrating end-to-end segment operability. It is extremely important that the IDPS is tested in a manner consistent with the way that the Data Processing Element will ultimately be used. This requires streaming Application Packets (AP) into the Ingest Subsystem to generate RDR products, and then using these in the Processing Subsystem to produce SDR/TDR and EDR products. Besides the requirement for having the test data spatially resampled to the NPOESS sensor granule and in the correct AP format, test data is required with enough fidelity to allow the end-to-end process to be verified; this means:

- Realistic spacecraft ephemeris and attitude auxiliary data (i.e., Spacecraft Diary packets)
- CCSDS packets for each NPP sensor that include sufficient information and realism to generate everything from IDPS Ingest RDRs to output SDRs and EDRs
- The appropriate associated MSD and Ancillary data
- A sufficient volume of continuous orbits of test data to ensure the robustness of the Operational code

Figure 3-2 shows the overall process for generating this type of proxy test data. The detailed steps underlying this process are:

- Identify an NPP/NPOESS orbit(s) matched to that of an EOS-Aqua orbit
- Extract heritage sensor L1B (SDR) information for granules along the orbit
- Generate NPOESS-sensor pixel geolocation and cross-sensor spatial mapping LUTs
- Apply any needed corrections to the heritage sensor SDR data (e.g., removing scan-dependent biases for AMSU-A data)
- Populate the NPOESS-sensor swath with heritage sensor SDRs using the cross-sensor spatial mapping LUTs
- Perform cross-sensor spectral mapping (if needed and possible) of heritage SDRs
- Implement sensor/calibration models for the NPOESS-sensor and generate consistent Earth-view, Engineering, and Calibration RDRs
- Reformat Earth-view, Engineering, and Calibration RDR data into CCSDS Application Packets (APs)
- Package Sensor and Spacecraft Diary APs, with extended headers, into a representative stream

The first thing to be addressed in the above process is the identification of the number of continuous orbits per dataset and which orbits to use. The number of orbits per dataset was dictated by the amount of drift between the NPOESS and EOS-Aqua orbits. Because of the difference in their orbit altitudes, there is approximately a 3 minute drift

Use or disclosure of data contained on this page is subject to the export restriction(s) on the title page of this document.

D45702, A. PDMO Released: 2009-02-18 (VERIFY REVISION STATUS)
PDMO

in time between the NPP/NPOESS and EOS-Aqua orbits. Since we wanted to keep the swaths of heritage sensors on EOS-Aqua well centered with respect to those of the NPOESS sensors, we limited the number of continuous orbits (and hence the relative drift) to 2. The considerations for selecting these two-orbit datasets were:

- Availability of heritage sensor data, especially data that has already been spectrally mapped to emulate NPOESS sensor bands
    - Availability of emulated CrIS data from Joel Susskind was a key factor in selecting the September 6th 2002 and January 25th 2003 Golden Days
- Latitude/longitude coverage and seasonal variability
- Orbits with clear, daytime pixels over land
- Orbits which provide a sampling of all IGBP land cover types
- Orbits which provide a wide range of surface/atmosphere conditions (e.g., skin temperature, column water vapor, cloud liquid water, aerosol optical thickness, …)
- Orbits covering areas known to have stressing conditions for the various EDR algorithms
- Orbits which have no “bad” or incomplete granules

The orbits for the 6 two-orbit datasets selected which meet the above criteria are shown in Figure 3-3. Each two-orbit dataset was matched with the corresponding EOS-Aqua orbits by matching the latitude and longitude of the respective satellites at the ascending node crossing beginning the second orbit. This was done through the selection of the TLE for the NPP/NPOESS orbit. Figure 3-4 shows that the simulated NPP/NPOESS orbit is indeed matched with the EOS-Aqua orbit at the middle of the two-orbit dataset.

The next step in the process is the spatial remapping of the SDR radiance data from the heritage sensor to the corresponding pixel in the NPOESS sensor. Because we have taken such pain in matching the orbits of the two sensors, the resulting match should be quite reasonable; however, there are still differences in the association of the radiance data from the original heritage-sensor with the other auxiliary conditions for the NPOESS sensor. In particular, after the pixels have been spatially remapped, there is some loss of consistency in the association of the physical conditions associated with the pixel and the radiance assigned to it. As can be seen in Figure 3-5, the pixel geolocation for VIIRS (top of figure) can be different from that of MODIS by as much as a couple of kilometers at edge of scan. This could affect algorithms such as the Land Surface Temperature (LST) that associates which LST regression coefficients to use for a given pixel with the land cover type viewed by the pixel, as determined by its geolocation. Also, the sensor zenith angle will be noticeably different (bottom of figure), so that algorithms which use the sensor zenith angle either directly or through an LUT will be using a slightly different angle than the one which should be used with the pixel spectral radiance. All of these are expected to be minor effects, since we have taken great pain to align the heritage sensor swath with that of the corresponding NPOESS sensor.

Use or disclosure of data contained on this page is subject to the export restriction(s) on the title page of this document.

D45702, A. PDMO Released: 2009-02-18 (VERIFY REVISION STATUS)
PDMO

The next consideration is the spectral remapping of the heritage sensor data. As noted in the previous section, the current MODIS-to-VIIRS band mapping associates each VIIRS band with a single MODIS band, except for the DNB. This mapping, Table 3-1, is based on the best spectral match between the respective sensor bands. The DNB is constructed as a weighted sum of MODIS bands 1, 2, 4 and 17, with the weights based on the transmittance of the DNB bandpass filter at each MODIS band center wavelength and the predicted SNR for each band.

The spectral mapping from AIRS to CrIS has been provided to the community by Dr. J. Susskind. The spectral mapping approach taken was to run a common RTM (having the same physics for both sensors, just different spectral channels) to generate the respective AIRS and CrIS radiances for a large set of environmental scenes. Using this matchup data for a range of atmosphere/surface conditions, a regression-based model was developed for mapping the AIRS spectral radiance to that of CrIS.

We have adopted that same procedure for spectrally mapping the AMSU-A/HSB SDR data to look like ATMS. ATMS has both “heritage” and new spectral bands compared with AMSU-A/HSB. These are shown in Figure 3-6. The new ATMS bands include a window channel at 51.76GHz and two moisture sounding channels at 183.31 +/- 1.8GHz and 183.31 +/- 4.5GHz. There is also a shift of the HSB 150GHz channel to 165GHz for ATMS. There should be considerable correlation between the new ATMS bands and the heritage bands from AMSU/HSB. Following the spectral mapping approach for AIRS-to-CrIS, simulated TOA radiances were generated for both the ATMS and AMSU/HSB bands using the AER OSS MW RTM on our global environmental datasets. These are shown for two different months in Figure 3-7. Regression-based models were then developed for the new ATMS bands using the simulated radiance matchup data. The results of this approach to spectral mapping produce brightness temperatures for the new ATMS bands that are accurate to within the expected noise for each band. This is shown for the new moisture sounding bands in Figure 3-8. Regardless of whether we tested on the same data that was used to train the regression algorithm or used unseen data for a different season, the results were virtually the same, almost no bias error and a precision error that is comparable to the expected noise for the band. Unlike the moisture sounding bands, the new window band at 51.76GHz required using 4 heritage AMSU bands to achieve the desired precision and accuracy in the spectral mapping. As can be seen in the bottom of Figure 3-9, regression with the two heritage bands on either side of the new ATMS band produced a bi-modal distribution in the brightness temperature error. However, by using all 4 of the lower window channels of AMSU-A, we were able to achieve an accuracy in the spectral mapping comparable to that obtained for the moisture sounding channels, as shown in Figure 3-10. The final thing that needed to be demonstrated was that regression coefficients developed from simulated data would work when applied to real data. We accomplished this by taking the simulated data for just the heritage ATMS bands from HSB and dropping one of these bands, using the regression coefficients developed from the remaining bands to determine the radiance for the missing band. We then applied those same regression coefficients to the real HSB data and computed the radiance for the missing band. By looking at the similarity in the errors of the simulated brightness temperatures obtained by regression for both the synthetic and

Use or disclosure of data contained on this page is subject to the export restriction(s) on the title page of this document.

D45702, A. PDMO Released: 2009-02-18 (VERIFY REVISION STATUS)
PDMO

real data, we demonstrated that the real data behaves the same as the synthetic data with regression coefficients determined from the synthetic data alone. This is shown in Figure 3-11.

3.3 Upgrading NPP VIIRS Proxy Data for Field Terminal Compression Studies

Revision of the NPP VIIRS proxy datasets was undertaken to remove several known artifacts in earlier versions of the data that were produced for testing the end-to-end functionality of the IDPS Operational Software. The primary motivation for revising the test data was to address certain issues in the earlier datasets that would impact the compression studies being undertaken for the Field Terminal Segment (FTS). For example, the replication of radiance values that occurs for VIIRS pixels falling beyond the MODIS edge-of-swath will obviously produce overly optimistic compression results. Nevertheless, the process of upgrading the VIIRS proxy data for FTS has also resulted in more accurate radiance, reflectance and brightness temperature values for improved end-to-end testing of IDPS. While these pixels will not be used for reporting performance, the more accurate values that result from the new approximations should lead to more representative performance of the operational algorithms being run by IDPS and used to assess other things, like latency. Ultimately, all of the NPP proxy data will be redelivered to IDPS for verifying Build 1.5x2 and beyond.

We have always been aware of artifacts in the NPP proxy data, but since these had no impact on the use of the data for testing the IDPS Operational software we did not address them. For example, pixel replication was our initial approach to filling in radiance values for those VIIRS pixels that fall beyond the MODIS edge-of-swath. Also, the pixel striping for VIIRS band M10 is the result of using the 1km data from MODIS band 6, which is known to have striping because of fill values in the 1km aggregated data. However, a number of the problems with the proxy data only surfaced during chain testing of the VIIRS Science Algorithms in support of IPAC (the IDPS Performance Acceptance Criteria). The remaining artifacts in the proxy data were identified as part of the process of rebuilding the datasets for use in the FTS compression studies. In particular we examined all granules for each of the 6 two-orbit datasets comprising the NPP proxy data to identify any artifacts that needed to be corrected. These included saturated pixels, pixels with zero radiance, and pixels identified as bad either because of spatial mapping problems or because of negative radiance values from MODIS.

3.3.1 Mirroring Instead of Replicating Pixels beyond MODIS Edge-of-Swath

There really is no “valid” approach for populating VIIRS pixels that fall outside the MODIS swath, since we have no knowledge of the actual radiance values that would be seen by these pixels based on the geophysical properties and solar and sensor viewing angles at the pixel locations. Since these VIIRS pixels are not used in assessing performance, it doesn’t make much difference what approach is used in populating this part of the VIIRS swath. As mentioned in the preceding section, our initial approach for filling in radiance values of VIIRS pixels that fall outside the MODIS edge-of-swath was to replicate the radiance values outward from the first and last in-scan pixels of the swath for each in-track detector. While this approach was better than earlier schemes of using a checkerboard pattern of completely unrelated radiance values, it left

Use or disclosure of data contained on this page is subject to the export restriction(s) on the title page of this document.

D45702, A. PDMO Released: 2009-02-18 (VERIFY REVISION STATUS)
PDMO

unphysical striping at both edges of the VIIRS swath, where for example radiance from land pixels would be replicated over the ocean or vice versa. This can be seen in the left-hand image of Figure 3-12. While the performance of the algorithms for these pixels is not a factor, the impact of this constant striping does have implications for image compression studies. The presence of replicated pixels in the VIIRS imagery would have produced overly optimistic image compression ratios, making it difficult to realistically asses the compression ratios needed to achieve a given data transfer rate for Field Terminals. We needed to come up with an approach that would produce the same amount of scene detail for those pixels outside the MODIS edge-of-swath as that existing within the swath. The solution we arrived at was to mirror pixels beyond the MODIS edge-of-swath rather than replicate them. In this process, the first and last in-scan pixels of the swath for each in-track detector are located. For every pixel outward from either the first or last pixel, we select the radiance values from the corresponding position in-ward from these pixels. The effect of this process is shown in the right-hand image of Figure 3-12. Note that this image now has the same level of detail outside the MODIS swath as within, thereby producing a much more realistic assessment of image compressibility for a specified level of performance.

3.3.2 Fixing Pixel Striping in VIIRS Band M10

MODIS band 6 is one of the reflective solar bands that sample the scene at a 500m nadir resolution. It is used in its native resolution to emulate VIIRS band I3. In order to emulate VIIRS band M10, which has the same band-pass as I3, we use the MODIS MYD21KM L1B product for band 6, where the pixels have been aggregated to produce a 1km resolution pixel. A majority of the band 6 detectors on Aqua-MODIS are either anomalous or non-functional. The MODIS L1B code does not calibrate Earth-view pixels for non-functional detectors. However, to facilitate building images with the L1B production data, the scaled integer values for the non-functional detectors are interpolated from the nearest live detectors and are flagged to alert users, so that they can decide whether to use pixels from the non-functional detector gaps. On aggregating the scaled integer values from their native 500 meter resolution to 1km, those 1km pixels containing non-functional detector data are given fill values denoting aggregation failure. This produces the severe pixel striping shown in the left-hand sensor-space imagery of Figure 3-13. When the MODIS pixels are sampled to populate the VIIRS swath, the nearest-neighbor sampling in map-space produces a complex striping pattern in VIIRS sensor space, which is shown in the right-hand image of Figure 3-13. The effect of this striping on image compression is not clear, but whether optimistic or pessimistic, the result is not realistic. To correct this problem, we need only realize that the imagery for band I3, though not perfect, is not flawed by this striping. Thus the approach to fixing the striping for band M10 is to identify each pixel with a fill-value due to aggregation failure and replace it by the average of the radiance values from the corresponding 2x2 imagery-resolution pixel data emulated for VIIRS band I3. The result of this processing, as well as the pixel mirroring described in Section 3.3.1, is shown in Figure 3-14. Note that there is no hint of the pixel striping in the corrected imagery.

Use or disclosure of data contained on this page is subject to the export restriction(s) on the title page of this document.

D45702, A. PDMO Released: 2009-02-18 (VERIFY REVISION STATUS)
PDMO

3.3.3 Improved Radiance Values for Replacing Saturated Pixels

The MODIS reflective solar bands which have significant problems with saturation are bands 8, 9 and 15, used to emulate VIIRS bands M1, M2 and M6, respectively. It is not surprising that these bands saturate more easily than the other MODIS bands used to emulate VIIRS since they are primarily used for retrieving ocean color products for MODIS and hence have high gain settings to retrieve the faint signatures from the water-leaving radiance at TOA. Bands 8 and 9 tend to saturate over clouds, depending on optical depth, with band 9 usually saturating before band 8. MODIS band 15 not only saturates for any clouds, it also easily saturates over land.

In previous versions of the proxy data, saturated pixels have been handled in a variety of ways. Initially, they were replaced by a value of 1.1 times the maximum radiance of the VIIRS bands they were emulating, which only caused the VIIRS pixels to also show up as saturated in the final product. The next approach at replacing saturated pixels was to directly substitute radiance values from alternative MODIS bands that didn't saturate. While this does produce radiance variations over regions that were previously completely saturated, the magnitude of these radiances might not accurately represent that of the bands they were selected to replace. This not only produces imagery with possibly incorrect entropy, the radiance values used may also cause the VIIRS algorithms to not perform in a realistic fashion in terms of testing the functionality and latency of the operational software.

The approach employed in the most recent set of VIIRS proxy data is to still use radiance values from those bands that don't saturate, but to use them in a way that relies on the physical behavior of the spectral radiance under those conditions that cause the pixels to saturate in the first place. A number of simulations of the TOA spectral reflectance for cloud-covered ocean scenes were run. The Coupled Ocean Atmosphere RTM, COART, was used to generate the TOA spectral reflectance for wavelengths from 0.35 to 0.9 microns in 0.001 micron steps. Since the wavelengths of interest for bands M1 and M2 are well below 550 nm, the effect of absorption by atmospheric gases is not significant; hence, the simulations were all performed using just the US62 standard atmosphere. A maritime aerosol with an AOT of 0.1 at 550nm was also assumed for all of the simulations. What was varied in the simulations was the cloud phase (water or ice), optical depth (1 and 10), and cloud top height (1-2 km and 4-5 km for water clouds, and 4-5 km alone for ice clouds). In all of these simulations the droplet size distribution of the clouds was chosen such that the effective droplet radius r_e is 10 microns. The results of these simulations are shown in Figure 3-15. Several interesting features can be seen in this figure. First, the main factor affecting the TOA reflectance is the optical thickness of the cloud, where the results for different cloud properties other than optical depth only provide slight variations in the spectral reflectance. Another prominent feature is that for wavelengths less than approximately 550 nm, the logarithm of the spectral reflectance at TOA appears to decrease approximately linearly with the logarithm of the wavelength. Finally, as the optical thickness of the cloud increases, the variation of the spectral reflectance as a function of wavelength becomes relatively flat.

Use or disclosure of data contained on this page is subject to the export restriction(s) on the title page of this document.

D45702, A. PDMO Released: 2009-02-18 (VERIFY REVISION STATUS)
PDMO

The above observations suggest that when the TOA reflectance in bands M1 and M2 are both saturated, the reflectance for these bands can be estimated by linearly extrapolating the logarithm of the reflectance from bands M3 and M4 with the logarithm of the corresponding wavelengths; that is

$$\rho(\lambda_{M1,M2}) = \exp\left\{ \frac{\ln\left(\rho_{M4} / \rho_{M3} \right)}{\ln\left(\lambda_{M4} / \lambda_{M3} \right)} \ln\left(\lambda_{M1,M2} / \lambda_{M3} \right) + \ln(\rho_{M3}) \right\} \quad .$$

Note that when the clouds are optically thick and the reflectance in bands M4 and M3 are almost the same, this approximation is equivalent to the previous approach of setting the reflectance in bands M1 and M2 equal to that of M3. However, for conditions where the clouds are not optically thick, the above procedure of extrapolating the reflectance for bands M1 and M2 should produce a significantly more accurate result. To demonstrate this, we looked at the MODIS granule shown in Figure 3-16. The images on the left side of the figure are the original MODIS reflectances for bands 8 and 9 (VIIRS bands M1 and M2), with fill values for the saturated pixels, while the images on the right side replace the fill values with reflectances produced either from the extrapolation approach described above or an interpolation approach that will be described below. In order to assess the improvement in the predicted reflectance for saturated pixels, we looked at those pixels which saturate in band M2 but not in band M1. The fact that the pixels saturate in band M2 but not in M1 indicates that these pixels have optically thin clouds in them, for which the above extrapolation procedure should give an improved estimate of reflectance. Since we are looking at those pixels which also do not saturate in band M1, we can directly compare the reflectance computed by the extrapolation technique shown above with the previous approach of just using the reflectance from band M3 (MODIS band 3). Figure 3-17 shows histograms of the relative error achieved with the two approaches. Clearly, the extrapolation approach provides a much smaller bias error, although the precision error is about the same as the previous approach. One would expect that the results would improve further for more optically thick clouds, where both bands M1 and M2 saturate. One would also expect that the extrapolation approach will do better for band M2 than for M1, since the difference in wavelength from that of band M3 and M4 is smaller.

As discussed above, there are some instances where the reflectance in band M2 (MODIS band 9) saturates but the reflectance in band M1 does not. In this case, we can replace the above extrapolation procedure for estimating the reflectance in band M2 with an interpolation approach, again based on a linear relationship between the logarithm of the reflectance and that of the wavelength; that is,

$$\rho(\lambda_{M2}) = \exp\left\{ \frac{\ln \lambda_{M2} - \ln \lambda_{M1}}{\ln \lambda_{M3} - \ln \lambda_{M1}} \ln \rho_{M3} + \frac{\ln \lambda_{M3} - \ln \lambda_{M2}}{\ln \lambda_{M3} - \ln \lambda_{M1}} \ln \rho_{M1} \right\}$$

This algorithm should be even more accurate than the extrapolation procedure shown previously, especially for the low cloud optical thickness conditions where M2 saturates

Use or disclosure of data contained on this page is subject to the export restriction(s) on the title page of this document.

D45702, A. PDMO Released: 2009-02-18 (VERIFY REVISION STATUS)
PDMO

but M1 does not. To demonstrate this, we looked at all unsaturated pixels in Figure 3-16 and compared the error in emulating the reflectance for band M2 from the above equation with that from simply substituting the reflectance from band M3. This result is shown in Figure 3-18. Here both the accuracy and precision of the above procedure is much better than the previous M3 replacement approach.

Although relatively rare, pixels from MODIS bands 3 and 4 (VIIRS bands M3 and M4) do occasionally saturate over optically thick clouds. When this occurs, it not only affects the reflectance for these bands, but also that for bands M1 and M2, which use M3 and M4 in generating their saturated pixel replacement values. To deal with this, we note that from Figure 3-15, the spectral reflectance is relatively flat as a function of wavelength for optically thick clouds, such as those which would cause bands M3 and M4 to saturate. This allows for replacing band M3 and M4 reflectances with that from band M5 (MODIS band 1), which practically never saturates.

Band M6 presents a special problem with saturation compared with the other bands. The MODIS surrogate for band M6 is band 15, which not only saturates for all cloud and aerosol conditions, but also over most land backgrounds. The bands surrounding M6 are M5 (MODIS band 1) and M7 (MODIS band 2), both of which rarely saturate. Thus the obvious approach for replacing the reflectance of saturated M6 pixels would be to interpolate between the reflectance of bands M5 and M7. However, the way in which one needs to interpolate depends on whether the pixel is observing a cloud or a surface background, and if the latter, which type of surface is being observed. For clouds and most non-vegetated terrain surfaces, the TOA reflectance should vary relatively smoothly between bands M5 and M7, so that the same interpolation scheme described above can be employed to provide reflectance values for the saturated M6 pixels. If the background is vegetation dominated, however, there is a sharp rise in reflectance at the chlorophyll edge, which occurs at just about the location of MODIS band 15 or VIIRS band M6. This is shown in Figure 3-19. In this case, the best value of reflectance to use for replacing a saturated M6 pixel is the reflectance for band M7. Thus, the prescription is to check the TOA NDVI value of a saturated M6 pixel to see if $\mathrm{NDVI} = \frac{\rho_{M7} - \rho_{M5}}{\rho_{M7} + \rho_{M5}} \geq 0.3$. If it is, then the reflectance of the saturated M6 pixel is set to that of band M7 (MODIS band 2). If the TOA NDVI of the pixel is less than 0.3, then the replacement value for the band M6 reflectance is obtained from the interpolation scheme described above.

All of the approaches discussed above for replacing saturated pixels deal with reflectance rather than radiance. However, the original data extracted from the MODIS L1B granules is radiance. Also, the sensor model requires radiance as an input, so it is necessary to convert the replaced reflectance values back into radiance. The conversion between radiance and reflectance being used is given by,

$$\rho \equiv \frac{\pi L D^2}{F_0 \cos \vartheta_0},$$

Use or disclosure of data contained on this page is subject to the export restriction(s) on the title page of this document.

D45702, A. PDMO Released: 2009-02-18 (VERIFY REVISION STATUS)
PDMO

where ρ is reflectance, L is radiance in $W/m^2/\mu m/sr$, F_0 is the extraterrestrial solar irradiance in $W/m^2/\mu m$, D is the Earth-Sun distance in AU, and θ_0 is the cosine of the solar zenith angle.

Because12-bit linear quantization is used for all TIR bands, MODIS MWIR bands 20 (M12) and 22 (M13) may saturate at hot spots during the daytime in arid and semi-arid regions. To address this problem, we locate the few thermal-emissive band (TEB) pixels that saturate or are NaN and replace them by the maximum radiance of the surrounding nearest neighbors. This is also done for the few remaining saturated and NaN RSB pixels.

3.3.4 Adjusting MODIS Radiance Values for Consistency with VIIRS RSRs

A problem that became evident after running the initial VIIRS-proxy data through the chain of algorithms was that the M12-M13 cloud test in the VIIRS cloud mask called every pixel cloudy in the daytime granules. Since these results were atypical of anything observed with MODIS-proxy data, further investigations were carried out to identify and resolve the issue. The main result of these investigations was an observation that the difference in brightness temperatures between bands M12 and M13 was much larger for the VIIRS SDRs coming out of the calibration code than exists for the MODIS SDRs used in establishing many of the threshold tests used by the VIIRS cloud mask and other VIIRS algorithms. Rather than seeing brightness temperature differences of around 1 K, these differences were on the order of 10 K and higher. The cause of this increase in the brightness temperature differences for the VIIRS SDRs had to do with differences in the MODIS and VIIRS bands and how the MODIS radiances are used in generating VIIRS radiances and brightness temperatures. Figure 3-21 shows the relative spectral response (RSR) functions for both the VIIRS and MODIS bands. Note that the differences between the MODIS and VIIRS bands are significant. The SDR calibration code directly uses radiances from MODIS bands 20 and 22 as the TOA radiances for VIIRS bands M12 and M13. However, it then uses the VIIRS RSRs to compute the corresponding M12 and M13 brightness temperatures.

Figure 3-22 shows the problem with this procedure. Assume a scene that produces a TOA brightness temperature of 280 K for both MODIS bands 20 and 22, resulting in a brightness temperature difference of zero. Using the Aqua-MODIS RSRs, this would translate into radiances of 0.1940 and 0.2904 $W/m^2/um/sr$ respectively for the two bands. The SDR calibration code uses these MODIS radiances as surrogate for the corresponding VIIRS radiances; however, it computes the brightness temperatures for these radiances using a radiance-to-brightness temperature LUT based on the VIIRS RSRs. This transforms the radiances of 0.1940 and 0.2904 $W/m^2/um/sr$ into brightness temperatures of 284 and 275.6K, respectively. Thus, where the data started with a zero brightness temperature difference between MODIS bands 20 and 22, they now have a VIIRS brightness temperature difference of around 10 K. This significant growth in the brightness temperature difference is not a result of any physical effect; it is merely a consequence of using inconsistent definitions for the bands when dealing with band-averaged radiance and the radiance-to-brightness temperature LUTs.

One solution to the problem that had been proposed was to use radiance-to-brightness temperature LUTs based on MODIS rather than VIIRS RSRs in the VIIRS SDR

Use or disclosure of data contained on this page is subject to the export restriction(s) on the title page of this document.

D45702, A. PDMO Released: 2009-02-18 (VERIFY REVISION STATUS)
PDMO

calibration code. However, this approach would not allow us to verify IPAC testing of the SDR calibration code with the final IDPS operational LUTs. Instead of this approach, we modified the MODIS radiances input to the sensor model such that when radiance-to-brightness temperatures LUTs based on the VIIRS RSRs are used with these radiances, MODIS brightness temperatures are obtained. Figure 3-23 shows the process used to adjust the MODIS radiances. The process begins with the radiances from the MODIS thermal emissive bands being used to emulate the corresponding VIIRS band. Using radiance-to-brightness temperature LUTs based on the MODIS RSRs, we convert the radiances to MODIS brightness temperatures. We legislate that the VIIRS brightness temperatures will be the same as the MODIS brightness temperatures. Then using the VIIRS radiance-to-brightness temperature LUTs in the reverse operation to go from brightness temperatures to radiances, we compute the input VIIRS radiances that will produce MODIS brightness temperatures when the VIIRS radiance-to-brightness temperature LUTs are applied. By comparing the VIIRS brightness temperatures generated from the adjusted radiances to the MODIS brightness temperatures, we can verify that the radiances have been adjusted correctly.

A similar approach has been used to adjust the radiance values for the VIIRS reflective solar bands (RSBs) such that they will produce reflectance values that match those of the corresponding MODIS RSBs. In this case, the radiance values simply have to be scaled by the ratio of the band-averaged VIIRS solar irradiance to that of MODIS in order to arrive at the right MODIS reflectance values when divided by the VIIRS band-averaged solar irradiance; that is,

$$L_{VIIRS} = L_{MODIS} \frac{\int F_0(\lambda) RSR(\lambda)_{VIIRS}\, d\lambda}{\int F_0(\lambda) RSR(\lambda)_{MODIS}\, d\lambda}.$$

For the denominator in the above expression, we use the band-averaged extraterrestrial solar irradiance for each band provided in the MODIS L1B data.

3.3.5 Pixels Assigned a Zero Radiance

For nighttime granules or day/night granules with zero or very low radiance, the MODIS reflective solar bands, except band 26 which emulates VIIRS band M9, use a fill value of 65535, signifying either missing RSB data at night or completely missing L1A scans. When this fill value is observed, the corresponding VIIRS bands are assigned a value of zero radiance. The SI data for MODIS band 26, the 1.38 micron band, actually reports values even at night. In most instances, this data represents just sensor noise and can have values less than the offset used in converting the SI values to radiance, resulting in a negative radiance. If the computed radiance for band M9 is negative, we set it to zero. Even when the radiance data is positive under these very low radiance conditions, it is not useful and should be set to zero like the other RSBs. To remove radiance in band M9 due solely to noise, we look for all-zero radiance pixels in band M8 as an indication that M9 should also be zero, and we set the radiance in M9 to zero when this occurs. Finally, there are a handful of granules where the spatial mapping between VIIRS and MODIS has failed for some scans. Examples of this are shown in Figure 3-24. In these cases, the radiance of the pixels in the effected scans is again set to zero.

Use or disclosure of data contained on this page is subject to the export restriction(s) on the title page of this document.

D45702, A. PDMO Released: 2009-02-18 (VERIFY REVISION STATUS)
PDMO

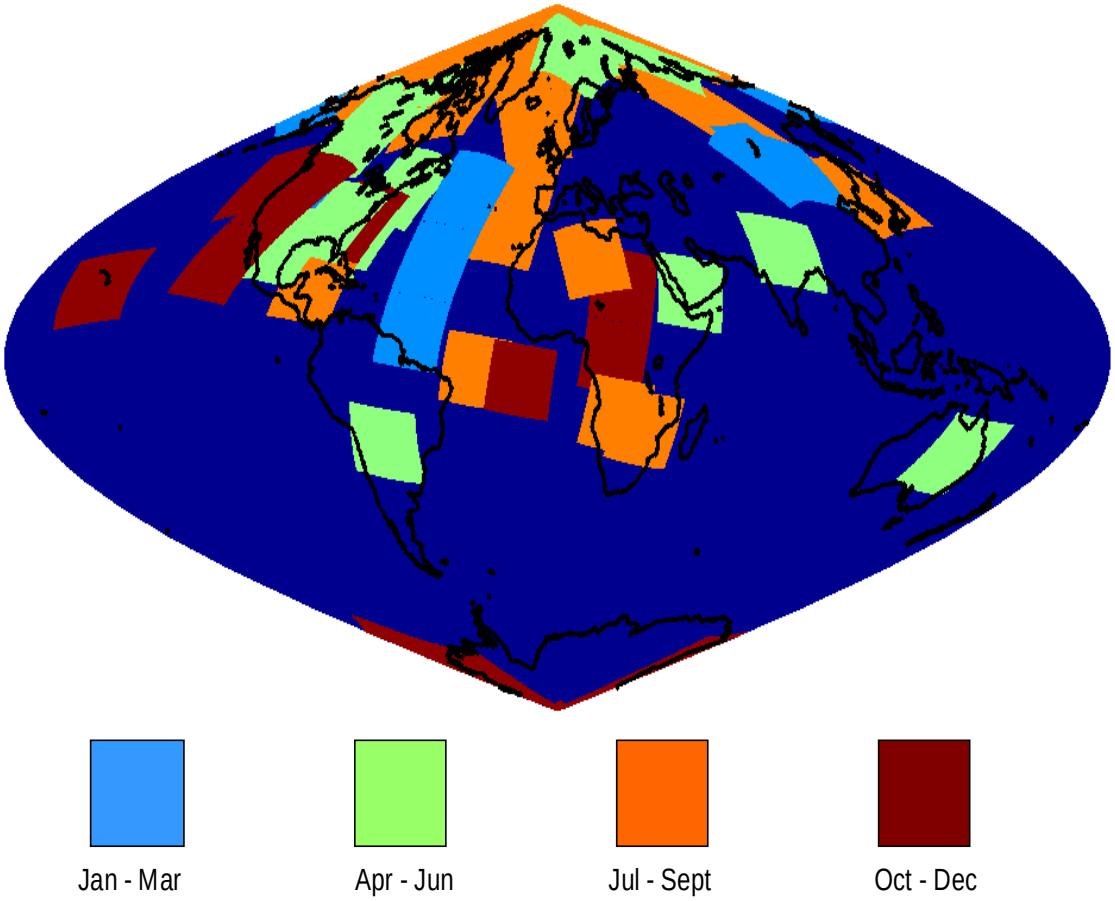

Figure 3-1. Geographical and seasonal coverage by proxy granules selected for extended performance testing

Use or disclosure of data contained on this page is subject to the export restriction(s) on the title page of this document.

D45702, A. PDMO Released: 2009-02-18 (VERIFY REVISION STATUS)
PDMO

Table 3-1. MODIS to VIIRS nearest-neighbor spectral mapping scheme

VIIRS Band	Spectral Range (um)	Nadir HSR (m)	MODIS Band(s)	Range	HSR
DNB	0.500 - 0.900				
M1	0.402 - 0.422	750	8	0.405 - 0.420	1000
M2	0.436 - 0.454	750	9	0.438 - 0.448	1000
M3	0.478 - 0.498	750	3 10	0.459 - 0.479 0.483 - 0.493	500 1000
M4	0.545 - 0.565	750	4 or 12	0.545 - 0.565 0.546 - 0.556	500 1000
I1	0.600 - 0.680	375	1	0.620 - 0.670	250
M5	0.662 - 0.682	750	13 or 1	0.662 - 0.672 0.620 - 0.670	1000 1000
M6	0.739 - 0.754	750	15	0.743 - 0.753	1000
I2	0.846 - 0.885	375	2	0.841 - 0.876	250
M7	0.846 - 0.885	750	16 or 2	0.862 - 0.877 0.841 - 0.876	1000 250
M8	1.230 - 1.250	750	5	SAME	500
M9	1.371 - 1.386	750	26	1.360 - 1.390	1000
I3	1.580 - 1.640	375	6	1.628 - 1.652	500
M10	1.580 - 1.640	750	6	1.628 - 1.652	500
M11	2.225 - 2.275	750	7	2.105 - 2.155	500
I4	3.550 - 3.930	375	20	3.660 - 3.840	1000
M12	3.660 - 3.840	750	20	SAME	1000
M13	3.973 - 4.128	750	21 or 22	3.929 - 3.989 3.929 - 3.989	1000 1000
M14	8.400 - 8.700	750	29	SAME	1000
M15	10.263 - 11.263	750	31	10.780 - 11.280	1000
I5	10.500 - 12.400	375	31 or 32	10.780 - 11.280 11.770 - 12.270	1000 1000
M16	11.538 - 12.488	750	32	11.770 - 12.270	1000

Use or disclosure of data contained on this page is subject to the export restriction(s) on the title page of this document.

D45702, A. PDMO Released: 2009-02-18 (VERIFY REVISION STATUS)
PDMO

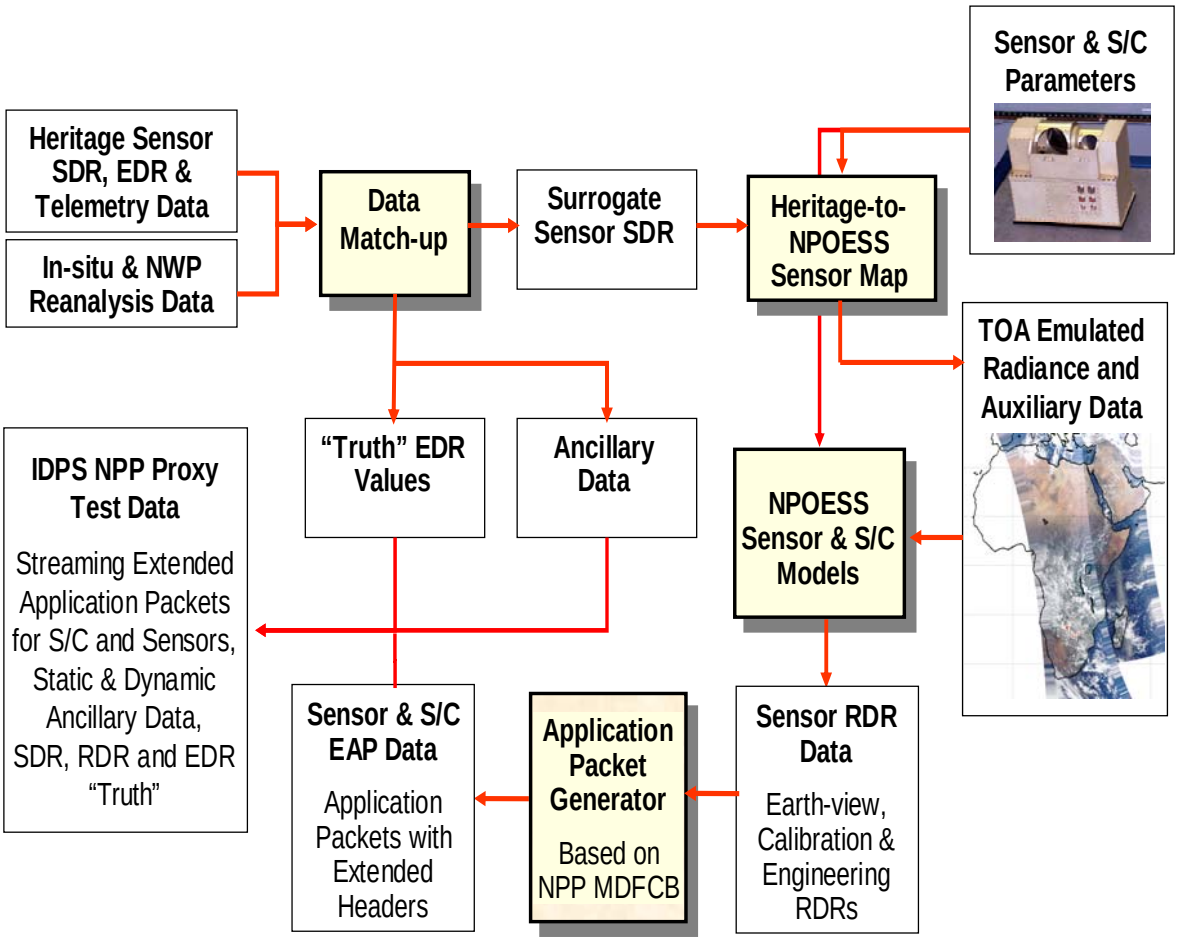

Figure 3-2. End-to-end process for generating proxy data used for assessing readiness of NPP ground processing

Use or disclosure of data contained on this page is subject to the export restriction(s) on the title page of this document.

D45702, A. PDMO Released: 2009-02-18 (VERIFY REVISION STATUS)
PDMO

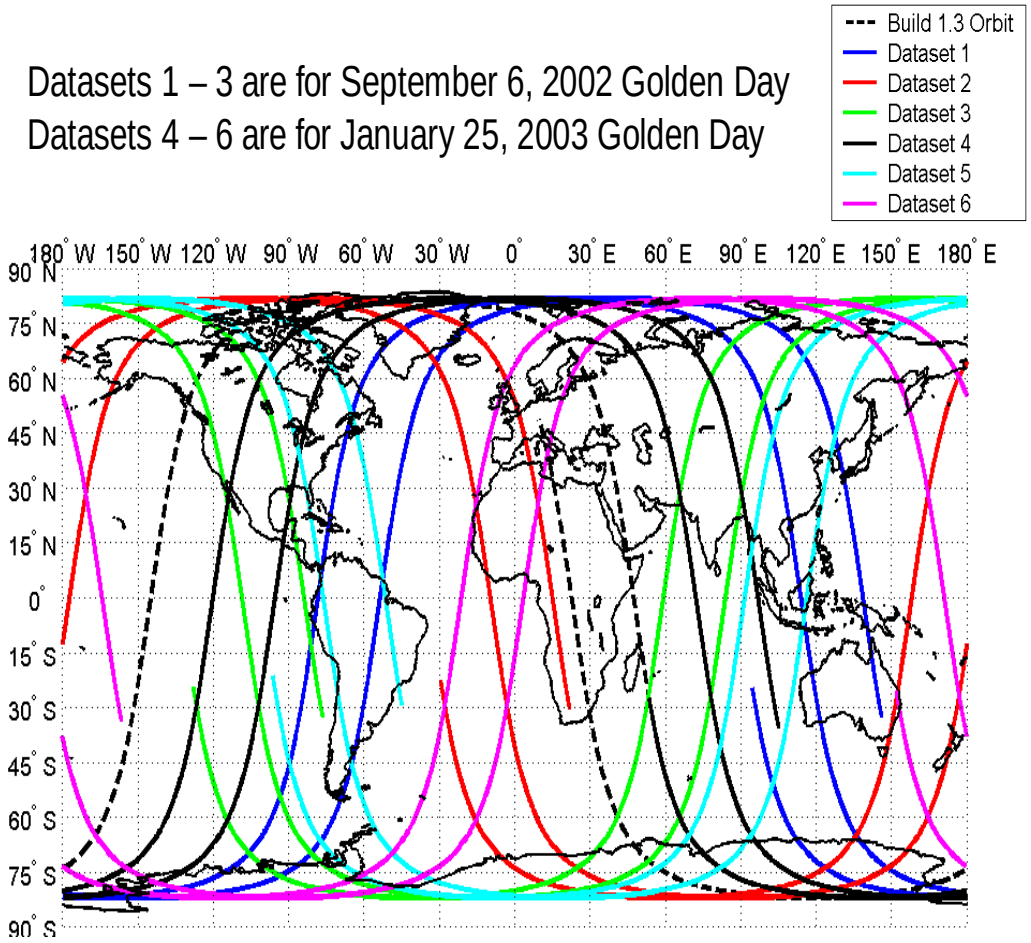

Figure 3-3. Spacecraft ephemeris for each of the 6 two-orbit NPP proxy datasets

Use or disclosure of data contained on this page is subject to the export restriction(s) on the title page of this document.

D45702, A. PDMO Released: 2009-02-18 (VERIFY REVISION STATUS)
PDMO

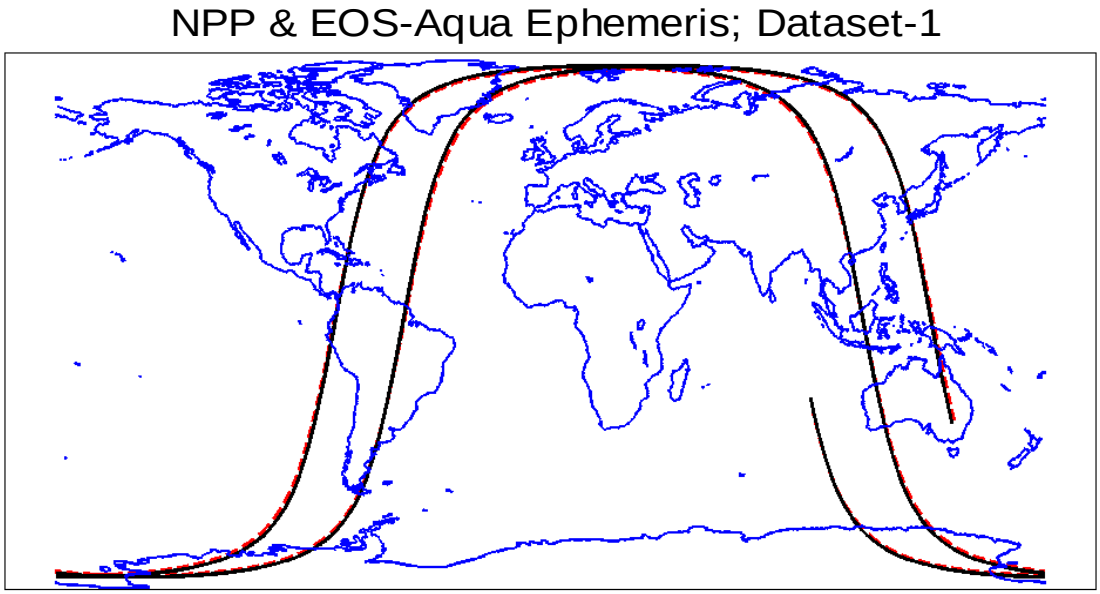

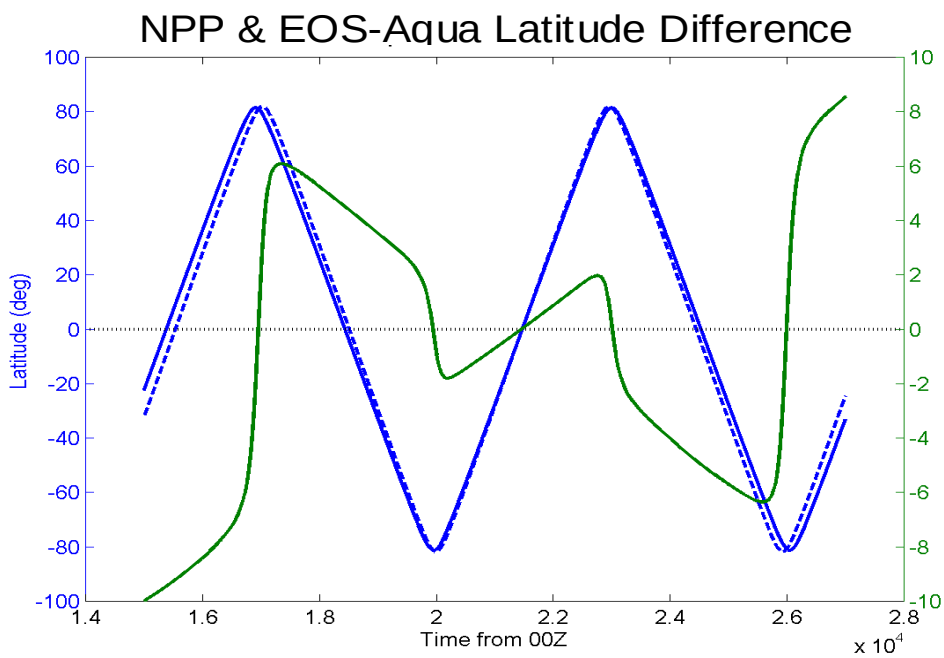

Figure 3-4. Alignment of NPP and EOS-Aqua orbits for each two-orbit proxy dataset

Use or disclosure of data contained on this page is subject to the export restriction(s) on the title page of this document.

D45702, A. PDMO Released: 2009-02-18 (VERIFY REVISION STATUS)
PDMO

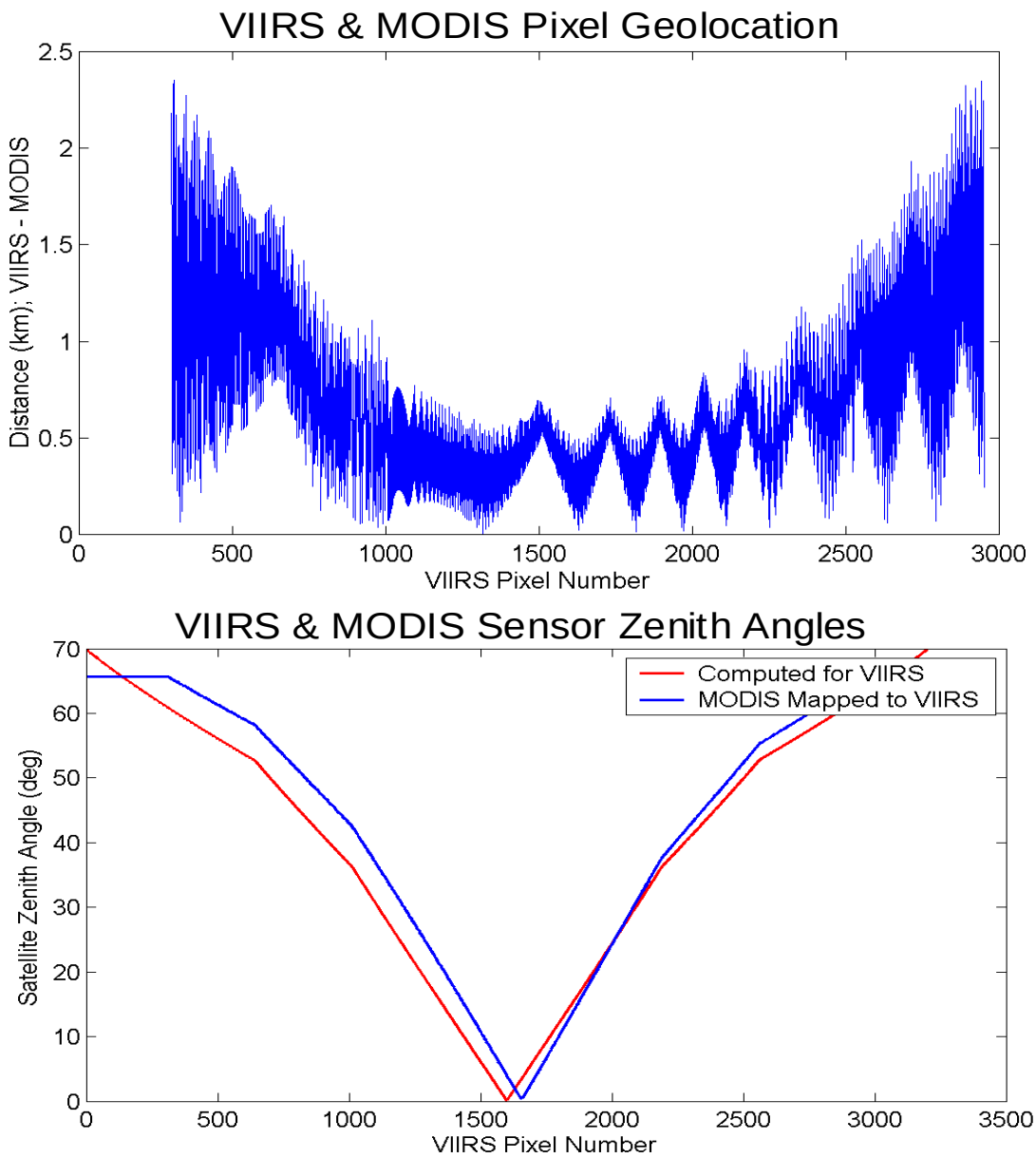

Figure 3-5. Example of differences in auxiliary data between that computed for VIIRS scan and that from heritage MODIS sensor providing the corresponding radiance values

Use or disclosure of data contained on this page is subject to the export restriction(s) on the title page of this document.

D45702, A. PDMO Released: 2009-02-18 (VERIFY REVISION STATUS)
PDMO

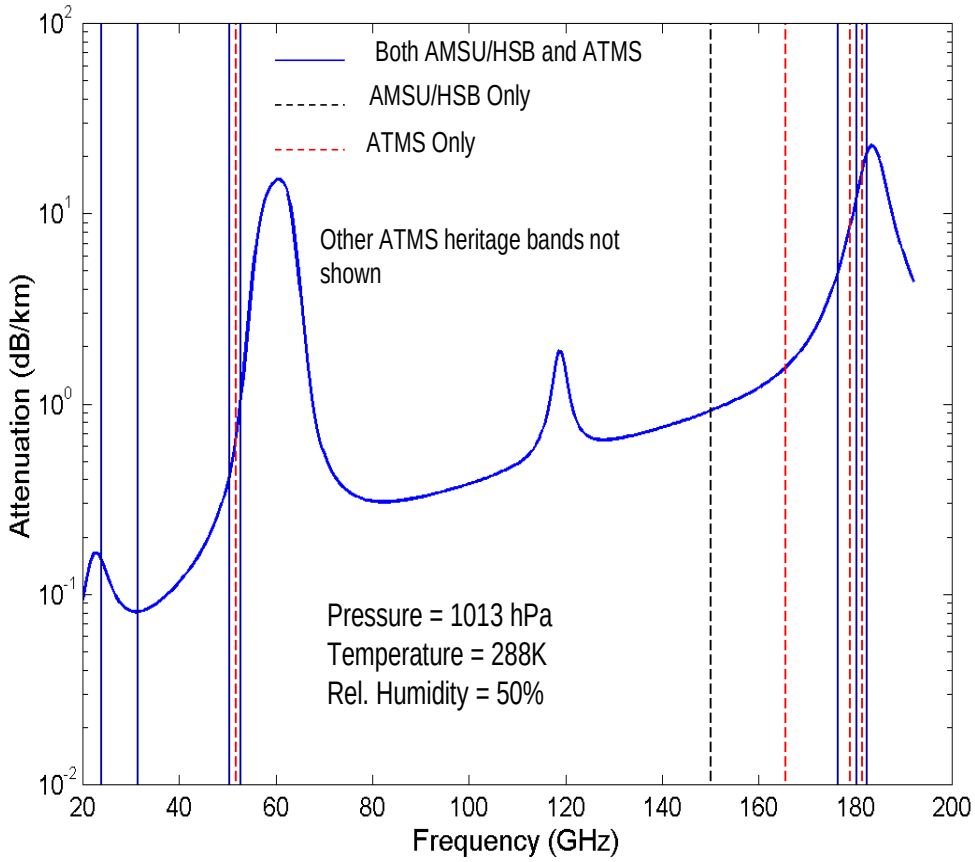

Figure 3-6. Relationship between the heritage AMSU-A / HSB bands and the bands used for ATMS

Use or disclosure of data contained on this page is subject to the export restriction(s) on the title page of this document.

D45702, A. PDMO Released: 2009-02-18 (VERIFY REVISION STATUS)
PDMO

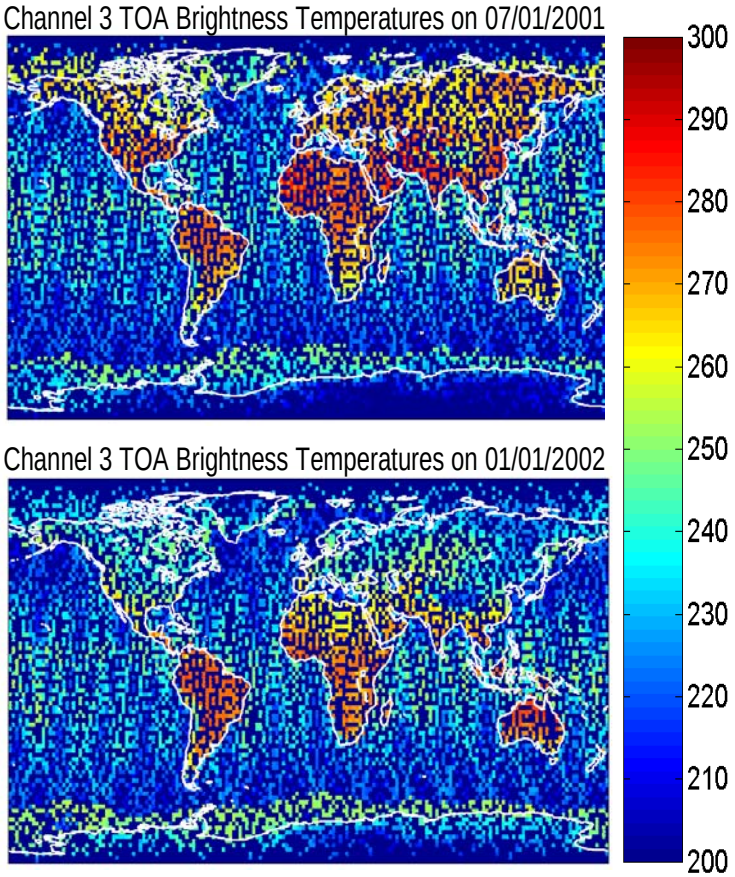

Figure 3-7. Simulated sensor brightness temperatures used to develop regression coefficients for AMSU/HSB-to-ATMS spectral mapping

Use or disclosure of data contained on this page is subject to the export restriction(s) on the title page of this document.

D45702, A. PDMO Released: 2009-02-18 (VERIFY REVISION STATUS)
PDMO

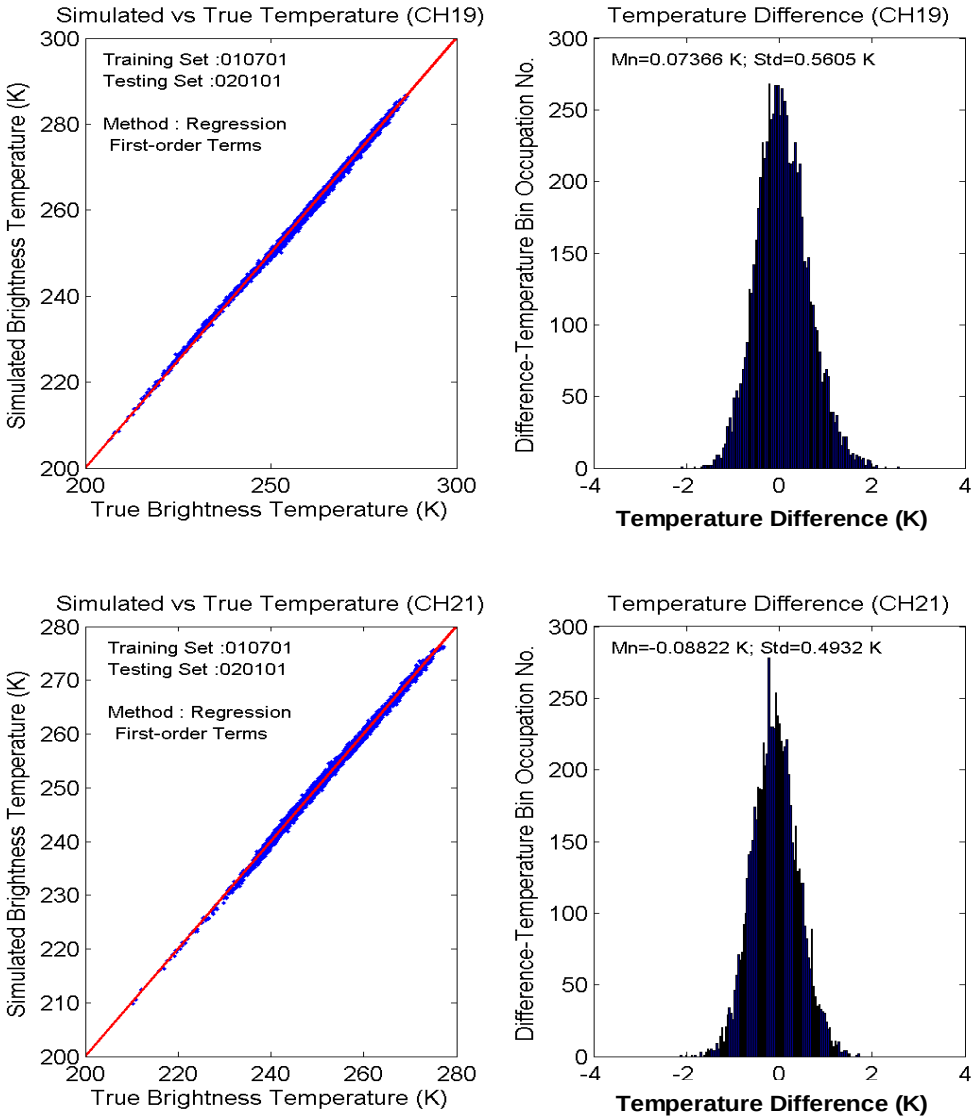

Figure 3-8. Predicted accuracy of spectral mapping for ATMS moisture-sounding channels 19 and 21

Use or disclosure of data contained on this page is subject to the export restriction(s) on the title page of this document.

D45702, A. PDMO Released: 2009-02-18 (VERIFY REVISION STATUS)
PDMO

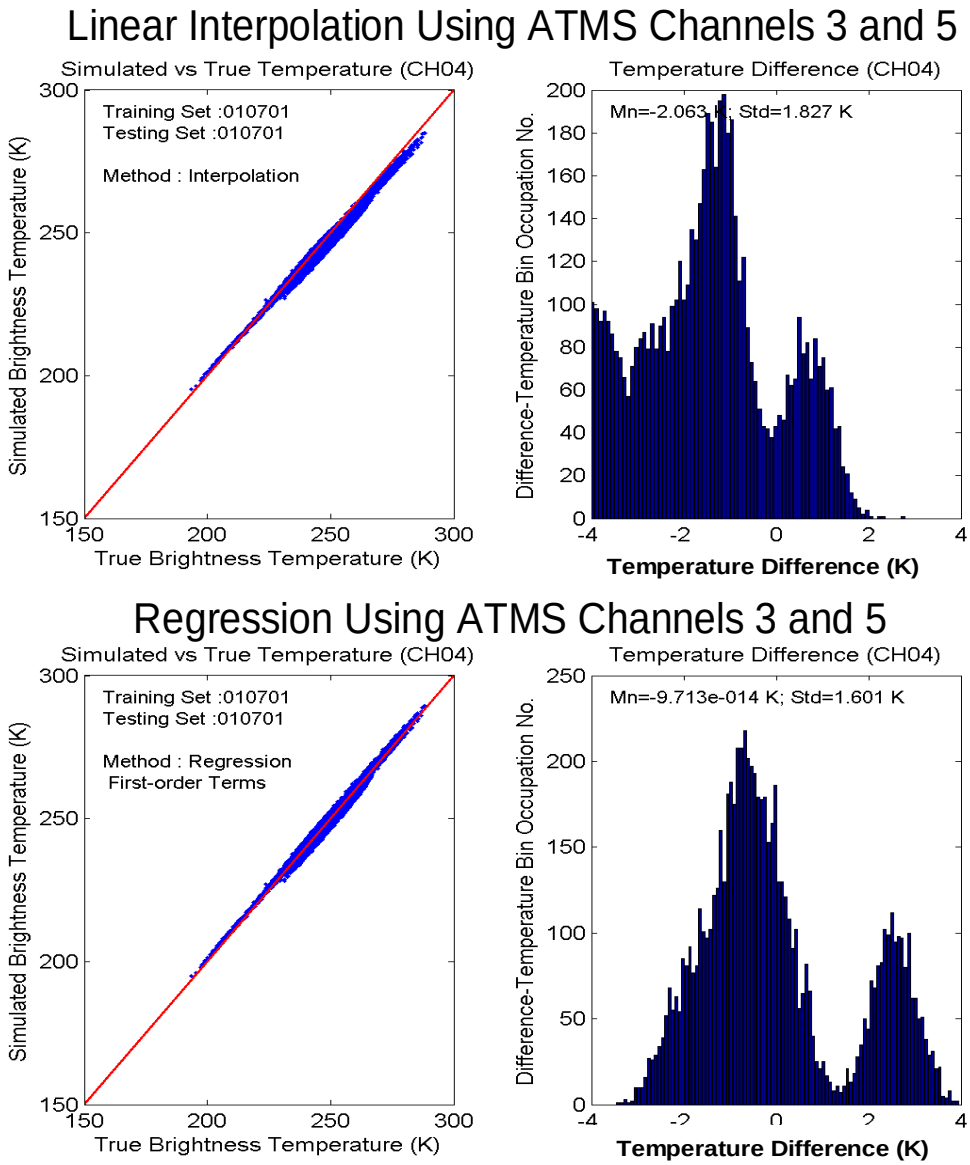

Figure 3-9. Predicted accuracy of synthesizing ATMS window channel 4 (51.76GHz) using either linear interpolation or statistical regression with brightness temperatures from channels 3 and 5

Use or disclosure of data contained on this page is subject to the export restriction(s) on the title page of this document.

D45702, A. PDMO Released: 2009-02-18 (VERIFY REVISION STATUS)
PDMO

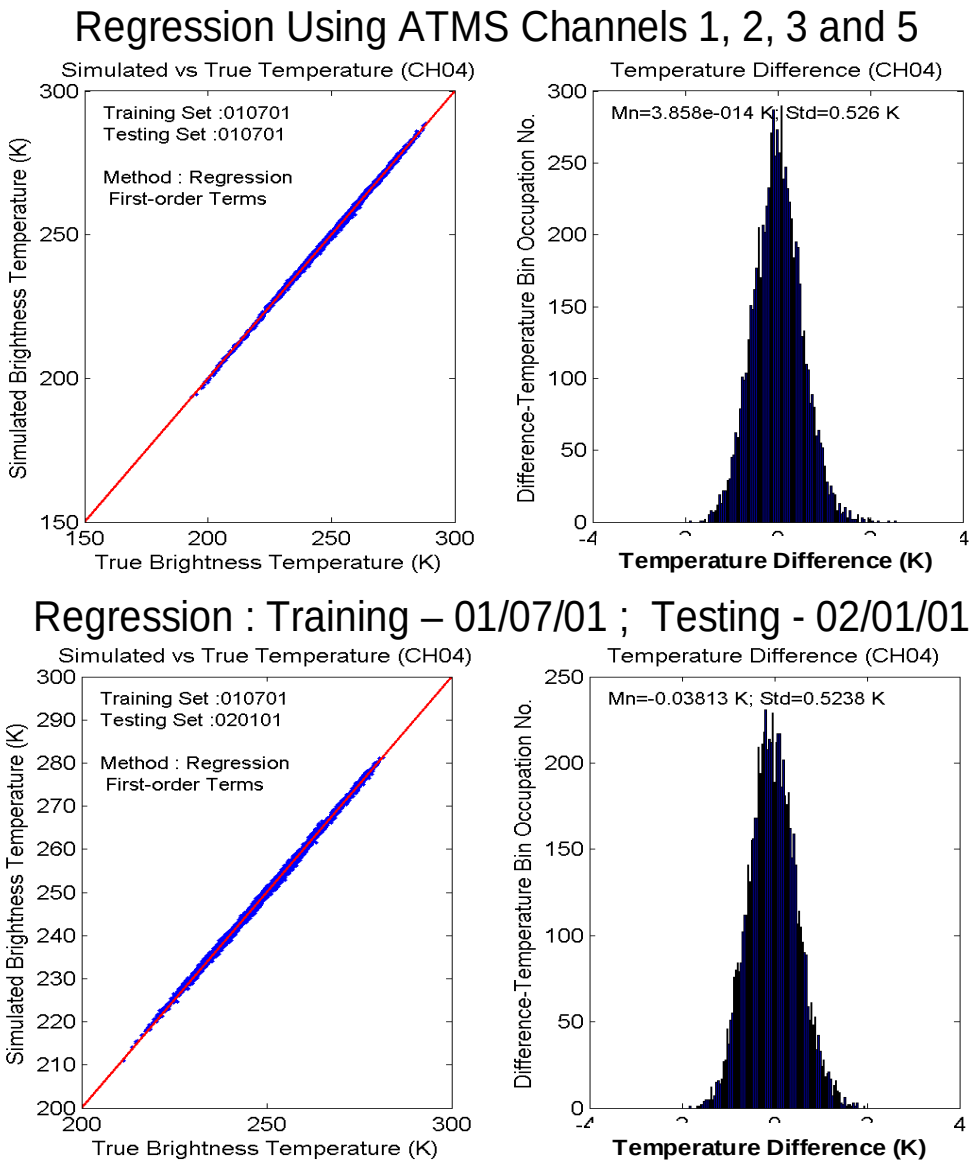

Figure 3-10. Predicted accuracy of synthesizing ATMS window channel 4 (51.76GHz) using statistical regression with brightness temperatures from channels 1, 2, 3 and 5

Use or disclosure of data contained on this page is subject to the export restriction(s) on the title page of this document.

D45702, A. PDMO Released: 2009-02-18 (VERIFY REVISION STATUS)
PDMO

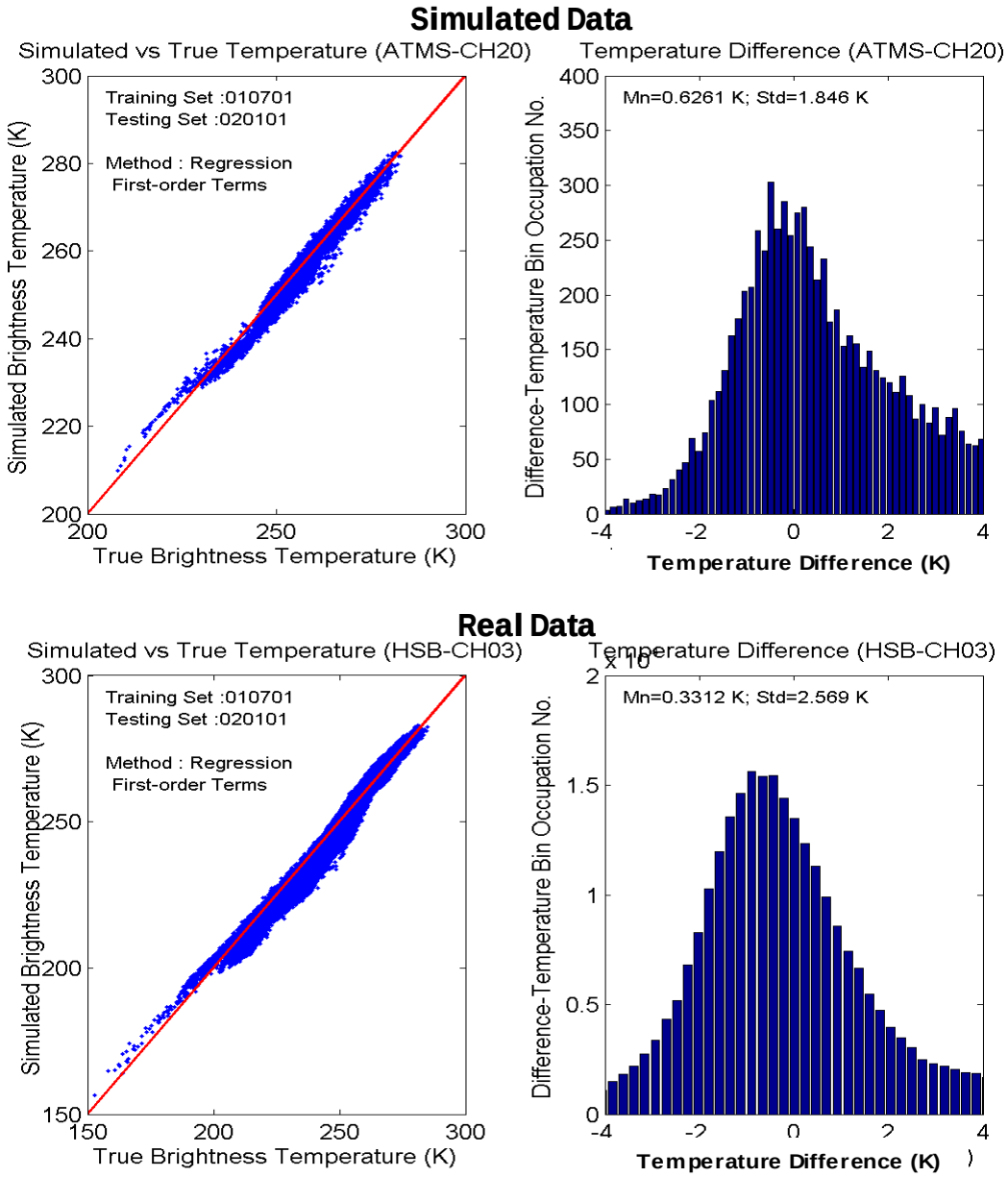

Figure 3-11. Verifying that regression coefficients trained on synthetic data give similar results when applied to real sensor data

Use or disclosure of data contained on this page is subject to the export restriction(s) on the title page of this document.

D45702, A. PDMO Released: 2009-02-18 (VERIFY REVISION STATUS)
PDMO

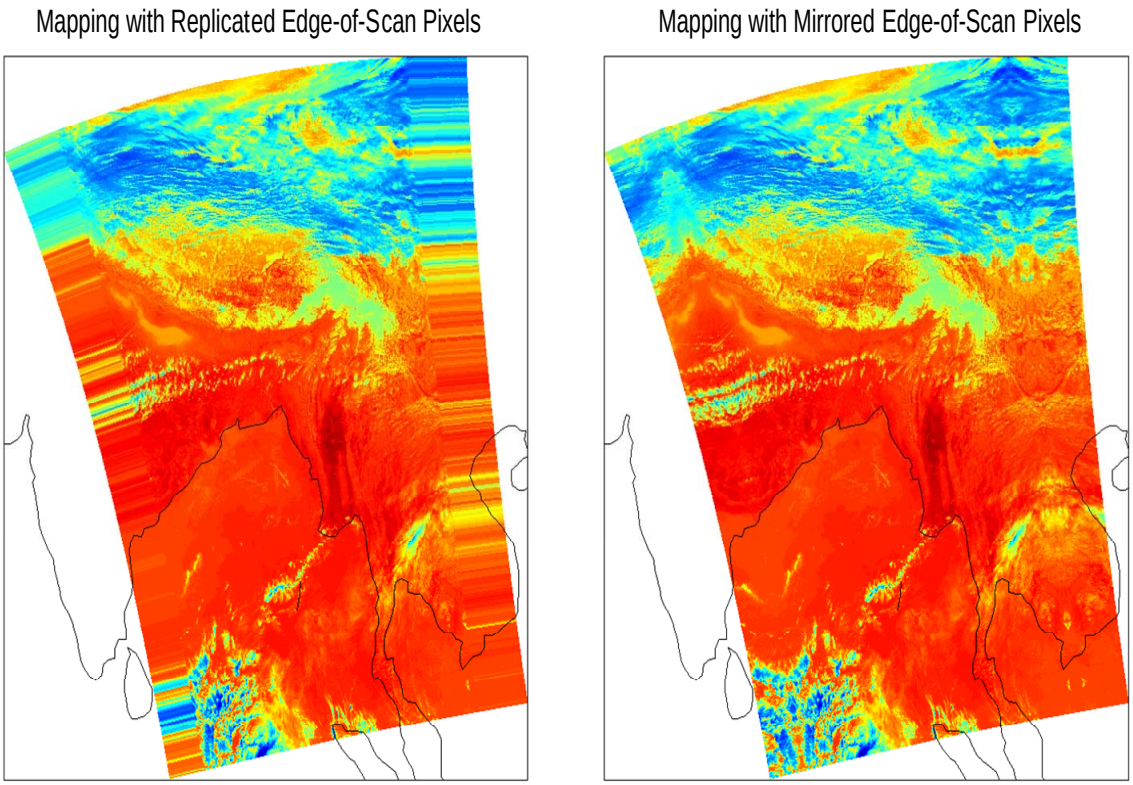

Figure 3-12. Results from pixel replication and mirroring approaches for populating radiance values of VIIRS pixels falling outside MODIS edge-of-swath

Use or disclosure of data contained on this page is subject to the export restriction(s) on the title page of this document.

D45702, A. PDMO Released: 2009-02-18 (VERIFY REVISION STATUS)
PDMO

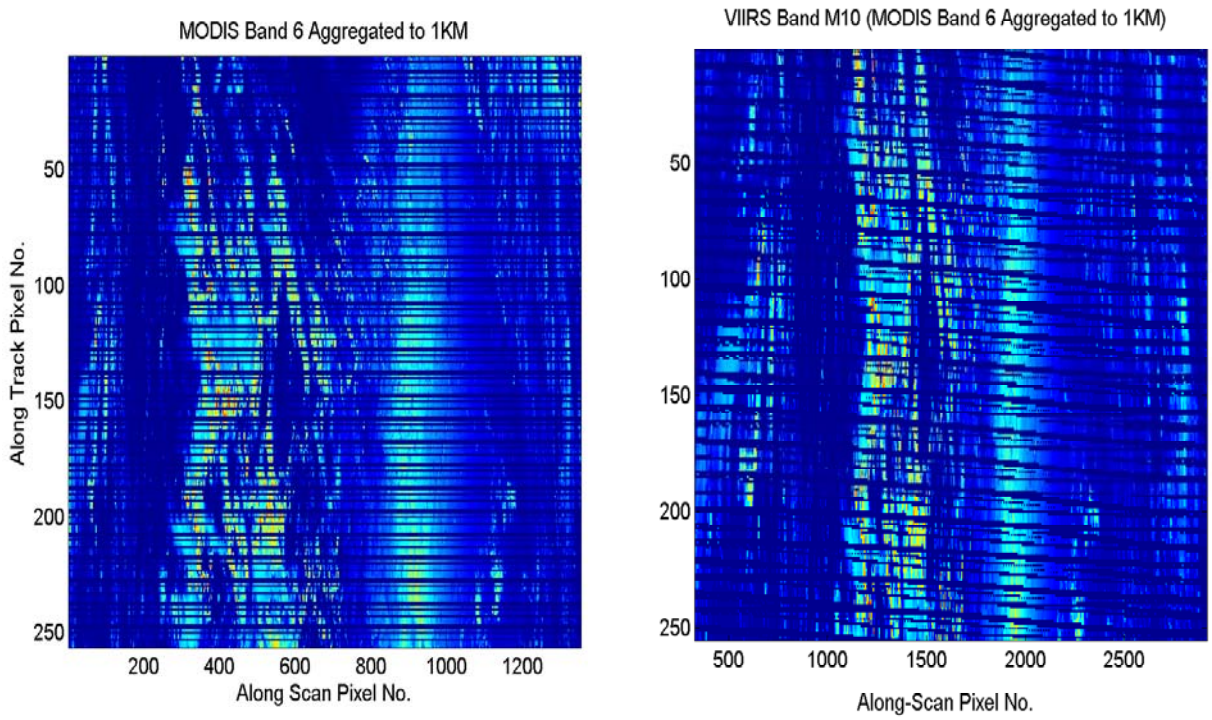

Figure 3-13. Simple pixel striping in MODIS band 6 becomes complex pixel striping for VIIRS band M10

Use or disclosure of data contained on this page is subject to the export restriction(s) on the title page of this document.

D45702, A. PDMO Released: 2009-02-18 (VERIFY REVISION STATUS)
PDMO

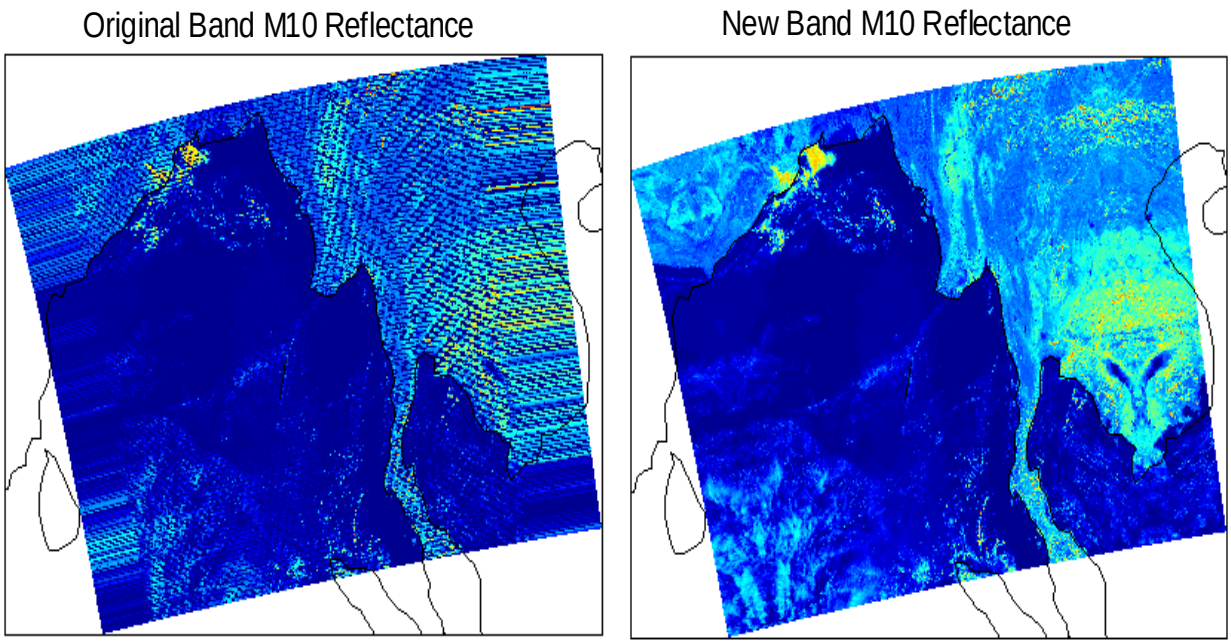

Figure 3-14. Map-space imagery for VIIRS band M10 before and after processing to remove pixel striping and edge-of-swath pixel replication

Use or disclosure of data contained on this page is subject to the export restriction(s) on the title page of this document.

D45702, A. PDMO Released: 2009-02-18 (VERIFY REVISION STATUS)
PDMO

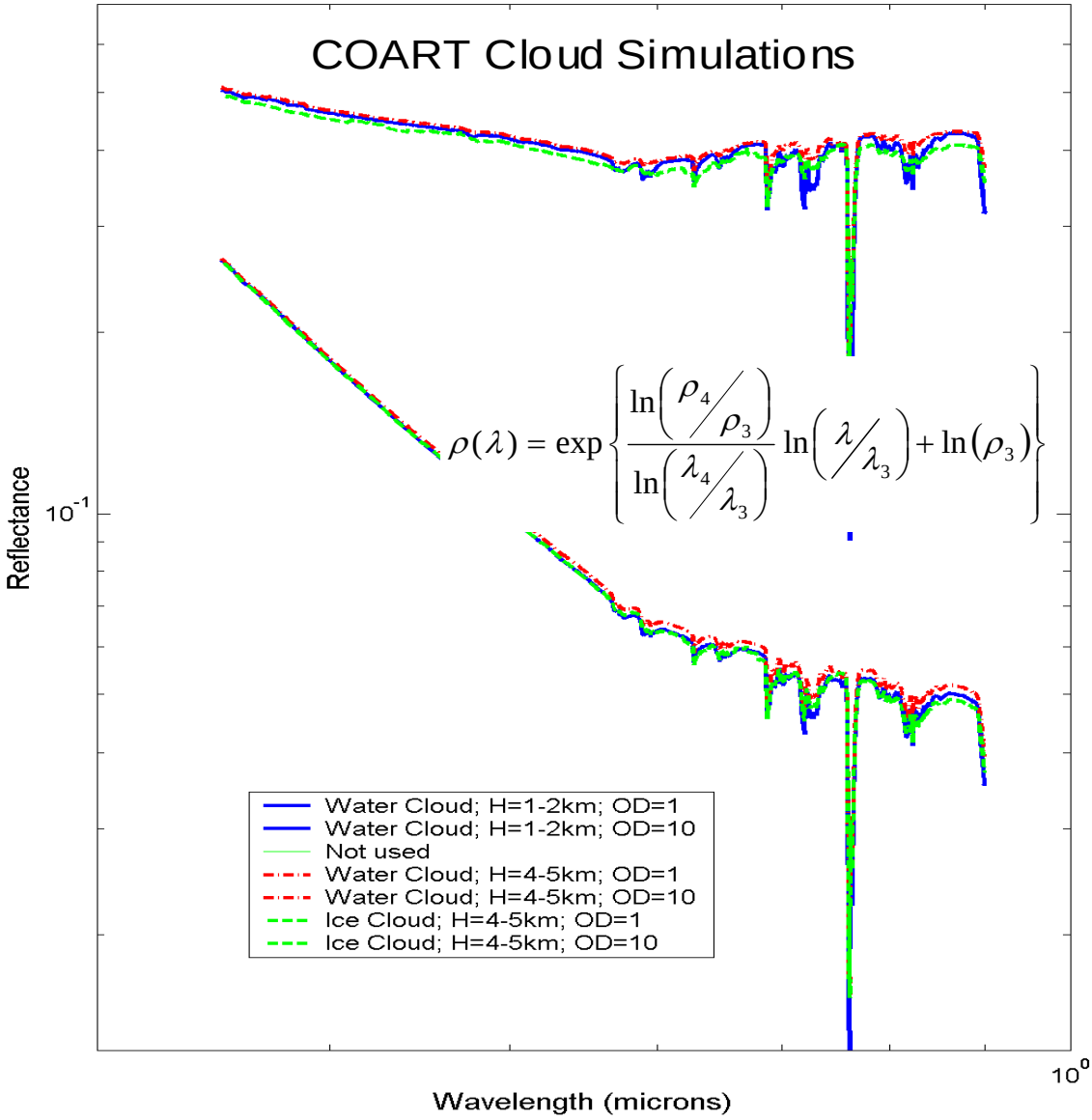

Figure 3-15. COART simulations of ocean scenes with clouds shows that the logarithm of the radiance varies approximately linearly with logarithm of the wavelength for wavelengths less than 0.55 microns

Use or disclosure of data contained on this page is subject to the export restriction(s) on the title page of this document.

D45702, A. PDMO Released: 2009-02-18 (VERIFY REVISION STATUS)
PDMO

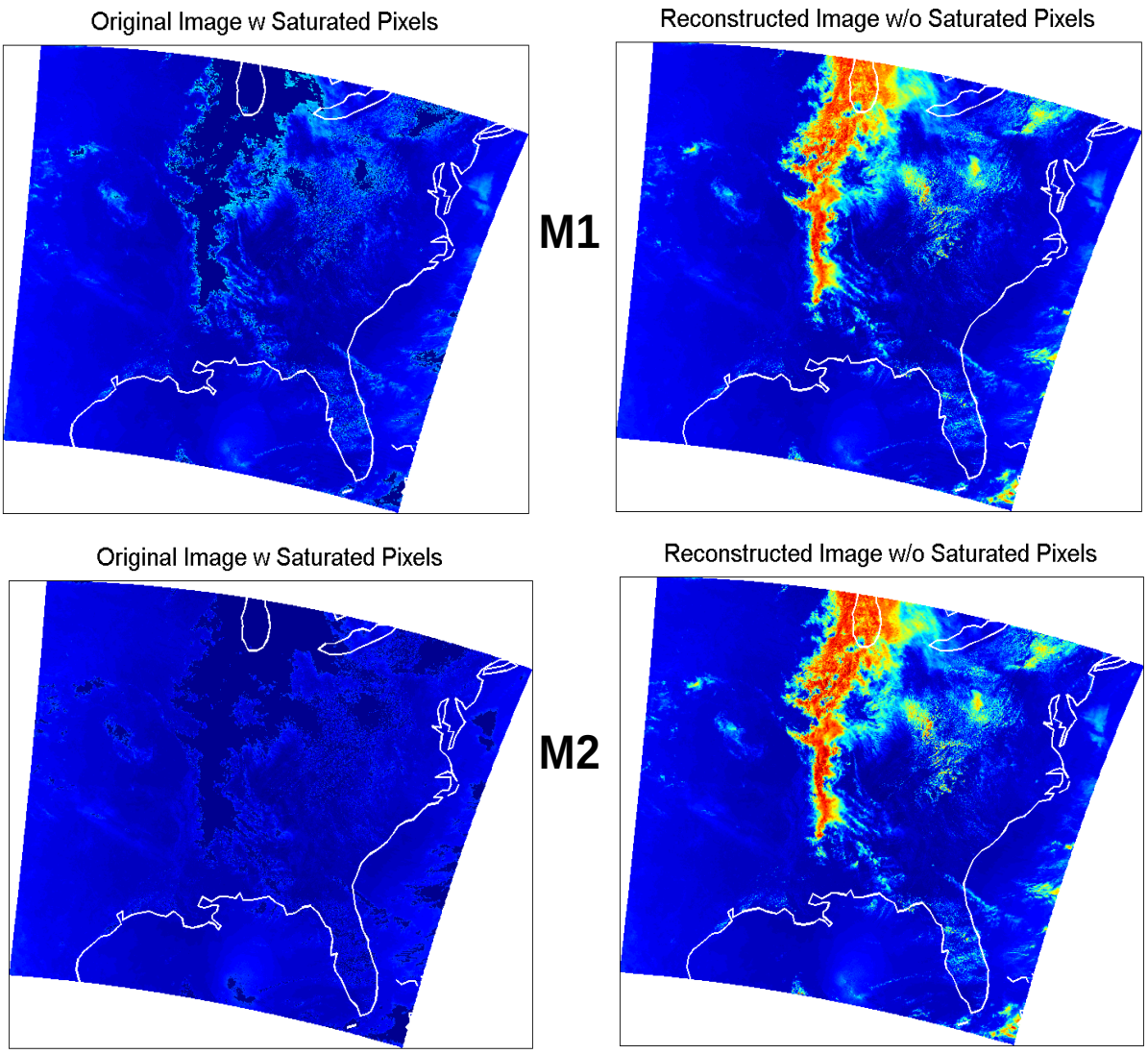

Figure 3-16. Results from using linear extrapolation approach to estimate the TOA reflectance for saturated pixels in bands M1 and M2

Use or disclosure of data contained on this page is subject to the export restriction(s) on the title page of this document.

D45702, A. PDMO Released: 2009-02-18 (VERIFY REVISION STATUS)
PDMO

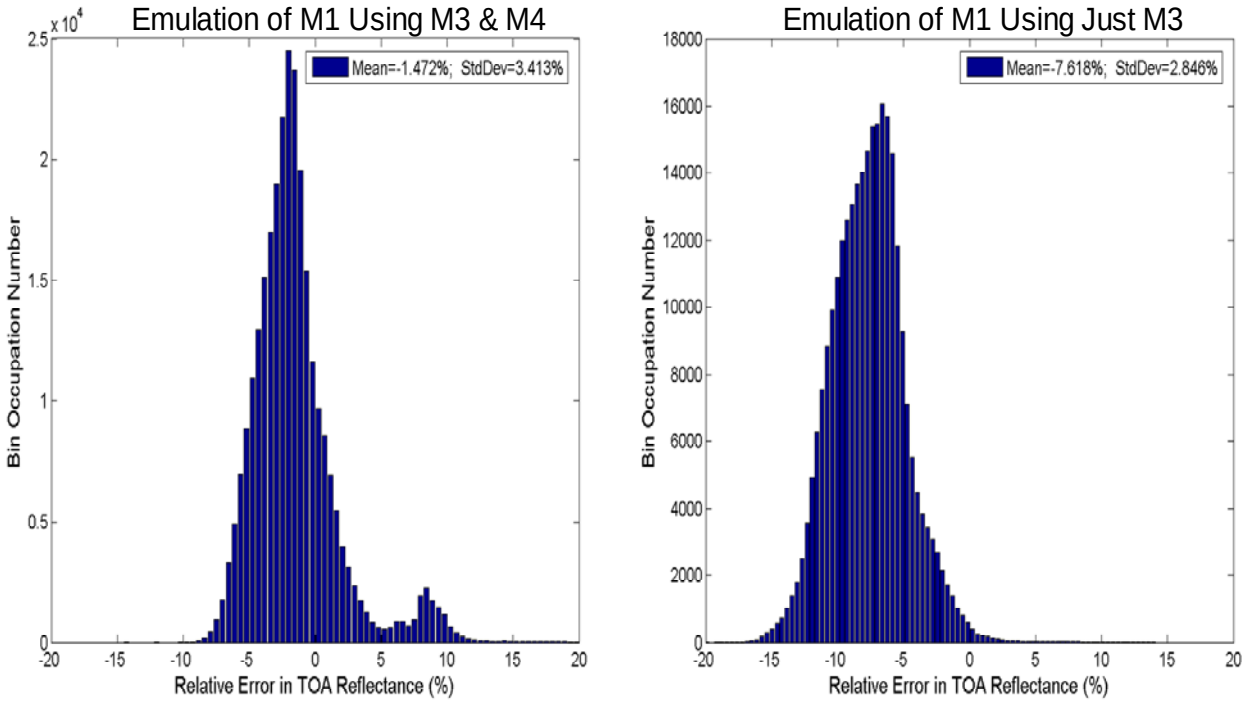

Figure 3-17. Comparison of error from linear extrapolation approach using reflectance from bands M3 and M4 to emulate band M1 to just using reflectance from Band M3

Use or disclosure of data contained on this page is subject to the export restriction(s) on the title page of this document.

D45702, A. PDMO Released: 2009-02-18 (VERIFY REVISION STATUS)
PDMO

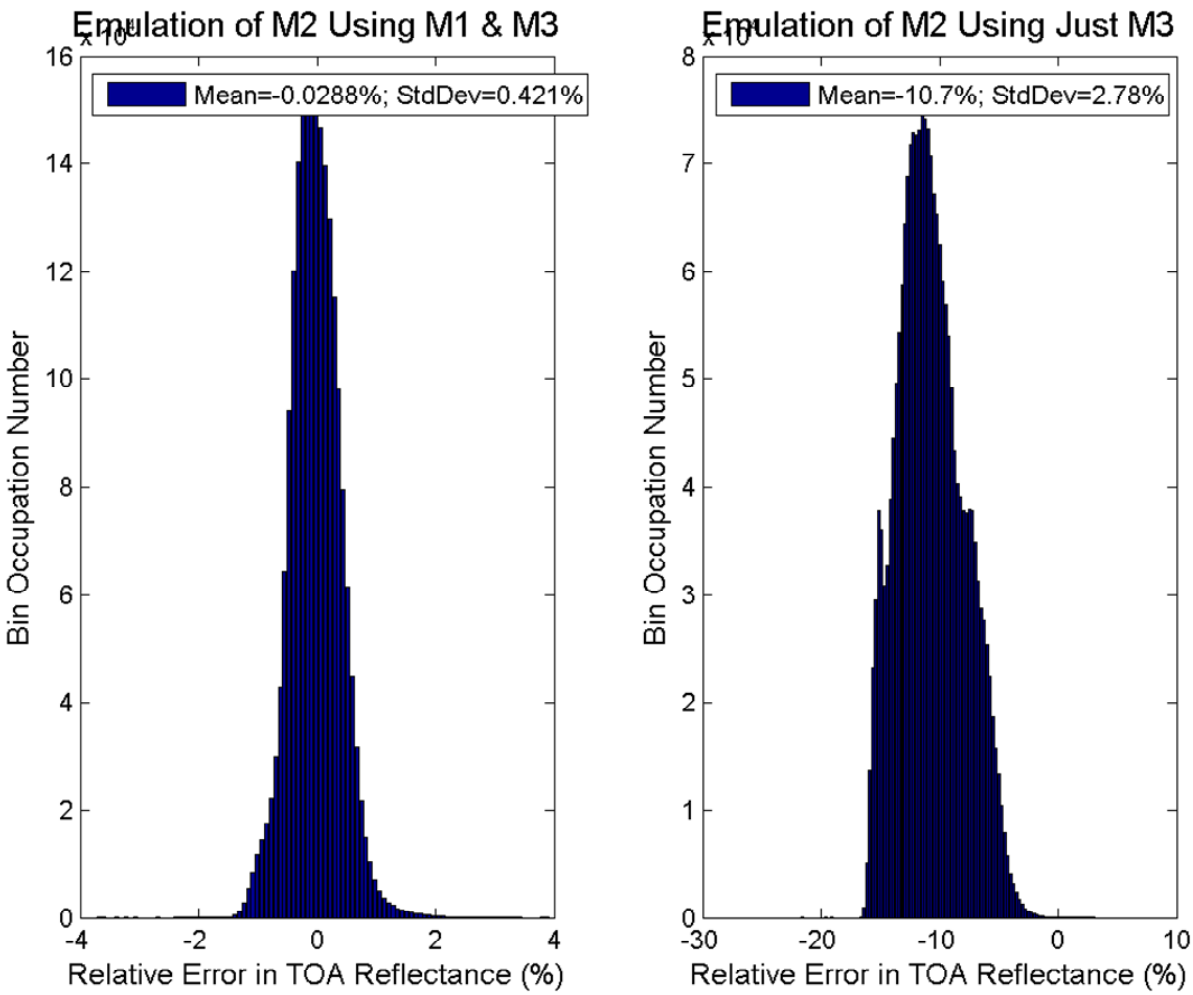

Figure 3-18. Comparison of error from linear interpolation approach using reflectance from bands M1 and M3 to emulate band M2 to just using reflectance from Band M3

Use or disclosure of data contained on this page is subject to the export restriction(s) on the title page of this document.

D45702, A. PDMO Released: 2009-02-18 (VERIFY REVISION STATUS)
PDMO

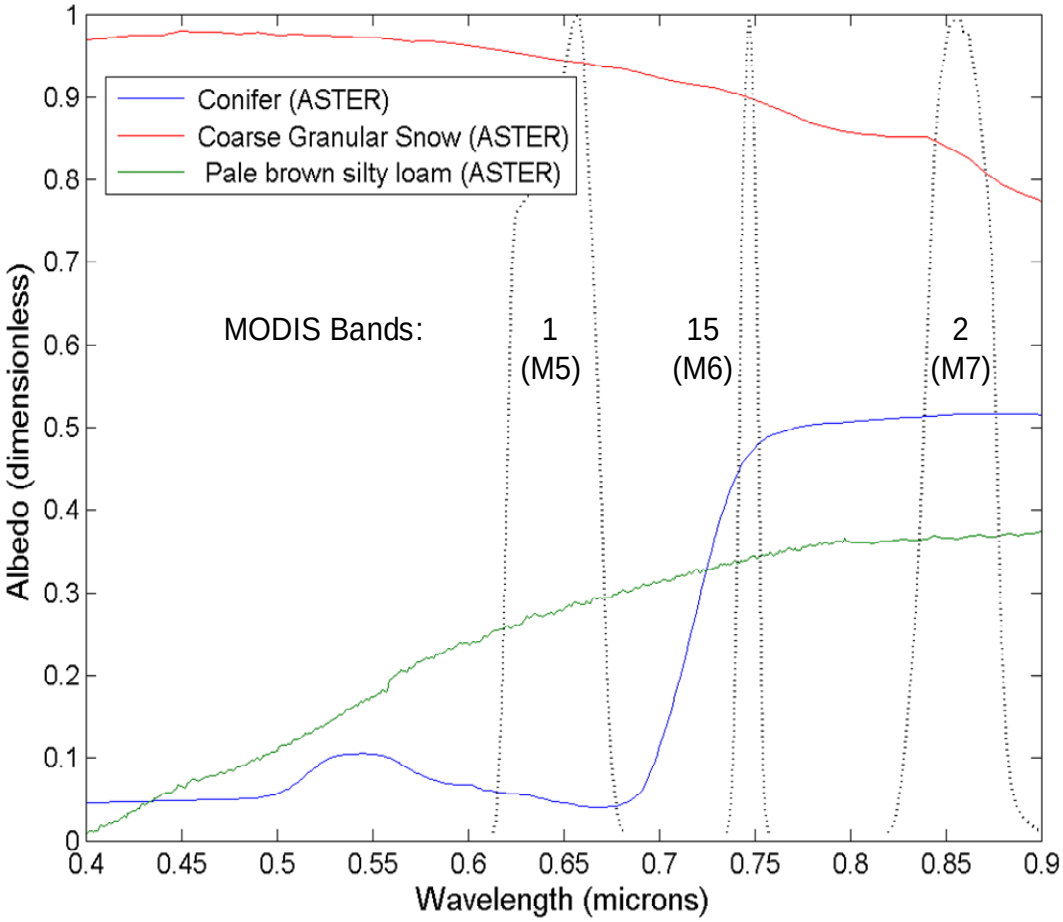

Figure 3-19. Approach for interpolating reflectance to replace band M6 saturated pixels is based on whether TOA reflectance has a vegetation signature, as determined by the TOA NDVI

Use or disclosure of data contained on this page is subject to the export restriction(s) on the title page of this document.

D45702, A. PDMO Released: 2009-02-18 (VERIFY REVISION STATUS)
PDMO

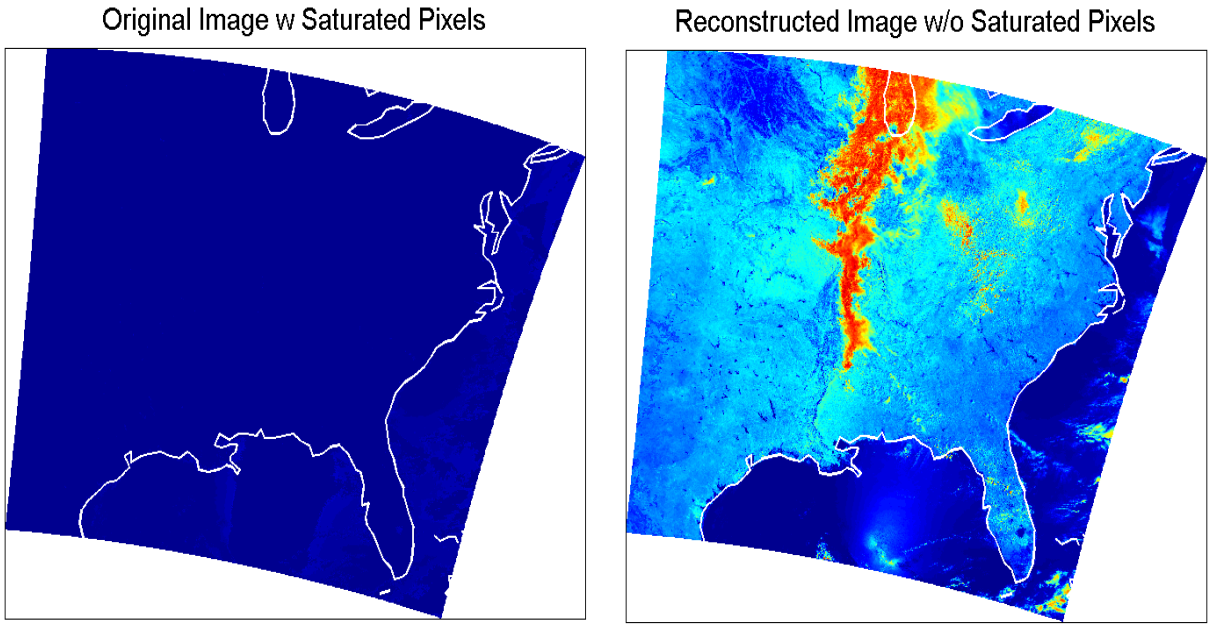

Figure 3-20. Results of employing interpolation approach based on TOA NDVI to estimate the TOA reflectance for saturated pixels in band M6

Use or disclosure of data contained on this page is subject to the export restriction(s) on the title page of this document.

D45702, A. PDMO Released: 2009-02-18 (VERIFY REVISION STATUS)
PDMO

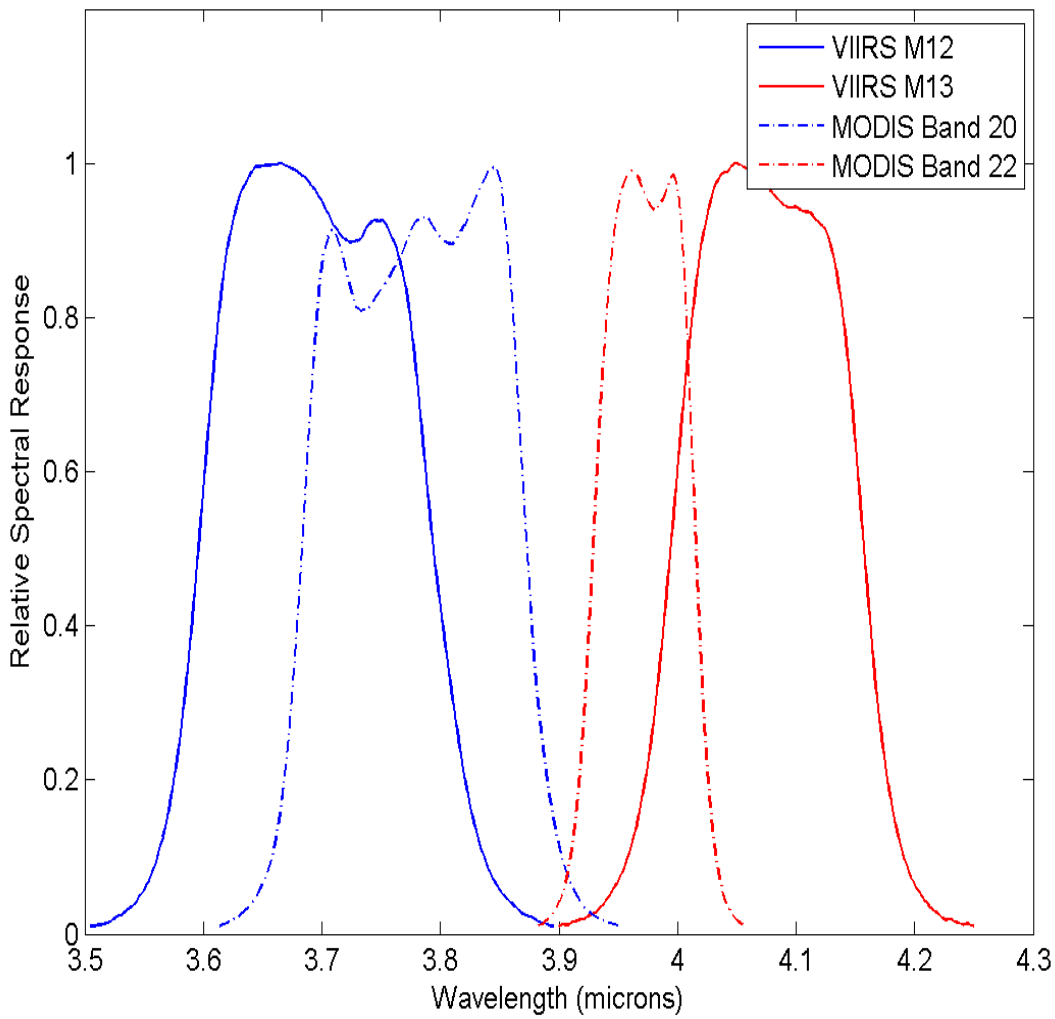

Figure 3-21. Relationship between the relative spectral responses for VIIRS bands M12 & M13 and those for MODIS bands 20 & 22

Use or disclosure of data contained on this page is subject to the export restriction(s) on the title page of this document.

D45702, A. PDMO Released: 2009-02-18 (VERIFY REVISION STATUS)
PDMO

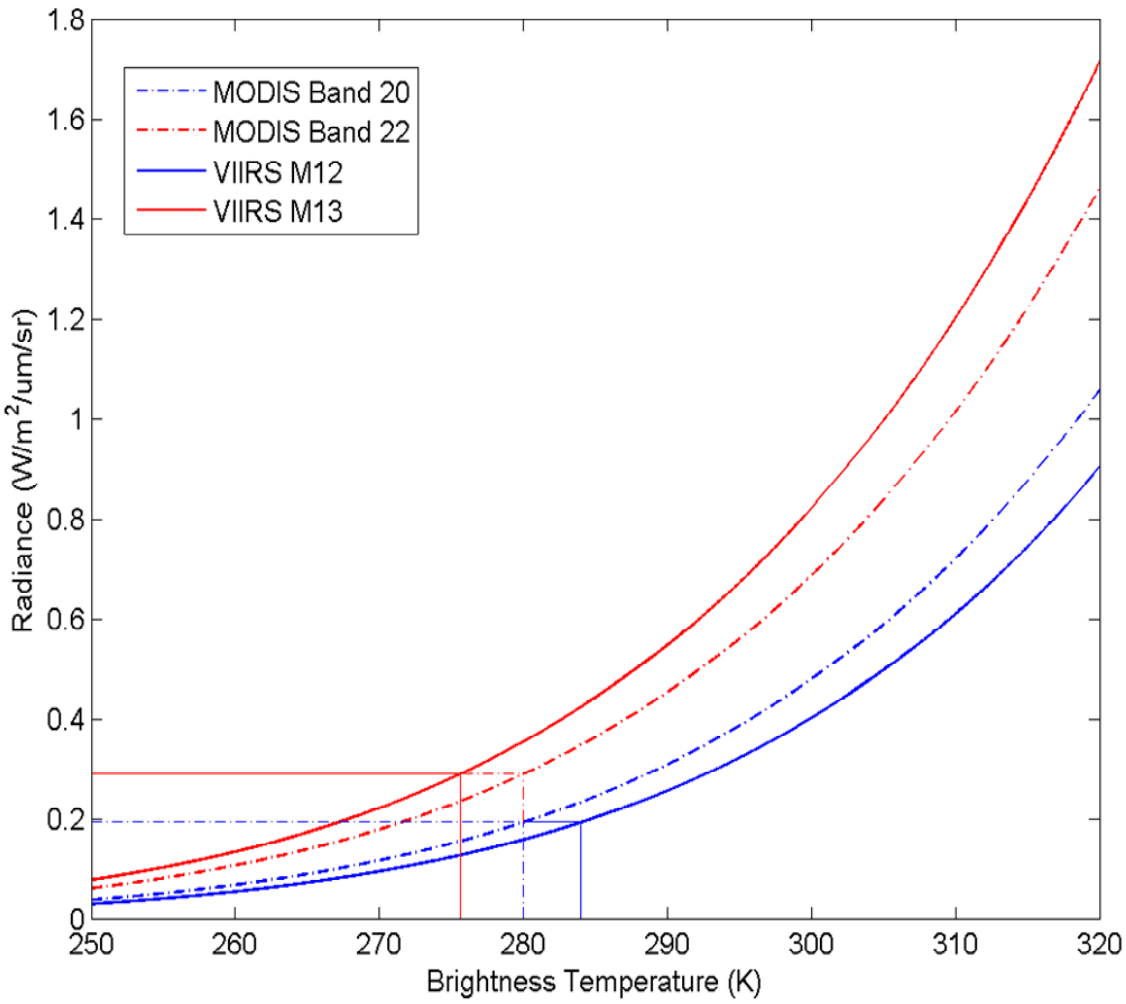

Figure 3-22. Illustration of problem with SDR calibration code brightness temperatures computed from MODIS radiances using VIIRS radiance-to-brightness temperature LUTs

Use or disclosure of data contained on this page is subject to the export restriction(s) on the title page of this document.

D45702, A. PDMO Released: 2009-02-18 (VERIFY REVISION STATUS)
PDMO

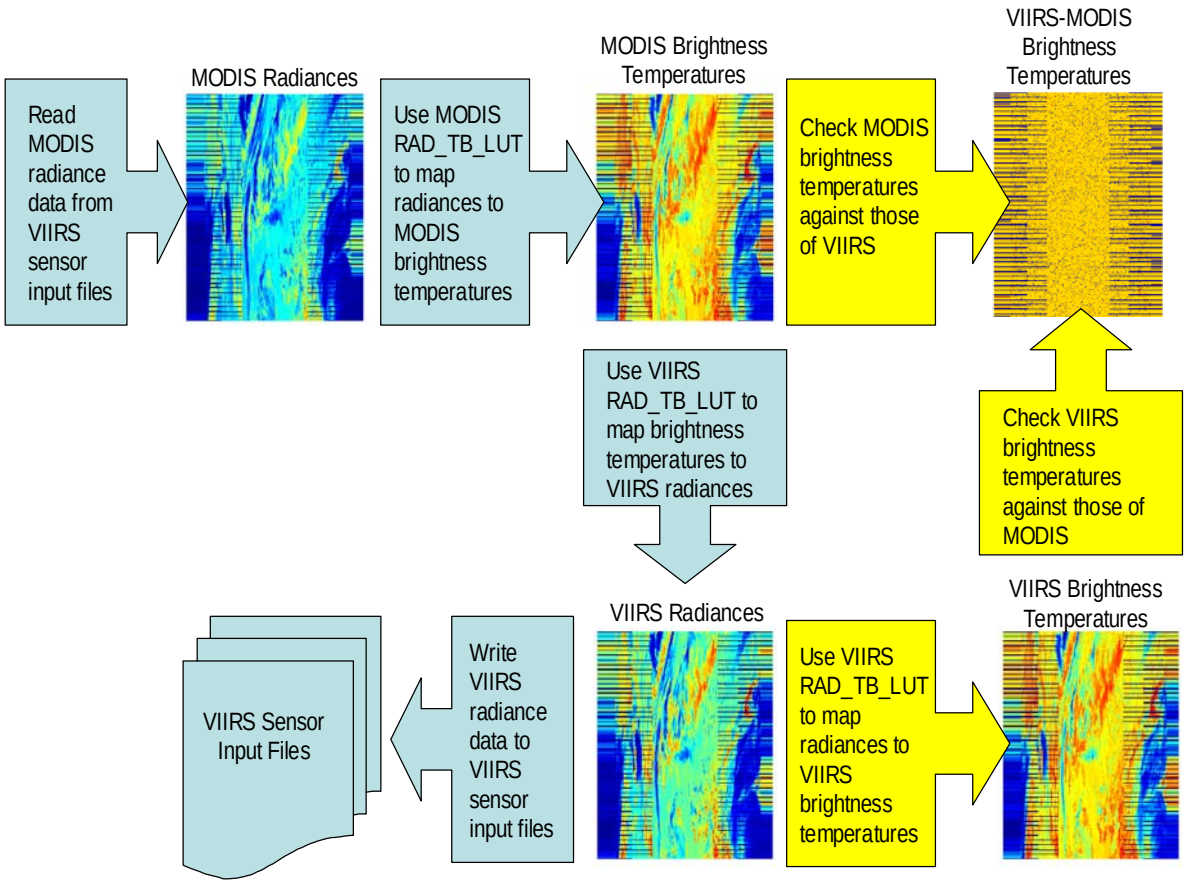

Figure 3-23. Approach to adjusting and checking radiances for VIIRS thermal-emissive bands

Use or disclosure of data contained on this page is subject to the export restriction(s) on the title page of this document.

D45702, A. PDMO Released: 2009-02-18 (VERIFY REVISION STATUS)
PDMO

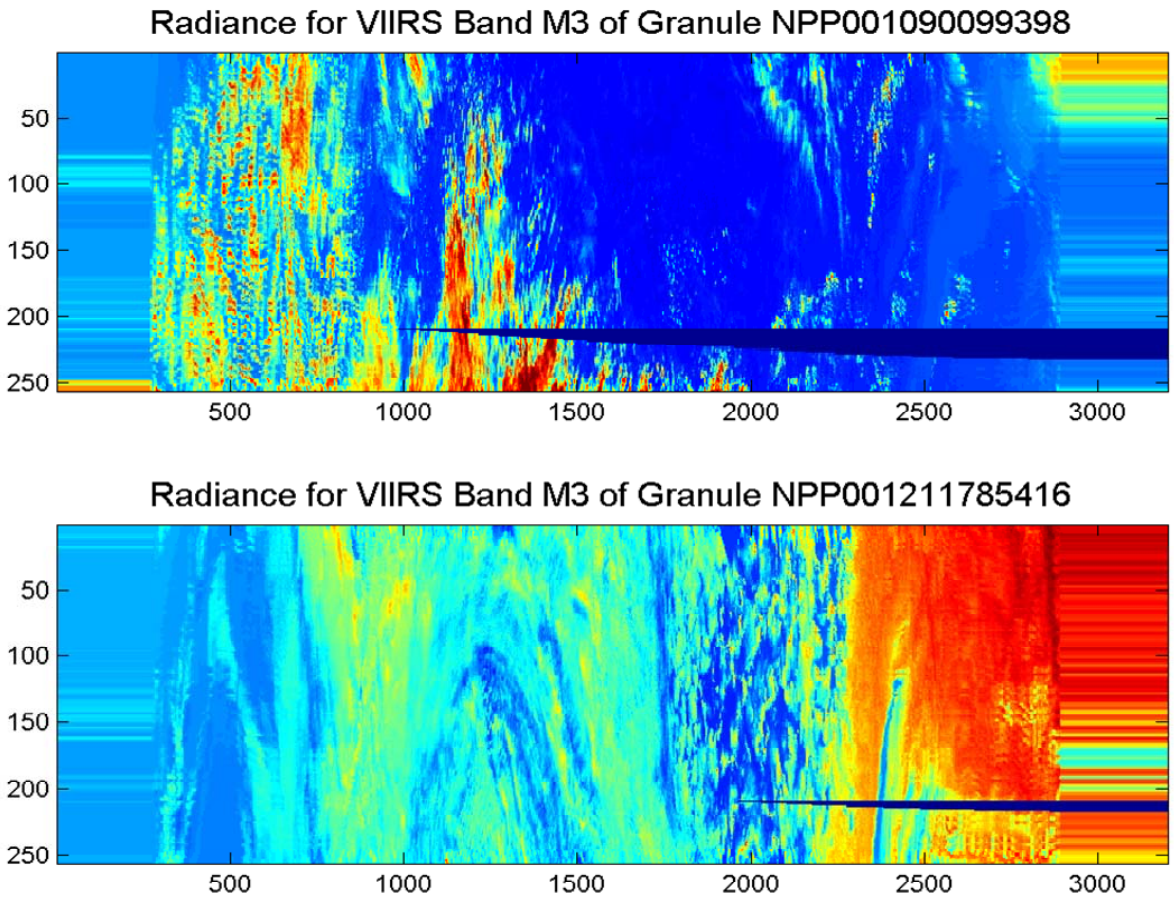

Figure 3-24. Examples of granules with problems in the MODIS to VIIRS spatial resampling

Use or disclosure of data contained on this page is subject to the export restriction(s) on the title page of this document.

D45702, A. PDMO Released: 2009-02-18 (VERIFY REVISION STATUS)
PDMO

4.0 SPECIAL GLOBAL TEST DATASETS FOR VERIFYING THE ACO/OCC ALGORITHMS

As described in the VIIRS Chain Test Report – Testing Process, Overview and SDR Verification, D44198, a new coupled ocean-atmosphere RTM capability, HydroMOD, was developed to generate global synthetic datasets for testing the ACO and OCC EDR algorithms. HydroMOD computes BRDFs at the ocean surface for both the water-leaving and surface-reflected contributions to the upwelling radiance. These BRDFs are used with an atmospheric RTM (MODTRAN or in one case 6S) to couple the separate ocean and atmosphere radiative transfer.

The in-water radiative transfer model used in HydroMOD is based on HydroLight. It computes a water-leaving BRDF based on a combination of measured and modeled ocean IOPs. The details behind the approach for generating realistic IOPs for the ocean pixels in the global synthetic dataset are described in the HydroMOD Final Report, the reference to which is provided in the chain test report cited above. However for the sake of completeness, a brief description is also provided here. In short, the Bricaud database was used with internal models in HydroMOD to generate realistic IOPs, including the realistic variability in the particle absorption and scattering spectra and the covarying CDOM absorption. The database consists of 1,129 measured particle absorption spectra (phytoplankton and detritus), ranging between 400 and 700 nm, along with the corresponding chlorophyll and chlorophyll-a concentrations. The other IOP contributors to the in-water scattering and absorption are based on State-of-Science models for CDOM absorption and particle scattering that are tied to the particle absorption and total chlorophyll concentration for each point. While the measured particle absorption spectra include the variability found in nature, random variability has to be added to the predicted CDOM absorption and particle scattering for each chlorophyll concentration and particle absorption spectrum taken from the Bricaud database. This process, described in much greater detail in the previously mentioned HydroMOD Final Report, produces a complete set of wavelength-dependent IOPs for each ocean pixel, which are subsequently used in the ocean radiative transfer. These same IOPs have been convolved with the relative spectral response functions for VIIRS bands M1-M5 to produce the band-averaged total absorption, due to particles (phytoplankton and detritus), CDOM and water, and the corresponding band-averaged total scattering. These IOPs, along with the total chlorophyll and chlorophyll-a concentrations then serve as “truth” for the corresponding retrieved products from the OCC algorithm.

The remote sensing reflectance is the other retrieved product (from the ACO algorithm) for which a truth value needs to be supplied. Unfortunately, this apparent optical property (AOP) is not directly available from the coupled ocean-atmosphere model. However, it can be reasonably approximated by the hemispherical-directional reflectance factor (HDRF) computed from the water-leaving component of the upwelling BRDF, since this BRDF is not overly sensitive to the angular distribution of the downwelling irradiance just beneath the ocean surface. The accuracy of this approximation has been examined by actually computing the remote sensing reflectance using HydroLight (with its simplistic atmospheric radiative transfer model) and comparing this with that based on the HDRF. The largest difference in RSR occurs

Use or disclosure of data contained on this page is subject to the export restriction(s) on the title page of this document.

D45702, A. PDMO Released: 2009-02-18 (VERIFY REVISION STATUS)
PDMO

for a solar zenith angle of 0 degree, which is also the zenith angle used for computing the RSR, so it is not surprising that the largest error occurs for this angle. The accuracy improves with decreasing visibility, as the irradiance distribution at the surface becomes increasingly isotropic. Like with the other IOPs, the wavelength-dependent RSR is convolved with the instrument line shape for each VIIRS band from M1 to M5, producing the corresponding band-averaged RSR.

4.1 New Global Synthetic and *In Situ* Datasets

4.1.1 Datasets for Assessing the Performance of the VIIRS OCC Algorithm

To assess the standalone performance of the OCC algorithm we have used a combination of global synthetic and *in situ* IOP-AOP datasets. These datasets contain biogeochemical values (e.g., chlorophyll and chlorophyll-a concentrations), absorption and scattering IOP values, and AOP values such as the spectral water-leaving radiance, surface irradiance, and remote-sensing reflectance. This information plus auxiliary values of latitude, longitude and SST are all that are required to assess the standalone performance of the OCC algorithm.

The NGST synthetic IOP-AOP dataset used to test the OCC algorithm is derived from the normal Global Synthetic Dataset described in Section 2.1 of this report. One of the key components to the coupled ocean-atmosphere RTM described in that section is the Hydrolight-BRDF or H-BRDF ocean RTM developed for NGST by Sequoia Scientific. H-BRDF uses the core code of Hydrolight to generate an ocean BRDF by cycling the sun through different locations in a black sky, generating the incident collimated irradiances necessary in defining the ocean BRDF. Given a set of ocean IOPs and the near-surface wind speed, H-BRDF outputs separate BRDFs for computing the water-leaving, surface reflected, and total upwelling radiances at the ocean surface. As will be discussed shortly, the water-leaving BRDF can be used to provide a relatively good estimate of the remote sensing reflectance at the ocean surface.

For realistic evaluation of the ACO and OCC algorithms, it is necessary to include the inherent variability in IOPs that occur in the ocean. The Bricaud database was used for providing the measured relationship between the particle absorption spectra and chlorophyll concentrations. This database contains 1,129 measured, chlorophyll-specific particle absorption spectra (phytoplankton & detritus), as well as the corresponding total chlorophyll and chlorophyll-a concentrations. Measurements are for tropical and mid-latitude Case 1 waters, with a mix of mesotrophic, oligotrophic, and eutrophic water types. The majority of chlorophyll values are less than 1mg/m^3, as shown by the distribution of chlorophyll concentration in Figure 4-1. The natural variability in the particle absorption spectra for a given chlorophyll concentration is already contained in the measured data, so no added random noise was needed to represent what's found in nature. For example, from Figure 4-1 we see that the measured a_p spectra near a chlorophyll concentration of 0.2mg/m^3 agrees "on average" with the new particle absorption model from Bricaud et al. while also providing the natural variability about this average value. The CDOM absorption and particle scattering values, on the other hand, are based on "average" IOP models, requiring that the correct amount of random variability be added to represent nature. To add the desired variability to these values, the coefficients of the "average" IOP models for these

Use or disclosure of data contained on this page is subject to the export restriction(s) on the title page of this document.

D45702, A. PDMO Released: 2009-02-18 (VERIFY REVISION STATUS)
PDMO

quantities have been replaced by normally-distributed random variables that have been constrained to reproduce the commonly observed ranges for these variables. For example, the standard model for co-varying CDOM absorption, $a_{CDOM}(\lambda) = 0.2\left[a_w(440) + a_p(440)\right]\exp\left[-0.014(\lambda - 440)\right]$, has been revised as $\tilde{a}_{CDOM}(\lambda) = F_{CDOM}\left[a_w(\lambda_0) + a_p(\lambda_0)\right]\exp\left[-S_{CDOM}(\lambda - \lambda_0)\right]$, with the random value of S_{CDOM}, the spectral slope parameter, assumed to have a mean value of 0.014 and a standard deviation of 0.002. With less information about the range of F_{CDOM}, the fraction of total absorption due to CDOM at λ_0, it was assumed to be normally distributed with μ_F=0.2 and σ_F=0.02. Figure 4-2a shows the variability in CDOM absorption resulting from this revision of the average model. Similarly, Figure 4-2b shows the effect of the revision of the recent particle scattering model by Morel et. al, (2002) to include the expected variability in the particle scattering. The spread of points in this figure compares visually with that found for Case 1 waters by Gordon and Morel (1983). Finally, the scattering phase function describing the directionality of the particle scattering was set as the weighted sum of small and large-particle phase functions, with the partitioning based on the chlorophyll concentration, from

- $$\beta_p(\Psi, Chl) = \alpha_s(Chl)\beta_s(\Psi) + [1 - \alpha_s(Chl)]\beta_l(\Psi),$$
  $$where\ \alpha_s = 0.855[0.5 - 0.25\log_{10} Chl]$$

Given these models, a large number of spectrally-dependent water-leaving BRDFs were generated by H-BRDF from the 1,129 samples of the Bricaud database, where for each sample we include a number of realizations of co-varying CDOM absorption and particle scattering as well as wind speeds of 5 and 11m/s. These water-leaving BRDFs were used to provide the corresponding values of the remote sensing reflectance via the hemispherical-directional reflectance factor (i.e., R_{rs} ~ HDRF/π). The R_{rs} computed in this fashion are typically accurate to within 5-8% (see Figure 4-3a). More importantly, the spectral ratios of R_{rs} that are actually used by the OCC algorithm are accurate to within a few percent, as shown in Figure 4-3b. The resulting wavelength-dependent R_{rs} were integrated with the relative spectral response function for VIIRS bands M1-M5 to provide the band-dependent R_{rs} input to the OCC algorithm. The input IOPs used in generating each R_{rs} were also convolved with these spectral response functions to produce the band-averaged total absorption, due to particles (phytoplankton and detritus), CDOM and water, and the corresponding band-averaged total scattering. These band-averaged IOPs, along with the total chlorophyll and chlorophyll-a concentrations then serve as “truth” for the corresponding retrieved products from the OCC algorithm.

A second set of synthetic IOP-AOP data used for assessing the performance of the IOP retrievals was obtained from the International Ocean-Color Coordinating Group, IOCCG, (http://www.ioccg.org/groups/OCAG_data.html). This dataset contains 1000 points (500 each for solar zenith angles of 30^0 and 60^0) of R_{rs} computed with Hydrolight for a given set of IOPs. Like with the previously described NGST synthetic dataset, the

Use or disclosure of data contained on this page is subject to the export restriction(s) on the title page of this document.

D45702, A. PDMO Released: 2009-02-18 (VERIFY REVISION STATUS)
PDMO

IOPs for the IOCCG synthetic data were simulated with optical and bio-optical parameters and models tied to actual field observations. The resulting IOP-AOP dataset covers a wide range of the variations found in natural waters. The details behind this dataset can be found at the above website and in IOCCG Report Number 5.

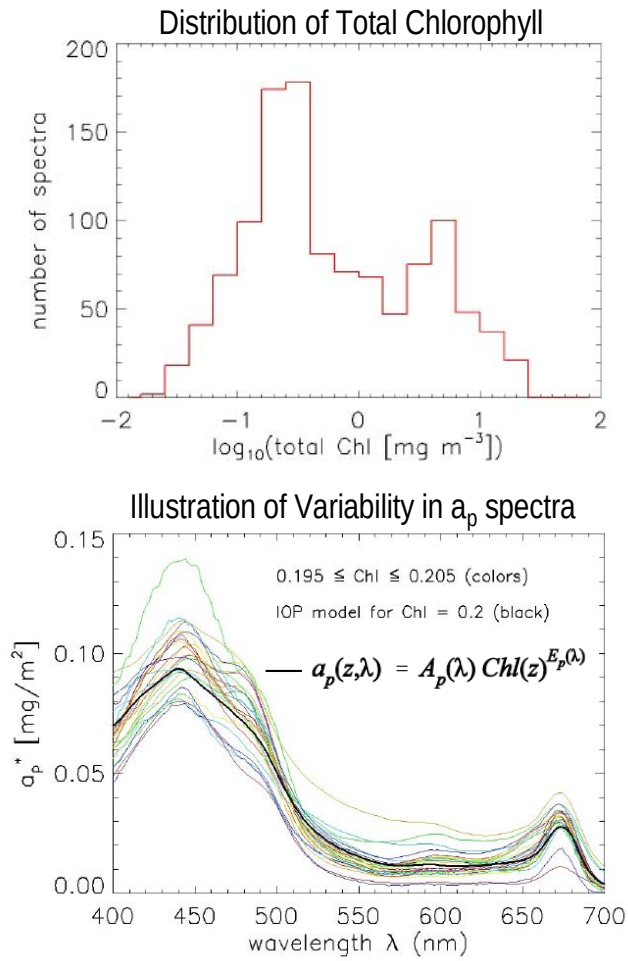

Figure 4-1. Chlorophyll concentration and specific absorption spectra from Bricaud database

Use or disclosure of data contained on this page is subject to the export restriction(s) on the title page of this document.

D45702, A. PDMO Released: 2009-02-18 (VERIFY REVISION STATUS)
PDMO

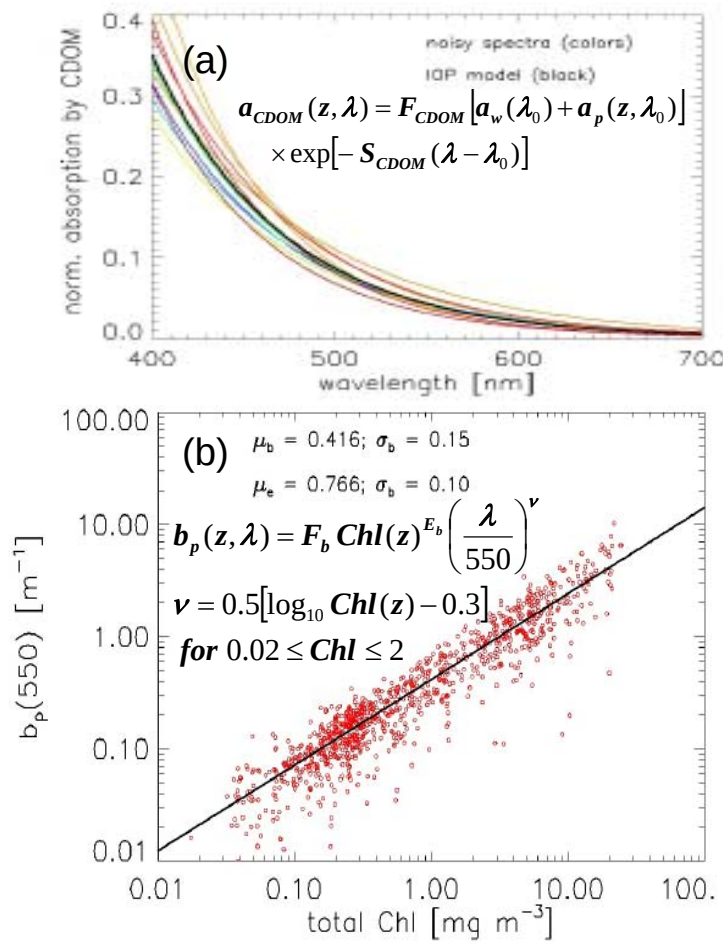

Figure 4-2. Addition of variability to other absorption and scattering IOPs

Use or disclosure of data contained on this page is subject to the export restriction(s) on the title page of this document.

D45702, A. PDMO Released: 2009-02-18 (VERIFY REVISION STATUS)
PDMO

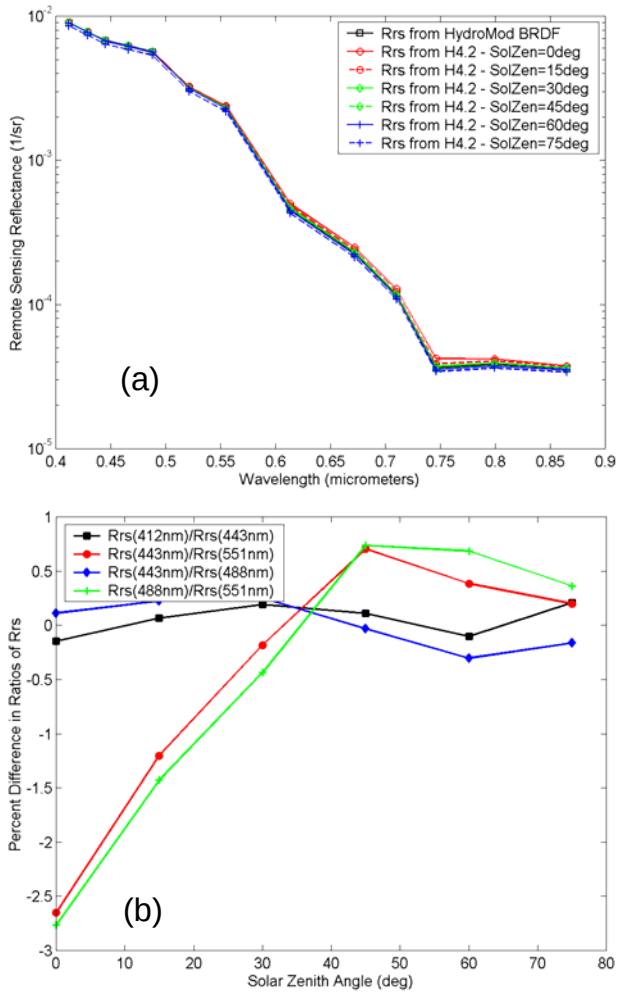

Figure 4-3. Accuracy of remote-sensing reflectance computed from water-leaving BRDF

Use or disclosure of data contained on this page is subject to the export restriction(s) on the title page of this document.

D45702, A. PDMO Released: 2009-02-18 (VERIFY REVISION STATUS)
PDMO

In addition to the previously described synthetic datasets, two sources of *in situ* IOP-AOP data were also used to assess the performance of the VIIRS OCC algorithm on real data. The NASA bio-Optical Marine Algorithm Dataset (NOMAD), Version 1.3, and the IOCCG *In Situ* Dataset. Figure 4-4 shows the locations where the IOP-AOP measurements were taken and the distribution of chlorophyll-a concentration for each dataset.

The NOMAD dataset consists of approximately 3,500 samples; however, not all samples contain the necessary IOP-AOP measurements needed for assessing OCC performance. The dataset was filtered to select those samples with valid values for the spectral water-leaving radiance and spectral surface irradiance in VIIRS bands M1-M4 (i.e., NOMAD wavelengths of 411, 443, 489 and 555nm), as well as chlorophyll-a concentration and SST. This reduced the number of samples to just 877. The remote-sensing reflectance was generated for each of the 877 valid samples, along with the "truth" chlorophyll-a and ancillary data (i.e., SST and latitude/longitude for determining the NDT) used by the VIIRS OCC algorithm. While the NOMAD dataset also contains a limited number of samples with IOP-a and IOP-b truth, there isn't a sufficient number to provide a statistical assessment of retrieval performance of these IOPs, so this dataset was only used for assessing the performance of the chlorophyll-a retrieval.

The IOCCG in situ dataset is an extraction from NASA's SeaWiFS Bio-optical Archive and Storage System and was used for the cross-comparison of IOP algorithms reported in IOCCG Report No. 5. This dataset of 656 samples provided values for the remote-sensing reflectance in VIIRS bands M1-M4 (i.e., SeaWiFS wavelengths of 412, 443, 490 and 555nm), as well as chlorophyll-a and band-dependent values of IOP-a along with its components (a_{ph} and a_{dg}). In addition to the R_{rs}, "truth" chlorophyll-a, and IOP-a information, ancillary data (i.e., SST and latitude/longitude for determining the NDT) used by the VIIRS OCC algorithm was also obtained, with SST values coming from global monthly-mean OISST data obtained from the Distributed Oceanographic Data System (DODS).

Use or disclosure of data contained on this page is subject to the export restriction(s) on the title page of this document.

D45702, A. PDMO Released: 2009-02-18 (VERIFY REVISION STATUS)
PDMO

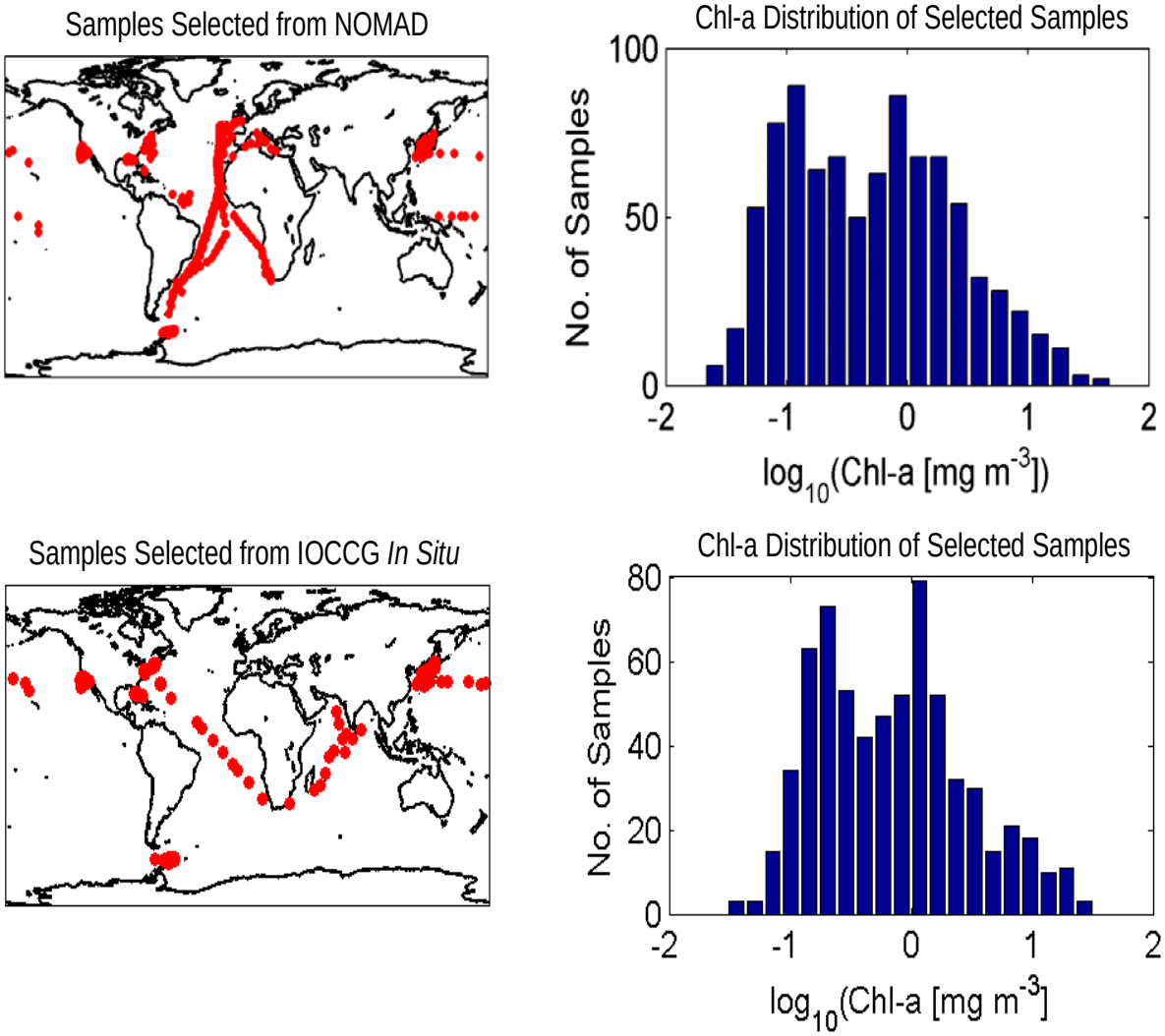

Figure 4-4. Real *in situ* data from NOMAD and IOCCG for testing the OCC algorithm

Use or disclosure of data contained on this page is subject to the export restriction(s) on the title page of this document.

D45702, A. PDMO Released: 2009-02-18 (VERIFY REVISION STATUS)
PDMO

4.1.2 Dataset for Assessing the Performance of the VIIRS ACO Algorithm

A new global synthetic dataset was also developed to debug and assess the performance of the VIIRS ACO algorithm and the ACO/OCC algorithm chain. The new synthetic data is based on the same RTM-generated LUTs and models used in the ACO code, which greatly facilitated the debugging of the ACO code by allowing us to check each step of the atmospheric correction process. However, this approach required us to perform an independent verification of the ACO LUTs and models used in generating the synthetic test data. Some of the details of this verification will be described below. Nevertheless, it should be noted that the reported performance of the ACO algorithm and ACO/OCC algorithm chain does not include the error due to the RTM itself, which is why the independent verification of the LUTs and models used by the ACO code was important

To generate the TOA radiance for a coupled ocean-atmosphere system, we followed the development in Gordon and Wang (1992), writing the TOA radiance as,

$$L_t(\lambda) = L_r(\lambda) + L_a(\lambda) + L_{ra}(\lambda) + T(\lambda)L_g(\lambda) + t(\lambda)L_{wc}(\lambda) + t(\lambda)L_W(\lambda),$$

Where L_r, L_a, and L_{ra} are the radiance contributions that result from multiple scattering by air molecules (Rayleigh scattering) in the absence of aerosols, multiple scattering by aerosols in the absence of air, and multiple scattering that includes just the interaction between molecular and aerosol scattering, respectively. This global synthetic dataset includes band-averaged spectral radiances at top-of-atmosphere from all sources except direct sun glitter, L_g, (which will, for the most part, be masked by both the 36 degree and wind-based exclusion zones of the VIIRS cloud mask) and whitecaps, L_{WC}. Because of concern about the sun-glitter correction algorithm currently being used in the ACO algorithm, pixels for which the sun-sensor geometry would result in any solar-contamination (i.e., normalized sun glitter radiance greater than 10^{-4}) were filtered out. The remaining terms contributing to the TOA radiance are the water-leaving radiance, L_W, and atmospheric diffuse transmittance, t. These will be discussed in more detail below.

The contributions to the TOA radiance from molecular (Rayleigh) and aerosol scattering were based on the “verified” Rayleigh and Aerosol Radiance LUTs used by the ACO code and generated from a vector-RTM that fully models polarization. The Rayleigh radiance LUTs for the seven VIIRS ocean color bands (M1-M7) were generated by Menghua Wang for various solar-sensor geometry and ocean surface wind speeds. Computations were carried out using the vector radiative transfer theory (accounting for polarization) for a Rayleigh-scattering atmosphere overlying a rough Fresnel-reflecting ocean surface. The ocean surface roughness, which depends on wind velocity, is modeled based on the assumption that the wind-ruffled sea surface consists of a collection of individual facets obeying the Cox-Munk slope statistics. As an approximation, the surface roughness is modeled with a further assumption that the wind-ruffled surface slope distribution is independent of the wind direction.

Use or disclosure of data contained on this page is subject to the export restriction(s) on the title page of this document.

D45702, A. PDMO Released: 2009-02-18 (VERIFY REVISION STATUS)
PDMO

The aerosol radiance LUTs compute the TOA aerosol and Rayleigh-aerosol interaction radiance, $L_a + L_{ra}$, for a given aerosol model, aerosol optical thickness, solar-zenith, sensor-zenith, and relative azimuth angles. These LUTs were generated by Menghua Wang using a vector radiative transfer model (including polarization) for a two-layer atmosphere (aerosols at the bottom mixed with 22% of molecules) bounded by a flat Fresnel reflecting ocean surface. The LUTs were generated with the 12 aerosol models from Shettle and Fenn that are currently used for the SeaWiFS and MODIS data processing. They are Oceanic with relative humidity (RH) of 99% (denote O99), Maritime with RH of 50%, 70%, 90%, and 99% (M50, M70, M90, and M99), Coastal with RH of 50%, 70%, 90%, and 99% (C50, C70, C90, and C99), and Tropospheric with RH of 50%, 90%, and 99% (T50, T90, T99). The LUTs are for the solar zenith angles up to 80 (Deg.).

The COART RTM was used to verify the components of the path radiance, L_r, L_a, and L_{ra}, provided by the ACO LUTs. The radiance from the Rayleigh and Aerosol+Rayleigh radiance LUTs has been compared to that from a scalar RTM, COART, to provide independent verification of the LUTs and our use of them. It's assumed that the VIIRS sensor will be insensitive to the polarization state of the backscattered radiance, so that we are only interested in the scalar radiance or total intensity from the Stokes vector. Based on other comparisons between scalar and vector RTMs reported in the literature, the comparison of the scalar radiance from the ACO LUTs against the radiance from a scalar RTM (e.g., COART) should be good to within ~5-8 percent. COART (Coupled Ocean Atmosphere Radiative Transfer) is based on a special version of DISORT, CDISORT, that allows for a change of media (e.g., atmosphere and ocean) in the solution of the equation of radiative transfer. It treats ocean layers as additional atmospheric layers, but with a different refractive index and optical properties (e.g., scattering by phytoplankton instead of aerosols). As a result, no artificial boundary condition is needed at the ocean-atmosphere interface, whereas DISORT has to consider the ocean surface as a boundary. Treatment of the wind-roughened atmosphere-ocean interface is based on the 1-D Cox-Munk surface slope distribution, which is related to the near-surface wind speed by $\sigma^2 = 0.003 + 0.00512W$. The model also includes both multiple reflections and shadowing among the surface wave facets.

Comparisons of the TOA Rayleigh radiance from the ACO LUTs with that from COART for a pure molecular atmosphere are shown for a variety of solar-sensor angles in Figures 4-5 through 4-8. We see that the relative difference is always within 8%, as expected, and typically less than a few percent. Figures 4-5 through 4-7 are for a flat ocean surface, for which neither the Rayleigh LUT nor COART includes the direct sun glitter radiance contribution; although both codes include the multiple-scattered radiation between the surface and the atmosphere. For a wind-roughened ocean surface, COART does include the direct sun glitter radiance contribution. This is seen in Figure 4-8, which is for a wind speed of 3m/s. To compare COART with the Rayleigh radiance LUT for a rough ocean surface, we filter out those sun-sensor angles for which the normalized sun glitter radiance is greater than 10^{-4}. Upon comparison of the normalized radiance from the two models for the angles that remain, we find relative errors similar to those found for the flat ocean case with the same sun-sensor geometry, Figure 4-5.

Use or disclosure of data contained on this page is subject to the export restriction(s) on the title page of this document.

D45702, A. PDMO Released: 2009-02-18 (VERIFY REVISION STATUS)
PDMO

To verify the aerosol and aerosol-Rayleigh radiance LUTs with COART, we first needed to ensure that COART is using the same aerosol optical properties as those used in generating the ACO LUTs. While both codes offer the Maritime aerosol models of Shettle and Fenn, it's not clear what value of relative humidity is employed with the COART model; this makes comparisons with the corresponding model from the aerosol radiance LUT problematic. However, COART allows the user to input the aerosol optical properties (i.e., aerosol optical thickness, single-scattering albedo, and asymmetry parameter) at up to 10 wavelengths. It also allows inputting of the full Mie scattering phase function instead of the Henyey-Greenstein approximation to the phase function based on the asymmetry parameter. An example of the values used for a Maritime aerosol at 70% relative humidity and with an AOT at 865nm of 0.12 is shown in Figure 4-9. Figure 4-10 shows the results of the TOA aerosol and aerosol-Rayliegh radiance from the ACO LUTs compared with that computed by the COART RTM for a flat ocean surface, a solar zenith angle of 30^0, relative azimuths of 0^0 and 90^0, and an AOT at 865nm of 0.3. Except at the specular reflection point in the plane of incidence and at large viewing angles, there is a general agreement to approximately 4%. We expected that the error in the plane of incidence within some range of angles about the specular reflection point would not be particularly accurate. This is due to inaccuracies with the ACO Aerosol Radiance LUT for these angles. Note that this is not a problem for the ocean color algorithm since these angles are within the solar glint exclusion region. The ACO LUT is also not expected to be accurate at large viewing angles, but these are never realized in the VIIRS scanning geometry. Finally, Figures 4-11 and 4-12 show comparisons of the TOA total path radiance (Rayleigh, aerosol and aerosol-Rayleigh interaction) from the ACO LUTs to that from the COART RTM for a flat ocean surface and as a function of sensor zenith angle for a solar zenith angle of 30^0 and relative azimuths of 0^0, 90^0, 130^0 and 180^0. Looking at those solar-sensor angles for which ocean color will be retrieved, we find that the total TOA path radiance from COART agrees with that of the ACO LUTs to within a few percent, as expected.

The water-leaving radiances, L_W, for this dataset came from the NASA Bio-optical Marine Algorithm Dataset (NOMAD), v1.3. There is a minor inconsistency in that these radiances are not based on the spectral surface irradiances corresponding to the scene conditions that give rise to the other components of the TOA radiance. Rather, they are consistent with the atmospheric and surface conditions of the NOMAD dataset. They are also only available as band-averaged radiances at center wavelengths that are close to, but not the same as, those of the VIIRS ocean bands. However, neither of these limitations should significantly impact the performance testing of either the ACO or OCC algorithms with this data.

The diffuse transmittance, t, computed from the Diffuse Transmittance LUT of the ACO code is used to transport the water-leaving radiance to the TOA. It is also used in generating the remote sensing reflectance from the water-leaving reflectance. The diffuse transmittance LUTs compute the diffuse transmittance for a given Rayleigh optical thickness, aerosol model and optical thickness, and solar or sensor zenith angle (depending on whether the diffuse transmittance in the sensor or solar direction is desired) for the 7 VIIRS ocean color bands. The LUTs follow the approach in Yang and Gordon (1997), where the diffuse transmittance is approximated by the exponential form

Use or disclosure of data contained on this page is subject to the export restriction(s) on the title page of this document.

D45702, A. PDMO Released: 2009-02-18 (VERIFY REVISION STATUS)
PDMO

$t(\lambda,\theta) = A(\theta)exp[-B(\theta)\tau_a]$, with the LUTs providing the coefficients $A(\theta)$ and $B(\theta)$ as a function of wavelength, aerosol model and solar or sensor zenith angle. The diffuse transmittance LUTs were generated by Menghua Wang using the vector radiative transfer (including the polarization) for the two-layer atmosphere (aerosols at the bottom mixed with 22% of molecules) bounded by a flat Fresnel reflecting ocean surface. They are based on the same 12 aerosol models used for generating the aerosol radiance LUTs.

An independent verification of the diffuse transmittance calculation in the ACO code was provided by the extended formulas in Wang (1999). For a general atmosphere composed of both air molecules and aerosols bounded by a Fresnel-reflecting ocean surface, the diffuse transmittance is well approximated by

$t(\lambda,\theta) = t_r(\lambda,\theta)\, t_a(\lambda,\theta)$, where,

$t_r(\lambda,\theta_V) \approx \exp[-C_r(\lambda,\theta)\tau_r(\lambda)/2\cos\theta]$ and

$t_a(\lambda,\theta_V) \approx \exp\{-a_0(\lambda)[1+\omega_a(\lambda)C_a(\lambda,\theta)]/\cos\theta\}$, with $a_0(\lambda) = [1-\omega_a(\lambda)F_a(\lambda)]\tau_a(\lambda)$ and

$F_a(\lambda) = \frac{1}{2}\int_0^1 P_a(\Theta,\lambda)\, d\cos\Theta,\ C_{r,a}(\lambda,\theta) \equiv Fitted\ \ Parameters$

For τ_a<0.6 and θ<60^0, this approximation calculates diffuse transmittance to within an accuracy of ~1%, typically with an accuracy of 0.5%. Figure 4-13 shows the results of comparing the diffuse transmittance from the ACO LUTs to that from the above model for a pure Rayleigh (i.e., molecular) atmosphere. It is interesting to note that even though the aerosol optical thickness is identically zero, there is still an effect due to the non-existent aerosol which depends on the aerosol model assumed. This is obviously the result of the diffuse transmittance LUT employed by ACO code, which is based on the simpler exponential approximation, $t(\lambda,\theta) = A(\theta)exp[-B(\theta)\tau_a]$, where A($\theta$) and B($\theta$) are pre-computed, fitted parameters in LUT for each of 12 aerosol models but which are independent of the AOT. The magnitude of this effect is negligible, less than 0.5%. Additional comparisons between the diffuse transmittance LUT and the above model are shown in Figures 4-14 and 4-15 for the low and high-end ranges of AOT used in generating the synthetic data.

Since the various LUTs in the ACO code do not include absorption by ozone, the TOA radiances need to be adjusted by the two-way ozone transmittance. The model in the ACO code that performs this calculation is straightforward and correct. However, there was an error in the ozone absorption coefficient at 555nm. After making the correction and adjusting some of the other ozone absorption coefficients, the comparison of the ozone transmittance from the ACO code to that computed from COART are now quite close, as shown in Figure 4-16.

Use or disclosure of data contained on this page is subject to the export restriction(s) on the title page of this document.

D45702, A. PDMO Released: 2009-02-18 (VERIFY REVISION STATUS)
PDMO

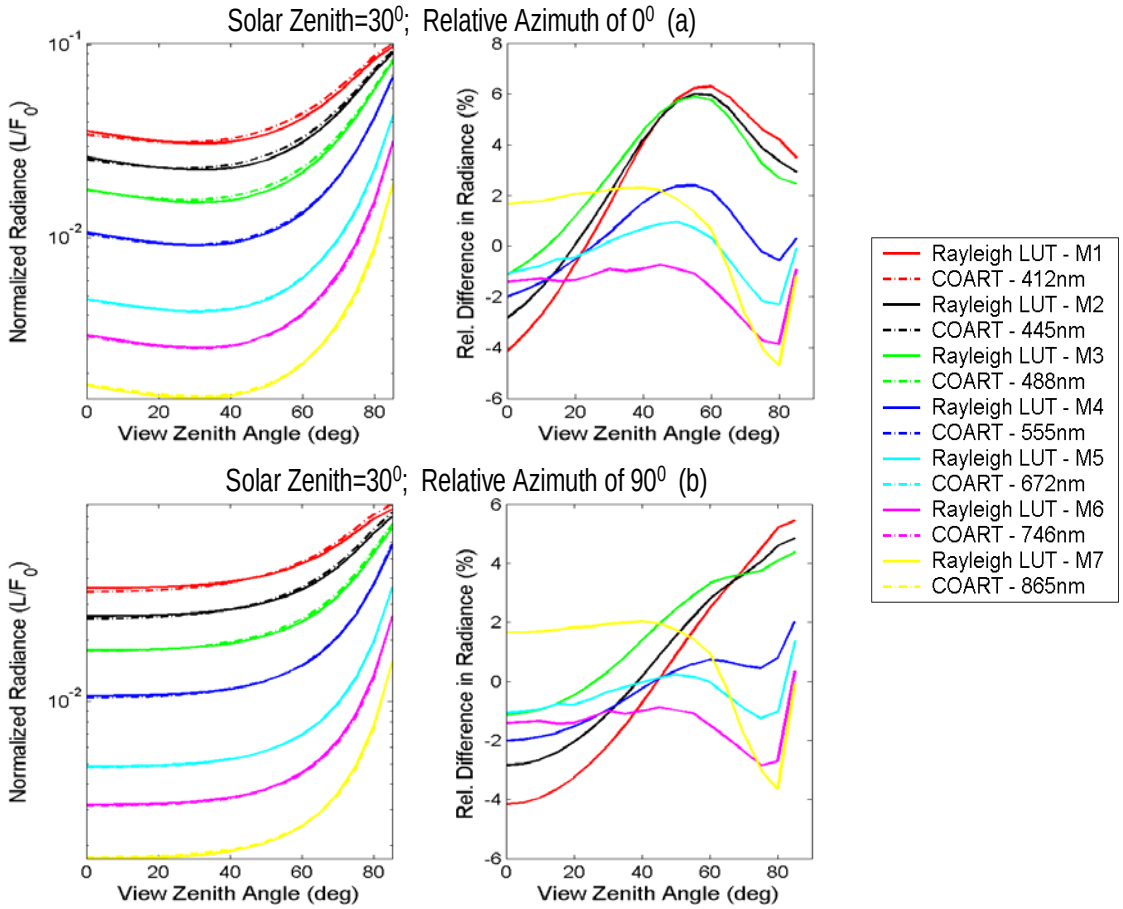

Figure 4-5. Comparison of TOA Rayleigh radiance from ACO LUT to COART RTM for a flat ocean surface as a function of sensor zenith angle for solar zenith angle of 30^0 and relative azimuths of 0^0 (a) and 90^0 (b)

Use or disclosure of data contained on this page is subject to the export restriction(s) on the title page of this document.

D45702, A. PDMO Released: 2009-02-18 (VERIFY REVISION STATUS)
PDMO

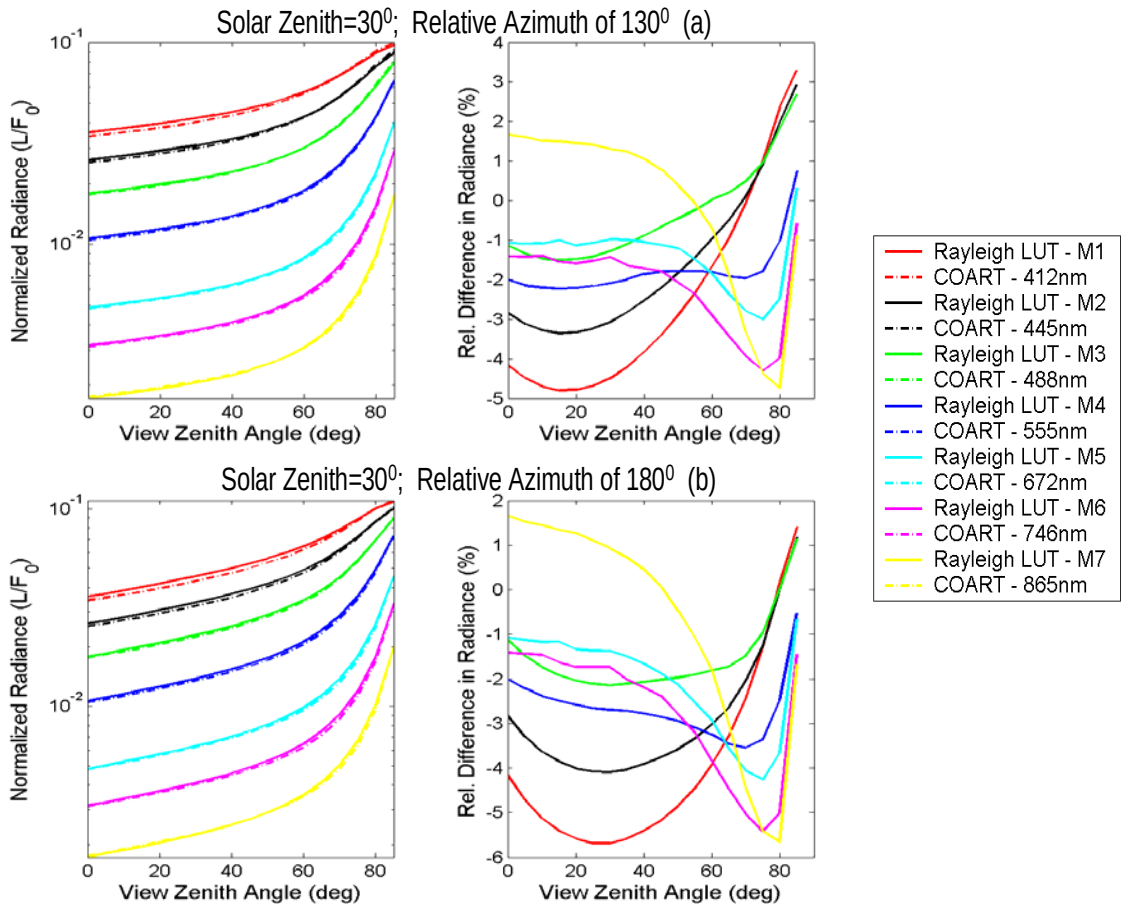

Figure 4-6. Comparison of TOA Rayleigh radiance from ACO LUT to COART RTM for a flat ocean surface as a function of sensor zenith angle for solar zenith angle of 30^0 and relative azimuths of 130^0 (a) and 180^0 (b)

Use or disclosure of data contained on this page is subject to the export restriction(s) on the title page of this document.

D45702, A. PDMO Released: 2009-02-18 (VERIFY REVISION STATUS)
PDMO

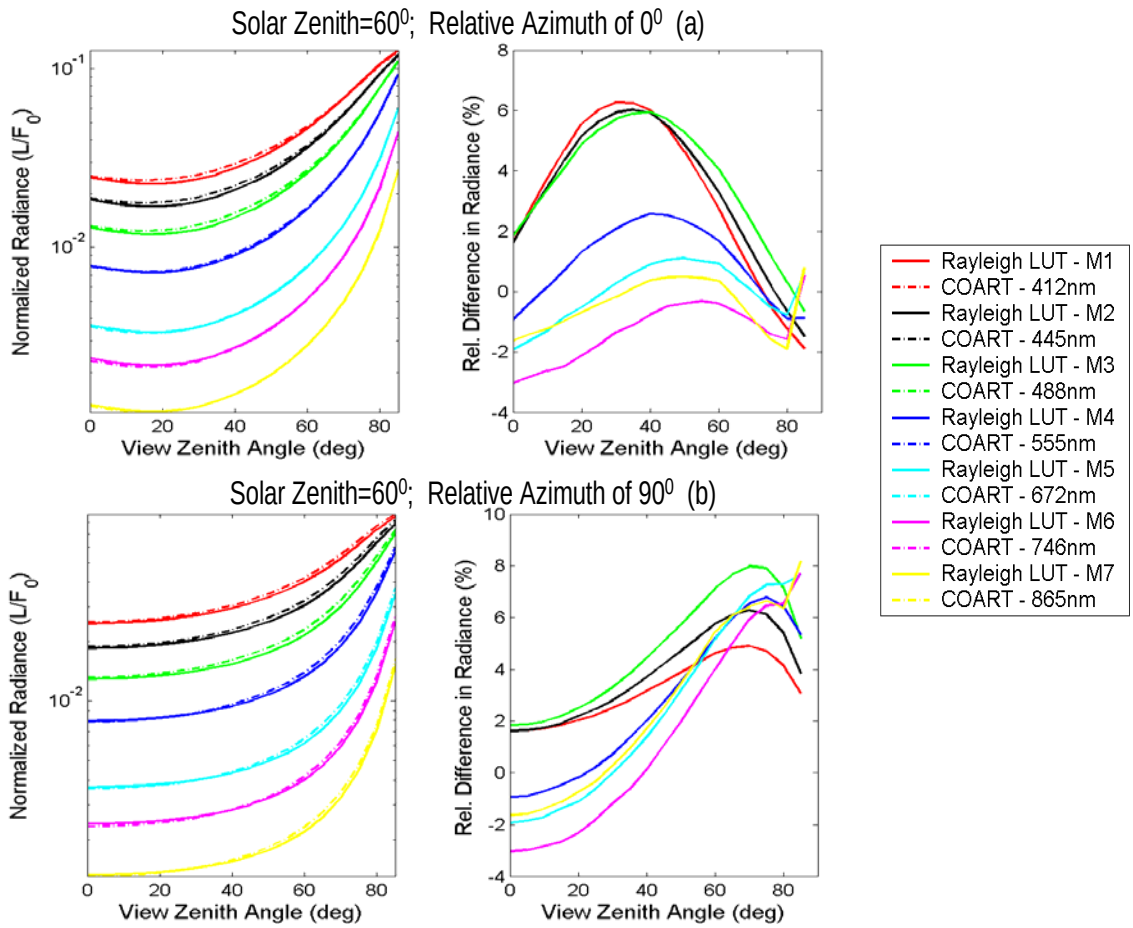

Figure 4-7. Comparison of TOA Rayleigh radiance from ACO LUT to COART RTM for a flat ocean surface as a function of sensor zenith angle for solar zenith angle of 60^0 and relative azimuths of 0^0 (a) and 90^0 (b)

Use or disclosure of data contained on this page is subject to the export restriction(s) on the title page of this document.

D45702, A. PDMO Released: 2009-02-18 (VERIFY REVISION STATUS)
PDMO

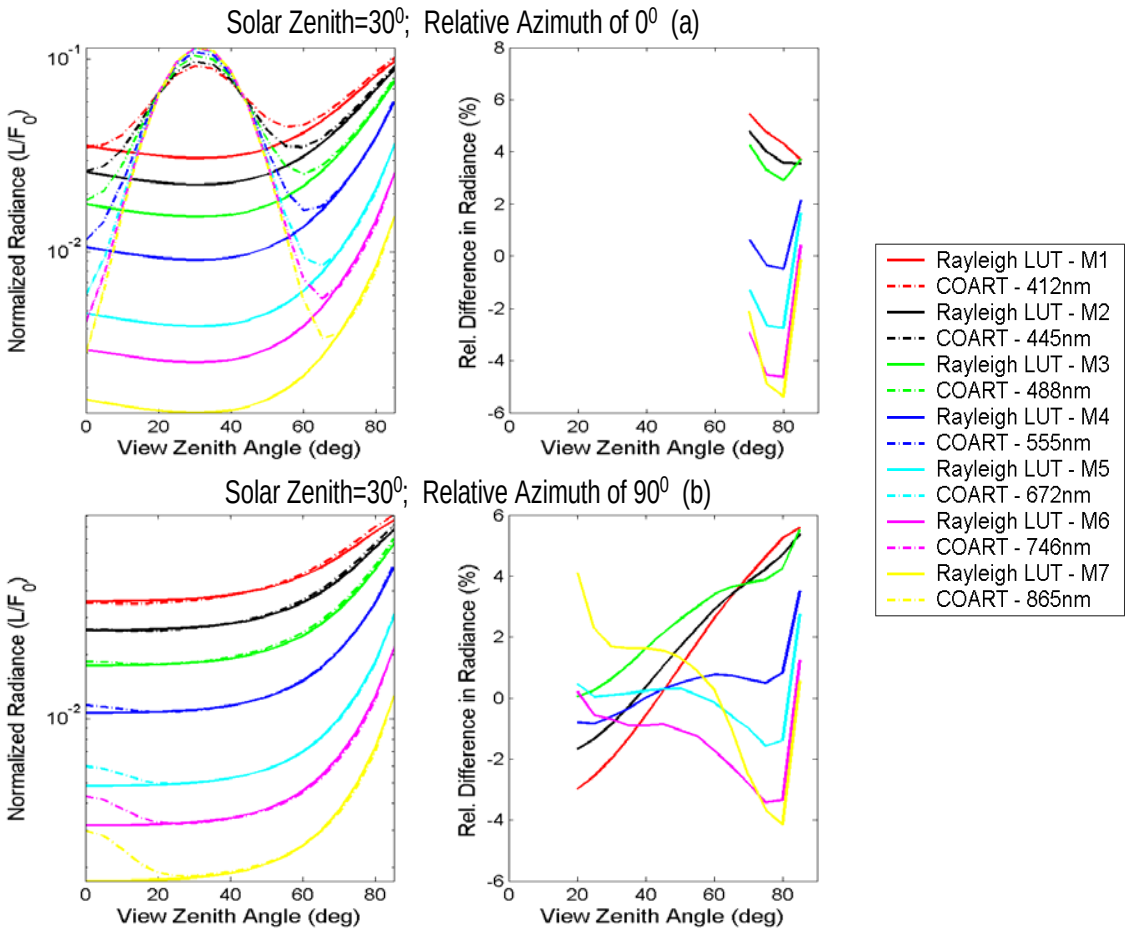

Figure 4-8. Comparison of TOA Rayleigh radiance from ACO LUT to COART RTM for a wind-roughened ocean surface as a function of sensor zenith angle for solar zenith angle of 30^0 and relative azimuths of 0^0 (a) and 90^0 (b)

Use or disclosure of data contained on this page is subject to the export restriction(s) on the title page of this document.

D45702, A. PDMO Released: 2009-02-18 (VERIFY REVISION STATUS)
PDMO

Wavelength	0.3750	0.4625	0.5500	0.6375	0.7250	0.8125	0.9000	0.9875	1.0750	1.1625
AOT	0.1664	0.1534	0.1435	0.1355	0.1288	0.1231	0.1181	0.1138	0.1099	0.1060
SSA	0.9840	0.9858	0.9870	0.9879	0.9877	0.9862	0.9850	0.9840	0.9833	0.9829

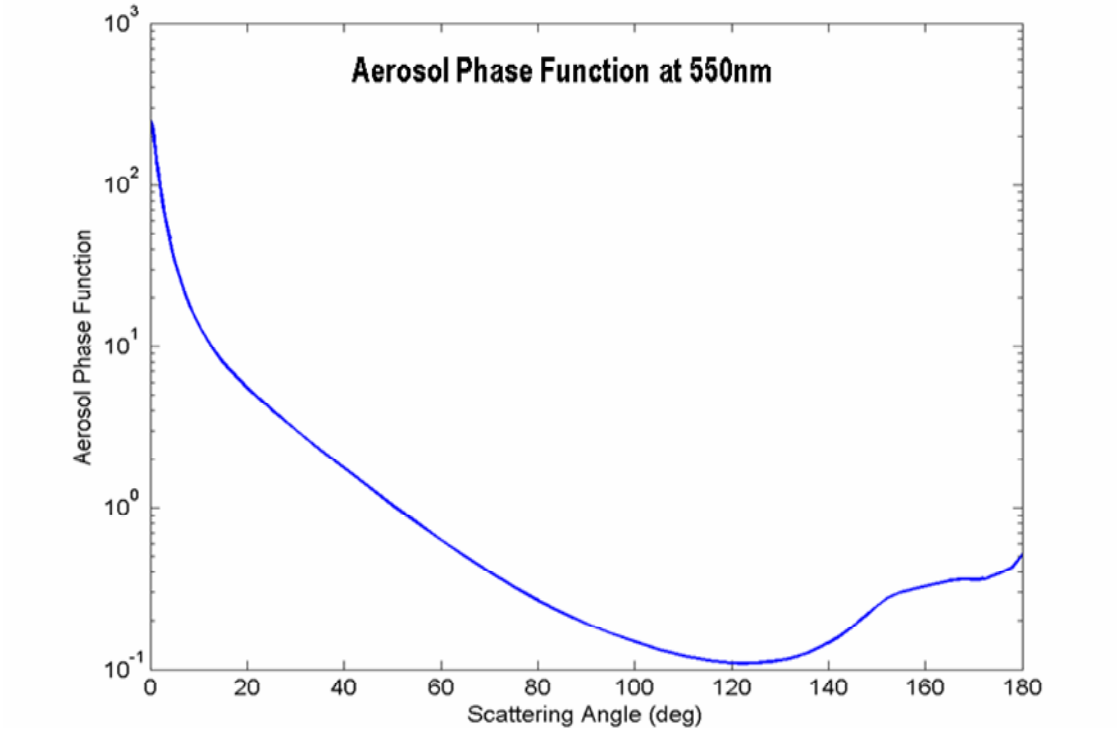

Figure 4-9. Example of Shettle and Fenn aerosol optical properties used in the Aerosol ACO LUTs and input into the COART RTM to verify the aerosol and aerosol-Rayleigh radiance produced by the LUTs. The Maritime Aerosol (70%RH) for an AOT at 865nm of 0.12 is shown here

Use or disclosure of data contained on this page is subject to the export restriction(s) on the title page of this document.

D45702, A. PDMO Released: 2009-02-18 (VERIFY REVISION STATUS)
PDMO

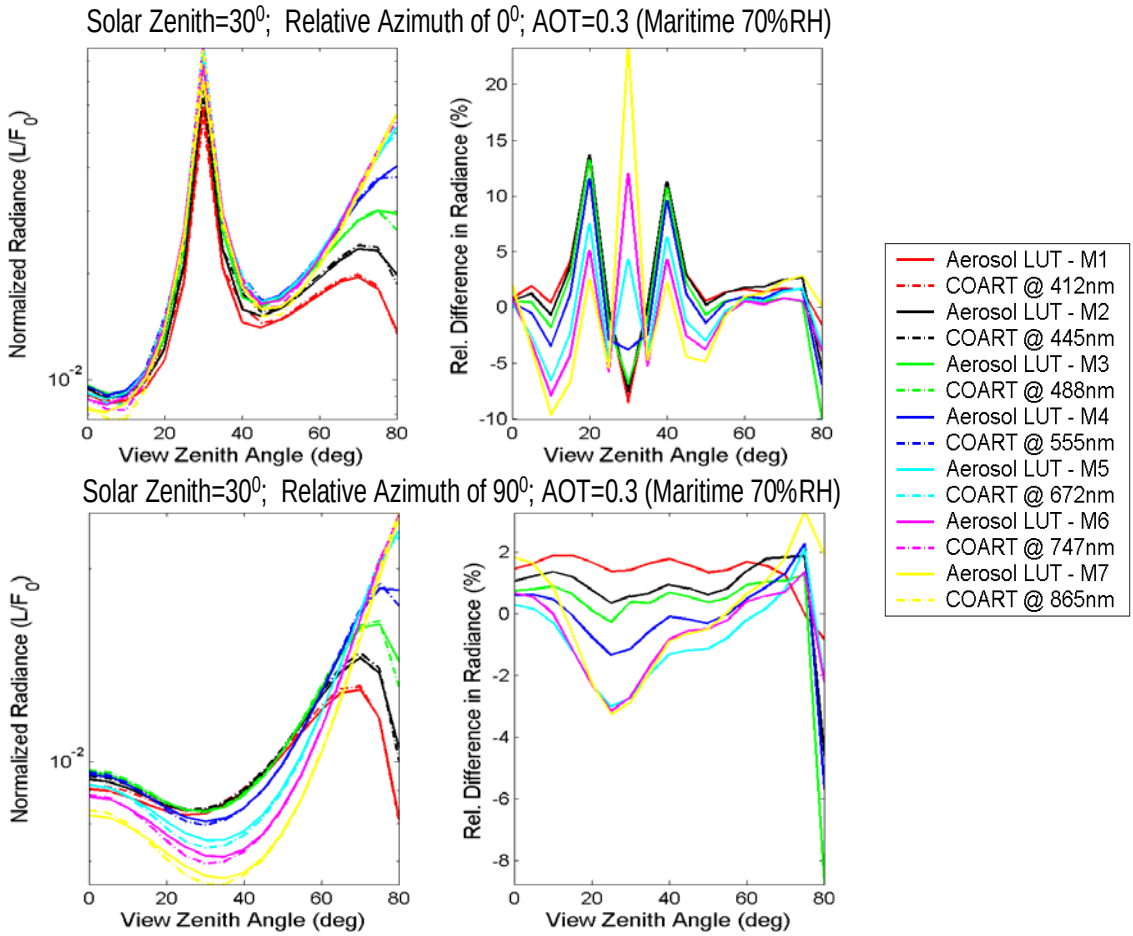

Figure 4-10. Comparison of TOA aerosol and aerosol-Rayleigh radiance from ACO LUT to COART RTM for a flat ocean surface as a function of sensor zenith angle for solar zenith angle of 30^0 and relative azimuths of 0^0 (a) and 90^0 (b)

Use or disclosure of data contained on this page is subject to the export restriction(s) on the title page of this document.

D45702, A. PDMO Released: 2009-02-18 (VERIFY REVISION STATUS)
PDMO

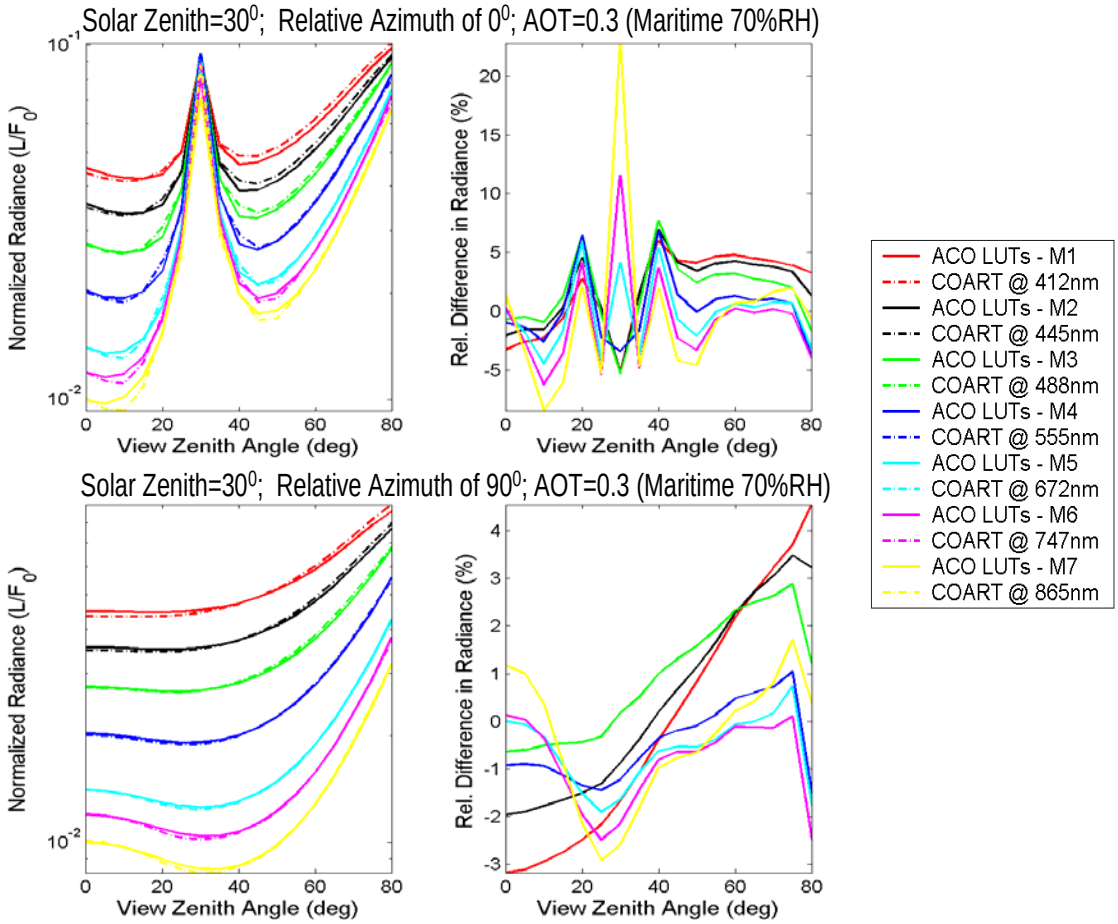

Figure 4-11. Comparison of TOA total path radiance (Rayleigh, aerosol and aerosol-Rayleigh) from ACO LUTs to COART RTM for a flat ocean surface as a function of sensor zenith angle for solar zenith angle of 30^0 and relative azimuths of 0^0 (a) and 90^0 (b)

Use or disclosure of data contained on this page is subject to the export restriction(s) on the title page of this document.

D45702, A. PDMO Released: 2009-02-18 (VERIFY REVISION STATUS)
PDMO

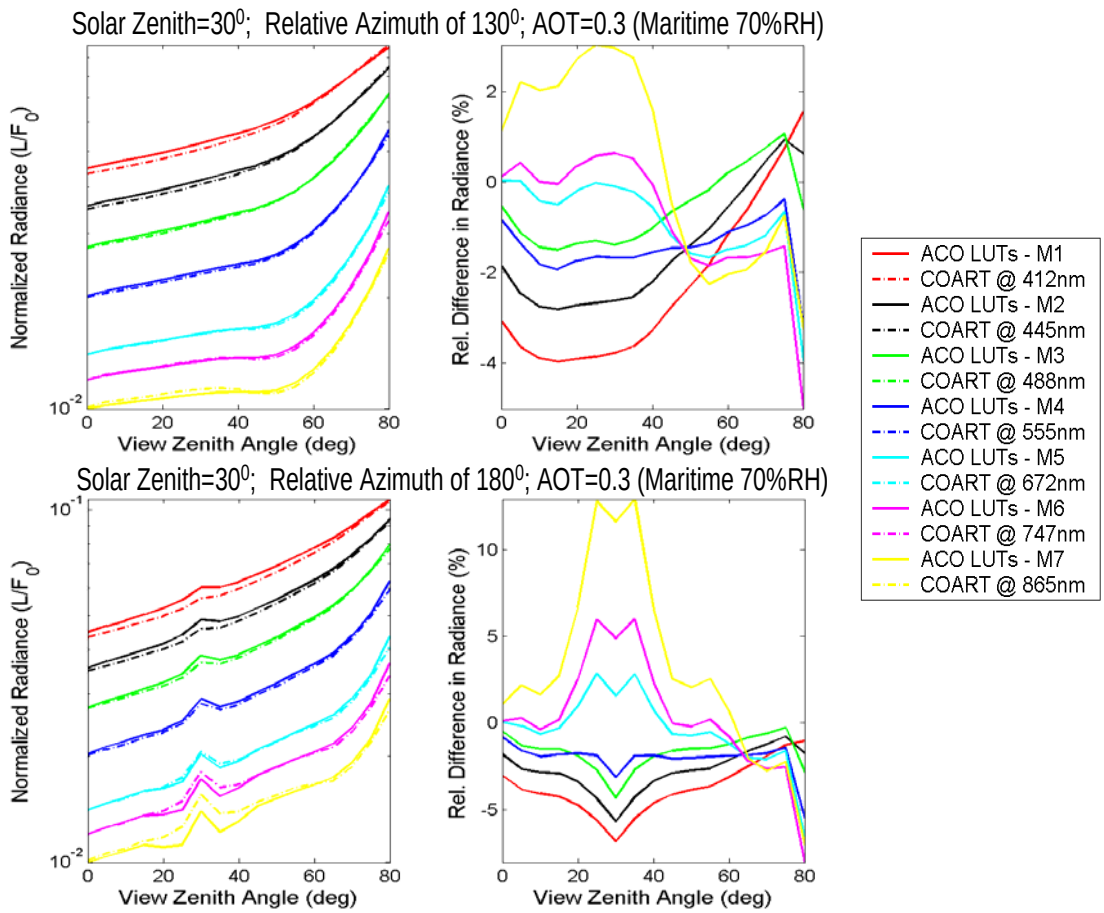

Figure 4-12. Comparison of TOA total path radiance (Rayleigh, aerosol and aerosol-Rayleigh) from ACO LUTs to COART RTM for a flat ocean surface as a function of sensor zenith angle for solar zenith angle of 30^0 and relative azimuths of 130^0 (a) and 180^0 (b)

Use or disclosure of data contained on this page is subject to the export restriction(s) on the title page of this document.

D45702, A. PDMO Released: 2009-02-18 (VERIFY REVISION STATUS)
PDMO

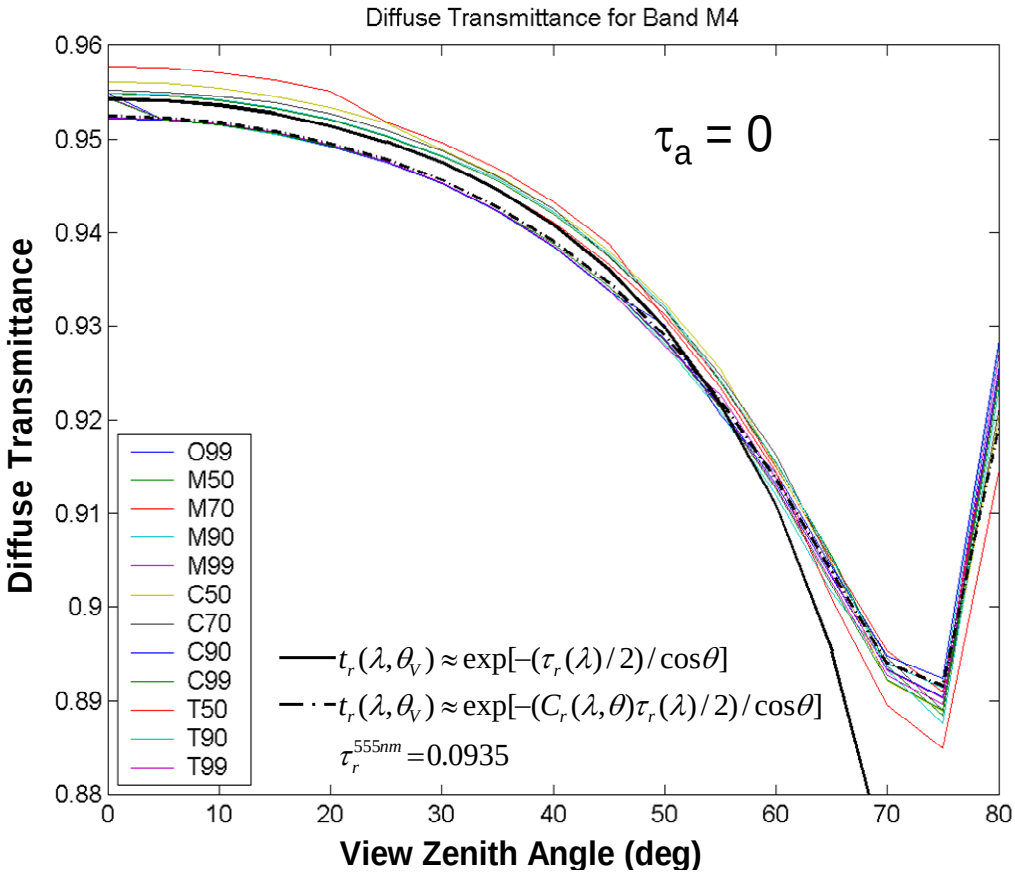

Figure 4-13. Anomalies produced by diffuse transmittance LUT for pure Rayleigh atmosphere

Use or disclosure of data contained on this page is subject to the export restriction(s) on the title page of this document.

D45702, A. PDMO Released: 2009-02-18 (VERIFY REVISION STATUS)
PDMO

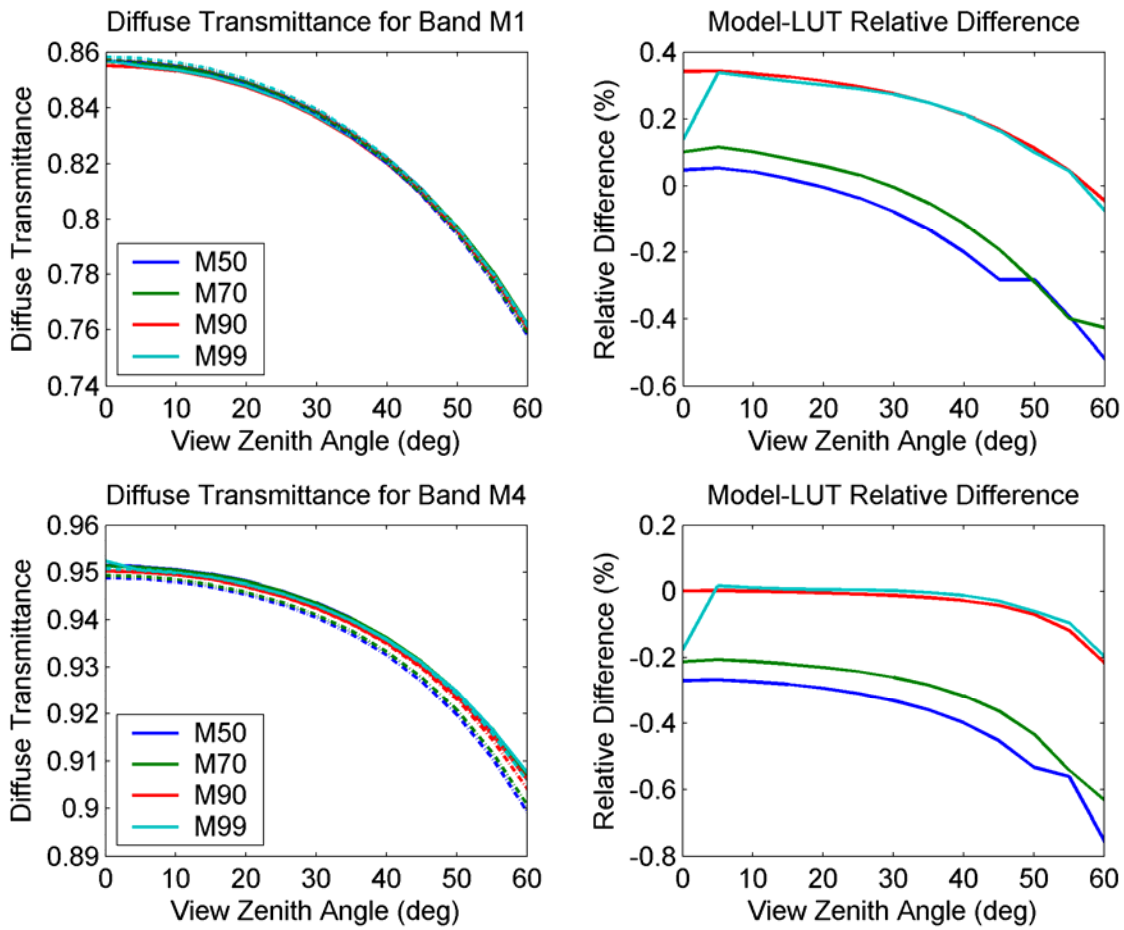

Figure 4-14. Accuracy of diffuse transmittance from ACO LUT at low end of open-ocean AOT range

Use or disclosure of data contained on this page is subject to the export restriction(s) on the title page of this document.

D45702, A. PDMO Released: 2009-02-18 (VERIFY REVISION STATUS)
PDMO

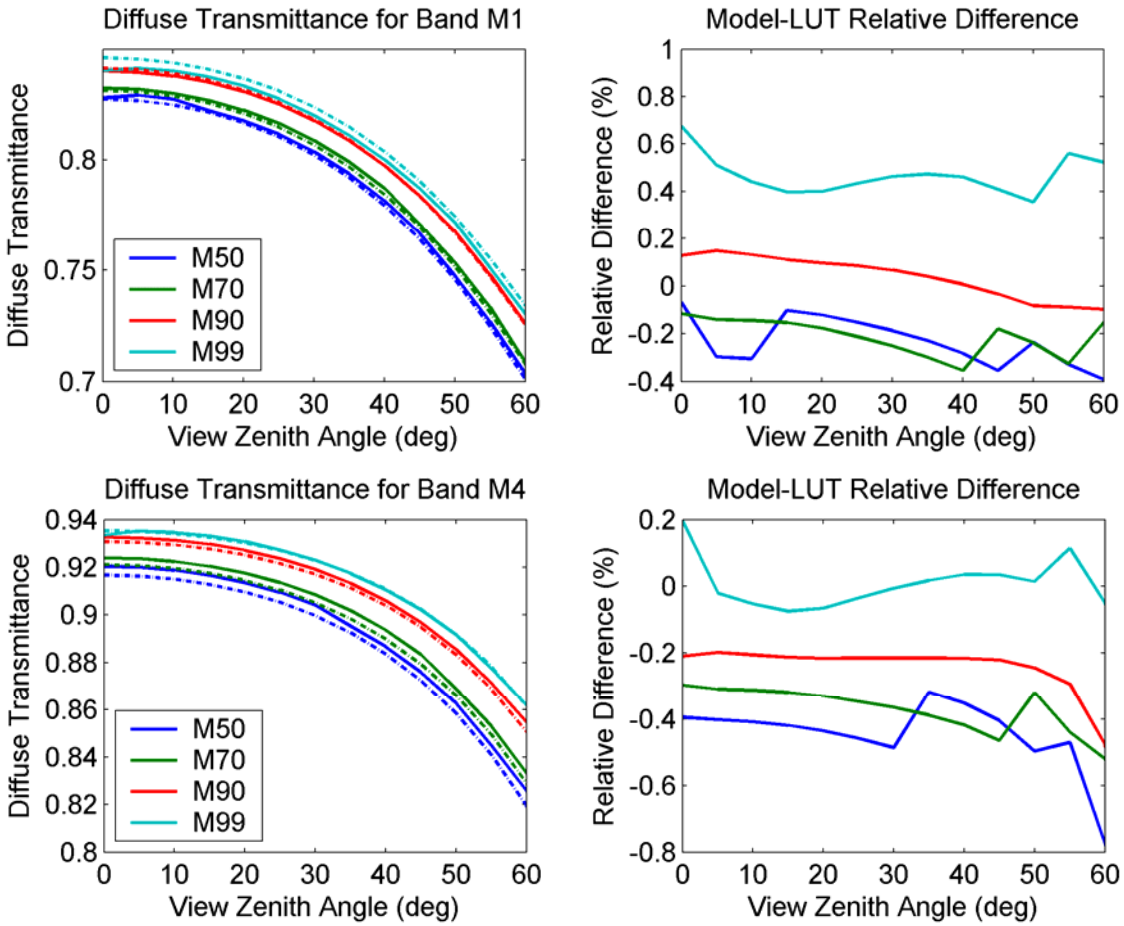

Figure 4-15. Accuracy of diffuse transmittance from ACO LUT at high end of open-ocean AOT range

Use or disclosure of data contained on this page is subject to the export restriction(s) on the title page of this document.

D45702, A. PDMO Released: 2009-02-18 (VERIFY REVISION STATUS)
PDMO

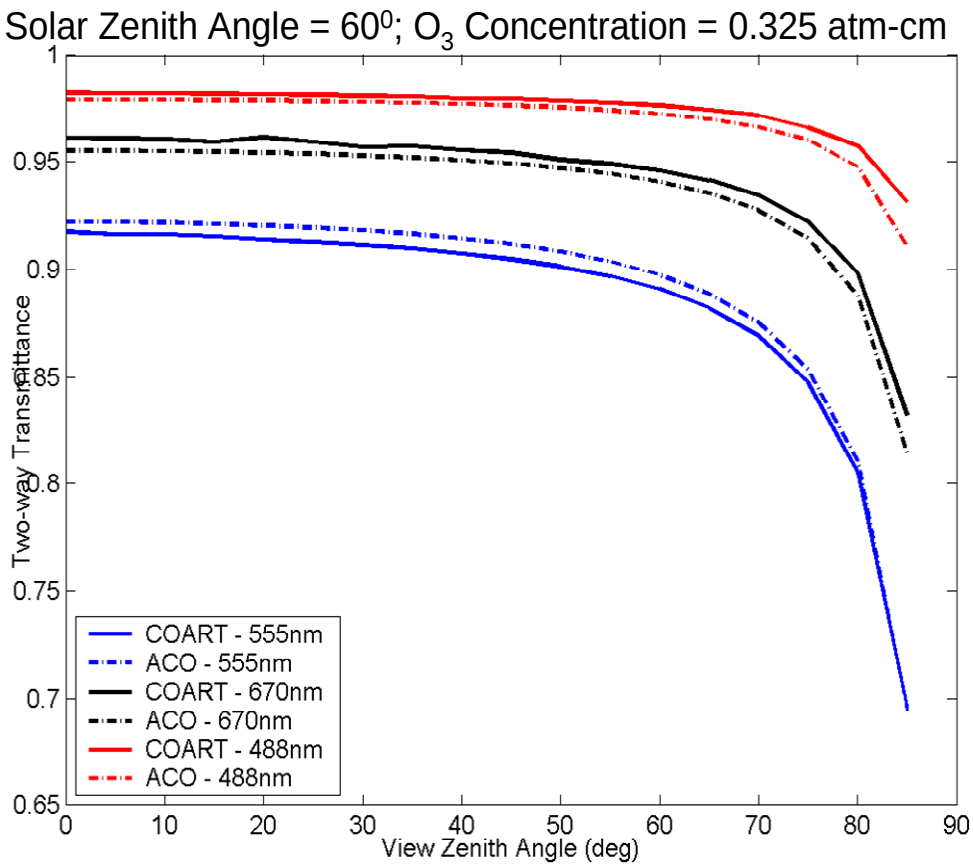

Figure 4-16. ACO model for two-way ozone transmittance has been verified against the COART RTM

Use or disclosure of data contained on this page is subject to the export restriction(s) on the title page of this document.

D45702, A. PDMO Released: 2009-02-18 (VERIFY REVISION STATUS)
PDMO

The samplings of spacecraft, sensor and scene conditions were based on our normal Global Synthetic Datasets. In particular, the sun-sensor geometries are consistent with NPP 1330 orbital plane and the VIIRS scanning geometry. Decimated sampling of the VIIRS scan includes samples from each of the aggregation zones. The geophysical properties used by the ACO LUTs to generate TOA radiance include the sensor zenith and azimuth, solar zenith and azimuth, surface pressure, wind speed and temperature, total column ozone, and MODIS 8-day AOT (MOD08E3). These were sampled from NCEP FNL datasets for each of 12 days, representing 1 day per month over a year. Samples were filtered for sun-glitter contamination, selecting only those samples with a normalized glitter radiance less than $1x10^{-4}$, and solar zenith angles greater than 70^0. An illustration of the samples selected for one particular day is shown in Figure 4-17.

Sensor effects for this dataset were limited to just the nominal noise currently expected from the VIIRS sensor. This was added based on both the aggregation zone corresponding to a particular pixel and the magnitude of the radiance observed by the pixel. Examples of the LUTs used to generate the sensor noise are shown in Figure 4-18, with the actual distribution of NEDN used for the NGST Global Synthetic Dataset shown in Figure 4-19.

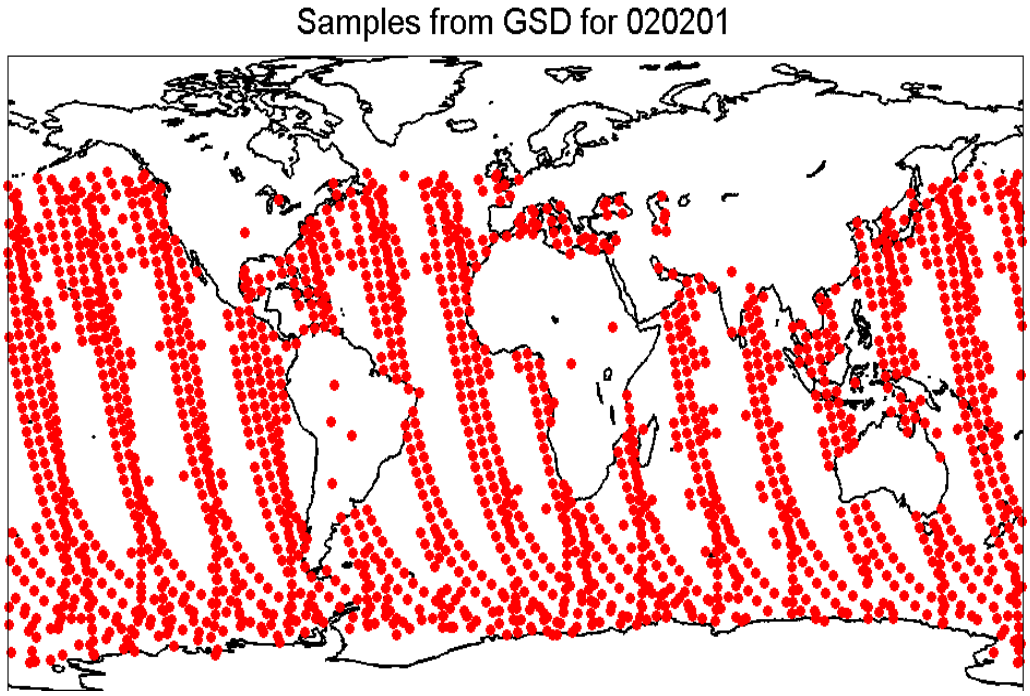

Figure 4-17. Sampling of geophysical properties and sun-sensor geometry based on Global Synthetic Datasets

Use or disclosure of data contained on this page is subject to the export restriction(s) on the title page of this document.

D45702, A. PDMO Released: 2009-02-18 (VERIFY REVISION STATUS)
PDMO

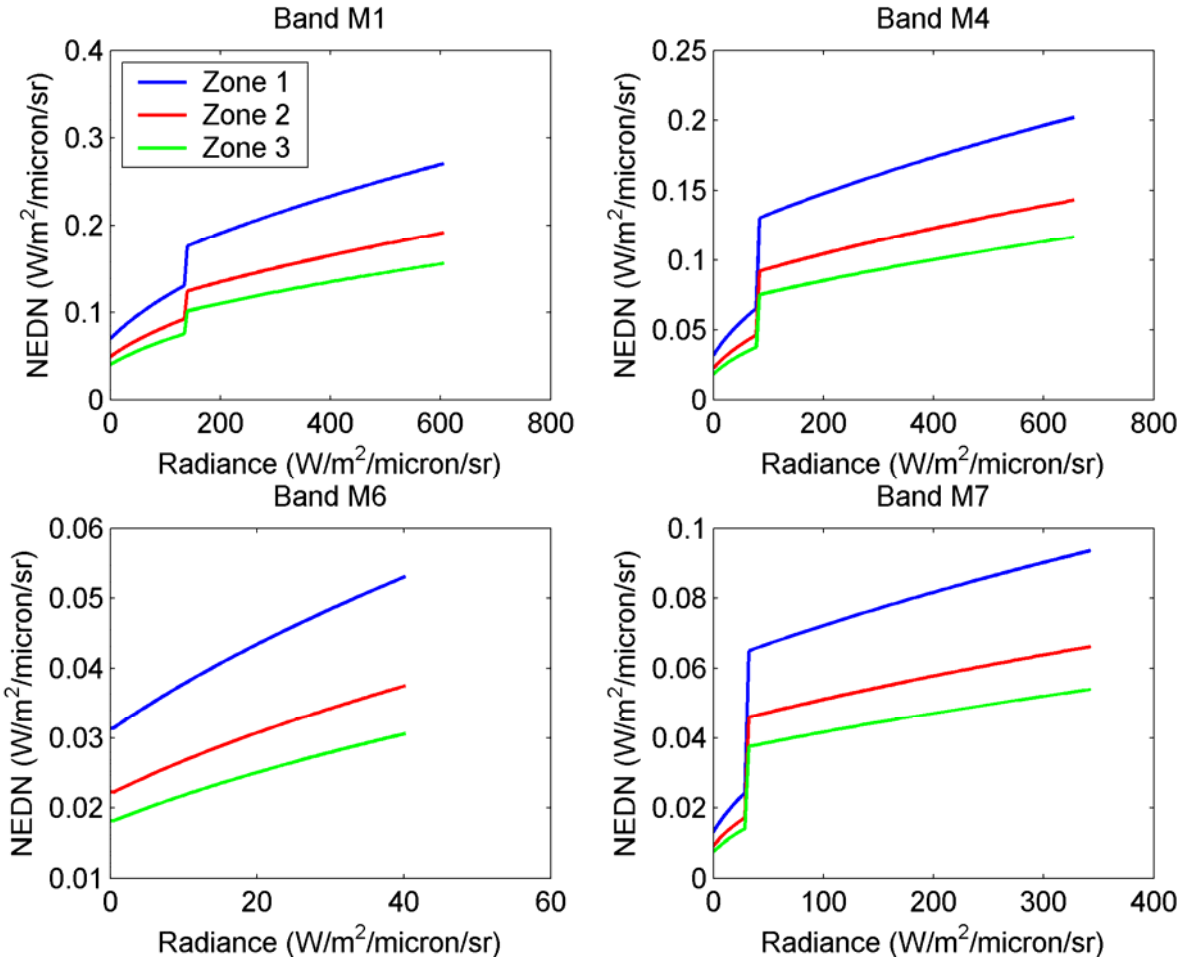

Figure 4-18. Nominal noise characteristics obtained from sun-sensor NEDN-Radiance LUTs

Use or disclosure of data contained on this page is subject to the export restriction(s) on the title page of this document.

D45702, A. PDMO Released: 2009-02-18 (VERIFY REVISION STATUS)
PDMO

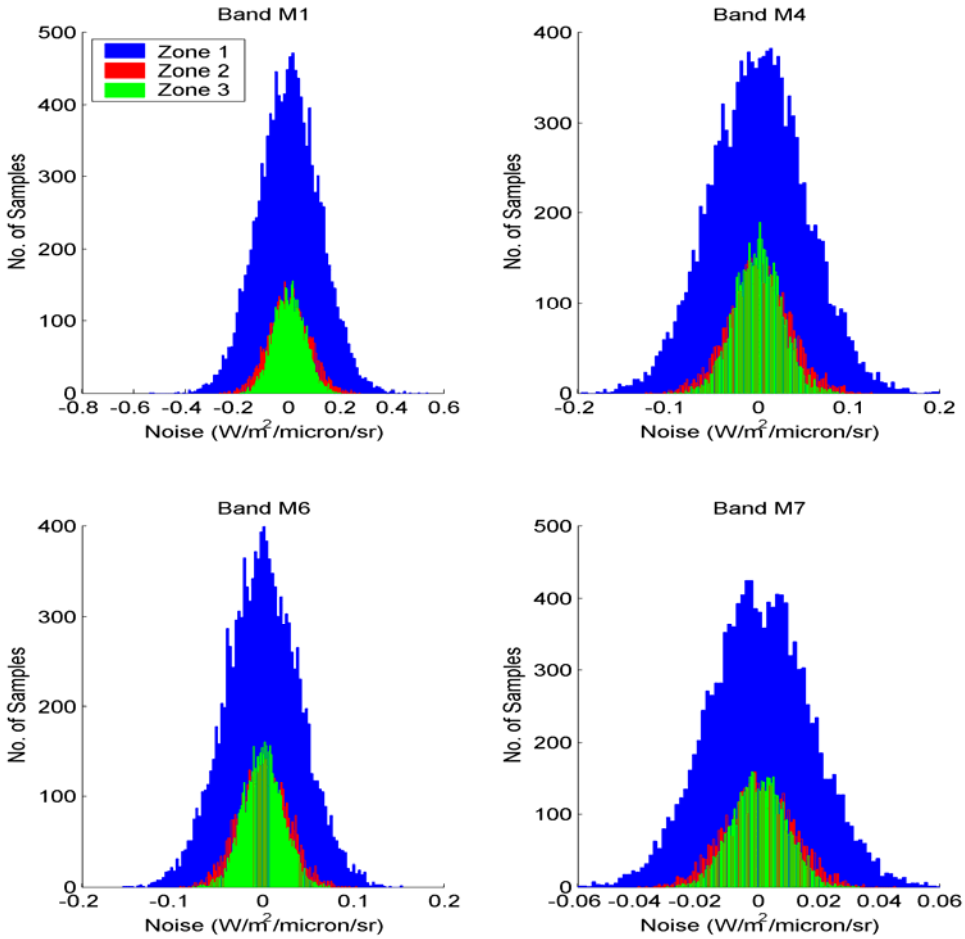

Figure 4-19. Distribution of sensor noise added to Global Synthetic Dataset TOA radiances

Use or disclosure of data contained on this page is subject to the export restriction(s) on the title page of this document.

D45702, A. PDMO Released: 2009-02-18 (VERIFY REVISION STATUS)
PDMO